Structure and Property Evolution Induced by the Phase Transitions in Several Antiferroelectric Materials

by

Teng Lu

Research School of Chemistry

A thesis submitted for the degree of Doctor of Philosophy of The Australian National University

Dec 2017

Declaration

This thesis is a collection of the major studies arising from my own independent research work during my PhD candidature. Except where specifically mentioned in the text, this thesis constitutes original work carried out by the candidate.

Teng Lu

Acknowledgements

First and foremost, I would like to express my sincere gratitude to my supervisor Prof. Yun Liu. It has been my honour to be her PhD student. Her patient guidance, immense knowledge, motivations, support, trust and tolerance were the foundations that allowed me to complete my PhD project with stimulating and productive outcomes. I would also like to thank my advisor Prof. Ray L. Withers, for his co-supervision. His profound knowledge, and insightful comments helped me lay a solid foundation with respect to crystal structure determination. I would also like to thank my thesis advisors Dr. Lassé Noren and Dr. Hua Chen for their excellent advice and assistance in X-ray and neutron diffraction, and electron microscopies.

I also give thanks to the beam scientists at the Australian Nuclear Science and Technology Organisation (ANSTO), Dr Andrew J. Studer and Dr Dehong Yu. The neutron facilities were beneficial techniques for my PhD study. Without their precious support, it would have been impossible to conduct the essential experiments.

I thank the members of the Functional Materials Research Group. Thanks for their assistance, instructions and discussions. They are a source of friendship as well as good advice and collaboration.

I would also like to thank my important collaborators, Prof. Yujun Feng, Prof. Zhuo Xu, Prof. Xiaoyong Wei and Dr. Ye Tian in Xi’an Jiaotong University and Prof. Genshui Wang, Prof. Xianlin Dong at Shanghai Institute of Ceramics, CAS. The high-quality samples you provided to me were interesting and meaningful.

Last but not the least, I would like to thank my family and friends, especially my parents and wife, Yi Wang, for their companionship, love, selfless sacrifices and encouragement. Their support helps me overcome the difficulties in my daily life.

Abstract

Antiferroelectric (AFE) materials are an important group of functional materials showing unique properties such as double polarization-electric field (*P*-*E*) hysteresis loop, and charge release under the pressure and temperature. These performances are strongly connected to the structural phase transitions induced by external conditions. Many investigations were carried out to optimize their properties but the structure-property relationship of such AFE materials still remain unclear. With this bearing in mind, in this thesis, I firstly investigate the crystal structure, domain structure and properties evolution under the external stimuli such as electric-field (E-field), mechanical force, and temperature in the typical $PbZrO_3$-based AFE materials. Secondly, a systematic study was conducted on the doped silver niobate ceramics to understand the impacts of the chemical composition and E-field cycling on these novel lead-free AFE materials.

The targeted materials of typical $PbZrO_3$-based samples were selected as La/Nb doped Pb(Zr, Sn, Ti)O_3 ternary systems with the composition $Pb_{0.97}La_{0.02}(Zr_{0.56}Sn_{0.33}Ti_{0.11})O_3$ (PLZST1), $Pb_{0.99}(Nb_{0.02}Zr_{0.73}Sn_{0.21}Ti_{0.04})O_3$ (PNZST1) and $Pb_{0.99}(Nb_{0.02}Zr_{0.65}Sn_{0.28}Ti_{0.05})O_3$ (PNZST2). These three compositions are representative, supplying diverse phase transition behaviours for studying. The *in-situ* neutron powder diffraction (NPD) of the PLZST1 material reveals that the pseudo-tetragonal AFE phase is transferred into the rhombohedral FE phase with an application of the sufficient E-field, and recovers after withdrawal of the external field. The resultant average structure change as a function of the E-field is in accordance with the reversible AFE-FE phase transition. However, the ω-dependent NPD patterns suggest this process is not fully reversible: in the induced FE state, the strain exhibits an elliptical distribution, which in turn leads to significant preferred orientation in the final AFE state. The formation of this preferred orientation provides an explanation for the properties variation appearing in AFE materials after exposure to the sufficiently high E-field.

X-ray diffraction pattern of PNZST1 sample indicates the orthorhombic AFE

phase while the result of NPD contradicts this conclusion with a rhombohedral FE phase. After careful characterization of the surface and bulk properties, it is found that the near surface and bulk regions show different phases. Additionally, the surface processing such as polishing and heat-treatment can induce an AFE/FE phase transition within micrometres of the surface. The *in-situ* hydrostatic-pressure neutron diffraction proves that the mechanical force helps stabilize the AFE phase of this composition. Therefore, the surface processing induced phase transitions can be attributed to the change of states of residual stress.

The *in-situ* NPD studies of PNZST2 material describe its structural variation as a function of E-field and temperature. Through the mode decomposition approach, the relationships between AFE/FE modes and octahedral rotation mode were systematically investigated. At room temperature, the pristine AFE phase can be poled into the meta-stable FE phase by applying the external E-field. At this stage, both AFE and FE phases consist of modes associated with octahedral rotation and A-site ionic displacements. The temperature-induced phase transition indicates that the octahedral rotation and ionic displacements are weakly coupled in the room-temperature FE phase and decoupled in the high-temperature FE phase. Furthermore, both temperature and E-field-induced phase transitions between the AFE and high-temperature FE phase demonstrate the critical role of coupling between the octahedral rotation and A-site ionic displacements in AFE structure stabilization.

The evolution of structure and electrical properties with composition in (1-x)$AgNbO_3$-$x$$LiTaO_3$ (ANLT100x) ($0 \leq x \leq 0.09$) ceramics have been systematically investigated by diffraction techniques, complemented by dielectric and polarisation measurements. The symmetry mode decomposition and Rietveld refinement of distortive modes were firstly used to analyse the origin of the anti/ferroelectricity observed. The in/out phase octahedral tilting around the *a*-axis (H2 mode) and the antiparallel ionic displacements (Λ3 mode), present large amplitudes in the pure $AgNbO_3$. These two modes vanish progressively with increasing x and their amplitudes experience a sudden drop when $x = 0.053$. Accompanied by the disappearance of these two modes, a new phase with $R3c$ symmetry appears and grows with further increasing $LiTaO_3$ content. The composition dependent amplitudes of the primary modes, and *R*3*c* phase fractions, lead to a comprehensive understanding of the dielectric and ferroelectric properties affected by $LiTaO_3$. For the composition located around the phase boundary, $x = 0.045$ and 0.06, FE wake-up effects were detected. The refinement of neutron diffraction patterns after different electric cyclicity describe an increase of ferroelectricity associated with the *R*3*c* phase fraction increments *i.e.*, field-cycling-induced phase transition from $Pmc2_1$ to *R*3*c*. The local probes such as the electron diffraction and piezoresponse microscopy (PFM), show that the in/antiphase octahedral rotation around the $<001>_p$ and the local strain state are the decisive factors for this field-cycling-induced phase transition. In summary, the wake-up effects can be regarded as the nucleation and growth of the *R*3*c* phase with increasing number of electric cycles.

Table of Contents

List of Figures

Glossary and List of abbreviations

Description	**Abbreviation**
Physical Property Abbreviations	
Polarisation vector	$\mathbf{P}$
Electric-field vector	$\mathbf{E}$
Dielectric susceptibility tensor	χ
Dielectric permittivity	ε
Dielectric loss	$tan\delta$
Dielectric displacement	$\mathbf{D}$
Stress tensor	X
Strain tensor	x
Piezoelectric coefficient tensor	d
Atomic position	$\mathbf{r}$
Atomic displacement	$\mathbf{u}$
Modulation wave-vector	$\mathbf{q}$
Global amplitude	A_τ
Curie temperature	T_{C}, T_0
Coercive field	E_C
Spontaneous polarisation	P_S
Remnant polarisation	P_r
Pressure	p
Frequency	f
Rotation angle	ω
Azimuthal angle	Ψ

Rotation angle between two adjacent octahedra	φ
Crystallography	
Lattice parameters	a, b, c, α, β, γ
A lattice plane in real space	(h k l)
A family of symmetry equivalent (h k l) planes	{h k l}
A real space direction	[u v w]
A family of symmetry equivalent [u v w] directions	<u v w>
A reflection in reciprocal space	[h k l]*
A family of symmetry equivalent [h k l]* reflections	<h k l>*
Bragg reflection in reciprocal space	**G**
The spacing between (h k l) planes	d_{hkl}
Materials	
$PbZrO_3$	PZ
$Pb(Zr_{1-x}Ti_x)O_3$	PZT
$Pb(Nb,Zr,Sn,Ti)O_3$	PNZST
$(Pb,La)(Zr,Sn,Ti)O_3$	PLZST
$AgNbO_3$	AN
$(1-x)AgNbO_3-xLiTaO_3$	ANLT100x
Instruments and Techniques	
Atomic force microscopy	AFM
Piezoresponse force microscopy	PFM
Switching spectroscopy Piezoresponse force microscopy	SS-PFM
Inductance, capacitance and resistance meter	*LCR* meter
Scanning electron microscopy	SEM
Energy-dispersive X-ray spectroscopy	EDS

X-ray powder diffraction	XPRD
Neutron powder diffraction	NPD
Electron diffraction	ED
Transmission electron microscopy	TEM
Dual AC resonance tracking	DART

Chapter 1 Introduction

This chapter introduces the basic concepts and background knowledge which are helpful to understand the research results presented in this thesis. It involves the descriptions of ferroelectricity, antiferroelectricity and related phase transitions. The perovskite structure, domain structure and simplified symmetry-mode crystallography are also addressed for better understanding the average and local structural origin of related properties. At the end of this chapter, the motivation and outline of this thesis are briefly stated.

1.1 Perovskite Structure

The perovskite is an important group of crystals, exhibiting interesting and useful functional properties such as piezoelectricity, ferroelectricity (*e.g.* $Pb(Zr,Ti)O_3$), antiferroelectricity (*e.g.* $PbZrO_3$), multiferroic behaviour (*e.g.* $BiFeO_3$), ionic conductivity ($La_{0.67-x}Li_xTiO_3$) and photovoltaic effects (*e.g.* $CH_3NH_3PbI_3$).[1-5] The general formula of perovskite is written as ABX_3 with a cubic space group *Pm*-3*m* (Figure 1-1). In this picture, the B-site ion is located at the corner, surrounded by 6 X ions. The BX6 octahedra are connected by the shared corners, constructing a 3-D framework. The A-site ions (or molecules) are located at the centre with a 12-fold coordination to X.

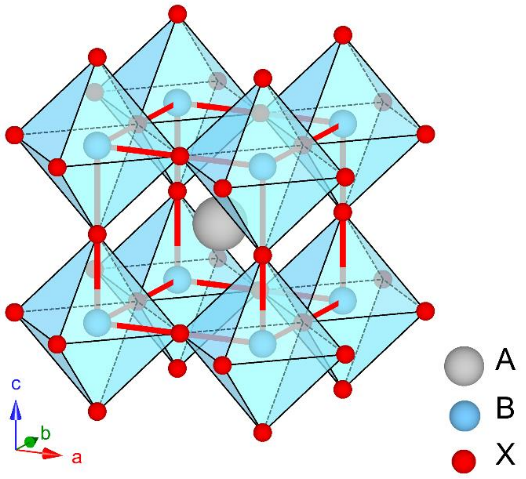

Figure 1-1 The parent cubic perovskite structure of ABX_3. The BX6 octahedra form the framework and A-site cation is located at the interstice.

Most perovskite materials, compared with the ideal cubic structure, exhibit lower symmetry because of the distortions under ambient conditions. The distortions can be briefly divided into two classes: 1) cation displacements and 2) octahedral tilting (Figure 1-2).[6, 7] These distortions are of significance to the anti-/ferroelectricity investigated in this thesis.

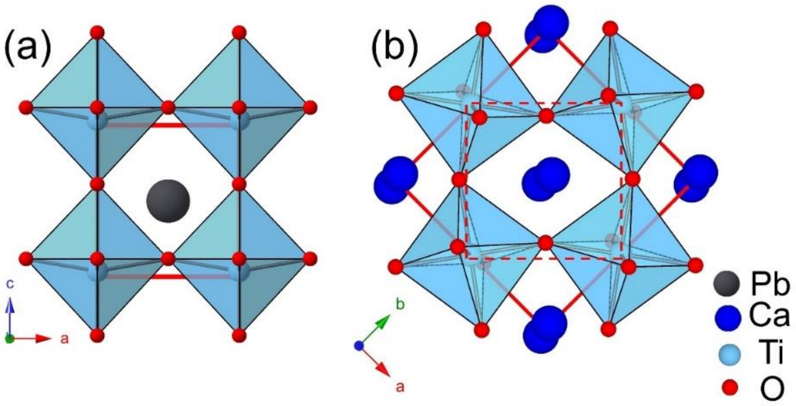

Figure 1-2 The structure of (a) tetragonal $PbTiO_3$ viewed along *b*-axis and (b) orthorhombic $CaTiO_3$ viewed along *c*-axis.

1.2 Ferroelectricity

1.2.1 Basic Concepts

The dielectric property describes the polarizability of insulating materials under an external electric field (E-field). When a dielectric material is placed in an external E-field, the positive and negative charges shift under the Coulomb force,[8] generating the dielectric polarisation, **P**. Due to this property, dielectric materials are widely used as the devices for charge storage. The surface charge density induced by the external E-field is described as the dielectric displacement, **D**:

$$\mathbf{D} = \varepsilon_0\mathbf{E}+\mathbf{P} = \varepsilon_0\mathbf{E} + \varepsilon_0\chi\mathbf{E} = \varepsilon_0\varepsilon_r\mathbf{E} \tag{1.1}$$

Where the dimensionless value ε_r is the relative dielectric permittivity, or dielectric constant used for polycrystalline materials in this thesis.[9]

For functional materials, there is no structural restriction for dielectric properties while the piezoelectricity is structure-dependent, and only obtained in the 20 non-centrosymmetric point groups. Piezoelectric properties reflect the capability of transferring applied-mechanical energy into electrical energy or vice versa. For the piezoelectric materials, the electrical charge (polarisation) can be generated by the external mechanical stress (direct piezoelectric effect), or the strain can be induced by applying E-field (converse piezoelectric effect).[10]

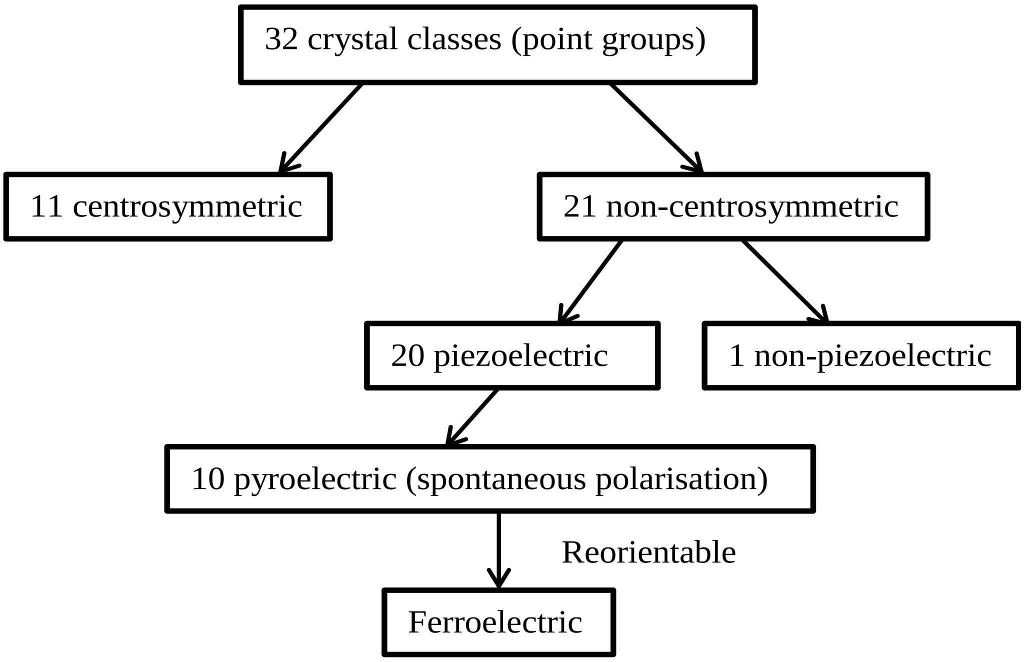

Figure 1-3 A schematic diagram of the relationship between piezoelectrics, pyroelectrics and ferroelectrics.

Among 20 non-centrosymmetric point groups, 10 contain a unique polar axis, allowing the appearance of a spontaneous polarization (P_S). Pyroelectric properties describe how the P_S varying as a function of the temperature. Among the pyroelectric materials, if the observed P_S in crystals contains at least 2 equivalent orientational states which can be switched from one to another by an external E-field, the materials are defined as the ferroelectrics (FEs). Figure 1-3 depicts a classic hierarchy of relationship among the piezoelectric, pyroelectric and ferroelectric materials.[11]

1.2.2 Ferroelectric Properties

FE materials generally undergo a phase transition from a high-symmetry paraelectric (PE) phase to a low-symmetry FE phase when cooling down from the high temperature. The FE-PE phase transition is associated with the dielectric anomaly at Curie temperature,

T_C, and at $T > T_C$, the reciprocal of the dielectric constant follows a Curie-Weiss law, which can be expressed as:[9]

$$\varepsilon = \frac{C}{(T - T_0)} \tag{1.2}$$

where C is the Curie constant and ε is the dimensionless dielectric constant. Note that here T_0 is the Curie-Weiss temperature, only being equal to T_C for the continuous phase transition.

The dielectric anomaly at the Curie temperature is a typical feature for FE materials. The soft-mode theory and the results of first principle calculation suggest this dielectric anomaly is attributed to the softening, destabilisation of the first Brillouin zone centre polar phonon mode in the PE phase.[12-18] Instead of the theory from the lattice dynamic point of view, the phenomenological theory, or known as the Landau-Ginzburg-Devonshire (LGD) theory, describes the PE-FE phase transition from a symmetry-based point of view. In this theory, the thermodynamic states of two phases are same at the transition line. The free energy G can be expressed as a Taylor expansion in powers of the order parameter. The concept of the order parameter is very useful in understanding the symmetry-mode description of the distorted structure, domains, *etc*. For the proper perovskite FE materials, the primary order parameter is the polarisation, P. Commonly, the FE phase presents a structural distortion with respect to its PE phase, indicating that the spontaneous strain, x_S is induced during the PE-FE phase transition. Therefore, precisely, LGD theory for FE materials need to consider the external E-field and elastic stress conditions. In this section, the strain field is ignored for simplicity and G is expressed as:

$$G = \frac{\alpha}{2}P^2 + \frac{\beta}{4}P^4 + \frac{\gamma}{6}P^6 - EP \tag{1.3}$$

The α is temperature-dependent while β and γ are temperature-independent. If $\beta > 0$, the transition is the 2nd order, (continuous) and for $\beta < 0$, the transition becomes 1st order, (discontinuous). To minimize the free energy, it can be deduced:

$$E = \alpha P + \beta P^3 + \gamma P^5 \tag{1.4}$$

$$\frac{\partial E}{\partial P} = \varepsilon = \alpha + 3\beta P^2 + 5\gamma P^4 \tag{1.5}$$

In the PE phase, $P = 0$ and in the FE phase, $P \neq 0$. The temperature-dependent P_S and ε are shown in Figure 1-4. Clearly, the dielectric anomaly is observed at the Curie temperature, where the thermodynamic energy is supposed to be the same for both phases. It is worthy to note that three energy minima can be reached when $T = T_C$ for the 1st order phase transition. At this stage, a double *P-E* hysteresis loop is obtained, but this behaviour is quite different from the antiferroelectric (AFE) properties mentioned in the following section.[19] The appearance of the double *P-E* hysteresis loop is not the sufficient criterion for designation as an AFE material, and therefore the structural analyses are required to understand the antiferroelectricity.

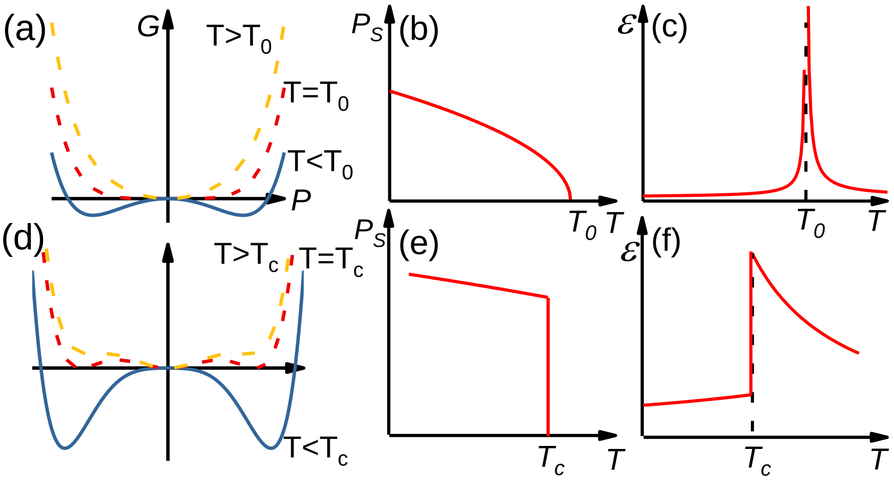

Figure 1-4 Free energy as a function of the polarisation for (a) 2nd order and (d) 1st order phase transition, spontaneous polarisation as a function of temperature for (b) 2nd order and (e) 1st order phase transition, dielectric constant as a function of temperature for (c) 2nd order and (f) 1st order phase transition.

According to the phenomenological theory, the order parameter contains several equivalent states in the FE phase.[20] Taking BaTiO$_3$ as an example, its time-averaged PE structure is cubic. When it transfers into the tetragonal FE phase in the absence of an E-field and mechanical stress, six <001>$_p$ directions are physically equivalent to form the polar axis (Figure 1-5a). Additionally, the lattice deformation during this PE-FE phase transition induces the spontaneous strain. In order to minimize the electrostatic and elastic energies of the system, regions with different polarisation states are developed. The region where the spontaneous polarisations are uniformly oriented is called the FE domain. The boundary separating different domains are domain walls.[11] For the tetragonal structure, 180° and 90° domains are formed.[21] If the structure of the FE phase belongs to the rhombohedral crystal system (Figure 1-5b), eight $<111>_p$ directions share the same probability of developing the polar axis. Therefore, 180°, 71° and 109° domains are formed instead of 90° domains.[22] Many factors such as E-fields, mechanical boundary conditions, heat-treatment, and microscopic defects can impact the formation of FE domains.[23-26]

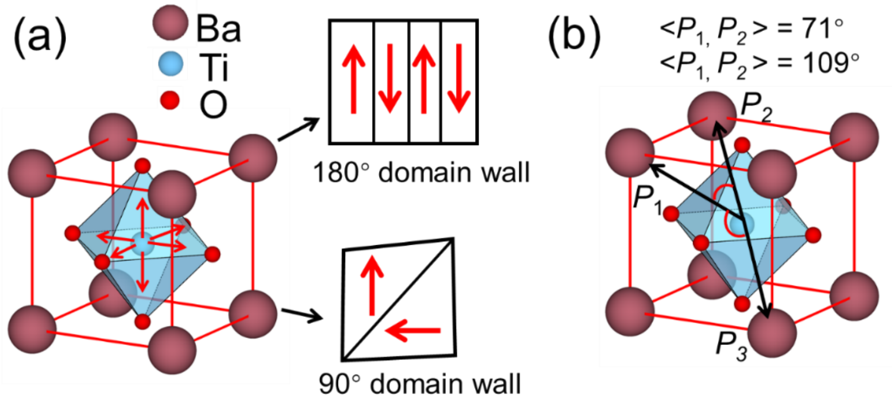

Figure 1-5 (a) Formation of 180° and 90° domains in the tetragonal $BaTiO_3$. (b) Formation of 71° and 109° domains in the rhombohedral $BaTiO_3$.

Another important property for FE materials is the reorientable P_S under an external E-field, which is usually characterized by the P-E hysteresis loop experimentally. Figure 1-6a schematically demonstrates a typical P-E hysteresis loop and underlying FE domain evolutions. At the beginning, no macroscopic polarisation is detected due to the randomly orientated FE domains. When the strength of the applied field is sufficiently high, all domains align in the same direction. At this stage, polarisation reaches a saturation level and shows a linear relationship with the E-field. The P_S is normally estimated by intersecting the polarisation axis with the saturated linear part. After removal of the E-field, some domains exhibit back switching but the measured polarisation is non-zero, which is defined as the remnant polarisation, P_r. In order to reach zero polarisation, an opposite E-field which is named as the coercive field, E_C, is required.[9]

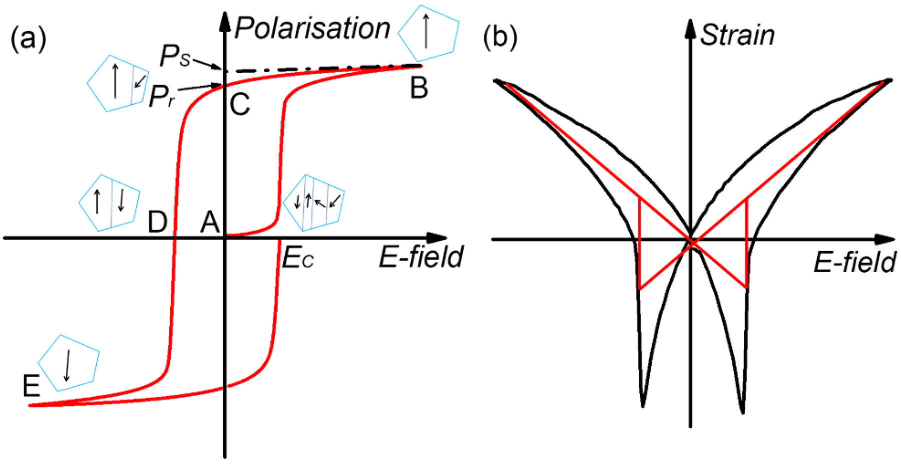

Figure 1-6 Schematic of a typical ferroelectric *P-E* hysteresis loop. (reproduced from D. Damjanovic[9])

Associated with the *P-E* hysteresis loop, the strain-electric field (*S-E*) hysteresis loop is shown in Figure 1-6b. Ideally, the relationship between the strain and E-field is linear except for the polarisation reversal (red line). However, due to the domain wall motion,[25] the shape of *S-E* loops is like a 'butterfly', presenting the non-linear relationship for most FE materials. As described above, FE materials contain several kinds of domains, which generally can be divided into 180° and non-180°, *e.g.*, 90°, 71° and 109°, domains. The spontaneous strain in the 180° domain remains the same but in the non-180° domain, their states are different. Thus, the non-180° domains are also ferroelastic. Clearly, in FE materials, non-180° domains exhibit different spontaneous polarisation as well as strain states, which makes a contribution to the electromechanical coupling.[27] Figure 1-7 schematically illustrates the contribution of 90° domain wall motion to the E-field-induced strain within one grain. As the polarisation aligned by the E-field, some domains' volumes expand, and the others shrink, generating the E-field-induced strain. The longitudinal strain generated by the domain wall motion strongly depends on the orientation of the grain, *e.g.*, the angle between the 001 crystallographic poles and applied field in Figure 1-7. For polycrystalline materials containing thousands of grains, overall longitudinal strain due to the non-180° domain wall motion needs to consider the domain volume fraction at different orientations with respect to the applied field.[28] The diffraction method is an semiquantitative approach for estimating these non-180° domain volume fractions. For example, in the perovskite FE materials with a tetragonal crystal structure, the volume fraction of 002 domains (f_{002}(MRD)) is calculated by the intensities of the (002) and (200) peaks:

$$f_{002}(\mathrm{MRD}) = 3(\frac{I_{002}}{I'_{002}}) / [\frac{I_{002}}{I'_{002}} + 2(\frac{I_{200}}{I'_{200}})] \tag{1.6}$$

where I denotes the relevant peak intensity, calculated by integrating the area of the diffraction peak, while I' is the intensity corresponding to a sample with random orientation.[29] Similarly, the volume fraction of 111 domains (f_{111}(MRD)) in the rhombohedral perovskite materials is calculated as:

$$f_{111}(\mathrm{MRD}) = 4(\frac{I_{111}}{I'_{111}}) / [\frac{I_{111}}{I'_{111}} + 3(\frac{I_{11\bar{1}}}{I'_{11\bar{1}}})] \tag{1.7}$$

This diffraction method of analysing the ferroelastic domain volume fraction is not restricted to the FE materials. In this thesis, I successfully adopt this method to investigate the ferroelastic domain evolution under an applied E-field in AFE materials, which helps to build a solid connection between the structure and properties.

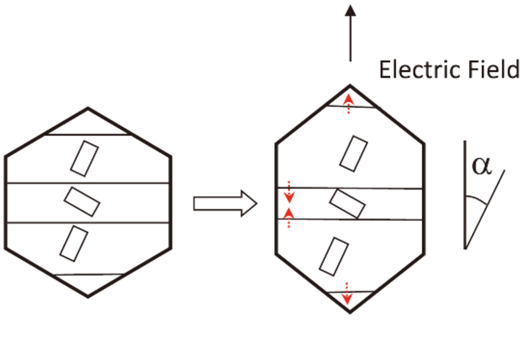

Figure 1-7 Schematic of 90° domain wall motion in response to the E-field. The square rectangle represents the tetragonal structure. The angle between the E-field vector and the longer crystallographic axis (or *c*-axis) is *α*. (reproduced from A. Pramanick *et al.*[29])

1.2.3 Ferroelectric Wake-up Effect

FE materials are widely investigated as promising components in electronic devices. Practical operating conditions demand that FE materials are stable under electrical loading and cycling. Most FE materials present loss of the switchable P_r after a certain number of bipolar cycles and this process is named as 'fatigue'.[30] The FE wake-up effect is the reverse process of fatigue, *i.e.*, the P_r increases within a certain number of the electrical cycles.[31] The wake-up effect has been reported in the many thin films such as PZT, and $SrBi_2Ta_2O_9$ (SBT).[31-35] The proposed mechanism mainly focuses on the defects and interfaces of the films, thereby connecting the wake-up effects with the activation of defect processes. Recently, the wake-up effect has been widely investigated in novel FE HfO_2-based thin films (Figure 1-8) and the underlying physical mechanism raised further discussion.[36, 37] A group led by Schroeder reports that defects diffusion and phase transition are the main reasons for the wake-up effects in Si-doped HfO_2 thin films.[38] The previous reports on the wake-up effect are mainly concentrated on FE materials, so it is of high scientific interest to clarify whether this behaviour is only restricted to FE materials. In this thesis, wake-up effects were observed in the materials with an AFE phase and the underlying physical mechanism is quite different from that in the FE materials.

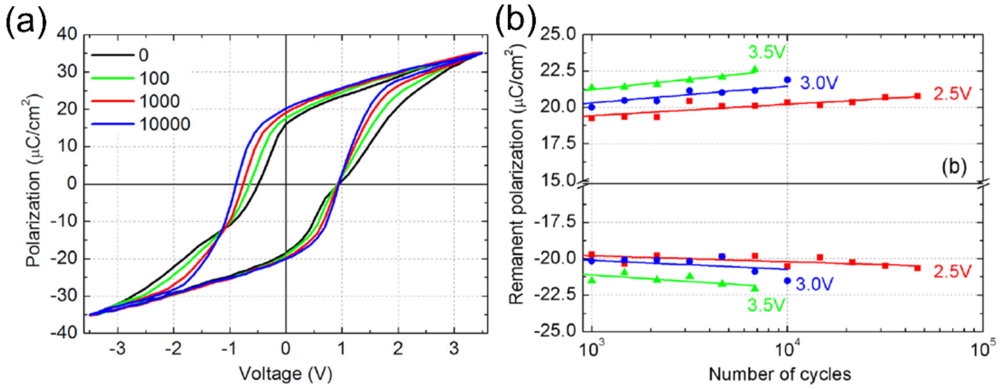

Figure 1-8 (a) Evolution of polarisation-voltage (*P-V*) hysteresis loops during the bipolar cycling. (b) The dependence of the remnant polarisation on the number of cycles and amplitude of bipolar cycling at 1 Hz. (reproduced from Zhou *et al.*[36]).

1.3 Antiferroelectricity

1.3.1 Basic Concepts

The concept of antiferroelectricity was first proposed by Kittel in 1951.[39] In Kittel's model, AFE crystals contain at least two sub-lattices with spontaneous polarisation, and the neighbouring sub-lattices exhibit antiparallel aligned spontaneous polarisation. As a result, no macroscopic polarisation is observed in AFE materials. It is worthwhile to compare the antipolar and AFE structures.[11, 40] As illustrated in Figure 1-9, the phase transition at T_C is associated with a cell-doubling, corresponding to a mode condensation at the Brillouin-zone boundary of the high-temperature phase. When $T < T_C$, both antipolar and AFE structures present antiparallel dipole alignments. Compared with the antipolar structure, AFE crystals display two unique features. Firstly, they present a dielectric anomaly near the T_C, and secondly, they can be transformed into an induced FE phase under applying the external E-field. Above all, the definition of antiferroelectricity involves the consideration in terms of both structure and properties.

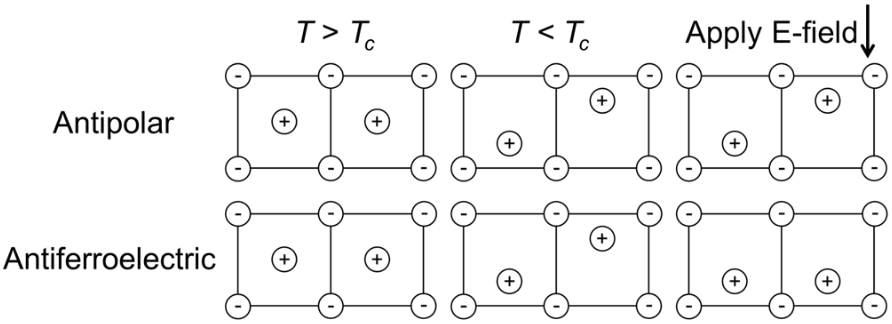

Figure 1-9 A schematic representation of the differences between the antipolar and antiferroelectric structures. (adapted from Lines and Glass[11])

1.3.2 Antiferroelectric Properties

From the definition of antiferroelectricity, one of the important AFE properties is the dielectric anomaly associated with the PE-AFE transition (Figure 1-10). Similar to FE materials, the dielectric constant in the PE state also follows the Curie-Weiss law expressed in Eq 1.5. Most researchers agree that this typical property results from the lower frequency of the polar mode while the FE phase is not stable at zero field.[15, 40-42]

Another important AFE property is the E-field induced AFE-FE phase transition.[45] Figure 1-11a shows the characteristic double *P-E* hysteresis loop. The polarisation exhibits sudden changes at the critical E-field ($E_{\text{AFE-FE}}$, forwarding switching field and $E_{\text{AFE-FE}}$, backward switching field), indicating the AFE-FE phase transition. Usually the AFE and induced-FE phases present large differences in unit-cell volume. In other words, the AFE-FE phase transition can incur a large strain change as shown in Figure 1-11b.

This strain variation also suggests the AFE-FE phase transition is sensitive to the applied mechanical force.[46, 47] For the AFE materials presenting double *P*-*E* hysteresis loop, after withdrawal of the applied field, the induced FE state will switch back AFE phase. In another word, the E-field induced AFE-FE phase transition is reversible. However, the E-field induced AFE-FE phase transition is irreversible in some materials and the typical *P*-*E* hysteresis loop is shown in Figure 1-11c. The *P*-*E* loop shows a linear relationship, corresponding to typical AFE behaviour, until the applied E-field reaching the critical value, $E_{\mathrm{AFE\text{-}FE}}$ during the first quarter cycle. After that, the following *P*-*E* hysteresis loop behaves as typical ferroelectrics.

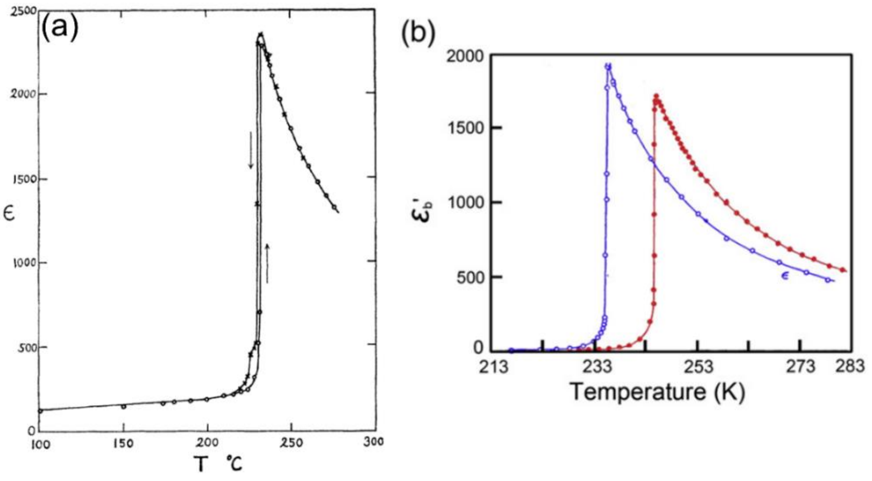

Figure 1-10 Temperature-dependent dielectric constant of (a) $PbZrO_3$ and (b) $Cu(HCOO)_2 \cdot 4H_2O$ (blue) and $Cu(HCOO)_2 \cdot 4D_2O$ (red). (reproduced from Shirane *et al.*[43] and Guo *et al.*[44])

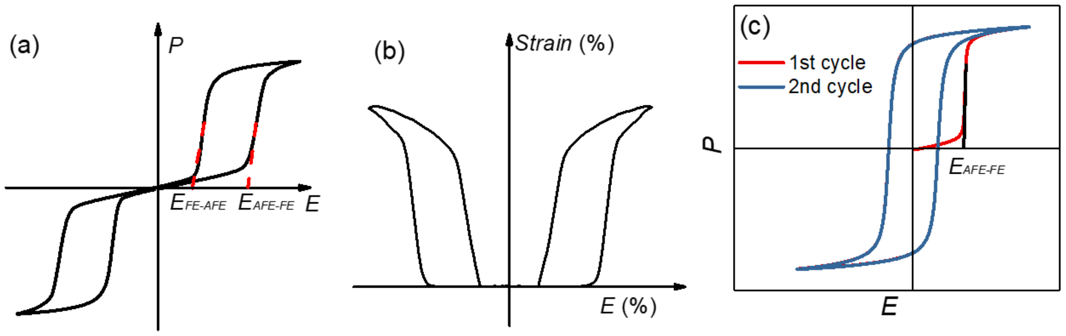

Figure 1-11 Schematic of the typical antiferroelectric (a) *P*-*E* and (b) *S*-*E* hysteresis loops for reversible E-field induced AFE-FE phase transition. (c) *P*-*E* hysteresis loop for the irreversible AFE-FE phase transition.

These two important AFE properties are associated with the PE-AFE and AFE-FE phase transition, respectively. The LGD theory with two order parameters (FE order parameter, *P* and structural or AFE order parameter *η*) are suitable to describe the phase transitions in AFE crystals. [48-50]

$$G(\eta,P,T) = \frac{\alpha}{2}\eta^2 + \frac{\beta}{4}\eta^4 + \frac{P^2}{2\chi_0} + \frac{\delta}{2}\eta^2 P^2 - EP \tag{1.8}$$

where $\alpha = a(T - T_C)$, coupling coefficient $\delta > 0$ and other coefficients are constant. In this section, the second-order transition ($\beta > 0$) is adopted for a detailed analysis. Minimizing the *G* with respect to *P* and *η*, the following equations are obtained:

$$\eta(\alpha + \beta\eta^2 + \delta P^2) = 0 \tag{1.9}$$

$$P(1 + \delta\chi_0\eta^2) = \chi_0 E \tag{1.10}$$

When the external E-field is zero, it is evident that the sample exhibits 2 stable states the PE (η = 0, P = 0) and AFE ($\eta \neq 0$, P = 0) states. The temperature-driven phase transition process is quite similar to that depicted in section 1.2.1. At $E \neq 0$, the sample can present FE (η = 0, $P \neq 0$) and intermediate (IM) ($\eta \neq 0$, $P \neq 0$) states, in which the equilibrium values: $\eta = \pm[(-\alpha-\delta P^2)/\beta]^{1/2}$, and *P* is the real root of:

$$\frac{\delta^2}{\beta}P^3 - \left(\frac{1}{\chi_0} - \frac{\alpha\delta}{\beta}\right)P + E = 0 \tag{1.11}$$

The minimum of the free energy with respect to *P* and *η* contains the stability conditions:

$$\frac{\partial^2 G}{\partial\eta^2} = \alpha + 3\beta\eta^2 + \delta P^2 > 0 \tag{1.12}$$

$$\frac{\partial^2 G}{\partial P^2} = \frac{1}{\chi_0} + \delta\eta^2 > 0 \tag{1.13}$$

$$\frac{\partial^2 G}{\partial\eta^2}\bullet\frac{\partial^2 G}{\partial P^2} - \left(\frac{\partial^2 G}{\partial\eta\partial P}\right)^2 = (\alpha + 3\beta\eta^2 + \delta P^2)\left(\frac{1}{\chi_0} + \delta\eta^2\right) - 4\delta^2\eta^2 P^2 > 0 \tag{1.14}$$

For the FE phase, $\eta = 0$, the above conditions can be simplified as:

$$\alpha + \delta P^2 > 0,\ P^2 > -\frac{\alpha}{\delta} \tag{1.15}$$

and for the IM state, *i.e.*, $\eta \neq 0$, the above conditions are calculated as:

$$\alpha + \delta P^2 < 0,\ P^2 < -\frac{\alpha}{\delta} \tag{1.16}$$

$$[\frac{(\alpha + 3\delta P^2)\delta}{\beta} - \frac{1}{\chi_0}](\alpha + \delta P^2) > 0,\ P^2 < \frac{\beta}{3\chi_0\delta^2} - \frac{\alpha}{3\delta} \tag{1.17}$$

From the above description, the FE-IM phase transition can be either continuous or discontinuous and the critical temperature T_0 is equal to:

$$T_0 = T_C - \frac{\beta}{a\chi_0\delta} \tag{1.18}$$

When the $T_0 < T < T_C$, the phase transition is continuous and the critical field (E_C) is calculated as:

$$E_C = \pm\frac{1}{\chi_0}(-\frac{\alpha}{\delta})^{\frac{1}{2}} \tag{1.19}$$

When the $T < T_0$, the phase transition is discontinuous, the two critical fields from the $\eta \neq 0$ boundary (E_{C1}) and the $\eta = 0$ boundary (E_{C2}) can be calculated as:

$$E_{C1} = \pm\frac{1}{\chi_0}(\frac{\beta}{3\chi_0\delta^2} - \frac{\alpha}{3\delta})^{\frac{1}{2}},\ E_{C2} = \pm\frac{1}{\chi_0}(-\frac{\alpha}{\delta})^{\frac{1}{2}} \tag{1.20}$$

From the above equations, the relationship between the critical field and temperature, and *P-E* functions are schematically drawn in Figure 1-12. Here, only the case for 2nd order phase transition is presented. For the first-order transition ($\beta < 0$), details can be found in the references.[48, 50]

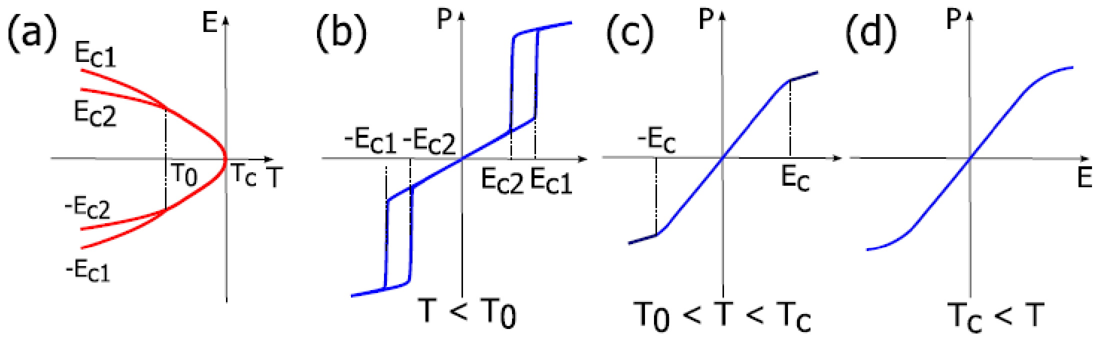

Figure 1-12 (a) Ec-T relationship and P-E hysteresis loop when (b) $T < T_0$, (c) $T_0 < T < T_c$ and (d) $T_c < T$ for a second-order transition. (reproduced from Tolédano and Guennou[50])

Although the two order parameters model can explain the typical AFE features phenomenologically, it is still hard to utilise empirically in a complicated AFE structure. For example, the order parameter, η can be either primary or secondary. Thus, the expression of the free energy needs to consider other order parameters and their coupling. In the following section, we will introduce the symmetry-mode based decomposition approach for better understanding of the order parameters from the structural point of view.

1.4 Mode Crystallography in Perovskite Materials

From the above description, the appearance of anti-/ferroelectricity requires the distortion of the cubic perovskite structure. The distorted structure can be regarded as the parent, high-symmetry structure plus some specific symmetry-breaking distortions or the mode condensation at the specific point in the first Brillouin zone of the parent structure. The details of the symmetry-mode decomposition can be found in Perez-Mato's paper.[20] Here some equations are simply exemplified for better understanding the notation and parameterization used in this thesis.

The $\mathbf{r}_0(\mu)$ is assumed to be the positions of atoms μ ($\mu = 1, ..s$) within an asymmetric unit of the parent structure with space group **G**. **H** is the lower space group, which is the subgroup of **G**. Its asymmetric unit will contain more atoms in comparison with **G** as a result of the splitting of the Wyckoff orbits. The atomic positions in **H** could be described as:

$$\mathbf{r}(\mu,i)=\mathbf{r}_0(\mu,i)+\mathbf{u}(\mu,i) \tag{1.21}$$

where $\mathbf{u}(\mu,i)$ denotes the atomic displacements within an asymmetric unit of the distorted structure, which can be decomposed into the displacements associated with different modes.

$$\mathbf{u}(\mu,i)=\sum_{\tau,m}A_{\tau,m}\mathbf{q}(\tau,m|\mu,i) \tag{1.22}$$

where $A_{\tau,m}$ denotes the amplitude of all possible allowed symmetry modes. $\mathbf{q}$ is a set of atomic displacements normalized within a primitive unit cell. $\mathbf{q}(\tau,m)$, the polarisation vectors or the modulation wave-vectors, defines the symmetry-adapted basis mode (τ, m). If taking the symmetry of the space group **H** into consideration, the displacement of an atom (μ',i') is given by:

$$\mathbf{u}(\mu',i')=\sum_{\tau,m}A_{\tau,m}\mathbf{Rq}(\tau,m|\mu,i) \tag{1.23}$$

where **R** suggests the symmetry operation $\{\mathbf{R}|\mathbf{t}\}$. The polarization vector was then normalized within a primitive unit cell of **H** lattice. The scalar product of the distortion with the normalized mode has the amplitude as:

$$A_{\tau,m}=\sum_{\mu,i}\mathrm{mult}(\mu,i)\mathbf{q}(\tau,m|\mu,i)\bullet\mathbf{u}(\mu,i) \tag{1.24}$$

where the $\mathrm{mult}(\mu,i)$ means the multiplicity within a primitive unit cell for the space group **H** of the related Wyckoff positions. Additionally, the total distortion is expressed as the combination of the modes for all allowed irreducible representations (irreps):

$$\mathbf{u}(\mu,i)=\sum_{\tau}A_{\tau}\mathbf{e}(\tau|\mu,i) \tag{1.25}$$

The amplitude of A_τ is calculated by $\left(\sum_m A_{\tau,m}^2\right)^{1/2}$ and the normalized polarisation vector $\boldsymbol{e}(\tau)$ is the linear combination of the basis modes $\mathbf{q}(\tau,m)$:

$$\mathbf{e}(\tau|\mu,i)=\sum_{m}a_{\tau,m}\mathbf{q}(\tau,m|\mu,i) \tag{1.26}$$

$$a_{\tau,m} = A_{\tau,m} / (\sum_{m} {A_{\tau,m}}^2)^{\frac{1}{2}} \tag{1.27}$$

From above expressions, any possible distortions τ of the parent structure could be described by the global amplitude A_τ and the normalized polarization vector $\{a_{\tau,m}\}$. If the condensation of some specific modes can directly lower the symmetry to **H**, these modes are named as the primary mode. The modes induced by primary modes are named as the induced or secondary modes. The primary modes are not only symmetry-adapted but also physically adapted. Usually the primary modes correspond to the primary order parameters.

In the following part, mode-decomposition on $CaTiO_3$ with the *Pbnm* space group is performed. Table 1 lists the basic structural information for both the parent and distorted $CaTiO_3$ structures. Note that the parent structure is transformed into the setting of *Pbnm* and atoms are located at the undistorted positions. Table 1-2 presents the results of symmetry-mode decomposition. After inducing the lattice strain, the lattice parameters of the distorted structure are related to the cubic parent structure by the transformation: $\mathbf{a} = \mathbf{a_p} + \mathbf{b_p}$; $\mathbf{b} = \mathbf{a_p} - \mathbf{b_p}$ and $\mathbf{c} = 2\mathbf{c_p}$. The *Pbnm* distortions are decomposed into five modes with irreps R4-, R5-, X5-, M2+, M3+. The atomic displacements associated with each irreps distortions are listed in Table 1-2. Clearly, the global amplitudes of three modes (R5-, X5- and M2+) are two orders of magnitude larger than other two modes. In other words, the distortions induced by these three modes dominated the final structure.

Table 1-1 The structure information for the parent and distorted structures of $CaTiO_3$. The details are adapted from the refinement results in references.[51, 52]

Space group	*Pbnm*				*Pm*-3*m* in *Pbnm* setting			
Unicell parameter	*a* = 5.388, *b* = 5.447, *c* = 7.654 Å				*a* = *b* = 5.5108, *c* = 7.7814 Å			
Atom	Wyckoff position	x	y	z	Wyckoff position	x	y	z
Ti	4b	0	0.5	0	4b	0	0.5	0
Ca	4c	0.99374	0.0341	0.25	4c	0	0	0.25
O1	4c	0.0705	0.4842	0.25	4c	0	0.5	0.25
O2	8d	0.7109	0.2884	0.0369	8d	0.75	0.25	0

The notation of the irreps (R5-, X5- and M2+) suggest that main distortions are associated with the condensation of the modes at R, X and M points, respectively, in the first Brillouin zone of the parent structure (Figure 1-13a). Figure 1-13b and c show the distorted structure associated with the R5- mode, whose modulation wave-vector is $\mathbf{q}_{x5-}$ = [1/2 1/2 1/2]*. The R5- mode is the pure octahedral tilting mode with the anti-phase tilting around the a_p and b_p axes, respectively, while no tilting around the c_p axis, which is consistent with the $a^-a^-c^0$ tilting system in Glazer notation. The M2+ mode, showing the 2nd largest amplitude, is also a pure octahedral tilting mode. As illustrated in Figure 1-13f, the adjacent octahedra present in-phase tilting around the c_p axis, *i.e.*, $a^0a^0c^+$ in Glazer notation. The X5- mode, associated with [1/2 0 0]* modulation wavevector, bring about the antipolar structure (Figure 1-13d and e). The Ca^{2+} in the top layer in Figure 1-13e moves along **b** while the O^{2-} (O2) in the same layer moves in the opposite direction. In the adjacent layer, displacements of both Ca1 and O2 reverse their directions but remain the same magnitude, forming a dipole moment antiparallel to that in the top layer.

Table 1-2 Decomposition of the *Pbnm* distorted structure with respect to the symmetrized displacive modes of the parent cubic *Pm*-3*m* perovskite structure. The atomic displacements induced by the irreps distortions.

Strain	x_1	x_2	x_3	x_4	x_5	x_6
Γ1+	-0.0172	-0.0172	-0.0172	0	0	0
Γ3+	0.00032	0.00032	-0.00064	0	0	0
Γ5+	0	0	0	0	0	-0.0107
Wave-vector	Irreps		δx	δy	δz	Aτ (Å)
[1/2 1/2 1/2]*	R4-	Ca	-0.00626	0	0	0.0739
		O2	0	0	0.00085	
		O1	-0.017	0	0	
[1/2 1/2 1/2]*	R5-	O2	0	0	0.03607	1.12381
		O1	0.07215	0	0	
[1/2 0 0]*	X5-	Ca	0	0.03409	0	0.41421
		O1	0	-0.01579	0	
[1/2 1/2 0]*	M2+	O2	-0.03878	0.03878	0	0.85417
[1/2 1/2 0]*	M3+	O2	-0.00035	-0.00035	0	0.00772

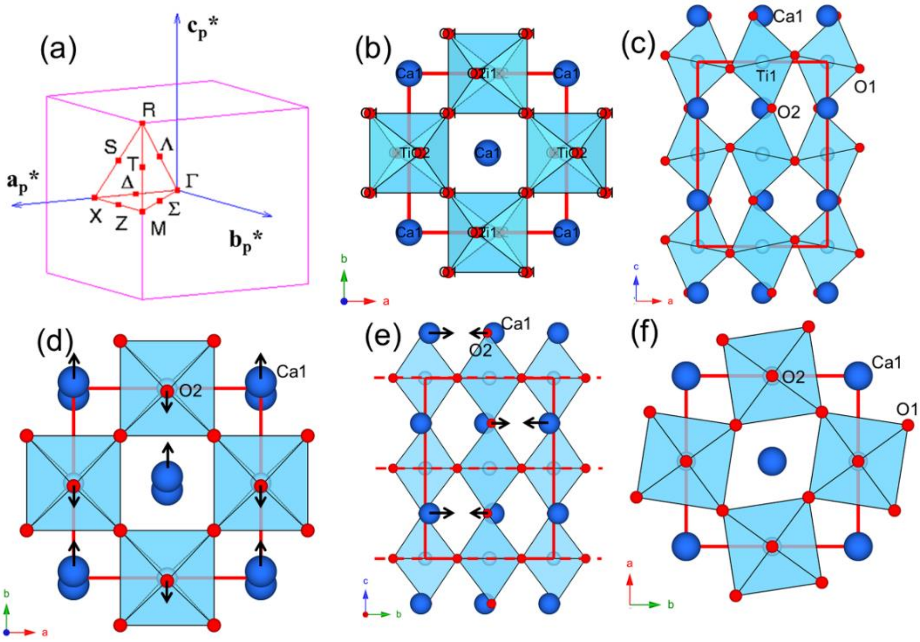

Figure 1-13 (a) The first Brillouin zone of the parent *Pm*-3*m* perovskite structure. The distorted structure induced by R5- viewed along (b) *c*-axis and (c) *b*-axis, by X5- mode viewed along (d) *c*-axis and (e) *b*-axis and by M2+ mode viewed along (f) *c*-axis.

The distortion involving these three modes is almost the same as the experimental result. However, none of the single modes can directly break the symmetry into the final *Pbnm* space group. Instead, any two of three are able to reduce the symmetry to *Pbnm*. Thus, two of them can be regarded as the primary modes. The remaining mode is the secondary or induced mode, which is coupled with the primary modes to lower the energy of the distorted structure. Generally, primary modes exhibit larger amplitudes than the secondary one, *i.e.*, in $CaTiO_3$, R5- and M2+ are the primary modes and X5- mode is induced according to the wave-vector relationship: $\mathbf{q}_{X5-} = \mathbf{q}_{R5-} - \mathbf{q}_{M2+}$.

The mode crystallography approach has many merits over conventional descriptions. For example, the primary distorted modes with large amplitudes dominate the distorted structure, which helps reduce the freedom of atoms for the structure refinement. Furthermore, most of the symmetry modes contain physical meaning, which is helpful to link the properties with the crystal structure. In this thesis, this method is applied to analyse the crystal structure change during the phase transition, thereby developing a more sophisticated understanding on the properties variation.

1.5 Material Systems under Investigation

The above mentioned AFE properties are attractive due to their potential applications, including as components in generators, energy storage devices and sensors.[53-59] The phase transitions in AFE materials provide the physical basis for their unique properties, so understanding the structural change associated with phase transitions is meaningful for the development of AFE materials.[47, 57, 60-62] As the first discovered AFE material, $PbZrO_3$ and its solid solutions have been widely investigated with respect to not only the basic science but also their practical applications since 1957. However, the environmental concerns on the toxicity of the lead element aroused researchers' enthusiasm for finding lead-free alternatives. In 2007, $AgNbO_3$ and its solid solutions began to attract researchers' attention as AFE materials since the discovery of the double *P-E* hysteresis loop.[63] In this thesis, the structure of $(Pb,La)(Zr,Sn,Ti)O_3$ (PLZST) and $Pb(Nb,Zr,Sn,Ti)O_3$ (PNZST) with several specific compositions was investigated *in-situ* under variable conditions such as temperature, E-field and mechanical stress in order to understand the origin of the related properties. Likewise, the structure and electrical properties of $(1-x)AgNbO_3$-$xLiTaO_3$ ceramics were systematically investigated in order to understand the influences of the chemical composition on the AFE properties of $AgNbO_3$. This section will present a brief review of the structure and properties of the related material systems, which will help understand the research presented in Chapter 3.

1.5.1 $PbZrO_3$-based Material Systems

The crystal structure of $PbZrO_3$ (PZO) under ambient conditions is shown in Figure 1-14. It shows an orthorhombic structure with the *Pbam* space group. The *Pbam* cell vectors can be expressed as: $\mathbf{a} \equiv \mathbf{a_p} + \mathbf{b_p}$; $\mathbf{b} \equiv 2(\mathbf{a_p} - \mathbf{b_p})$ and $\mathbf{c} \equiv 2\mathbf{c_p}$ with respect to the five-atom pseudo-cubic perovskite unit (subscript p).[64-66] In one PZO unit-cell, the Pb^{2+} ions present antiparallel displacements with a large amplitude along the $<110>_p$ (the black arrows) and the ZrO_6 octahedron preforms an antiphase tilting along the $<110>_p$ direction. Referring to the mode crystallography,[67-70] the distorted *Pbam* structure is dominated by two primary modes with respect to the pseudo-cubic perovskite structure: the $\mathbf{q}_\Sigma$, associated with the modulation wave-vector $[1/4\ 1/4\ 0]_p^*$ and $\mathbf{q_R} = [1/2\ 1/2\ 1/2]_p^*$. Under this description, the antiparallel Pb^{2+} and its counterpart anion displacements are associated with the $\mathbf{q}_{\Sigma}$ mode, therefore the $\mathbf{q}_{\Sigma}$ mode is termed as the AFE mode which decides the antiferroelectricity in the PZO. The $\mathbf{q}_{\mathbf{R}}$ mode is connected with the $a^{-}a^{-}c^{0}$ octahedra tilting, which belongs to the antiferrodistortive (AFD) mode.

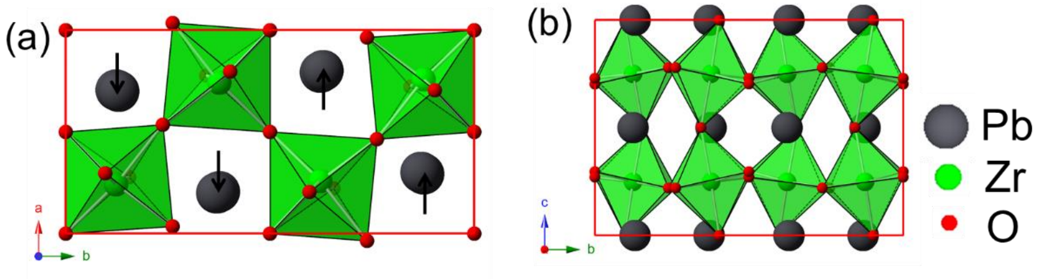

Figure 1-14 The refined structure of $PbZrO_3$ viewed along (b) *c*-axis and (c) *a*-axis.

The stable ground structure of PZO makes the E-field induced AFE-FE phase transition at room temperature quite difficult.[71] In order to solve this problem, chemical modifications on the prototype PZO are regarded as the most effective way. Among various examples, $(Pb_{0.97}La_{0.02})(Zr,Sn,Ti)O_3$ (PLZST) and $Pb_{0.99}Nb_{0.02}(Zr,Sn,Ti)_{0.98}O_3$ (PNZST) material systems present promising properties and attract plenty of investigations.[45, 53, 72-74] Berlincourt has depicted explicit phase diagrams for both material systems (Figure 1-17).[75] According to the phase diagram, the AFE phase shows two structures, the tetragonal (labelled as AFE_T) and orthorhombic (labelled as AFE_O) while the FE phase exists in three forms, the low temperature rhombohedral phase (FE_R(LT) with $R3c$ symmetry), the high temperature rhombohedral phase (FE_R(HT) with $R3m$ symmetry) and tetragonal phase (FE_T with $P4mm$ space group). When the composition is near the AFE/FE phase boundary, the double *P-E* hysteresis loop can be easily achieved. Additionally, for some specific compositions, *e.g.*, $(Pb_{0.97}La_{0.02})(Zr_{0.65}Sn_{0.22}Ti_{0.13})O_3$[76] and $Pb_{0.99}[(Zr_{0.56}Sn_{0.43})_{0.92}Ti_{0.08}]_{0.98}Nb_{0.02}O_3$[77], it is found that the induced FE phase remains metastable after withdrawal of the E-field.

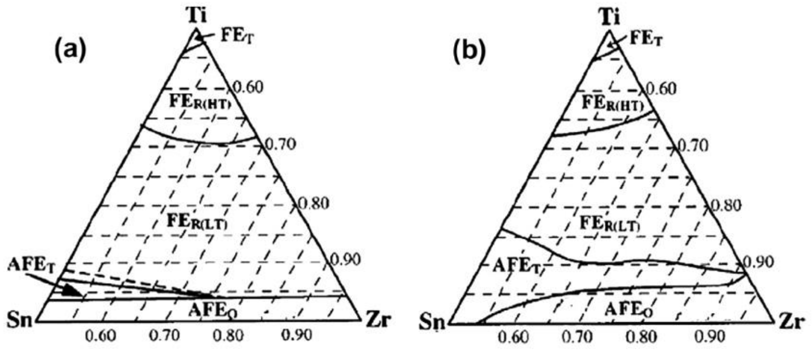

Figure 1-15 Phase diagrams of (a) $Pb_{0.99}Nb_{0.02}(Zr,Sn,Ti)_{0.98}O_3$ and (b) $(Pb_{0.97}La_{0.02})(Zr,Sn,Ti)O_3$ systems. (Reproduced from Berlincourt[75])

The average structure of the AFE_O phase is quite similar to the prototype PZO structure with *Pbam* space group. For the AFE_T phase, its average structure presents pseudo-tetragonal symmetry but according to TEM studies on specific compositions,[78-84] many samples exhibit incommensurate structures locally. It is stated that the incommensurate modulation wave-vector is also along the $<110>_p*$ direction, which is located at the Σ line. Now the wave-vector of $\mathbf{q}_\Sigma$ can be generally expressed as $\gamma[1\ 1\ 0]_p*$, where $1/\gamma$ equals 4 for the PZO and not an integer for these incommensurate structures. He and Tan[84] have built a sophisticated model to plot the incommensurate structure in real space (Figure 1-16a). They suggested that at a very fine scale, the structure is modulated by a commensurate wave, *i.e.*, the wave-vector equals $1/n[1\ 1\ 0]_p*$ (n is an integer and equals 7 or 8 in Figure 1-16a). The average effects of these fine strips with commensurate modulation lead to the observed incommensurate value. Figure 1-16b plots the crystal structure with $\mathbf{q}_\Sigma = 1/8[1\ 1\ 0]_p*$ AFE and $\mathbf{q}_\mathbf{R} = [1/2\ 1/2\ 1/2]_p*$ AFD modes. There are four Pb^{2+} ions displacing along the **a** while the neighbouring four are moving in the opposite direction with the same amplitude, together forming the zero-macroscopic polarization within one unit-cell. It is evident that the unit where Pb^{2+} displaces in the same direction (4 octahedra wide in Figure 1-16b) can be considered as the FE slabs. Thus, the black dash-line is the antiphase boundary between two FE slabs. When the incommensurate modulation wave-length increases, the average distance between the boundaries, *i.e.*, the thickness of the FE slabs increases. From this description, the incommensurate structure in chemically modified PZO samples is due to the competition between the FE and AFE ordering. Similar to the FE materials, domain structure is also formed in AFE materials when cooling down from their high symmetry structure. However, due to the complicated order parameters in AFE materials, the domain structure is also quite complex. For example, in the pure PZO, the AFE 60°, 90° and 180° domains are typical features.[85, 86] For the PLZST and PNZST with incommensurate modulation, 90° AFE domain patterns become dominant (Figure 1-16c and d).[84] Furthermore, the $a^-a^-c^0$ octahedral tilting results in the following primitive unit-cell relationship: $a_p = b_p > c_p$, indicating the 90° ferroelastic domains can be formed when cooling down from the cubic phase[74, 87] Obviously, knowing the evolution of the crystal structure and micro-sized domains are the key factors in understanding the AFE properties.

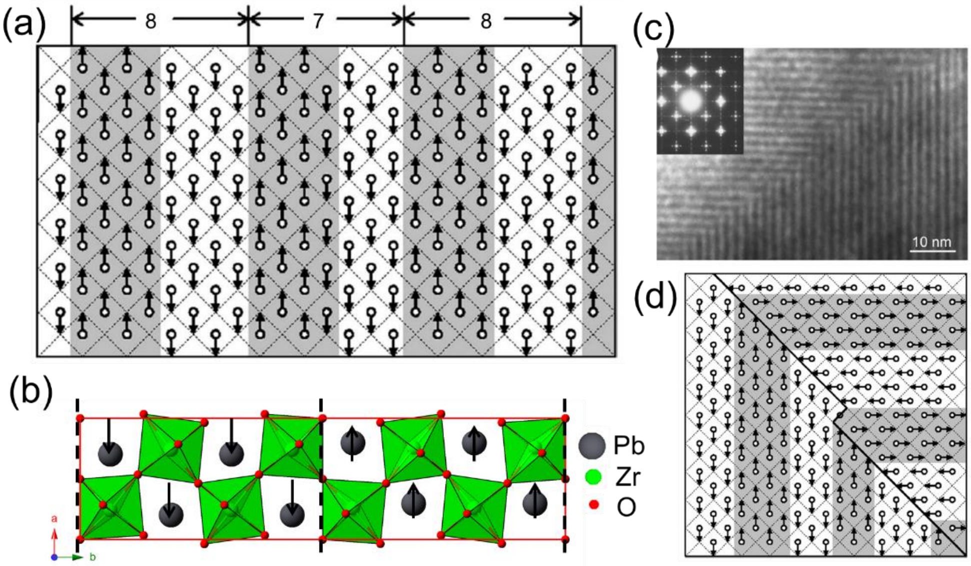

Figure 1-16 (a) Structure models for the incommensurate AFE PNZST materials. (b) Crystal structure of the distorted $PbZrO_3$ with $1/8[1\ 1\ 0]_p^*$ modulation wave-vector. (c) The high-resolution TEM image and associated electron diffraction patterns on the 90° domain wall. (d) Schematic of the 90° domains in the PNZST with incommensurate modulations. (Reproduced from He and Tan[84])

As mentioned in the previous section, the energy gap between the AFE phase and their FE counterparts is quite small. Many thermodynamic variables, including E-field, mechanical stress, strain gradient, temperature and even chemical composition can tune this energy difference, thus inducing the phase transitions in the AFE materials.

The E-field is the most prominent factor which is capable of switching the AFE and

FE phases, and the E-field induced AFE-FE phase transition is also the foundation for many potential applications such as energy storage devices.[88, 89 54, 90 91] Fesenko *et al.*[92] have done a systematic investigations on the single crystal $PbZrO_3$. They observed that the AFE_O phase transfers to the orthorhombic FE phase at ~220 kV/cm. For the PLZST and PNZST ceramics, the E-field induced phase transition behaviour shows some divergence in comparison with that observed in the single crystal $PbZrO_3$. A group led by Cross, using *in-situ* X-ray diffraction techniques, have reported that for the $Pb_{0.98}La_{0.02}(Zr_{0.55}Sn_{0.33}Ti_{0.12})_{0.995}O_3$, the induced FE phase shows rhombohedral symmetry. [93, 94] By using the *in-situ* TEM techniques, Tan *et al.*[84] assigned the space group of the induced FE phase in $Pb_{0.98}Nb_{0.02}[(Zr_{0.58}Sn_{0.42})_{0.955}Ti_{0.045}]_{0.98}O_3$ to $R3c$.

Generally, a large unit-cell volume change occurs during the AFE-FE phase transition, which conversely means that pressure, or mechanical force is capable of tuning the AFE/FE phase stability.[56, 95] Hańderek *et al.*[95] has successfully drawn the hydrostatic pressure – temperature phase diagram for both PZO single crystals and ceramics. In this research, it is suggested that when the temperature is fixed, hydrostatic pressure acts to stabilize the AFE phase (Figure 1-17a and b). Similarly, Dai *et al.*[61] present a pressure-E-field phase diagram of the polarized $Pb_{0.99}Nb_{0.02}(Zr_{0.75}Sn_{0.2}Ti_{0.05})_{0.98}O_3$ ceramics (Figure 1-17c). Obviously, for the chemically modified PZO, the AFE phase can be stabilized by the hydrostatic pressure. Apart from the hydrostatic pressure, uniaxial pressure makes a similar contribution. For $Pb_{0.99}Nb_{0.02}[(Zr_{0.57}Sn_{0.43})_{0.94}Ti_{0.06})]_{0.98}O_3$ investigated by Tan *et al.*[96], increasing uniaxial pressure causes the $E_{AFE\text{-}FE}$ to move toward higher values, suggesting the energy barrier between the AFE and FE phases increases. In addition to the properties characterisation, Avdeev *et al.*[47] have carried out an *in-situ* neutron diffraction study on the $Pb_{0.99}Nb_{0.02}(Zr_{0.95}Ti_{0.05})_{0.98}O_3$ and suggested that 2 kbar of hydrostatic pressure is able to transfer the pristine FE_R (LT) phase into the AFE_O phase. It is evident that the strain/stress exhibits obvious influence on the AFE properties, so nowadays strain engineering has been widely applied in order to reach expected properties.[56, 97-100] It is worthy to note that the surface processing, especially polishing, is an effective way to induce residual stress near the surface region, which causes a distorted surface layer.

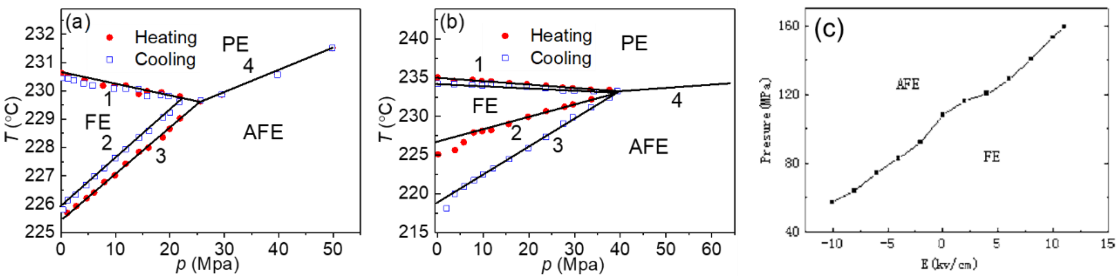

Figure 1-17 *Pressure – T* phase diagram in $PbZrO_3$ for (a) a single crystal and (b) a ceramic sample. Curve 1, 2 and 3 refer FE ↔ PE, AFE ↔ FE and AFE ↔ PE to phase transitions, respectively. (c) The pressure-electric field phase diagram for polarized $Pb_{0.99}Nb_{0.02}(Zr_{0.75}Sn_{0.2}Ti_{0.05})_{0.98}O_3$ ceramics (reproduced from Hańderek *et al.*[95] and Dai *et al.*[61])

Temperature is also a significant factor in triggering the phase transition in PZO-based AFE materials. For some specific compositions of PLZST and PNZST, they can be poled into the metastable FE phase when the composition is close to the AFE/FE phase boundary. The metastable FE phase can be depolarised by increasing the temperature. Chan *et al.*[76] reported that for the $Pb_{0.97}La_{0.02}(Zr_{0.65}Sn_{0.22}Ti_{0.13})O_3$ ceramic, a temperature-induced FE to AFE phase transition occurs around 90 °C. Similar results have also been discovered in other PNZST and PLZST material systems.[57, 101] This temperature-induced FE to AFE phase transition is usually accompanied by a sudden drop in the polarisation, which generates a large pyroelectric current. Most importantly, this process is ideal for the thermal energy harvesting and has begun to attract more attention recently.[102]

Owing to the potential applications of the PNZST and PLZST, a lot of studies on these material systems aim to utilize chemical modification to optimize the relative properties.[103] The crystal structure change, domain motions and their contributions to the properties during field induced phase transitions still need systematic investigations.

1.5.2 $AgNbO_3$-based Material Systems

The structure of $AgNbO_3$ under ambient conditions belongs to the perovskite family. In the beginning, it was suggested to be the centrosymmetric orthorhombic structure while the weak ferroelectricity (P_s ~ 0.04 μC/cm^2 at 293 K) seems to contradict the existence of an inversion center.[104, 105] Verwerft *et al.*[106] reported that the structure of the

AgNbO$_3$ at room temperature presented as distorted perovskite structure with orthorhombic symmetry via images and electron diffraction patterns. The unit-cell parameters can be expressed as: $\mathbf{a_O} \equiv \mathbf{a_p} + \mathbf{c_p}$; $\mathbf{b_O} \equiv 4\mathbf{b_p}$ and $\mathbf{c_O} \equiv \mathbf{a_p} - \mathbf{c_p}$. Furthermore, the $a^-b^-a^-/a^-b^+a^-$ octahedral tilting system was proposed in this distorted structure. In 2000, Fábry *et al.*[107] carried out the refinement on the diffraction data of AgNbO$_3$ by using the *Pbcm* space group.[108] The unit-cell parameters now are defined as $a_O \sim b_O \sim \sqrt{2}a_p$ and $c_O \sim 4c_p$ and in this study, the author stressed the difficulty in distinguishing the non-polar space group *Pbcm* from the polar space group *Pbc*2$_1$ via powder diffraction. In 2007, Fu *et al.*[63] successfully measured the double *P-E* hysteresis loop of the AgNbO$_3$ ceramics, confirming its antiferroelectricity (Figure 1-18a). However, only weak ferroelectricity was obtained under the low fields (Figure 1-18b). Therefore they believed atomic displacements were ordered in a ferrielectric rather than an antiferroelectric way.

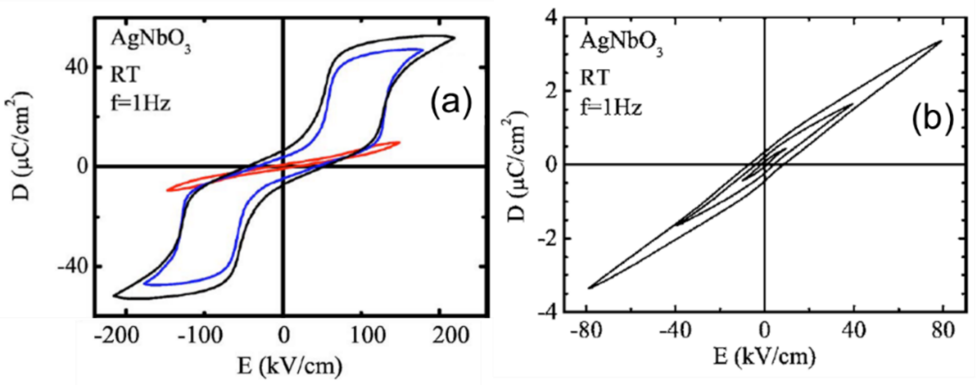

Figure 1-18 Dielectric displacements (*D*) – electric field (*E*) hysteresis loops of AgNbO$_3$ for (a) high fields and (b) low fields. Reproduced from Fu *et al.*[63]

In order to figure out the origin of this weak ferroelectricity, Yashima *et al.*[109] have conducted a detailed structural analysis including neutron and synchrotron powder diffractions, convergent beam and selected area electron diffractions (CBED and SAED) and density functional theory (DFT) calculation. In this study, the polar *Pmc*2$_1$ space group ($a_O \sim 4c_p$ and $b_O \sim c_O \sim \sqrt{2}a_p$) was proposed and both FE and AFE components were explained by this structure. Figure 1-19 exhibits the distorted structure for both *Pmca* (which is centrosymmetric *Pbcm* in the *Pmc*2$_1$ axes setting) and *Pmc*2$_1$ space groups. Both distorted structures contain the same octahedral tilting systems, which can be expressed as $a^-b^-c^+/a^-b^-c^-$ in Glazer notation. Without considering the atomic displacements, the unit-cell of *Pmca* are the same as that of the $Pmc2_1$ structure after a 1/4**a** translation. However, when taking the Ag^+ and Nb^{5+} displacements into consideration, the two distorted structures behave quite differently. As shown in Figure 1-19b, Ag1 and Nb1 within two octahedral layers (between the red dash-line) displace along **c** while in the neighbouring two layers, they displace along the opposite direction. Because of the glide plane perpendicular to the *c*-axis, the displacements along **c**/-**c** within each unit are same, forming the antiparallel aligned dipole moments. For the $Pmc2_1$ structure, the antiparallel aligned dipole moments are still observable but since the glide plane now is replaced by a screw axis, the displacements along the *c*-axis are not limited by the symmetry operation. Although the Nb1 and Nb2 still present antiparallel displacements, their amplitudes are no longer the same. The Ag3 and Ag2 also show similar behaviour. Therefore, the total P_S within one unit-cell of the $Pmc2_1$ structure is non-zero, which is proposed as the origin of the weak ferroelectricity. The mode crystallography provides a new insight into these two distorted structures in terms of the symmetry modes and the details will be presented in the Chapter 3.

The double *P-E* hysteresis loop in $AgNbO_3$ confirms the E-field induced AFE-FE phase transition. However, the structure of the induced FE phase at high voltage still remains ambiguous. Nevertheless, the largely induced polarisation (~ 52 μC/cm^2) and critical field (110 kV/cm) are ideal for energy storage devices. Recently, Tian *et al.*[59] report that $AgNbO_3$ ceramics can present a recoverable energy density of 2.1 J/cm^3 at 175 kV/cm, which is comparable to the lead-containing materials.

In addition to the E-field, the temperature-induced phase transitions of $AgNbO_3$ are quite complicated, which is reflected in their dielectric properties (Figure 1-20).[110] Corresponding to anomalies in the temperature-dependent dielectric spectra, $AgNbO_3$ contains seven phases: M_1, M_2, M_3, O_1, O_2, T and C phases. The details are summarized in Table 1-3. These complicated phase transitions can be essentially divided into two mechanisms: tilting of octahedra and displacements of particular ions.[111] Overall, the sharpest dielectric peak, *i.e.*, M_3-O_1 phase transition, is correlated to the AFE-PE phase transition. Taking this temperature as a boundary, the phase transitions occurring in the high temperature region (> 626 K) are well defined and belong to the first, *i.e.*, octahedral tilting, mechanism.[111-113] In contrast, the M_1-M_2 and M_2-M_3 phase transitions (M denotes the monoclinic distortions of the primitive unit-cell), which are associated with two diffusive dielectric peaks, still remain to be clarified. Levin *et al.*[114, 115] suggest the phase transitions within the M polymorphs are correlated to the local displacements. Through the characterisations made with the electron diffuse scattering and other local-structure techniques such as neutron pair distribution function (PDF) and X-ray absorption fine structure (EXAFS), it is suggested that the Nb^{5+} exhibit local off-centre displacements correlated along the $<0\ 0\ 1>_p$ direction. The M_2-M_3 phase transition is related to the change of the stages of the displacive ordering.

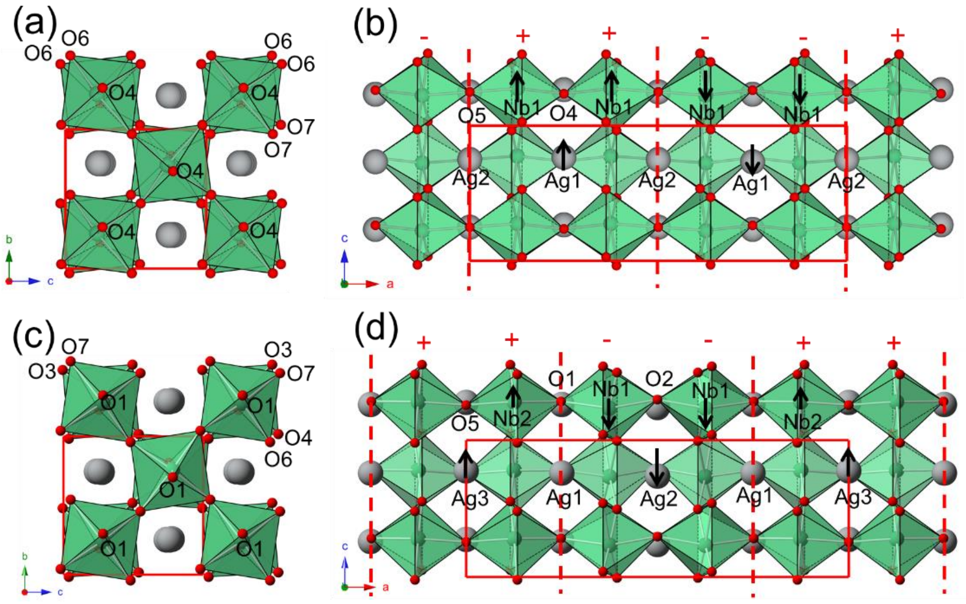

Figure 1-19 $AgNbO_3$ with *Pmca* structure viewed along the (a) *a* and (b) *b*-axis, and with *Pmc*2_1 structure viewed along the (c) *a* and (d) *b*-axis.

The local structure change induced dielectric anomalies are based on the assumption that all the M polymorphs belong to the *Pbcm* symmetry. However, in 1984, Kania *et al.* have reported that the weak ferroelectricity disappeared around 345 K, stressing the M1-M2 phase transition is associated with a depolarisation process. After discovering the origin of this weak ferroelectricity, researchers preferred to link the M_1-M_2 phase transition with the structural change between the *Pmc*2_1 and *Pbcm* symmetries. Principally, this phase transition occurs accompanied by a soft mode at the zone centre, but Raman spectra results do not show significant modes softening at the temperature around 340 K.[116, 117] Instead, the central peak presents more obvious change as a function of temperature, which has the close relationship with the freezing of the Nb-ion dynamics. In other words, the M1-M2 phase transition is also possibly related to the local structural variation.

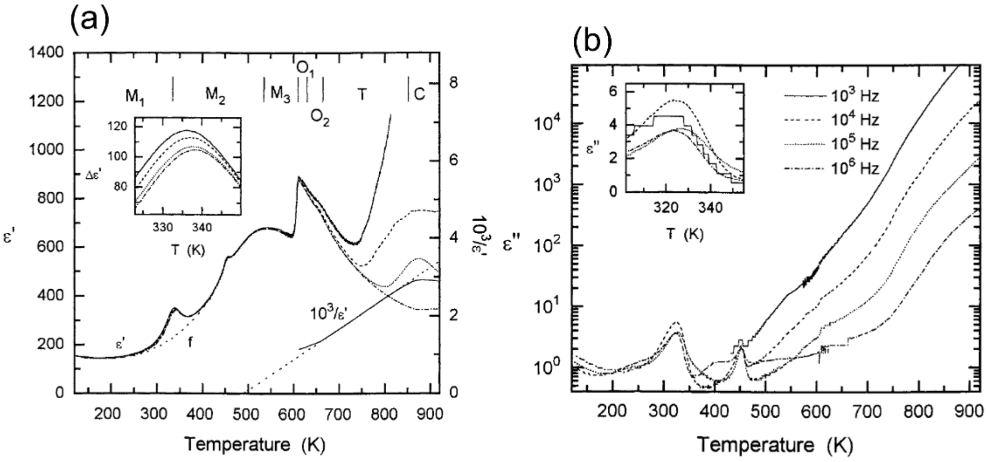

Figure 1-20 Temperature dependences of the (a) real and (b) imaginary parts of the dielectric constant for $AgNbO_3$ during the cooling process. (Reproduced from Kania[110])

Table 1-3 The phases of $AgNbO_3$ at different temperature. (Reproduced from Tan *et.al*[118])

Phase	Temperature (K)	Symmetry	Tilting system
M_1	< 340	$Pmc2_1$ or *Pbcm*	$a^-b^-c^+/a^-b^-c^-$
M_2	340-540	*Pbcm*	$a^-b^-c^+/a^-b^-c^-$
M_3	540-626	*Pbcm*	$a^-b^-c^+/a^-b^-c^-$
O_1	626-634	*Cmcm* or unknown	Undetermined
O_2	634-660	*Cmcm*	$a^0b^-c^+$
T	660-852	*P4/mbm*	$a^0b^0c^+$
C	> 852	*Pm*-3*m*	$a^0a^0a^0$

The *P-E* behaviour of $AgNbO_3$ under high field enables it to function as a lead-free alternative in energy storage device applications. Many investigations have attempted to enhance this property by chemical modifications.[119-121] Additionally, the large induced FE polarisation (~ 52 μC/cm^2) suggests $AgNbO_3$ as the potential end member in developing the lead-free piezoelectric materials.[63] Alkaline elements such as Li, Na and K modified $AgNbO_3$ materials have been systematically studied by Fu *et al.*[122-125] In this section, we only stress the impacts induced by Li^+. For $(Ag_{1-x}Li_x)NbO_3$ systems, both ceramics and single crystals have been synthesized. Due to the large difference in ionic radius between Li^+ (92 pm) and Ag^+ (128 pm)[126], the doping level of Li^+ is limited. Figure 1-21a and b show *P-E* hysteresis loops for $(Ag_{1-x}Li_x)NbO_3$ systems in the form of both ceramics and single crystal. With increasing Li content, a single *P-E* hysteresis loop with a large P_r is obtained. The value is ~ 26 μC/cm^2 for $(Ag_{0.901}Li_{0.091})NbO_3$ ceramics and ~ 24 μC/cm^2 for the $[001]_p$-cut crystal. By further characterizing the average structure, it is found that the Li^+ dopant can tune the room-temperature average structure from orthorhombic to rhombohedra. The $R3c$ space group is assigned to the samples with high $LiNbO_3$ content. Furthermore, as the room-temperature structure changed, the temperature-dependent dielectric spectra (Figure 1-21c and d) showed different behaviours after Li^+ doping. Instead of the complex temperature-induced phase transition for pure $AgNbO_3$, $(Ag_{0.9}Li_{0.1})NbO_3$ displays a relatively sharp dielectric peak around 600 K, which was assigned as the FE-PE phase transition. This relatively high T_C suggests good thermal stability for $(Ag_{0.9}Li_{0.1})NbO_3$, making these materials promising for lead-free piezoelectrics.

In addition to the average structure, the local structure is also influenced by the Li^+ doping. A group led by Reaney has done electron diffraction on the $(Ag_{1-x}Li_x)NbO_3$ and $(Ag_{1-x}Li_x)Nb_{0.5}Ta_{0.5}O_3$ material systems.[127, 128] For the $(Ag_{1-x}Li_x)NbO_3$ solid solutions, with increasing the doping level of Li^+ to 10%, $\mathbf{G_p} \pm [0\ 0\ 1/6]_p^*$ satellite reflections are observed, indicating the modulation wave-vector along the $[0\ 0\ 1]_p^*$ moves from the original $[0\ 0\ 1/4]_p^*$ in pure $AgNbO_3$ towards the zone centre. This behaviour is quite similar to that observed in the incommensurate PLZST/PNZST AFE materials mentioned above, *i.e.*, the Li dopant leads to competition between the AFE and FE structures. Furthermore, in the $(Ag_{1-x}Li_x)Nb_{0.5}Ta_{0.5}O_3$ material system, the increment of x makes the intensity of $\mathbf{G_p} \pm [0\ 0\ 1/4]_p^*$ satellite reflections weaker and streaked, which means the ordered cation displacements are disturbed by Li^+. From the above description, it is found that the Li^+ doped $AgNbO_3$ materials arouse many interesting phenomena in both the fundamental science and applications, which requires more systematically researches.

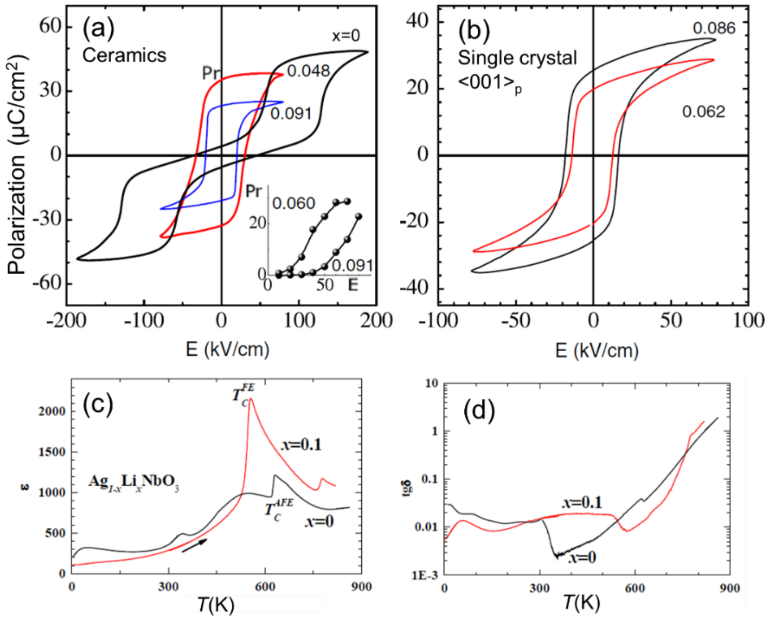

Figure 1-21 *P-E* hysteresis loops for $(Ag_{1-x}Li_x)NbO_3$ (a) ceramics and (b) $<001>_p$ oriented crystals. The inset shows the E-field dependence of P_r. (c) Temperature-dependent dielectric constant and (d) loss for $(Ag_{0.9}Li_{0.1})NbO_3$ ceramics. (Reproduced from Fu *et al.*[125])

1.6 Objectives and Outline of the Thesis

This thesis aims to address the structural origin of the unique properties in AFE materials. The project initially has concentrated on the classical AFE materials: PLZST and PNZST. Although plenty of work has been done on these material systems, the evolution of the structure, preferred orientation and associated lattice strain under variable external fields, including E-field, temperature and mechanical force still need comprehensive studies. The compositions of the PNZST and PLZST ceramics used in this work were chosen near the AFE/FE phase boundaries of the ternary systems. More specifically, the compositions for the studied PLZST and PNZST ceramics are $Pb_{0.97}La_{0.02}(Zr_{0.56}Sn_{0.33}Ti_{0.11})O_3$ (PLZST), $Pb_{0.99}(Nb_{0.02}Zr_{0.73}Sn_{0.21}Ti_{0.04})O_3$ (PNZST1) and $Pb_{0.99}(Nb_{0.02}Zr_{0.65}Sn_{0.28}Ti_{0.05})O_3$ (PNZST2), respectively. The PLZST sample is in the AFE_T region and close to the FE_R(LT) phase. The PNZST1 is located near the three-phase junction of AFE_O, AFE_T and FE_R(LT) phases while the PNZST2 is located at the phase boundary between the AFE_T and FE_R phases. These three compositions are quite representative, supplying diverse phase transition behaviours for studying.

The other material system investigated in this thesis is based on the novel AFE $AgNbO_3$ materials – (1-x)$AgNbO_3$-$x$$LiTaO_3$ ($0 \leq x \leq 9\%$) - as the Li^+ modified $AgNbO_3$ is both interesting in fundamental science and practical applications. Particular attention has been paid to their AFE/FE properties, phase transition behaviour and structural characteristics which are still lacking in the literature. Furthermore, the field-cycling dependent properties of AFE materials are seldom reported in previous investigations. This project also tries to study whether the field-cycling-induced AFE-FE phase transition can be achieved in the AFE material systems.

The structural, preferred orientation and lattice strain evolution during the phase transitions are mainly characterized by *in-situ* neutron scattering techniques. As a bulk probe, neutron scattering can reflect the structural information of the whole material, which can be connected to the samples' macroscopic properties. The lab X-ray diffraction is also used to characterize the structure. However, due to its smaller penetration depth, it can only reflect the structural information near the surface region, which matches the surface properties measured by the piezoresponse force microscopy (PFM). The combination of the bulk and surface probes provides an opportunity to study the impacts of surface processing on AFE materials. The details of these techniques will be discussed in the next chapters.

The strong focus of this PhD project has been devoted to taking the mode crystallography into account when considering the structure and properties and developing the structure-property relationships in the AFE materials. The results not only add to the repository of experimental observations, but also provide a novel insight into the field-induced phase transitions in the AFE materials. The main outcomes of my researches have been published in journal articles.

This thesis consists of the following chapters:

Chapter 1 is an introduction to the relevant background knowledge

Chapter 2 is an overview of the experimental methods used in this project.

Chapter 3 includes 3 peer-reviewed journal articles and 2 to-be-submitted manuscripts. Some additional data, most of which were used as Supporting Information for the publications, have also been attached to the corresponding articles.

Chapter 4 summarizes the main research outcomes into three sections according to the investigated material systems: 1) the crystal structure, associated preferred orientation evolution and their relationship to the electrical properties during the E-field induced AFE-FE transitions in PLZST; 2) the bulk and surface structure-properties relationship under different fields, including temperature, E-field and mechanical stress in PNZST; 3) systematic investigations on the evolution of the crystal structure and electrical properties of $(1\text{-}x)AgNbO_3\text{-}xLiTaO_3$ material systems and their phase transitions under the field cycling.

References:

1. H. Fu and R. E. Cohen, Nature **403** (6767), 281 (2000).
2. E. Sawaguchi, H. Maniwa and S. Hoshino, Phys. Rev. **83** (5), 1078-1078 (1951).
3. T. Zhao, A. Scholl, F. Zavaliche, K. Lee, M. Barry, A. Doran, M. Cruz, Y. Chu, C. Ederer and N. Spaldin, Nat. Mater. **5** (10), 823 (2006).
4. J. A. Alonso, J. Sanz, J. Santamaría, C. León, A. Várez and M. T. Fernández-Díaz, Angew. Chem. Int. Ed. **39** (3), 619-621 (2000).
5. Q. Dong, Y. Fang, Y. Shao, P. Mulligan, J. Qiu, L. Cao and J. Huang, Science **347** (6225), 967-970 (2015).
6. A. Glazer, Acta Crystallogr. Sect. B: Struct. Sci. **28** (11), 3384-3392 (1972).
7. A. Glazer, Acta Crystallogr., Sect. A: Cryst. Phys., Diffr., Theor. Gen. Crystallogr. **31** (6), 756-762 (1975).
8. A. K. Jonscher, *Universal relaxation law: a sequel to Dielectric relaxation in solids*. (Chelsea Dielectrics Press, 1996).
9. D. Damjanovic, Rep. Prog. Phys. **61** (9), 1267 (1998).
10. B. Jaffe, *Piezoelectric Ceramics*. (Academic Press, New York, 1971).
11. M. E. Lines and A. M. Glass, *Principles and applications of ferroelectrics and related materials*. (Oxford university press, New York, 1977).
12. W. Cochran, Adv. Phys. **9** (36), 387-423 (1960).
13. M. DiDomenico, S. H. Wemple, S. P. S. Porto and R. P. Bauman, Phys. Rev. **174** (2), 522-530 (1968).
14. G. Shirane, J. D. Axe, J. Harada and J. P. Remeika, Phys. Rev. B **2** (1), 155-159 (1970).
15. P. Ghosez, E. Cockayne, U. Waghmare and K. Rabe, Phys. Rev. B **60** (2), 836 (1999).
16. A. Postnikov, T. Neumann and G. Borstel, Phys. Rev. B **50** (2), 758 (1994).
17. R. E. Cohen and H. Krakauer, Phys. Rev. B **42** (10), 6416-6423 (1990).
18. R. E. Cohen, Nature **358** (6382), 136-138 (1992).
19. W. J. Merz, Phys. Rev. **91** (3), 513-517 (1953).
20. J. M. Perez-Mato, D. Orobengoa and M. I. Aroyo, Acta Crystallogr. Sect. A: Found. Crystallogr. **66** (5), 558-590 (2010).
21. F. Jona and G. Shirane, *Ferroelectric crystals*. (Pergamon, New York, 1962).
22. G. Arlt and P. Sasko, J. Appl. Phys. **51** (9), 4956-4960 (1980).
23. J. K. Shang and X. Tan, Acta Mater. **49** (15), 2993-2999 (2001).
24. J. Munoz-Saldana, M. Hoffmann and G. Schneider, J. Mater. Res. **18** (08), 1777-1786 (2003).
25. J. Y. Li, R. C. Rogan, E. Ustundag and K. Bhattacharya, Nat. Mater. **4** (10), 776-781 (2005).
26. L. A. Schmitt, H. Kungl, M. Hinterstein, L. Riekehr, H.-J. Kleebe, M. J. Hoffmann, R.-A. Eichel and H. Fuess, J. Am. Ceram. Soc. **98** (1), 269-277 (2015).
27. D. Damjanovic, J. Appl. Phys. **82** (4), 1788-1797 (1997).
28. J. L. Jones, M. Hoffman and K. J. Bowman, J. Appl. Phys. **98** (2), 024115 (2005).
29. A. Pramanick, D. Damjanovic, J. E. Daniels, J. C. Nino and J. L. Jones, J. Am. Ceram. Soc. **94** (2), 293-309 (2011).
30. D. Lupascu and J. Rödel, Adv. Eng. Mater. **7** (10), 882-898 (2005).
31. S. Okamura, M. Takaoka, T. Nishida and T. Shiosaki, Jpn. J. Appl. Phys. **39** (9S), 5481 (2000).
32. G. L. Yuan, J.-M. Liu, S. T. Zhang, D. Wu, Y. P. Wang, Z. G. Liu, H. L. W. Chan and C. L. Choy, Appl. Phys. Lett. **84** (6), 954-956 (2004).
33. M. Kohli, P. Muralt and N. Setter, Appl. Phys. Lett. **72** (24), 3217-3219 (1998).
34. N. Menou, C. Muller, I. S. Baturin, V. Y. Shur and J.-L. Hodeau, J. Appl. Phys. **97** (6), 064108

(2005).
35. S. Alkoy, E. M. Alkoy, K. Uchiyama and T. Shiosaki, Jpn. J. Appl. Phys. **45** (9S), 7275 (2006).
36. D. Zhou, J. Xu, Q. Li, Y. Guan, F. Cao, X. Dong, J. Müller, T. Schenk and U. Schröder, Appl. Phys. Lett. **103** (19), 192904 (2013).
37. T. Schenk, U. Schroeder, M. Pešić, M. Popovici, Y. V. Pershin and T. Mikolajick, ACS Appl. Mater. Interfaces **6** (22), 19744-19751 (2014).
38. M. Pešić, F. P. G. Fengler, L. Larcher, A. Padovani, T. Schenk, E. D. Grimley, X. Sang, J. M. LeBeau, S. Slesazeck and U. Schroeder, Adv. Funct. Mater. **26** (25), 4601-4612 (2016).
39. C. Kittel, Phys. Rev. **82** (5), 729-732 (1951).
40. J. F. Scott, Rev. Mod. Phys. **46** (1), 83-128 (1974).
41. K. Roleder, M. Maglione, M. Fontana and J. Dec, J. Phys.: Condens. Matter **8** (49), 10669 (1996).
42. T. Ostapchuk, J. Petzelt, V. Zelezny, S. Kamba, V. Bovtun, V. Porokhonskyy, A. Pashkin, P. Kuzel, M. Glinchuk and I. Bykov, J. Phys.: Condens. Matter **13** (11), 2677 (2001).
43. G. Shirane, E. Sawaguchi and Y. Takagi, Phys. Rev. **84** (3), 476-481 (1951).
44. M. Guo, H.-L. Cai and R.-G. Xiong, Inorg. Chem. Commun. **13** (12), 1590-1598 (2010).
45. W. Pan, Q. Zhang, A. Bhalla and L. E. Cross, J. Am. Ceram. Soc. **72** (4), 571-578 (1989).
46. P. Yang and D. A. Payne, J. Appl. Phys. **71** (3), 1361-1367 (1992).
47. M. Avdeev, J. D. Jorgensen, S. Short, G. A. Samara, E. L. Venturini, P. Yang and B. Morosin, Phys. Rev. B **73** (6), 064105 (2006).
48. E. Balashova and A. Tagantsev, Phys. Rev. B **48** (14), 9979 (1993).
49. A. K. Tagantsev, K. Vaideeswaran, S. B. Vakhrushev, A. V. Filimonov, R. G. Burkovsky, A. Shaganov, D. Andronikova, A. I. Rudskoy, A. Q. R. Baron, H. Uchiyama, D. Chernyshov, A. Bosak, Z. Ujma, K. Roleder, A. Majchrowski, J. H. Ko and N. Setter, Nat. Commun. **4** (2013).
50. P. Tolédano and M. Guennou, Phys. Rev. B **94** (1), 014107 (2016).
51. R. Buttner and E. Maslen, Acta Crystallogr. Sect. B: Struct. Sci. **48** (5), 644-649 (1992).
52. R. Ali and M. Yashima, J. Solid State Chem. **178** (9), 2867-2872 (2005).
53. W. Y. Pan, C. Q. Dam, Q. M. Zhang and L. E. Cross, J. Appl. Phys. **66** (12), 6014-6023 (1989).
54. X. Hao, Z. Yue, J. Xu, S. An and C.-W. Nan, J. Appl. Phys. **110** (6), 064109 (2011).
55. M. S. Mirshekarloo, K. Yao and T. Sritharan, Adv. Funct. Mater. **22** (19), 4159-4164 (2012).
56. J. Ge, D. Remiens, X. Dong, Y. Chen, J. Costecalde, F. Gao, F. Cao and G. Wang, Appl. Phys. Lett. **105** (11), 112908 (2014).
57. F. Zhuo, Q. Li, J. Gao, Y. Wang, Q. Yan, Z. Xia, Y. Zhang and X. Chu, J. Mater. Chem. C **4** (29), 7110-7118 (2016).
58. M. Pešić, M. Hoffmann, C. Richter, T. Mikolajick and U. Schroeder, Adv. Funct. Mater. **26** (41), 7486-7494 (2016).
59. Y. Tian, L. Jin, H. Zhang, Z. Xu, X. Wei, E. Politova, S. Y. Stefanovich, N. V. Tarakina, I. Abrahams and H. Yan, J. Mater. Chem. A **4** (44), 17279-17287 (2016).
60. T. Lu, A. J. Studer, L. Noren, W. Hu, D. Yu, B. McBride, Y. Feng, R. L. Withers, H. Chen, Z. Xu and Y. Liu, Sci. Rep. **6**, 23659 (2016).
61. Z. Dai, Z. Xu and X. Yao, Appl. Phys. Lett. **92** (7), 072904 (2008).
62. T. Lu, A. J. Studer, D. Cortie, K. Lau, D. Yu, Y. Feng, H. Chen, Z. Xu, R. L. Withers, G. J. McIntyre and Y. Liu, ACS Appl. Mater. Interfaces **8** (23), 14313-14317 (2016).
63. D. S. Fu, M. Endo, H. Taniguchi, T. Taniyama and M. Itoh, Appl. Phys. Lett. **90** (25), 3 (2007).
64. F. Jona, G. Shirane, F. Mazzi and R. Pepinsky, Phys. Rev. **105** (3), 849-856 (1957).

65. D. L. Corker, A. M. Glazer, J. Dec, K. Roleder and R. W. Whatmore, Acta Crystallogr. Sect. B: Struct. Sci. **53** (1), 135-142 (1997).

66. H. Fujishita and S. Katano, J. Phys. Soc. Jpn. **66** (11), 3484-3488 (1997).

67. H. T. Stokes, D. M. Hatch and J. D. Wells, Phys. Rev. B **43** (13), 11010 (1991).

68. J. Íñiguez, M. Stengel, S. Prosandeev and L. Bellaiche, Phys. Rev. B **90** (22), 220103 (2014).

69. H. Fujishita and S. Hoshino, J. Phys. Soc. Jpn. **53** (1), 226-234 (1984).

70. H. Fujishita, Y. Ishikawa, S. Tanaka, A. Ogawaguchi and S. Katano, J. Phys. Soc. Jpn. **72** (6), 1426-1435 (2003).

71. E. Sawaguchi and T. Kittaka, J. Phys. Soc. Jpn. **7** (3), 336-337 (1952).

72. K. Markowski, S.-E. Park, S. Yoshikawa and L. E. Cross, J. Am. Ceram. Soc. **79** (12), 3297-3304 (1996).

73. Y. J. Feng, Z. Xu and X. Yao, Mater. Sci. Eng., B **99** (1), 499-501 (2003).

74. J. Frederick, X. Tan and W. Jo, J. Am. Ceram. Soc. **94** (4), 1149-1155 (2011).

75. D. A. Berlincourt, IEEE Trans. Sonics Ultrason. **13**, 116 (1966).

76. W.-H. Chan, Z. Xu, J. Zhai, E. Colla and H. Chen, J. Electroceram. **21** (1-4), 145-148 (2008).

77. H. Guo and X. Tan, Phys. Rev. B **91** (14), 144104 (2015).

78. J. S. Speck, M. De Graef, A. P. Wilkinson, A. K. Cheetham and D. R. Clarke, J. Appl. Phys. **73** (11), 7261-7267 (1993).

79. Z. Xu, D. Viehland, P. Yang and D. A. Payne, J. Appl. Phys. **74** (5), 3406-3413 (1993).

80. D. Viehland, D. Forst and J. F. Li, J. Appl. Phys. **75** (8), 4137-4143 (1994).

81. D. Viehland, D. Forst, Z. Xu and J.-F. Li, J. Am. Ceram. Soc. **78** (8), 2101-2112 (1995).

82. D. Forst, J. F. Li and Z. K. Xu, J. Am. Ceram. Soc. **81** (9), 2225-2236 (1998).

83. H. He and X. Tan, Appl. Phys. Lett. **85** (15), 3187-3189 (2004).

84. H. He and X. Tan, Phys. Rev. B **72** (2), 024102 (2005).

85. T. Michiyoshi, S. Ryuichi and T. Kaoru, Jpn. J. Appl. Phys. **21** (2R), 291 (1982).

86. D. Viehland, Phys. Rev. B **52** (2), 778-791 (1995).

87. H. Cao and A. G. Evans, J. Am. Ceram. Soc. **76** (4), 890-896 (1993).

88. Z. Liu, X. Chen, W. Peng, C. Xu, X. Dong, F. Cao and G. Wang, Appl. Phys. Lett. **106** (26), 262901 (2015).

89. X. Wang, J. Shen, T. Yang, Y. Dong and Y. Liu, J. Alloys Compd. **655**, 309-313 (2016).

90. X. Hao, Y. Wang, L. Zhang, L. Zhang and S. An, Appl. Phys. Lett. **102** (16), 163903 (2013).

91. M. Sharifzadeh Mirshekarloo, K. Yao and T. Sritharan, Appl. Phys. Lett. **97** (14), 142902 (2010).

92. O. Fesenko, R. Kolesova and Y. G. Sindeyev, Ferroelectrics **20** (1), 177-178 (1978).

93. C. T. Blue, J. C. Hicks, S. E. Park, S. Yoshikawa and L. E. Cross, Appl. Phys. Lett. **68** (21), 2942-2944 (1996).

94. S. E. Park, M.-J. Pan, K. Markowski, S. Yoshikawa and L. E. Cross, J. Appl. Phys. **82** (4), 1798-1803 (1997).

95. J. Handerek, M. Pisarski and Z. Ujma, J. Phys. C: Solid State Phys. **14** (14), 2007 (1981).

96. X. Tan, J. Frederick, C. Ma, E. Aulbach, M. Marsilius, W. Hong, T. Granzow, W. Jo and J. Rödel, Phys. Rev. B **81** (1), 014103 (2010).

97. H.-J. Liu, C.-W. Liang, W.-I. Liang, H.-J. Chen, J.-C. Yang, C.-Y. Peng, G.-F. Wang, F.-N. Chu, Y.-C. Chen, H.-Y. Lee, L. Chang, S.-J. Lin and Y.-H. Chu, Phys. Rev. B **85** (1), 014104 (2012).

98. S. E. Reyes-Lillo and K. M. Rabe, Phys. Rev. B **88** (18), 180102 (2013).

99. B. Peng, Q. Zhang, X. Li, T. Sun, H. Fan, S. Ke, M. Ye, Y. Wang, W. Lu and H. Niu, Adv.

Electron. Mater. **1** (5) (2015).

100. C. Xu, Y. Li, B. Xu, J. Íñiguez, W. Duan and L. Bellaiche, Adv. Funct. Mater. **27** (3) (2017).
101. S. Patel, F. Weyland, X. Tan and N. Novak, Energy Technology.
102. G. Vats, A. Kumar, N. Ortega, C. R. Bowen and R. S. Katiyar, Energy Environ. Sci. **9** (4), 1335-1345 (2016).
103. X. Hao, J. Zhai, L. B. Kong and Z. Xu, Prog. Mater Sci. **63**, 1-57 (2014).
104. M. Łukaszewski, A. Kania and A. Ratuszna, J. Cryst. Growth **48** (3), 493-495 (1980).
105. A. Kania, K. Roleder and M. Łukaszewski, Ferroelectrics **52** (1), 265-269 (1983).
106. M. Verwerft, G. van Tendeloo, J. van Landuyt, W. Coene and S. Amelinckx, phys. stat. sol. (a) **109** (1), 67-78 (1988).
107. J. Fabry, Z. Zikmund, A. Kania and V. Petricek, Acta Crystallogr. Sect. C: Cryst. Struct. Commun. **56** (8), 916-918 (2000).
108. L. E. Cross, Nature **181** (4603), 178-179 (1958).
109. M. Yashima, S. Matsuyama, R. Sano, M. Itoh, K. Tsuda and D. S. Fu, Chem. Mater. **23** (7), 1643-1645 (2011).
110. A. Kania, J. Phys. D: Appl. Phys. **34** (10), 1447 (2001).
111. P. Sciau, A. Kania, B. Dkhil, E. Suard and A. Ratuszna, J. Phys.: Condens. Matter **16** (16), 2795 (2004).
112. M. Verwerft, D. Van Dyck, V. A. M. Brabers, J. van Landuyt and S. Amelinckx, phys. stat. sol. (a) **112** (2), 451-466 (1989).
113. A. Ratuszna, J. Pawluk and A. Kania, Phase Transitions **76** (6), 611-620 (2003).
114. I. Levin, V. Krayzman, J. C. Woicik, J. Karapetrova, T. Proffen, M. G. Tucker and I. M. Reaney, Phys. Rev. B **79** (10), 104113 (2009).
115. V. Krayzman and I. Levin, J. Phys.: Condens. Matter **22** (40), 404201 (2010).
116. M. D. Fontana, G. E. Kugel, A. Kania and K. Roleder, Jpn. J. Appl. Phys. **24** (S2), 516 (1985).
117. A. Niewiadomski, A. Kania, G. E. Kugel, M. Hafid and D. Sitko, Mater. Res. Bull. **65**, 123-131 (2015).
118. X. Tan, C. Ma, J. Frederick, S. Beckman and K. G. Webber, J. Am. Ceram. Soc. **94** (12), 4091-4107 (2011).
119. L. Zhao, Q. Liu, J. Gao, S. Zhang and J. F. Li, Adv. Mater. **29** (31), 1701824 (2017).
120. Y. Tian, L. Jin, H. Zhang, Z. Xu, X. Wei, G. Viola, I. Abrahams and H. Yan, J. Mater. Chem. A **5**, 17525 (2017).
121. L. Zhao, Q. Liu, S. Zhang and J.-F. Li, J. Mater. Chem. C **4** (36), 8380 (2016).
122. D. Fu, M. Endo, H. Taniguchi, T. Taniyama, S.-y. Koshihara and M. Itoh, Appl. Phys. Lett. **92** (17), 172905 (2008).
123. D. Fu, M. Itoh and S.-y. Koshihara, J. Appl. Phys. **106** (10), 104104 (2009).
124. D. Fu, T. Arioka, H. Taniguchi, T. Taniyama and M. Itoh, Appl. Phys. Lett. **99** (1), 012904 (2011).
125. D. Fu, M. Endo, H. Taniguchi, T. Taniyama, M. Itoh and S.-y. Koshihara, J. Phys.: Condens. Matter **23** (7), 075901 (2011).
126. R. D. Shannon, Acta Crystallogr., Sect. A: Cryst. Phys., Diffr., Theor. Gen. Crystallogr. **32** (5), 751-767 (1976).
127. H. U. Khan, I. Sterianou, Y. Han, J. Pokorny and I. M. Reaney, J. Appl. Phys. **108** (6), 064117 (2010).
128. H. U. Khan, I. Sterianou, S. Miao, J. Pokorny and I. M. Reaney, J. Appl. Phys. **111** (2), 024107 (2012).

Chapter 2 Experimental Methods

This chapter mainly introduces the structural characterization and electrical properties measurement utilized in this thesis project. The synthesis work is not stressed in this thesis as the characterization techniques are more important to help understand the main results presented in Chapter 3.

2.1 Structural Characterization Techniques

Diffraction methods are the most important scientific tools for examining the crystalline structures of materials. In our experiment, Lab X-ray powder diffraction (XRPD) and neutron powder diffraction (NPD) methods are used to investigate the long range ordered, average crystal structures of the materials. Electron diffraction (ED), because of its sensitivity to weak features of reciprocal space such as structured diffuse scattering, is utilized to investigate the short-range order or disorder behaviour on the local scale. Although the interaction between the incident radiation (X-rays, neutron and electron) and the crystals is slightly different for each technique, the plane waves incident on a crystal are still scattered at the angle determined by Bragg's law: [1]

$$2d_{hkl}\sin\theta = n\lambda \tag{2.1}$$

As shown in Figure 2-1, d_{hkl} is the spacing for (*hkl*) lattice plane and θ is the angle between the incident beam and lattice plane, λ is the wavelength of the incident radiation and n is an integer. Bragg's law also can be expressed in a vector notation. For example, it can define the vector $\mathbf{K}$ which equals $\mathbf{k_e}$ - $\mathbf{k_i}$, where $\mathbf{k_i}$ is the wave-vector of the incident wave and $\mathbf{k_e}$ is the wave-vector of the scattered wave. When the **K** is perpendicular to the (*hkl*) lattice plane, the Bragg's law is satisfied and now the **K** is named as the diffracted vector for this (*hkl*) plane (Figure 2-1). Clearly, in order to collect the diffracted signals, the wavelength of the radiation should match the interatomic distance. The typical wavelength used for X-ray and neutron diffraction is in a range from 0.5 Å to 2.5 Å. The wavelength of the electron is determined by their kinetic energy, and for the ED carried out with a transmission electron microscope (TEM) with a 300 kV accelerating voltage,

$\lambda \sim 0.0197$ Å, which is 2 orders of smaller magnitude in comparison with X-ray and neutron.

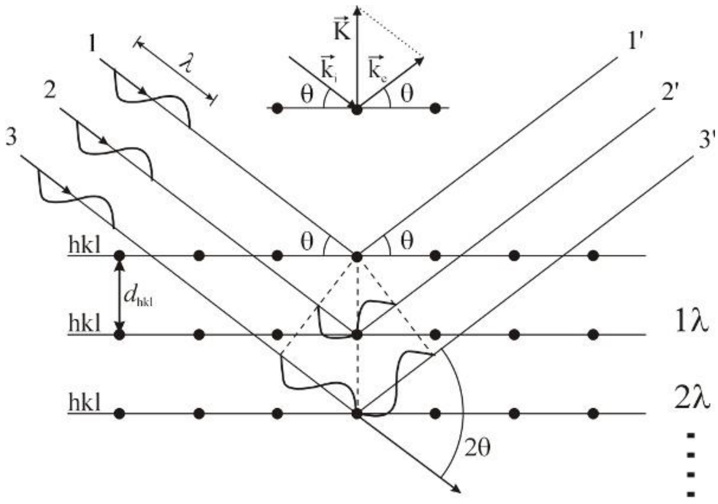

Figure 2-1 Schematic of Bragg's law for diffractions. (Reproduced from De Graef and McHenry[2])

X-rays are electromagnetic waves which initially interact with the electron cloud surrounding the atoms in the crystal. For a single atom, the X-ray scattering factor is proportional to its atomic number, Z, or, more strictly, to the number of electrons held by the atom. Therefore, it is hard to probe light atoms such as Li with X-rays. Another problem is that the scattering amplitude will vary with 2θ, consequently, the high angle Bragg peaks generally exhibit lower intensities.[3]

Neutrons belong to matter waves (de Broglie waves) which interact with the nucleus of the atom. The neutron scattering lengths of atoms are quite different from that observed for X-rays. Figure 2-2 depicts the coherent neutron scattering length for different elements.[4] Clearly, neutrons are capable of revealing the information about light elements even in the presence of heavier atoms. Additionally, for neutron scattering, the scattering power is quite isotropic, *i.e.*, the high angle peaks will not lose their intensity. Another unique property of neutrons is that they possess a magnetic dipole moment, which can interact with the unpaired electrons of atoms reveal magnetic structures.[3]

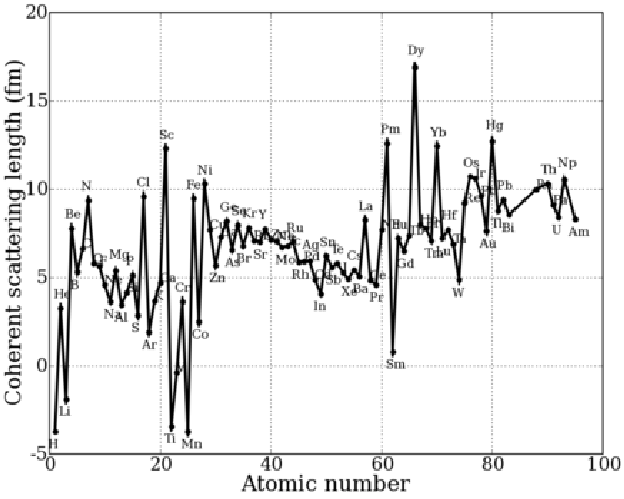

Figure 2-2 Coherent neutron scattering length for different elements (reproduced from Sears[4])

Electrons are charged particles and an ionizing source of radiation. The interaction between electrons and the specimen will generate different kinds of signals (Figure 2-3). Some signals, such as X-ray energy-dispersive spectrometry (XEDS), are used to fingerprint chemical elements. The secondary emissions such as backscattered electrons (BSE) and secondary electrons (SE) are important signals used by the scanning electron microscopy (SEM), which is a technique to map samples' morphology and detect impure phases.[5]

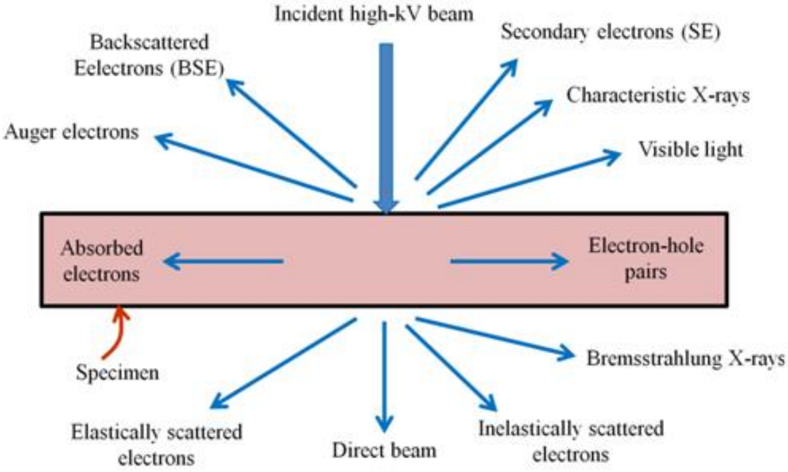

Figure 2-3 Signals generated when a high-energy beam of electrons interacts with a thin specimen (Reproduced from Williams and Carter [6]).

Rather than collecting the electrons from the reflection mode mentioned above, the ED patterns require the elastically scattered electrons in transmission model, *i.e.*, ED needs electrons passing through the targeted sample. In order to collect reliable signals, the thickness of the sample should be less than 100 nm. The probe size used for ED is quite small, thus reflecting the local structure information within one grain or domain region. The strong interaction between electrons and matter results in the intense patterns, which can reveal weak features of reciprocal space, especially the diffuse scattering. The intense electron beam also has some drawbacks. *E.g.*, the intense electron beam may damage the specimen and multiple scattering effects such as secondary diffractions makes the interpretation difficult. [6]

2.1.1 X-ray Diffraction

X-ray diffraction in this thesis was carried out on a PANalytical Empyrean diffractometer, and the X-ray source is CuKα ($\lambda_{K\alpha 1}$ = 1.5406 Å and $\lambda_{K\alpha 2}$ = 1.5443 Å). The reflection geometry used for X-ray diffraction is shown in Figure 2-3. Instead of the common point detector, the Empyrean diffractometer is equipped with a 1-D pixel detector, which can detect a certain 2θ range simultaneously, which helps improve the efficiency. The normal set-up for the XRPD is the symmetric θ-2θ scan, which always keeps incident angle equal to the diffracted angle.

The lab XRPD using this set-up has two main disadvantages. Firstly, as the collected diffraction patterns are mainly from the contribution of the lattice planes parallel to the sample surface, the patterns are easily influenced by the preferred orientation. In order to avoid that, as far as possible, powder samples are required rather than the ceramic pellets. However, since the pellet form is more reliable to analyse the measured properties, X-ray diffraction on the pellets is sometimes also necessary. Secondly, penetration depth, which is mainly influenced by the energy of X-ray, incident beam angle, absorption coefficients and the density of the materials, is also limited for the lab X-ray diffractometer. For the CuKα source, the rough penetration depths for $PbZrO_3$ and $AgNbO_3$ at $\theta \sim 45$ ° are 7 μm and 20 μm, respectively, which is much smaller than the pellets' thickness.[7] Therefore, the XRD patterns for the ceramic pellets in this thesis, especially for the $PbZrO_3$-based materials, only reflect the structural information near the surface.

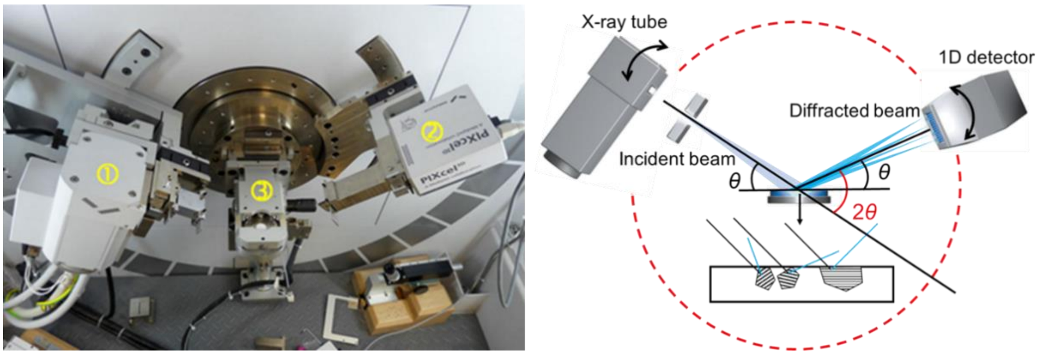

Figure 2-4 The reflection geometry used for Lab X-ray diffraction.

2.1.2 Neutron Diffraction

NPD in this thesis was conducted on the high intensity diffraction beamline (Wombat) at the Australian Nuclear Science and Technology Organisation (ANSTO).[8] The complete layout of the WOMBAT beamline is shown in Figure 2-5. The neutron beam from the OPAL reactor comes through the neutron guide. The monochromator which is made with the Ge single crystals is used to tune the wavelength for the experiment. In this thesis, $\lambda \sim 2.41$ and 1.64 Å are selected for the studies presented in Chapter 3. Then the neutron beam is incident on the sample at the sample stage. The oscillating collimator is applied to reduce neutrons diffracted by the environment. After going through the collimator, the diffracted neutron beam is collected by a large two-dimensional (2D) curved position sensitive detector (PSD) covering an angular range of 120° with a minimum resolution of 0.0625°. The high intensity neutron beam can pass through the whole pellet sample, reflecting the structural information of the bulk materials. Additionally, the penetration ability of this neutron beam makes it easier to develop the sample environment for *in-situ* characterization.

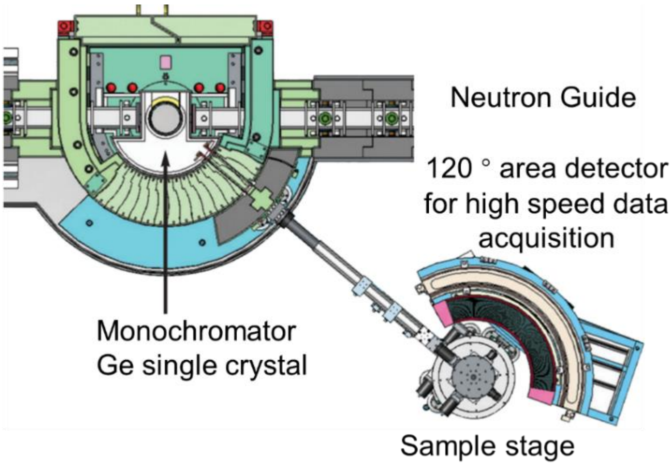

Figure 2-5 Diagram for the instrumental layout of WOMBAT and the schematic of the reflection/transmission geometry.

The sample holders used in this thesis are summarized in Figure 2-6, Figure 2-6a shows a schematic of the experimental set-up for the *in-situ* structure characterization under E-field. The pellet sample was fixed to a central stage and coated with the silver paste on the surface. The conductive wires were attached to the silver coatings to supplying the E-field. The sample stage is able to rotate anti-clockwise around the normal direction, enabling the analysis of the crystallographic texture. The angle between the incident beam and applied E-field is defined as ω and initially, the pellets were parallel to the incident beam, *i.e.*, ω = -90°. At each field point, a set of 13 diffraction patterns separated by 15° ω angle were collected to investigate the preferred orientation. With the application of the curved position sensitive detectors, WOMBAT collected the data with scattering vectors (**K**) at multiple angles to the E-field.[9-11] In Figure 2-6(a), the ψ indicates the angle between the **K** and E-field, **E**, modulo 180° and from the geometry, the relationship among the ψ, ω and θ is: $\psi = \omega - \theta + 90°$. After plotting the diffraction patterns corresponding to different sample orientations (ω), it can draw a straight line for the data at the constant ψ. For quantitative analysis, these ω-dependent diffraction patterns need to be transformed for Rietveld refinement at multiple orientations.[11] The integration of these patterns collected at different ψ values was utilized to analyse the average structure of the samples. Furthermore, the top-loading furnace was available at the same time (Figure 2-6b), which enables the *in-situ* characterisations at different temperature and E-field. Figure 2-6c shows the picture and schematic of the Paris-Edinburgh high pressure cell which is manually operated with a hydraulic hand pump. This set-up is used to monitor the structural change induced by a mechanical load. For the sample preparation, the target powers and metal lead (the internal standard for the pressure) were loaded into the metal gasket and fluorinert was used as a pressuring transmitting medium. After putting the press on the centre stage, the neutron beam went through the gasket and unravelled the structure of the samples.

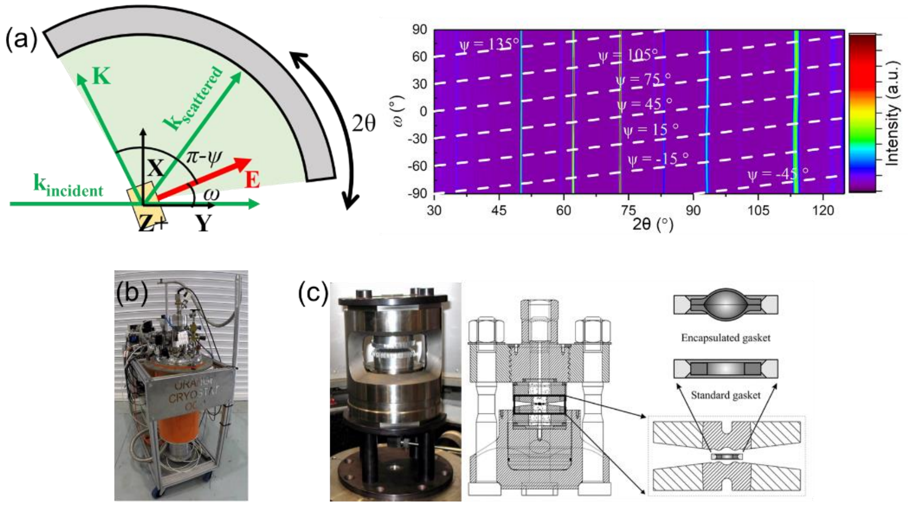

Figure 2-6 (a) Schematic of the experimental set-up of the *in-situ* neutron diffraction at different E-field and example of the collected diffraction patterns under an *in-situ* applied E-field. Dotted lines represent constant values of ψ, which are dependent on 2θ due to detector geometry. (Reproduced from Simons *et.al.*[11]) (b) Cryostat-furnace and (c) press used for *in-situ* neutron diffractions at different temperature and pressure, respectively.

2.1.3 Electron Diffraction

Electron diffraction is an associated function of the TEM and captures the structural information in reciprocal space, reflecting the order and disorder information of the crystals. For a perfect, three dimensionally ordered structure, it will show 3D lattice points in the reciprocal space. In the reciprocal lattice, the lattice vector is defined as **g**. As shown in Figure 2-7a, when **K** = **g**, the Bragg condition is satisfied. It can draw a sphere with $|\mathbf{k_i}| = \frac{1}{\lambda}$ in reciprocal space. The reciprocal-lattice points are observable in the diffraction patterns only when this sphere cuts through them. This sphere is named as the 'Ewald sphere' which is a 3D sphere in reciprocal space. However, instead of 3D images, the diffraction patterns are the projection planes of the Ewald sphere. It is worthy to note that the wavelength used for ED is 0.0197 Å for 300 keV, *i.e.*, the radius of the sphere is ~ 500 nm^{-1} and the surface is almost planar which satisfies the Bragg condition for reciprocal-lattice points. The direction of the incident beam is expressed as $<uvw>$ and the diffraction spot is denoted as $<hkl>^*$. When the plane of points in the reciprocal space is perpendicular to the incident beam, $uh+vk+wl=0$, this region is named as 'zero-order Laue zone' (ZOLZ). If $uh+vk+wl = n > 0$ (n is an integer), the planes of points are called the 'higher-order Laue zones' (HOLZ). The first of these, *i.e.*, $n = 1$, is the 'first-order Laue zone' (FOLZ). Generally, for the perovskite structure, the projection plane can only collect the information for ZOLZ, but for the TEM with high accelerating voltage or crystals with larger unit-cell, HOLZ patterns are available on the projection plane, which are quite useful for structural analysis (Figure 2-7b).

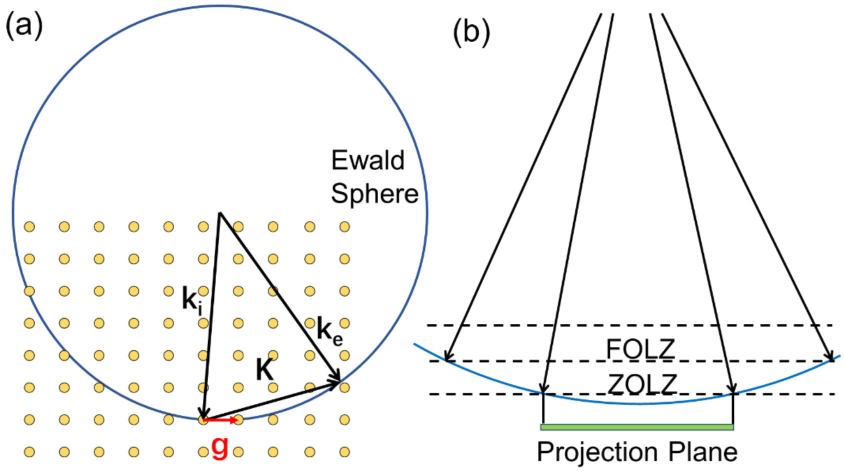

Figure 2-7 (a) The Ewald sphere of reflection is shown intersecting of reciprocal-lattice points. (b) The Ewald sphere intercepts points in higher order Laue zones. (Reproduced from Williams and Carter [6])

The abovementioned condition of a crystal is perfect, 3D ordered structure while these only ideally exist. The real samples for ED are very thin, therefore their reciprocal lattice points elongate in one direction to rods. Additionally, disordered structures are widespread in real materials. With changes in the degree of ordering, sharp Bragg reflections transfer into diffuse scattering. Table 2-1 summarizes the relationship between the ordered degrees of the crystals in real space and the relative diffuse scattering in reciprocal space. The intensity of the scattered electrons makes it possible to observe these weak structured diffuse intensity distributions, which means the EDP can supply local structural order/disorder information.

Table 2-1 The relationship between the ordered degrees of the crystals in real space and the relative diffuse scattering in reciprocal space.

Real Space crystals	Ordered dimensions	Reciprocal Space	Diffuse dimensions
1D ordered chain	1	Set of parallel diffuse planes	2
2D ordered arry	2	Set of parallel diffuse lines	1
3D ordered crystal	3	3D lattice points	0

In this thesis, EDPs were collected by using a JEOL 2100 TEM operating at 300 kV. For the sample preparation, the powdered sample was dispersed in n-butanol and dropped onto lacy carbon coted grids for the TEM. The double tilting axes enable the EDP collection at different grain orientations. In order to reveal the diffuse scattering character, long exposures were adopted.

2.2 Rietveld Analysis

Rietveld analysis is a non-linear least squares refinement procedure to fit an experimental powder diffraction pattern with a structural model, which allows for the determination of the crystal structural parameters including the unit-cell parameters and atomic coordinates at the end.[12] The principle of this method is to minimize the differences between the calculated and experimental data, so the refinement results are mainly determined through statistical techniques. The statistical descriptions contain two drawbacks: 1) the variation of the parameters during the refinement does not take physical meaning into account, which can lead to the final structure being chemically unreasonable; 2) Some systematic errors such as peak asymmetry is not evident in the final statistical results but are visually obvious. Therefore, the results of Rietveld refinement are judged not only by the statistical parameters but also the difference plot and the chemical reasonableness of the structural model. [13, 14]

Generally, the statistical parameters used to analyse the Rietveld refinement are R_p, R_{wp}, R_{exp}, R_{Bragg} and χ^2. The software for refinement optimizes the model function to minimize the R parameters, especially the weighted profile R-factor (R_{wp}), which is calculated as follows:

$$R_{wp}^2 = \sum_i w_i (y_{C,i} - y_{O,i})^2 / \sum_i w_i (y_{O,i})^2 \tag{2.2}$$

Where the C is short for calculated and O is short for observable. Furthermore, when the model is ideal, the best possible R_{wp} quantity is obtained and it is called the expected R factor (R_{exp}) at this time. The "goodness of fit" parameter, χ^2 equals $(R_{\mathrm{wp}}/R_{\mathrm{exp}})^2$. It is evident that the R_{wp} takes the whole pattern, involving both the peaks and background, into consideration, thus easily influenced by the quality of the data. Instead, R_{Bragg} parameter is a measure of the fit to the integrated intensity of each peak, reflecting the difference between the experimental and calculated peak intensities (I^{obs} and I^{calc}). This parameter provides a valuable indication of the structural model used for refinement.

As described in Chapter 1, the structure investigated in this project are distorted perovskite structures with lower symmetry. The complexity of the superstructural distortion makes the Rietveld refinement a challenging task. For example, $AgNbO_3$ with $Pmc2_1$ space group contains 12 independent atomic sites and 32 freedoms available to be refined only considering the atomic coordinates. The refinement process will be very time consuming because there are diverse sequences to refine these 32 parameters. However, the Rietveld refinement in terms of the symmetry modes will become dramatically simplified. Figure 2-8 illustrates the interfaces for Rietveld refinement of the atomic coordinates and the distortion-mode amplitudes, respectively. From the mode crystallography point of view, the primary modes decide the distorted structure and generally they present large distortive amplitudes. Obviously, the primary modes should be taken into consideration firstly in the refinement. Additionally, these primary modes have corresponding physical meaning, so this method provides a convenient way to judge whether the refinement results are physically reasonable. Additionally, the distortion-mode description is a decomposition of the lower symmetry structure into the different modes of the parent symmetry. When fixing the amplitudes of specific modes at zero, it can maintain a distorted structure with other symmetries. Overall, the symmetry-mode refinement is a useful and convenient tool to identify and refine the structural distortions.

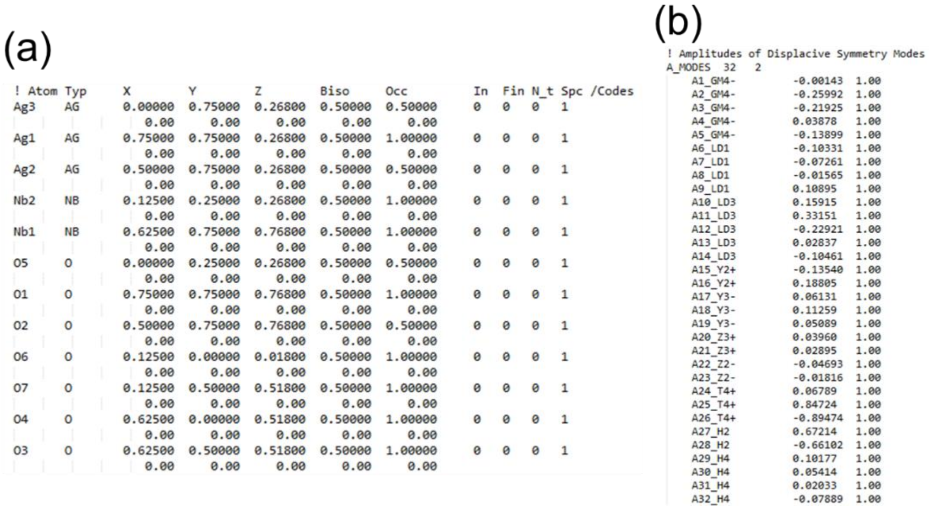

(a)

```
! Atom Typ      X        Y        Z        Biso     Occ        In   Fin N_t Spc /Codes
Ag3    AG       0.00000  0.75000  0.26800  0.50000  0.50000    0    0    0   1
                   0.00     0.00     0.00     0.00     0.00
Ag1    AG       0.75000  0.75000  0.26800  0.50000  1.00000    0    0    0   1
                   0.00     0.00     0.00     0.00     0.00
Ag2    AG       0.50000  0.75000  0.26800  0.50000  0.50000    0    0    0   1
                   0.00     0.00     0.00     0.00     0.00
Nb2    NB       0.12500  0.25000  0.26800  0.50000  1.00000    0    0    0   1
                   0.00     0.00     0.00     0.00     0.00
Nb1    NB       0.62500  0.75000  0.76800  0.50000  1.00000    0    0    0   1
                   0.00     0.00     0.00     0.00     0.00
O5     O        0.00000  0.25000  0.26800  0.50000  0.50000    0    0    0   1
                   0.00     0.00     0.00     0.00     0.00
O1     O        0.75000  0.75000  0.76800  0.50000  1.00000    0    0    0   1
                   0.00     0.00     0.00     0.00     0.00
O2     O        0.50000  0.75000  0.76800  0.50000  0.50000    0    0    0   1
                   0.00     0.00     0.00     0.00     0.00
O6     O        0.12500  0.00000  0.01800  0.50000  1.00000    0    0    0   1
                   0.00     0.00     0.00     0.00     0.00
O7     O        0.12500  0.50000  0.51800  0.50000  1.00000    0    0    0   1
                   0.00     0.00     0.00     0.00     0.00
O4     O        0.62500  0.00000  0.51800  0.50000  1.00000    0    0    0   1
                   0.00     0.00     0.00     0.00     0.00
O3     O        0.62500  0.50000  0.51800  0.50000  1.00000    0    0    0   1
                   0.00     0.00     0.00     0.00     0.00
```

(b)

```
! Amplitudes of Displacive Symmetry Modes
A_MODES  32   2
   A1_GM4-          -0.00143  1.00
   A2_GM4-          -0.25992  1.00
   A3_GM4-          -0.21925  1.00
   A4_GM4-          0.03878   1.00
   A5_GM4-          -0.13899  1.00
   A6_LD1           -0.10331  1.00
   A7_LD1           -0.07261  1.00
   A8_LD1           -0.01565  1.00
   A9_LD1           0.10895   1.00
   A10_LD3          0.15915   1.00
   A11_LD3          0.33151   1.00
   A12_LD3          -0.22921  1.00
   A13_LD3          0.02837   1.00
   A14_LD3          -0.10461  1.00
   A15_Y2+          -0.13540  1.00
   A16_Y2+          0.18805   1.00
   A17_Y3-          0.06131   1.00
   A18_Y3-          0.11259   1.00
   A19_Y3-          0.05089   1.00
   A20_Z3+          0.03960   1.00
   A21_Z3+          0.02895   1.00
   A22_Z2-          -0.04693  1.00
   A23_Z2-          -0.01816  1.00
   A24_T4+          0.06789   1.00
   A25_T4+          0.84724   1.00
   A26_T4+          -0.89474  1.00
   A27_H2           0.67214   1.00
   A28_H2           -0.66102  1.00
   A29_H4           0.10177   1.00
   A30_H4           0.05414   1.00
   A31_H4           0.02033   1.00
   A32_H4           -0.07889  1.00
```

Figure 2-8 Schematic of the interfaces used for Rietveld refinement of (a) atomic coordinates and (b) distortion-mode amplitudes.

The software used for Rietveld refinement in this thesis is the Fullprof suite[15] which is a powerful tool for working with symmetry modes in the description of distorted structures. It is important to note that when fitting the experimental data, the input parameters can vary without significantly changing the statistical parameters of the Rietveld refinement. The resultant errors indicate their influences on the goodness of fit and both proposed structural model, diffraction techniques and correlation with other variables will influence these values.

2.3 Piezoresponse Force Microscopy

Piezoresponse force microscopy (PFM) is a commercially available function of atomic force microscopy (AFM). Before introducing the basic principle for PFM, it is worthy to mention the basic function of AFM and the underlying mechanism. AFM is mainly used to map the surface morphology of samples, which is achieved by scanning a tip over the sample surface and modifying the tip-surface distance using a feedback loop.

The topography image can be done by either contact or non-contact (AC) mode. In AC mode, generally the cantilever is mechanically oscillated by a piezoelectric actuator located on the cantilever holder (Note that the excitation source is not restricted to piezoelectric materials). Then the signal generator sweeps a wide range of frequencies and locates one near the resonance of the cantilever. When the tip approaches the surface, the tip-surface force (repulsive or attractive) modifies the resonance peak, and the topography is mapped by the feedback loop (Figure 2-9). Mapping the local physical and chemical properties, such as surface potential and current are also available because these properties can generate a force interaction between the tip and sample. Among these wide applications, PFM is a useful technique to image the local domain structures and dipole switching behaviour.

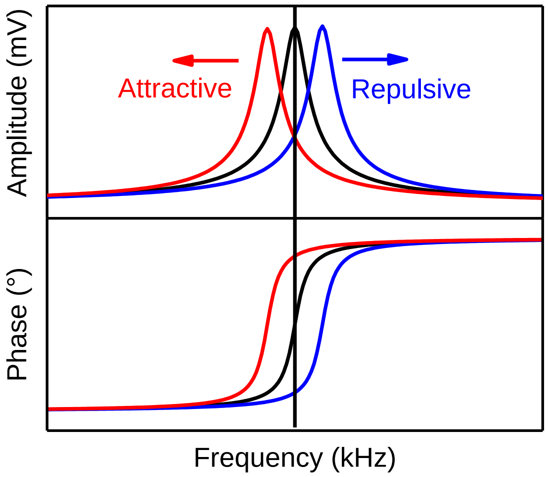

Figure 2-9 A shift in resonance frequency as the tip-surface interaction changes. The black line is the resonance frequency for the free oscillation. The blue and red lines denote the peak shift induced by repulsive and attractive force, respectively.

The PFM technique is based on the detection of bias-induced surface deformation. Therefore, it works in the contact mode, measuring the topography and piezoresponse of samples at the same time. By applying an ac voltage on the tip, the tip deflection for the vertical PFM (VPFM) is: $d=d_0+d_{33}V_{ac}\cos(\omega t+\varphi)$ where the d_{33} is the local piezoelectric coefficient. In Figure 2-10a and b, the polarization vectors with the same d_{33} lie in parallel and antiparallel to the E-field, respectively. They show the same amplitude but the polarization direction, which is decided by the phase difference, φ, between the tip bias and surface oscillation, is 180° different. Obviously, the phase contrast is very evident but the amplitude, $d_{33}V_{ac}$, of these local piezoresponse signals are usually very weak. Applying high drive voltages will induce other problems such as polarization reversal and damage to the samples. Therefore, the contact resonance is proposed to act as an amplifier to improve the piezoresponse signals. In this way, the quality factor, Q (~100 in air), is gained for enhancing the amplitudes, *i.e.*, $A= d_{33}QV_{ac}$. As the contact resonant frequency depends on the tip-sample stiffness, so it is every sensitive to the surface and tip conditions. Generally, a rough surface is not allowed for PFM measurement because it induces strong crosstalk between the piezoresponse and topography. Even though, the contact resonant frequency will not remain constant during the scanning, and the resonance frequency is required to be tracked so the excitation signals can change accordingly to keep Q factor constant. With the development of the instruments, the most effective resonance tracking methods are the Dual AC Resonance Tracking (DART) and band excitation (BE).[16, 17] The DART method uses two separate oscillating voltages with the frequencies near the same resonance while BE synthesized signal contains a continuous band of frequencies to excite the sample and monitoring the response spectra. The details of these two technologies are not included in this thesis.

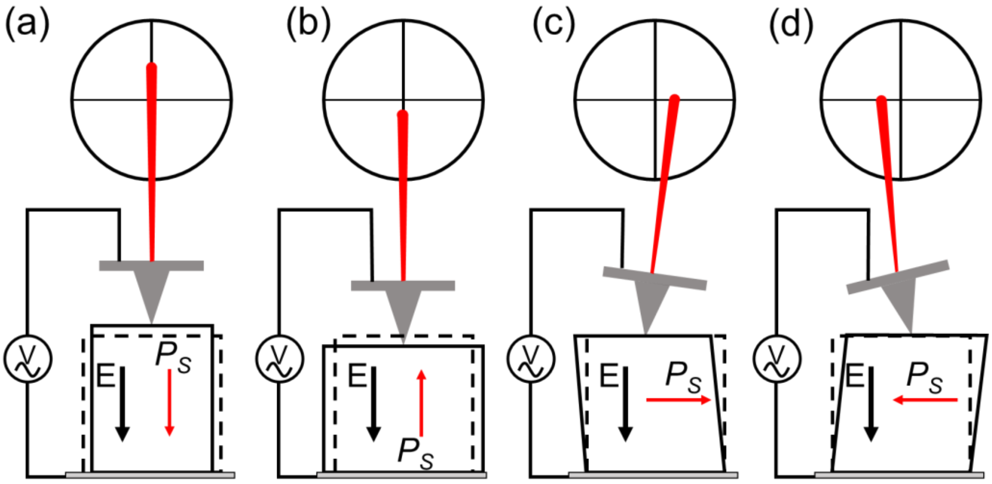

Figure 2-10 The deformation of the ferroelectric materials under a biased tip. E-field is parallel (a) or antiparallel (b) to the spontaneous polarization. (c), (d) Shear deformation when the E-field is perpendicular to the spontaneous polarization. (Reproduced from Balke *et.al.*[18])

In addition to mapping the local domain structure, PFM is capable of investigating the local domain, or polarization switching behaviour by the built-in spectroscopic mode, *i.e.*, switching spectroscopic PFM (SS-PFM). The waveform used for SS-PFM is a triangular pulse wave superimposed with an AC signal (Figure 2-11a). Between each dc voltage step, the offset is zero and the applied ac signal is used to detect the piezoresponse, which equals $A\cos\varphi$, where A is the amplitude and φ is the phase. Generally, pulse-off states provide reliable hysteretic behaviour because a strong electro-static force is involved in the pulse-on states. The results of SS-PFM, *PR* hysteresis loop (Figure 2-11b) are very similar to the macroscopic *P-E* hysteresis loop but it only probes the domain switching at a single location under a sharp tip.[18] Figure 2-11c illustrates the domain evolution under the biased tip and both nucleation (1 and 4) and growth (2 and 3) processes are involved. Obviously, the surface domain can be aligned by the biased tip. In this project, the local poling process is achieved by scanning a region with a relatively strong dc bias.

In this thesis, the topography, PFM image, SS-PFM and local poling processes were conducted was a commercial AFM instrument (Cypher, Asylum Research) with Olympus AC240^{TM} (spring constant $k \sim 2$ N/m and resonance frequency $f \sim 70$ kHz) and Asylum01 ($k \sim 2$ N/m and $f \sim 70$ kHz) probes. In order to avoid the impact of the surface topography, all the ceramic pellets were polished to the roughness ~ 10 nm. The high voltage cantilever holder (up to 100 V) was adopted for SS-PFM and local poling experiments.

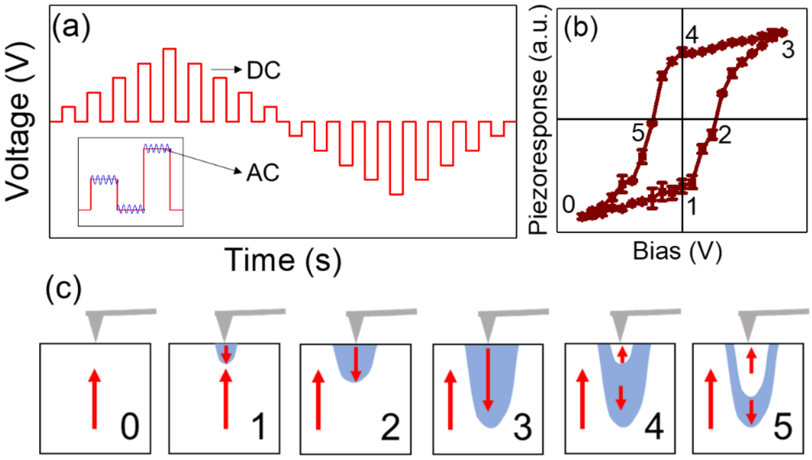

Figure 2-11 Schematic representation of the SS-PFM process. (a) the measurement

waveform and (b) experimental piezoresponse hysteresis loop. (c) The domain evolution process at the different point of PR hysteresis loop. (Reproduced from Jesse *et.al.*[19])

2.4 Electrical Properties Measurement Techniques

The dielectric and ferroelectric properties measurements are two important techniques involved in this thesis. Before the electrical characterisations, the ceramic pellets were coated with high temperature silver paste on each side followed by heat treatment at 700 °C for 15min to ensure good electrical contact. Sometimes poling is required before the properties measurements. The poling of ceramics was conducted by a homebuilt apparatus. Silicone oil was used to prohibit the dielectric breakdown of the ceramic edges and the hot-plate was used to heat the samples to elevated temperatures. The sample stage was connected to a high voltage power supply (PS350, Standford Research Systems, Inc), which can provide a dc voltage up to 5 kV. Generally, the poling field was decided by the coercive field of the samples and poling time was sustained for 10 minutes.

2.4.1 Dielectric Measurements

The dielectric properties, dielectric constant and dielectric loss of the samples in this thesis were achieved with a precise LCR meter (Agilent E4980A) with 1 V ac excitation signal over a frequency range of 20 Hz ~ 2 MHz. The high temperature dielectric measurement (room temperature to 600 °C) were realized with a commercial system (ADVANTECH, 610L) and low temperature measurement (10 K ~ 450 K) was achieved with a high vacuum sample environment (Edwards, T-station 75) and CTI-Cryogenics Cryostat (Janis, 8200 compressor). The sample environment systems and LCR meters communicated with a computer software which can control the target temperature, ramping rate and record the measured data.

2.4.2 Ferroelectric Measurements

Polarization-electric field (*P-E*) hysteresis loops of the ceramics in this thesis were measured with a TFAnalyzer 2000 with an aixACCT FE test unit. The analyzer contains a modified Sawyer-Tower circuit and the transferred charges are calculated by time-integrating measured currents. A triangular voltage signal (0.1-10 Hz, up to 5000 V) was applied to the samples while the magnitude was decided by the critical field and breakdown field of the samples. All the ceramics were immersed into silicone oil to avoid edge breakdown problems. Furthermore, for the samples requiring large E-fields, *e.g.*, the critical field for $AgNbO_3$ is ~ 130 kV/cm, a partially coated electrode was used. The E-field induced longitudinal strain (or *S-E* hysteresis loop) was measured by a laser interferometer with the *P-E* hysteresis loop simultaneously. It is worthy to note that sometimes AFE materials are easy to be switched into the metastable FE state, therefore prepole pulse was not applied for the measurement. Figure 2-12 shows the influence on *P-E* and *S-E* hysteresis loops caused by the prepole pulse. The signal generator enables the fatigue measurement, whose waveform is square rather than triangular (frequency ~ 0.1 – 100 Hz, magnitude, up to 5000 V). The fatigue measurement was used to learn the polar behaviours of FE/AFE materials under E-field cycling. In addition, internal heater (up to 200 °C) in the bulk sample cell was used to *in-situ* monitoring the temperature dependent *P-E* and *S-E* properties.

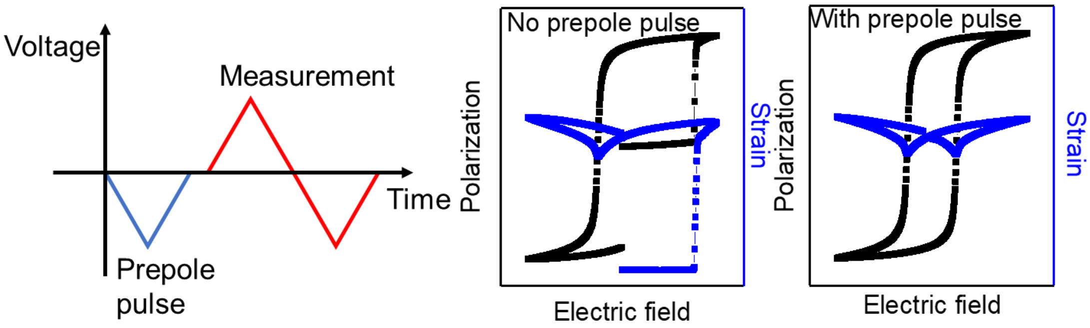

Figure 2-12 The impacts of pre-pole pulse on *P-E* and *S-E* hysteresis loops.

References

1. C. Giacovazzo, *Fundamentals of crystallography*. (Oxford university press, New York, 2002).
2. M. De Graef and M. E. McHenry, *Structure of materials: an introduction to crystallography, diffraction and symmetry*. (Cambridge University Press, New York, 2012).
3. A. R. West, *Basic solid state chemistry*. (John Wiley & Sons, 1999).
4. V. F. Sears, Neutron news **3** (3), 26-37 (1992).
5. P. J. Goodhew, J. Humphreys and R. Beanland, *Electron microscopy and analysis*. (Taylor & Francis, London, 2001).
6. D. B. Williams and C. B. Carter, in *Transmission electron microscopy* (Springer, 1996), pp. 3-17.
7. A. Wilson and V. Geist, in *Cryst. Res. Technol.* (1993), Vol. 28, pp. 110-110.
8. A. J. Studer, M. E. Hagen and T. J. Noakes, Physica B **385**, 1013-1015 (2006).
9. J. E. Daniels, T. R. Finlayson, A. J. Studer, M. Hoffman and J. L. Jones, J. Appl. Phys. **101** (9), 094104 (2007).
10. J. E. Daniels, W. Jo, J. Rödel and J. L. Jones, Appl. Phys. Lett. **95** (3), 032904 (2009).
11. H. Simons, J. E. Daniels, A. J. Studer, J. L. Jones, and M. Hoffman, J. Electroceram. 32, 283 (2014).
12. H. Rietveld, J. Appl. Crystallogr. **2** (2), 65-71 (1969).
13. C. Buchsbaum and M. U. Schmidt, Acta Crystallogr. Sect. B: Struct. Sci. **63** (6), 926-932 (2007).
14. B. H. Toby, Powder Diffr. **21** (1), 67-70 (2006).
15. J. Rodriguez-Carvajal, presented at the satellite meeting on powder diffraction of the XV congress of the IUCr, 1990 (unpublished).
16. B. J. Rodriguez, C. Callahan, S. V. Kalinin and R. Proksch, Nanotechnology **18** (47), 475504 (2007).
17. S. Jesse, S. V. Kalinin, R. Proksch, A. Baddorf and B. Rodriguez, Nanotechnology **18** (43), 435503 (2007).
18. N. Balke, I. Bdikin, S. V. Kalinin and A. L. Kholkin, J. Am. Ceram. Soc. **92** (8), 1629-1647 (2009).
19. S. Jesse, H. N. Lee and S. V. Kalinin, Rev. Sci. Instrum. **77** (7), 073702 (2006).

Chapter 3 Major Journal Publications

3.1 Electric-Field-Induced AFE-FE Transitions and Associated Strain/Preferred Orientation in Antiferroelectric PLZST

The research presented in this publication was solely completed by the author of this thesis. The author was the main investigator of the neutron beam proposal and carried out the designed neutron experiment with the technical assistance of the instrument scientist of WOMBAT. The author has done all the properties and structural characterization, interpreted the results and written the manuscript.

www.nature.com/scientificreports

SCIENTIFIC REPORTS

OPEN

Received: 18 August 2015
Accepted: 11 March 2016
Published: 30 March 2016

Electric-field-induced AFE-FE transitions and associated strain/preferred orientation in antiferroelectric PLZST

Teng Lu[1], Andrew J. Studer[2], Lasse Noren[1], Wanbiao Hu[1], Dehong Yu[2], Bethany McBride[1], Yujun Feng[3], Ray L. Withers[1], Hua Chen[4], Zhuo Xu[3] & Yun Liu[1]

Electric-field-induced, antiferroelectric-ferroelectric (AFE-FE) phase transitions are common for AFE materials. To date, the strain and preferred orientation evolution as well as the role of the intermediate FE state during the successive AFE-FE-AFE phase transitions has not been clear. To this end, we have herein studied a typical AFE $Pb_{0.97}La_{0.02}(Zr_{0.56}Sn_{0.33}Ti_{0.11})O_3$ (PLZST) material using *in-situ* neutron diffraction. It is striking that the AFE-FE phase transition is not fully reversible: in the electric-field-induced FE state, the induced strain exhibits an elliptical distribution, which in turn leads to significant preferred orientation in the final AFE state after withdrawal of the applied electric-field. The ω-dependent neutron diffraction patterns show clear evidence of the induced strain distribution and associated preferred orientation arising from the AFE-FE phase transition. The current work also provides an explanation for several temperature and electric-field dependent dielectric anomalies as well as unrecovered strain change which appear in AFE materials after exposure to sufficiently high electric fields.

Antiferroelectricity (AFE) arises from anti-parallel alignment of off-center, ionic displacements in materials (of Pb^{2+} ions in the case of the first AFE compound to be discovered, $PbZrO_3$[1]) and was initially proposed by Kittel in 1951[2]. The distinctive electromechanical coupling properties of AFE materials have attracted increasing attention ever since. A typical example is the lightly lanthanum-doped, lead zirconate stannate titanate (PLZST) system. At particular composition regions within this system, PLZST exhibits large electric-field-induced (E-field-induced) strain (*e.g.* maximum 0.87% for bulk ceramics and 0.49% for thin films[3,4]), potentially enabling a range of applications, such as actuators, sensors, electrocaloric devices, energy harvesting and storage devices[4–7]. Such high strains have long been considered to be related to a reversible, E-field-induced, tetragonal antiferroelectric (AFE_T) to rhombohedral ferroelectric (FE_R) phase transition[8]. That the initial physical properties of fresh samples behave differently to those of poled samples suggests that the AFE_T-FE_R transition may not be fully reversible. Likewise, the fact that the physical properties of PLZST as a function of increasing E-field are initially linear but then exhibit clear hysteresis behaviour[9] as well as a strong field and/or temperature dependence, again suggests that a simple reversible AFE_T-FE_R transition is not the whole story.

Park *et al.*[10] claimed a decoupling of the transverse and longitudinal strain changes accompanying the AFE_T to FE_R phase transition, and attributed it to preferentially oriented AFE domains induced by the externally applied electric field. The X-ray diffraction (XRD) study used, however, had limitations in (1) the lack of any direct *in-situ* characterisation evidence for changes in the AFE domain configuration with applied field, including the formation of preferentially oriented AFE domains and their associated dynamic behavior; and (2) the XRD patterns were only collected before and after exposure to an E-field of 50 kV/cm, much higher than the critical field (37 kV/cm) for AFE-FE phase switching. It is thus unclear what exactly happens for samples at lower fields before and after the phase transition. Furthermore, how do the average structure and the preferred orientation relate to

[1]Research School of Chemistry, The Australian National University, ACT 2601, Australia. [2]Bragg Institute, The Australia Neutron Science and Technology Organisation, Lucas Height, Australia. [3]Electronic Materials Research Laboratory, Xian Jiaotong University, Xian 710049, Shaanxi, China. [4]Centre for Advanced Microscopy, The Australian National University, ACT 2601, Australia. Correspondence and requests for materials should be addressed to Y.L. (email: yun.liu@anu.edu.au)

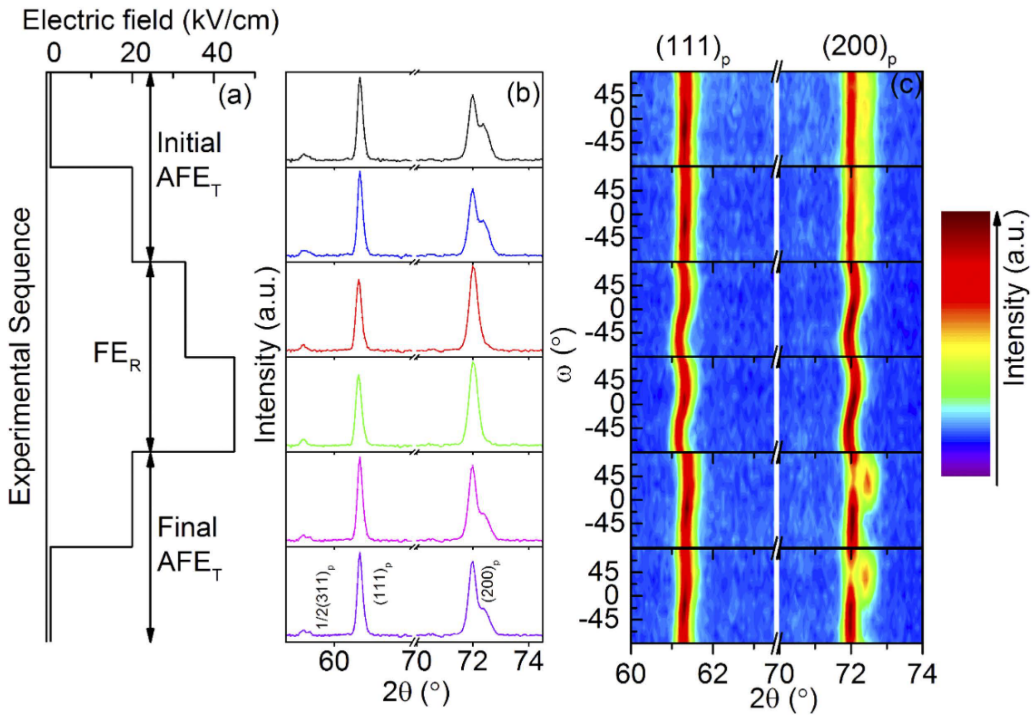

Figure 1. ***In-situ* neutron diffraction patterns (NDPs) collected at room temperature.** (**a**) A schematic drawing to describe the experimental sequence of applied E-fields, resulting in three different states *i.e.* the initial AFE$_T$ state, the intermediate FE$_R$ state and the final AFE$_T$ state, determined by their average NDPs partially presented in (**b**) ($57.5° < 2\theta < 74.5°$). (**c**) The ω-dependence of the $(111)_p$ and $(200)_p$ peaks. Both the ω-averaged NDPs (**b**) as well as the ω-dependent NDPs (**c**) were collected *in-situ* under the applied E-fields shown in (**a**).

one another? And to what extent does such preferred orientation affect the measured physical properties? These questions need to be answered in order to guide the development and optimization of AFE materials of this type for practical applications.

In this work, *in-situ* neutron powder diffraction is employed to investigate the evolution of preferred orientation and strain in a $Pb_{0.97}La_{0.02}(Zr_{0.56}Sn_{0.33}Ti_{0.11})O_3$ (PLZST in what follows) sample as a function of applied E-field. Note that the fresh PLZST sample with the chemical composition just given is in the AFE$_T$ tetragonal phase region, as reported previously[3,8]. In conjunction with dielectric, ferroelectric properties measurements, we aim to attain a comprehensive understanding of the E-field-induced, AFE$_T$ (initial)- > FE$_R$- > AFE$_T$ (final) phase transition and the associated impacts on properties, thereby providing new insight to the design and development of AFE materials.

Results and Discussion

In-situ neutron powder diffraction.

Detail as regards sample preparation, *in-situ* neutron powder diffraction under applied E-field (including experimental setup and procedures followed) is presented in the "Methods" section below. Fig. 1a shows the experimental sequence of external E-fields applied (0 kV/cm → 20 kV/cm → 33 kV/cm → 45 kV/cm → 20 kV/cm → 0 kV/cm). Fig. 1b shows the corresponding $57.5° < 2\theta < 74.5°$ regions of the ω-averaged, neutron diffraction patterns (NDPs) obtained as a function of E-field. Note that the NDPs in (b) were summed and averaged over the 13 ω-dependent patterns, collected at rotation angles from $\omega = -90°$ to $+90°$ in incremental steps of 15°. Fig. 1c maps the ω-dependence of the characteristic $(111)_p$ and $(200)_p$ peaks, subscript p for the underlying parent perovskite structure.

All patterns (Fig. 1b,c) are indexed with respect to the underlying parent perovskite structure (labelled with the subscript p). Note that when the applied E-field is below 33 kV/cm, the shape of the $(111)_p$ peak appears symmetric while the $(200)_p$ peak is clearly split into two peaks with a relative intensity ratio of ~2:1 (Fig. 1b), consistent with pseudo-tetragonal metric symmetry, as expected. In addition, distinct ½$(111)_p$ (not shown in Fig. 1b) and split ½$(311)_p$ type satellite reflections are also observed, in good agreement with our own electron diffraction results (Fig. S1a) as well as those previously obtained from similar composition samples[11,12]. Satellite reflections of this type are highly likely to be associated with $a^-a^-c^0$ ZrO_6 octahedral tilting as also occurs in $PbZrO_3$ itself, but not directly relevant to the Pb ion displacements responsible for the AFE structure[11]. Indeed, Íniguez *et al.*[13] have recently shown that $a^-a^-c^0$ ZrO_6 octahedral tilting is essential to the stabilization of the AFE structure of $PbZrO_3$. Given that our PLZST sample can be thought of as being composed of $PbZrO_3$ (56%), $PbSnO_3$ (33%) and $PbTiO_3$ (11%), it should be expected that the same $a^-a^-c^0$ pattern of octahedral rotation characteristic of the dominant $PbZrO_3$ component also occurs in our sample). In the case of $PbZrO_3$, the pattern of off-centre Pb ion displacements giving rise to its AFE structure is associated with the modulation wave-vector $\mathbf{q} = {}^{1}/_{4}\ [110]_{p}^{*}$[13]. In the case of PLZST and related samples, it is well known that the equivalent single-**q**, primary modulation wave-vector is of ${}^{1}/_{n}\ [110]_{p}^{*}$ type[11,12,14] where the value of n is larger than 4 and dependent on composition. In our case, n was ~10 via electron diffraction (Fig. S1b). Such satellite reflections, however, were not observed in the NDPs.

Considering our focus in this work is the E-field-induced evolution of the average structure and associated phenomena, the NDPs of the $\mathrm{AFE_T}$ phase at this stage were therefore described as a pseudotetragonal phase with $a = b = \sqrt{2}a_p$ and $c = 2c_p$, where the corresponding primitive, parent perovskite, unit-cell parameters were refined to be $a_p = b_p > c_p$ [$a_p = 4.1087(5)$ Å and $c_p = 4.0870(5)$ Å] to accommodate octahedral tilting. Note that the following discussion is mainly based on the parent perovskite structure. With an increase in the applied E-field up to, or beyond, 33 kV/cm, note that the $(200, 020)_p/(002)_p$ and $½(311)_p/½(113)_p$ doublet peaks appear to merge together while the $(111)_p$ peak remains unsplit, suggesting the formation of a new phase of pseudocubic metric symmetry. It is clear that the new phase is ferroelectric (FE) from the E-field dependent *P*-E loops. The previous *in-situ* XRD study[8] of a similar PLZST sample with higher resolution showed that the high field phase is indeed a FE rhombohedral structure, although very close to metrically cubic. The refined rhombohedral lattice parameters (using the whole NDP pattern) under this assumption are $a_R = 4.1070(5)$ Å and $\alpha = 89.93(3)°$, in the rhombohedral setting. The continued presence of observable ${}^{1}/_{2}(111)_p$ and $½(311)_p$ satellite reflections is not inconsistent with $a^-a^-a^-$ octahedral tilting[15,16], indicating a rhombohedral *R3c* space group symmetry. This $\mathrm{AFE_T}$-$\mathrm{FE_R}$ phase transition occurs when the applied E-field becomes sufficiently large. With decreasing E-field from the maximum applied field of 45 kV/cm, the PLZST sample reverts, as expected, to the $\mathrm{AFE_T}$ phase.

In terms of the NDPs shown in Fig. 1b,c, the sample can be classified into three states: the initial $\mathrm{AFE_T}$, the intermediate $\mathrm{FE_R}$ and the final $\mathrm{AFE_T}$ states. The ω-averaged, NDPs of the initial and final $\mathrm{AFE_T}$ states (Fig. 1b) suggest that the field-induced AFE-FE phase transition is quite reversible. The ω-dependent NDPs in Fig. 1c, however, clearly demonstrate an irreversible change in the preferred orientation, or texture, of the $\mathrm{AFE_T}$ phase on cycling through the phase transition. The fact that the ω-dependent NDPs collected at 0 kV/cm and 20 kV/cm, respectively, are almost identical showing that insufficiently strong, applied E-fields have minimal impact on preferred orientation in the $\mathrm{AFE_T}$ state.

Once the applied E-field becomes sufficiently strong, however, it induces the phase transition from the $\mathrm{AFE_T}$ to the $\mathrm{FE_R}$ state signified by the $(200)_p$ reflections merging into a single peak while the $(111)_p$ peak remains unaffected. Note that the exact diffraction peak positions in the $\mathrm{FE_R}$ state now depend strongly on ω, showing a characteristic *S*-shape trajectory (Fig. 1c). With further increase in the E-field within the $\mathrm{FE_R}$ region of stability, note that the ω-dependent NDPs again show no obvious change. Upon reducing the E-field sufficiently to undergo the transition back to the final $\mathrm{AFE_T}$ state, note that the ω-dependence of the $(200)_p$ reflection doublet now exhibits very strong texture, by contrast with the initial $\mathrm{AFE_T}$ state. As can be seen in the bottom two panels of Fig. 1c, starting from the $+\omega$ side (in the vicinity of 90°), the intensity of the doublet $(200, 020)_p$ peak (on the low angle side) is strong while that of the (nominally 50% weaker) $(002)_p$ peak is barely visible. Upon decreasing $+\omega$ to 30°, however, the relative intensities of the split $(200, 020)_p$ and $(002)_p$ peaks are now much closer to 1:1. The $(002)_p$ peak on the high angle side becomes much stronger and broader, also separating itself quite significantly from the $(200, 020)_p$ peak on the low angle side. Upon further decreasing ω to the $-\omega$ side, the intensity of the (002) peak gradually disappears until $\omega = -60°$ when it becomes barely observable again. From these *in-situ* NDPs, it is also clear that the ω-dependent NDPs are independent of applied E-field within the region of stability of the $\mathrm{AFE_T}$ state *i.e.* before and after the phase transition, the 20 kV/cm change in external field has little impact on the ω-dependent NDPs. This result differs with Park *et al*,'[10] suggestion that the formation of preferred orientation within the $\mathrm{AFE_T}$ state occurs as soon as an E-field is applied. Our results show that it is the E-field-induced phase transition that has a quite considerable impact on the texture of the PLZST samples.

Preferred orientation implies a non-random distribution of grain orientations and/or domains within the pellet. For the $\mathrm{AFE_T}$ state, it is well established that changes in the intensity ratio of the low angle $(200, 020)_p$ peak to the high angle $(002)_p$ peak reflect any such preferred orientation and are clearly present only in the final $\mathrm{AFE_T}$ state (see the bottom 2 panels of Fig. 1c). This is often ignored for reversible AFE-FE phase transitions, although not in the work of Park *et al.*[10]. Within the $\mathrm{FE_R}$ state, the observed variation in peak position as a function of ω implies changes in internal and/or intergranular strain for ferroelectric materials under an applied E-field[17–19]. In order to quantify the observed evolution in preferred orientation, the parameter f_{200}(MRD)[17] (MRD = Multiple of Random Distribution), proportional to the relative domain fractions along the a_p and c_p directions, is used as an index and calculated as follows:

$$f_{200}\,(\mathrm{MRD}) = 3\left(\frac{I_{200}}{I'_{200}}\right) \Big/ \left[\left(\frac{I_{200}}{I'_{200}}\right) + 2\left(\frac{I_{002}}{I'_{002}}\right)\right] \tag{1}$$

where I denotes the peak intensity, calculated by multi-peak fitting of the final $\mathrm{AFE_T}$ NDPs using two pseudo-Voigt profiles, while I' is defined as the peak intensity for the sample with random orientation. Note that the I' value here was approximated by summing and averaging the observed intensities over all 13 measured ω values. (It is not available to measure the polycrystalline sample (a pellet here) with random orientation after the application of a high voltage)[20].

In order to clearly demonstrate the appearance of preferred orientation, the azimuthal angle, ψ, was used instead of the rotation angle ω for further analysis. The parameter ψ is the angle between the diffraction vector, $\mathbf{g}_{hkl}$, of the (*hkl*) plane and the applied field $\mathbf{E}$, modulo 180°. In general, the relationship between ψ and ω is: $\psi = \omega - \theta_{hkl} + 90°$, where θ_{hkl} is the Bragg angle for the particular (*hkl*) reflection. For the $(200)_p$ peak in particular, $\theta_{200} \approx 36°$, as shown in Fig. 2a. The f_{200} (MRD) curves for the initial and final $\mathrm{AFE_T}$ states with respect to ψ are

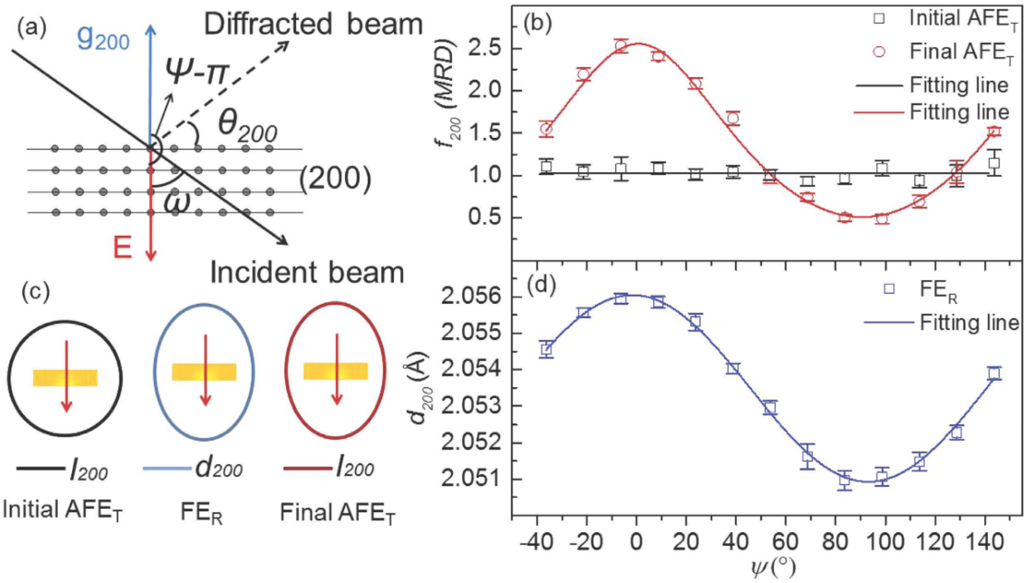

Figure 2. ψ-dependence of the strain and associated preferential orientation evolution during the E-field induced AFE-FE phase transition. (**a**) A schematic drawing of the neutron diffraction geometry, especially for the (200) lattice plane, describing the relationship between ψ and ω. ψ is the angle between the diffraction vector, $\mathbf{g}_{hkl}$, perpendicular to the (*hkl*) planes and the applied field **E,** modulo 180° in this neutron diffraction setup. (**b**) $f_{200}(MRD)$ that proportionally reflects the domain fraction along a_p and c_p directions, as a function of ψ for the initial and final AFE$_T$: $f_{200}(MRD)$ of the initial AFE$_T$ state remains unchanged and for the final AFE$_T$ it can be fitted by the function (combining elliptical function of I_{200} with $f_{200}(MRD)$ calculation formula) with the maximum value appeared at the ψ value of ~0°. (**c**) The schematic diagrams demonstrate how the d_{200} and I_{200} vary during the AFE-FE phase transition (distance from the centre of the pellets denotes the amplitude): the I_{200} is isotropic, regardless of the E-field in the initial AFE$_T$ state (black line); in the FE$_R$ state, the d_{200} expands along the applied E-field and contracts along the direction perpendicular to the field direction and in the final AFE$_T$ state, the I_{200} exhibits the similar preferred orientation with d_{200} in the FE$_R$ state. (**d**) The d_{200} value changes as a function of ψ and the associated curve can be fitted by an elliptical function with the maximum value approximately at $\psi = 0°$ and 180° and the minimum value at $\psi = 90°$.

shown in Fig. 2b. For the initial AFE$_T$ state, the intensities, and hence f_{200}(MRD) for the $(200)_p$ reflections, remains constant at all values of ψ (see the black line in Fig. 2b), indicating that samples in the initial AFE$_T$ state are isotropic *i.e.* there is no observable preferred orientation, or texture (see the black lines in Fig. 2c).

By contrast, in the final AFE$_T$ state, the calculated f_{200}(MRD) versus ψ curve has a distinct *S*-shape profile, indicating clear preferred orientation. Note, however, that there is no obvious strain *i.e.* no obvious change in the $d_{200,020}$ or d_{002} peak positions (*cf.* the bottom 2 panels of Fig. 1c). To further understand the mechanism underlying such E-field-induced changes, it is essential to link the behaviour of the initial AFE$_T$ state to that of the intermediate FE$_R$ state to the final AFE$_T$ state.

In the intermediate FE$_R$ phase, the originally split $(200)_p$ peaks merge together. The d_{200} spacing for this single peak, however, now varies strongly with ψ, as shown in Fig. 2d. It is well accepted in the literature that this d_{200} spacing change is primarily responsible for observed macroscopic elastic strain during the poling process in rhombohedral ferroelectric (FE) materials, assuming that E-field-induced domain switching does not need to be taken into account[18]. The measured d-ψ curve can in fact be well fitted by the following elliptical function

$$d_{200} = d_{200}^{max} cos^2\psi + d_{200}^{min} sin^2\psi \tag{2}$$

where $d_{200}^{\max} = 2.0559(1)$ Å at $\psi = 0 \pm 1°$ and $d_{200}^{\min} = 2.0509(2)$ Å at $\psi = 90 \pm 1°$. Note that the maximum d_{200} value occurs when the $\mathbf{g}_{200}$ diffraction vector, perpendicular to the (200) planes, is parallel to the applied E-field, indicating the sample in the FE$_R$ state exhibits a strong expansion along the direction parallel to the E-field. Similarly, the minimum value at $\psi = 90°$ implies an associated contraction along the direction perpendicular to the E-field *i.e.* parallel to the surface of the pellets. Using this fitting function, the distribution of d_{200} within the pellet *i.e.* the elastic strain can be schematically depicted in terms of an elliptical shape (see the blue line in Fig. 2c).

Once the sample enters into the final AFE$_T$ state, the single $(200)_p$ peak in the FE$_R$ state splits back into a $(200, 020)_p$ and $(002)_p$ doublet. Because the sum of the measured $I_{200,020}$ and I_{002} intensities remains constant after normalising the overall intensity of the NDPs, *i.e.*, $I_{200,020} + I_{002} =$ constant, so f_{200}(MRD) can be simply calculated by using I_{200} alone. It is well known that preferred orientation is a consequence of the minimization of overall energy. The elastic strain observed in the FE$_R$ state should thus be very closely related to the preferred orientation observed in the final AFE$_T$ state. Experimentally, I_{200} follows the same form as the elliptical function given above for d_{200} (eq. 2). Thus the f_{200}(MRD) versus ψ distribution of the final AFE$_T$ state is indeed well fitted by a function

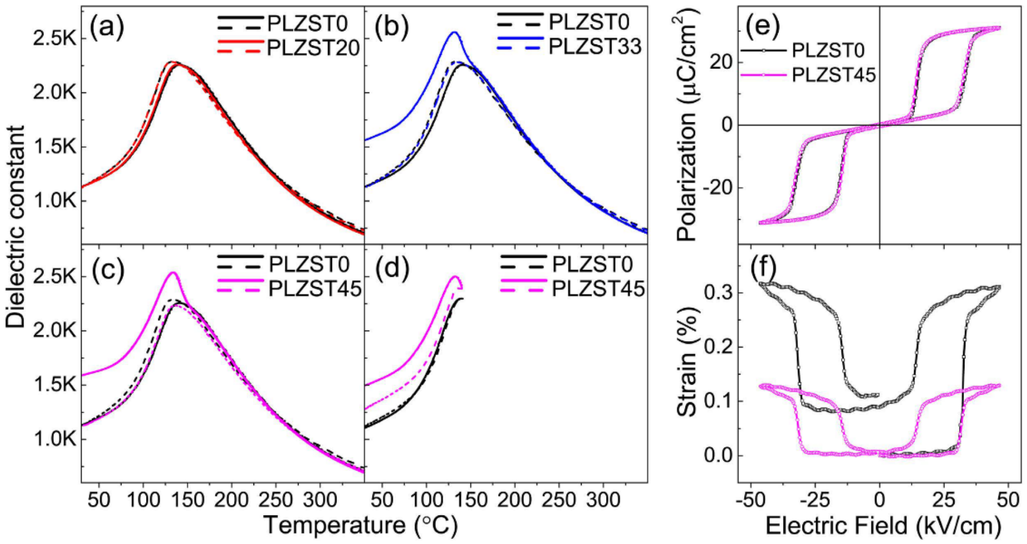

Figure 3. Dielectric and ferroelectric properties of the PLZST ceramics after applying different E-fields. Temperature-dependent dielectric spectra of the samples after applying (**a**) 20, (**b**) 33 and (**c**) 45 kV/cm field, measured during the heating (solid line) and cooling (dashed line) in the temperature range of 30–350 °C, where the black solid and dashed lines curves are measured from the fresh sample for the reference. (**d**) Temperature-dependent dielectric spectra of the PLZST0 and PLZST45 measured in the temperature range from the room temperature to 140 °C. The first cycle of *P–E* (**e**) and *S-E* (**f**) hysteresis loops of PLZST0 and PLZST45 are measured at 1 Hz.

that replacing elliptical function I_{200} into the eq. 1 (see the red line in Fig. 2b). The maximum and minimum of f_{200}(MRD) appear at exactly the same ψ values as that found for d_{200} in the FE_R state. Obviously, the close relationship between d_{200} in the FE_R state and f_{200}(MRD) in the final AFE_T state further supports the contention that the elastic strain observed in the FE_R state is the main driving force for the preferred orientation distribution when the sample returns from the FE_R state to the final AFE_T state.

Clearly the texture of the final AFE_T state is not the same as that of the initial AFE_T state and is strongly dependent on the applied E-field history of the particular sample. In the initial AFE state, PLZST exhibits a pseudo-tetragonal average structure and no preferred orientation. Likewise, there is still no preferred orientation when the applied E-field, *e.g.* at 20 kV/cm, is insufficient to induce the AFE_T to FE_R transition. This result is different to the prediction made by Park *et al.*[10], where it was suggested that the initial, randomly oriented AFE domains would become preferentially oriented AFE domains under an applied field. Once the E-field is high enough to induce the AFE_T-FE_R phase transition, considerable strain change appears in the intermediate FE_R state. The strain is no longer homogeneous as a consequence of the elongation of the rhombohedral unit cell in the direction along the applied E-field and its contraction in the direction perpendicular to this field (see the black line in Fig. 2c). This results in an elliptical distribution of d_{200} (proportional to the structural strain) as a function of ψ (the middle panel of Fig. 2c). This phase transition induced strain is again E-field independent as long as the FE_R phase remains. Upon the reverse phase transformation, clear preferred orientation in the final AFE_T state becomes apparent and appears to be directly determined by the strain distribution in the intermediate FE_R state (*cf. e.g.* Fig. 2b,d), *i.e.* the a_p-axis of the pseudotetragonal cell prefers to align parallel to the E-field while the c_p-axis aligns perpendicular to the E-field (see the red line in Fig. 2c). This preferred orientation in the final AFE_T state is again independent of the applied weak E-field as long as the final AFE_T state remains. Such strain driven preferred orientation was also reported in pre-poled FE materials[21], in reasonable agreement with our conclusions.

Electric properties. It now becomes interesting to investigate how this texture evolution affects measured physical properties. We have thus also investigated the dielectric, ferroelectric and antiferroelectric properties change of the PLZST samples after exposure to different E-field strengths. All measurements have been carried out using fresh samples (labelled PLZST0) as well as samples which have been exposed to applied E-fields of 20, 33 and 45 kV/cm only once (labelled PLZST 20, 33 and 45 respectively), in order to avoid any influence from repeated high electric field exposure on the texture of the material.

Fig. 3 shows the measured temperature-dependent dielectric spectra collected from samples after exposure to the designated E-fields. The dielectric constant of the PLZST0 sample exhibits a plateau region over the temperature range 131–160 °C. This has previously been attributed to the multi-cell cubic (MCC) state existing in PZST-based AFE materials[22,23], a consequence of the Sn substitution that disrupts the antiferroelectric-paraelectric transformation. In addition, thermal dielectric hysteresis was observed and the dielectric maximum occurs at lower temperature for the cooling process, indicative of the nature of a first-order phase transition[24]. Although dielectric plateaus are observed in all PLZST samples, their temperature-dependent dielectric properties differ. PLZST20 (Fig. 3b) shows very nearly the same dielectric behaviour as PLZST0 on both heating and cooling. This is attributed to the fact that the average structures and *a/c* domain configurations of PLZST20 are very similar to those of PLZST0, as also indicated by the *in-situ* NDPs and the fact that the AFE-FE phase transition has not yet been triggered when the applied E-field is below 33 kV/cm. In comparison, the PLZST33 (Fig. 3c) and PLZST45 (Fig. 3d) samples exhibit a relatively sharp dielectric peak around 131 °C and a significantly higher dielectric constant than PLZST0 and PLZST20 during the heating process. By contrast, on cooling, both samples revert to the same trend behaviour as the PLZST0 sample *i.e.* a broadened dielectric peak and a reduced magnitude in the maximum dielectric constant.

The above dielectric phenomena are clearly correlated with the presence or absence of preferred orientation and associated strain in the starting samples for dielectric measurement *i.e.* with their applied E-field history prior to the temperature-dependent, dielectric measurements. The different dielectric behaviour of the PLZST33 and PLZST45 samples for dielectric measurements upon *e.g.* heating can be explained by the preferred orientation and associated strain induced by the prior, E-field-induced, AFE-FE phase transition, as discussed above. As the E-field is sufficient to induce the intermediate FE stage, the strain in the FE state drives the formation of preferred orientation *e.g.*, a_p-axis prefers align parallel to the E-field at the final AFE stage. Such a realignment is likely to enhance the dielectric constant measured in the same direction. The preferred orientation in the final AFE_T state thus significantly enhances the dielectric constant for both the PLZST33 and PLZST45 samples.

On the other hand, the fact that the dielectric constant behaviours of the PLZST33 and PLZST45 samples exhibit no obvious change by comparison with the PLZST0 sample during the cooling process is equally interesting. Note that the cooling temperature process starts from the paraelectric (PE) state at 350 °C, far above T_{max}, the temperature point where the dielectric constant is at a maximum. The initial preferred orientation would thus have disappeared in order to minimize the free energy. The dielectric constant therefore remains the same as the fresh sample during the cooling process. If, however, the temperature is only increased to 140 °C for 40 mins on heating and then dropped back down to room temperature, it is found that the dielectric constant of PLZST45 (Fig. 3d), during the cooling cycle, is still slightly larger than that of PLZST0 measured under the same conditions since the some degree of preferred orientation still remains at 140 °C. It is suggested that when heating PLZST up to the temperature range of the dielectric plateau, some of the AFE phase transforms into the PE phase. This phenomenon indirectly supports the statement that the MCC region formed as a result of Sn doping disrupts the antiferroelectric-paraelectric transformation.

The polarisation-field and strain-field hysteresis loops (*P-E* and *S-E*, respectively) of the PLZST0 and PLZST45 samples are presented in Fig. 3e,f. It is found that both samples have the same double *P-E* hysteresis loops but the strain-field hysteresis loops are quite different for the two samples. The PLSZT0 sample shows a large strain variation (0.32%) and does not return to its original point (the zero point) after the first cycle. This can again be explained by the AFE_T-FE_R phase transition induced irreversible strain and associated preferential orientation as abovementioned. The PLZST45 sample, on the other hand, shows a small strain change (~0.14%) when the same E-field is applied and its strain loop returns to its original point at 0 kV/cm. This can be attributed to the reversible part of the strain evolution during the AFE-FE phase transition occurring in this material. This result explains why the first and second strain hysteresis loops are never the same in this type of AFE materials, such as PLZST in this work and $Pb_{0.99}Nb_{0.02}[(Zr_{0.57}Sn_{0.43})_{0.94}Ti_{0.06}]_{0.98}O_3$[25].

Conclusions

In summary, the results from an *in-situ* neutron powder diffraction investigation of $Pb_{0.97}La_{0.02}(Zr_{0.56}Sn_{0.33}Ti_{0.11})O_3$ show that an applied E-field not only induces an AFE_T-FE_R phase transition but also produces a significant elliptical strain distribution in the FE_R state as well as corresponding preferred orientation in the final AFE_T state obtained upon withdrawal of the E-field. The strict reversibility of the phase transition and recovery of the initial AFE_T phase after the withdrawal of the E-field is thus called into question. As a result, the dielectric polarisation of AFE materials is enhanced after exposure to sufficiently high E-fields. It also explains the different strain behaviour between the first and second strain-field cycles of such materials.

We believe this work provides a complete picture to describe the micro-structure and properties of antiferroelectric PLZST ceramics. It also provides critical experimental evidence correcting Park *et al.*'s[10] original prediction on E-field-induced preferred orientation in the initial AFE phase. The approach used in this work to directly observe the strain and preferred orientation during the E-field-induced AFE_T-FE_R phase transition and associated mechanism may also be applicable to other kinds of materials with similar behaviour, indicating a new method for designing multi-functional composites via interface strain transfer. Furthermore, the current work suggests that to achieve a high and reversible strain in AFE materials, the operating E-field needs to be optimized. It also paves the way to minimize irreversible factors to improve the energy recovery and storage capabilities of AFE materials when used for energy storage applications.

Method

Sample preparation. Powder samples of $Pb_{0.97}La_{0.02}(Zr_{0.56}Sn_{0.33}Ti_{0.11})O_3$ were synthesized by conventional solid state reaction, following the procedure outlined in the reference[26], before being pressed into ceramic pellets. All sample pellets were then heat-treated at 300 °C for 6 hrs in order to release residual stress resulting from the manufacturing process before characterizing the structure and properties. Electrodes were applied by coating silver paint onto the pellet surfaces and then heat-treating them at 550 °C to achieve good electrical contact.

***In-situ* neutron diffraction.** *In-situ* neutron diffraction patterns were collected at a wavelength of 2.41 Å using WOMBAT, the high-intensity powder diffractometer installed on the Opal reactor of the Bragg Institute at the Australian Nuclear Science and Technology Organisation[27]. The *in-situ* neutron diffraction set-up used is shown in Fig. 4 and the collection strategy is same as the one used by Wang *et al.*[28] and Simons *et al.*[29]. A sample holder was used to fix the sample pellet to a central stage which could then be rotated around the vertical ω

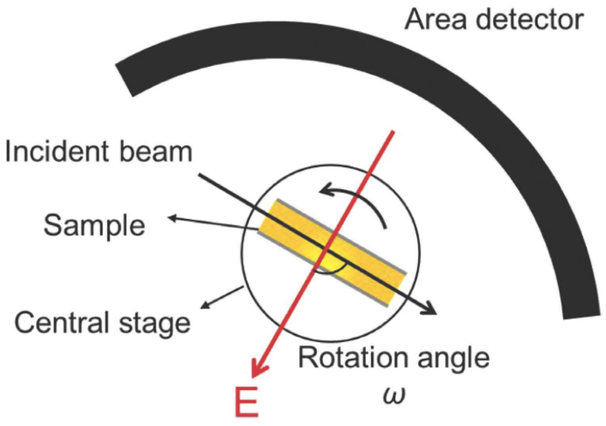

Figure 4. The schematic of the setup of the *in-situ* neutron diffraction experiment. Yellow pellet denotes PLZST ceramic sample with Ag electrode (shown as grey lines). The rotation angle ω was initially set to $-90°$.

axis. Conducting wires were attached to the silver coatings on either side of the pellet to enable a voltage to be applied. The external E-field was always applied normal to the ceramic pellet surface using the E-field sequence 0 kV/cm → 20 kV/cm → 33 kV/cm → 45 kV/cm → 20 kV/cm → 0 kV/cm. At each field point, the sample was initially set so that the applied field was orthogonal to the incident beam (*i.e.* at $\omega = -90°$, where ω is the rotation angle between the incident beam and the applied E-field). The sample stage was then rotated anticlockwise from $\omega = -90°$ to $+90°$ in-plane at increments of 15°. In total, 13 patterns were therefore collected for each individual E-field.

Electrical properties. The ceramic pellet samples with silver electrodes were exposed to an E-field of 20, 33 or 45 kV/cm for 15 min at room temperature in a silicone oil bath. The temperature dependent-dielectric constants were measured at 10 kHz using a high precision inductance, capacitance and resistance meter (LCR meter, Agilent 4980 A). The polarization-field (P-E) and strain-field (S-E) hysteresis loops were investigated using an aixACCT FE test unit in conjunction with a laser interferometer.

References

1. Sawaguchi, E., Maniwa, H. & Hoshino, S. Antiferroelectric Structure of Lead Zirconate. *Phys. Rev.* **83,** 1078–1078 (1951).
2. Kittel, C. Theory of Antiferroelectric Crystals. *Phys. Rev.* **82,** 729–732 (1951).
3. Pan, W., Zhang, Q., Bhalla, A. & Cross, L. E. Field-Forced Antiferroelectric-to-Ferroelectric Switching in Modified Lead Zirconate Titanate Stannate Ceramics. *J. Am. Ceram. Soc.* **72,** 571–578 (1989).
4. Sharifzadeh Mirshekarloo, M., Yao, K. & Sritharan, T. Large strain and high energy storage density in orthorhombic perovskite $(Pb_{0.97}La_{0.02})(Zr_{1-x-y}Sn_xTi_y)O_3$ antiferroelectric thin films. *Appl. Phys. Lett.* **97,** 142902 (2010).
5. Hao, X., Wang, Y., Zhang, L., Zhang, L. & An, S. Composition-dependent dielectric and energy-storage properties of (Pb, La)(Zr, Sn, Ti)O_3 antiferroelectric thick films. *Appl. Phys. Lett.* **102,** 163903 (2013).
6. Liu, Z. *et al.* Temperature-dependent stability of energy storage properties of $Pb_{0.97}La_{0.02}(Zr_{0.58}Sn_{0.335}Ti_{0.085})O_3$ antiferroelectric ceramics for pulse power capacitors. *Appl. Phys. Lett.* **106,** 262901 (2015).
7. Zhao, Y., Hao, X. & Zhang, Q. A giant electrocaloric effect of a $Pb_{0.97}La_{0.02}(Zr_{0.75}Sn_{0.18}Ti_{0.07})O_3$ antiferroelectric thick film at room temperature. *J. Mater. Chem. C* **3,** 1694–1699 (2015).
8. Blue, C. T., Hicks, J. C., Park, S. E., Yoshikawa, S. & Cross, L. E. *In situ* x-ray diffraction study of the antiferroelectric-ferroelectric phase transition in PLSnZT. *Appl. Phys. Lett.* **68,** 2942–2944 (1996).
9. Yang, T. & Yao, X. Field-Induced Phase Transition in Antiferroelectric Creamics of (Pb, La)(Zr, Sn, Ti)O_3. *Ferroelectrics* **381,** 105–110 (2009).
10. Park, S.-E., Pan, M.-J., Markowski, K., Yoshikawa, S. & Cross, L. E. Electric field induced phase transition of antiferroelectric lead lanthanum zirconate titanate stannate ceramics. *J. Appl. Phys.* **82,** 1798–1803 (1997).
11. Xu, Z., Viehland, D., Yang, P. & Payne, D. A. Hot-stage transmission electron microscopy studies of phase transformations in tin-modified lead zirconate titanate. *J. Appl. Phys.* **74,** 3406–3413 (1993).
12. Speck, J. S., De Graef, M., Wilkinson, A. P., Cheetham, A. K. & Clarke, D. R. Hierarchical domain structures and *in situ* domain migration in the antiferroelectric ceramic PLSnZT. *J. Appl. Phys.* **73,** 7261–7267 (1993).
13. Íñiguez, J., Stengel, M., Prosandeev, S. & Bellaiche, L. First-principles study of the multimode antiferroelectric transition in $PbZrO_3$. *Phys. Rev. B* **90,** 220103 (2014).
14. He, H. & Tan, X. Electric-field-induced transformation of incommensurate modulations in antiferroelectric $Pb_{0.99}Nb_{0.02}[(Zr_{1-x}Sn_x)_{1-y}Tiy]_{0.98}O_3$. *Phys. Rev. B* **72,** 024102 (2005).
15. Glazer, A. Simple ways of determining perovskite structures. *Acta Crystallogr., Sect. A* **31,** 756–762 (1975).
16. Woodward, P. Octahedral Tilting in Perovskites. I. Geometrical Considerations. *Acta Crystallogr., Sect. B: Struct. Sci* **53,** 32–43 (1997).
17. Jones, J. L., Slamovich, E. B. & Bowman, K. J. Domain texture distributions in tetragonal lead zirconate titanate by x-ray and neutron diffraction. *J. Appl. Phys.* **97,** 034113 (2005).
18. Hall, D., Steuwer, A., Cherdhirunkorn, B., Mori, T. & Withers, P. Analysis of elastic strain and crystallographic texture in poled rhombohedral PZT ceramics. *Acta Mater.* **54,** 3075–3083 (2006).
19. Daniels, J. E., Jo, W., Rödel, J. & Jones, J. L. Electric-field-induced phase transformation at a lead-free morphotropic phase boundary: Case study in a 93%$(Bi_{0.5}Na_{0.5})TiO_3$–7%$BaTiO_3$ piezoelectric ceramic. *Appl. Phys. Lett.* **95,** 032904 (2009).
20. Daniels, J. E., Jo, W., Rödel, J., Honkimäki, V. & Jones, J. L. Electric-field-induced phase-change behavior in $(Bi_{0.5}Na_{0.5})TiO_3$–$BaTiO_3$–$(K_{0.5}Na_{0.5})NbO_3$: A combinatorial investigation. *Acta Mater.* **58,** 2103–2111 (2010).
21. Daniels, J. E. *et al.* Two-step polarization reversal in biased ferroelectrics. *J. Appl. Phys.* **115,** 224104 (2014).

22. Chan, W.-H., Xu, Z., Zhang, Y., Hung, T. F. & Chen, H. Microstructural evolution and macroscopic property relationship in antiferroelectric lead lanthanum stannate zirconate titanate ceramics. *J. Appl. Phys.* **94,** 4563–4565 (2003).
23. Viehland, D., Forst, D., Xu, Z. & Li, J.-F. Incommensurately Modulated Polar Structures in Antiferroelectric Sn-Modified Lead Zirconate Titanate: The Modulated Structure and Its Influences on Electrically Induced Polarizations and Strains. *J. Am. Ceram. Soc.* **78,** 2101–2112 (1995).
24. Ricinschi, D., Tura, V., Mitoseriu, L. & Okuyama, M. Landau theory-based analysis of grain-size dependence of ferroelectric-to-paraelectric phase transition and its thermal hysteresis in barium titanate ceramics. *J. Phys. Condens. Matter* **11,** 1601 (1999).
25. Tan, X., Frederick, J., Ma, C., Jo, W. & Rödel, J. Can an Electric Field Induce an Antiferroelectric Phase Out of a Ferroelectric Phase? *Phys. Rev. Lett.* **105,** 255702 (2010).
26. Zhang, L., Feng, Y., Xu, Z. & Sheng, Z. Electron emission from La-doped Pb(Zr, Sn, Ti)O$_3$ anti-ferroelectrics by pulse electric field and the relevant physical mechanism. *Chin. Sci. Bull.* **54,** 3489–3493 (2009).
27. Studer, A. J., Hagen, M. E. & Noakes, T. J. Wombat: The high-intensity powder diffractometer at the OPAL reactor. *Physica B* **385–386,** Part 2, 1013–1015 (2006).
28. Wang, J. *et al.* A correlated electron diffraction, *in situ* neutron diffraction and dielectric properties investigation of poled (1−x) Bi$_{0.5}$Na$_{0.5}$TiO$_3$-xBaTiO$_3$ ceramics. *J. Appl. Phys.* **110,** 084114 (2011).
29. Simons, H., Daniels, J. E., Studer, A. J., Jones, J. L. & Hoffman, M. Measurement and analysis of field-induced crystallographic texture using curved position-sensitive diffraction detectors. *J. Electroceram.* **32,** 283–291 (2014).

Acknowledgements

TL, YL and RLW thank the Australian Research Council (ARC) for financial support from in the form of a joint ARC Discovery Project. YL also acknowledges the ARC's support in the form of an ARC Future Fellowship. The authors also thank the Australian Nuclear Science and Technology Organization for support in the form of beam time.

Author Contributions

T.L., A.J.S., D.Y. and B.M. collected the neutron data, Y.F. and Z.X. prepared the ceramic samples, Y.L. applied the beam-time, planned the experiment and supervised the students. T.L. did all property measurements and analyses. T.L., W.H., R.L.W. and Y.L. drafted and revised the MP. L.N. and H.C. provided their help in strain analysis. All authors contributed to discussion, data analysis and manuscript polishing.

Additional Information

Supplementary information accompanies this paper at http://www.nature.com/srep

Competing financial interests: The authors declare no competing financial interests.

How to cite this article: Lu, T. *et al.* Electric-field-induced AFE-FE transitions and associated strain/preferred orientation in antiferroelectric PLZST. *Sci. Rep.* **6**, 23659; doi: 10.1038/srep23659 (2016).

Supporting information

The electron diffraction patterns of the PLZST samples

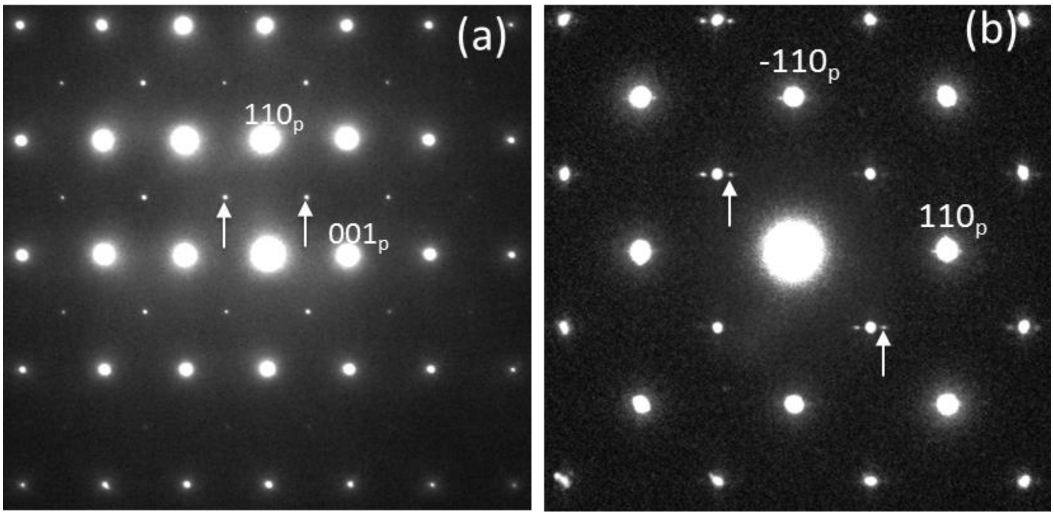

Figure S1 (a) the <1-10>$_P$ and (b) <001>$_p$ zone axis electron diffraction patterns (EDPs) of the PLZST sample. It shows clearly the G$\pm$1/2[111]*$_p$ satellite diffraction spots which is possibly related to the octahedral tilting. In addition, although the pattern is not so clear, the 1/n[110]*$_p$ type incommensurate spots are unambiguous and n was ~ 10 in our case.

3.2 Susceptible Ferroelectric/Antiferroelectric Phase Transition near the Surface of Nb-Doped Lead Zirconate Stannate Titanate from Surface Processing

The research presented in this publication was mainly completed by the author of this thesis. The author has independently done all the structural and property measurements in this paper. The neutron data were collected under the help of the instrument scientist of WOMBAT. The author analysed and interpreted the experimental results and wrote the manuscript.

ACS APPLIED MATERIALS & INTERFACES

Letter

www.acsami.org

Susceptible Ferroelectric/Antiferroelectric Phase Transition near the Surface of Nb-Doped Lead Zirconate Stannate Titanate from Surface Processing

Teng Lu,[†] Andrew J. Studer,[‡] David Cortie,[†,‡] Kenny Lau,[†] Dehong Yu,[‡] Yujun Feng,[§] Hua Chen,[∥] Zhuo Xu,[§] Ray L. Withers,[†] Garry J. McIntyre,[‡] and Yun Liu*,[†]

[†]Research School of Chemistry and [∥]Centre for Advanced Microscopy, The Australian National University, Canberra, Australian Capital Territory 2601, Australia

[‡]Australia Nuclear Science and Technology Organisation, Lucas Height, New South Wales 2234, Australia

[§]Electronic Materials Research Laboratory, Xian Jiaotong University, Xian 710049, Shaanxi, China

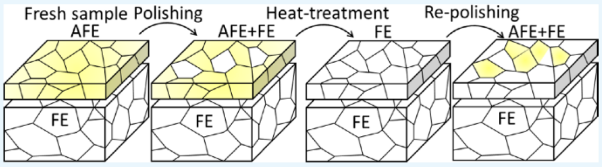

ABSTRACT: This work systematically investigated the structure and property of the near-surface and bulk regions of $Pb_{0.99}(Nb_{0.02}Zr_{0.73}Sn_{0.21}Ti_{0.04})O_3$ ceramics using a combination of X-ray and neutron diffraction, piezoresponse force microscopy, and conventional ferroelectric/piezoelectric characterization. It is found that mechanical force can induce an antiferroelectric/ferroelectric phase transition within micrometers of the surface. Such a phase transition is strongly dependent on the processing scenario, leading to differences from the bulk region. This work provides crucial insights into the sensitivity of this class of AFE materials. Clearly, surface processing conditions must be taken into account for both accurate structural determination and practical applications.

KEYWORDS: *antiferroelectrics, ferroelectrics, neutron diffraction, X-ray diffraction, PFM, PNZST, surface*

Antiferroelectric materials, with specific compositions in the ternary $PbZrO_3$−$PbSnO_3$−$PbTiO_3$ system, are widely studied for their promising applications as actuators, sensors as well as in energy storage and electrocaloric devices.[1−6] In terms of the $PbZrO_3$−$PbSnO_3$−$PbTiO_3$ phase diagram,[7] materials can exist in an antiferroelectric orthorhombic (AFE_O), an antiferroelectric tetragonal (AFE_T) or a ferroelectric rhombohedral (FE_R) state at room temperature. The resultant state depends strongly but not only upon the chemical composition. It is found that the stability of these antiferroelectric (AFE) and ferroelectric (FE) phases is also very sensitive to external factors, such as applied electric field, mechanical stress and temperature.[8−11] With a composition close to the AFE/FE phase boundary, the appearance of competing phases even strongly depends on the history of processing conditions such as heat-treatment, mechanical pressing, and electrical-poling.[12−15] Although such phenomena have been mentioned previously, the whole picture, especially the relation of the structure and property at the near-surface region and in the bulk, is still ambiguous.

In this work, we therefore initiate a systematical investigation to see whether or not the sensitivity of near-surface structure and properties to external conditions extends into the bulk. A $Pb_{0.99}(Nb_{0.02}Zr_{0.73}Sn_{0.21}Ti_{0.04})O_3$ (PNZST) ceramic was thus chosen as an example material for this study. X-ray and neutron powder diffraction (XRPD and NPD, respectively) are employed to distinguish between near-surface (on the micrometer scale) and bulk structure based on the different beam penetration depths of X-rays and neutrons.[16,17] In addition, piezoresponse force microscopy (PFM) and bulk property measurements are used to differentiate between the surface and bulk properties of the material.

$Pb_{0.99}(Nb_{0.02}Zr_{0.73}Sn_{0.21}Ti_{0.04})O_3$ (PNZST) ceramics were prepared by conventional solid state reaction as previously reported.[15] For comparison purposes, four PNZST sample pieces and one powder sample were cut or cracked from the one initial piece of ceramic. The four cut samples have surface sizes of 10 mm × 5 mm and a thickness of ∼0.8 mm to 1.5 mm depending on processing conditions. The sample 1 was not processed, i.e., it has a fresh (or as synthesized) surface. Sample 2's surface was polished prior to the investigation. Sample 3 was processed in the following way: polishing the surface→ heat-treatment (600 °C for 12 h). The sample 4 was prepared as follows: polishing the surface→ heat-treatment (600 °C for 12 h) → repolishing the surface.

XRPD patterns of the samples 1−4 were collected using a PANalytical X'pert Empyrean diffractometer (Cu $K\alpha$ radiation, 45 kV, 40 mA). The unit cell parameters were calculated by Le-Bail fitting using pseudo-Voigt profiles (Jana2006).[18,19] Figure 1a shows the room temperature XRPD patterns of the sample 1 to 4. All the patterns are indexed based on a parent cubic perovskite structure (labeled with the subscript p). The sample 1 exhibits a nonsplit and symmetric $(111)_p$ peak as well as an unambiguous 2:1 split in the $(200)_p$ peaks. Additionally, the

Received: March 7, 2016
Accepted: May 23, 2016
Published: May 23, 2016

DOI: 10.1021/acsami.6b02868
ACS Appl. Mater. Interfaces 2016, 8, 14313−14317

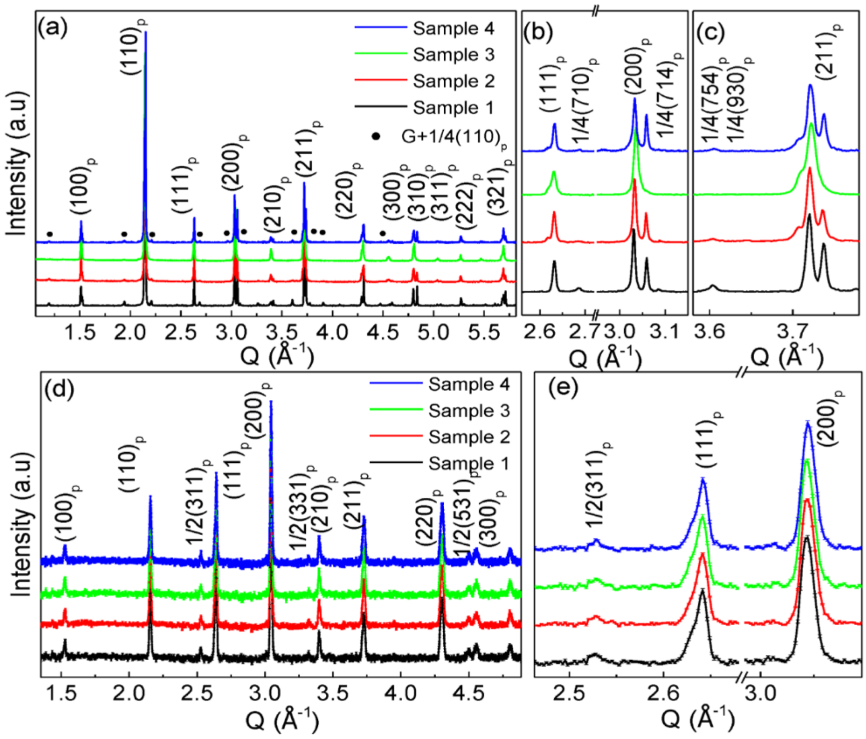

Figure 1. (a) XPRD patterns of the samples 1−4, (b) details of the region around the parent $(111)_p$ and $(200)_p$ peaks and (c) the $(211)_p$ peaks; and (d) neutron diffraction patterns of the samples 1−4 and (e) details of the region around $(111)_p$ and $(200)_p$ peaks.

weak but clear presence of G ± $1/4(110)_p$ satellite reflections (G denotes parent reflections) such as $1/4(710)_p$, $1/4(714)_p$, and $1/4(754)_p$ are also observed in the selected peak regions presented in Figure 1b, c. This is consistent with antiparallel Pb cation displacements along the pseudocubic $[1-10]_p$ direction, associated with the wave vector $\mathbf{q} = [1/4\ 1/4\ 0]_p{}^*$, which is in good agreement with the AFE distortion observed in the prototype $PbZrO_3$ (AFE_O structure, space group: *Pbam*).[20] The refined *Pbam* orthorhombic unit-cell parameters of the sample 1 (calculated by Le-Bail whole pattern fitting) are a = 5.8440(5) Å, b = 11.7045(5) Å, and c = 8.1935(5) Å.

The sample 2 again exhibits the 2:1 split $(200)_p$ parent reflections as well as G ± $1/4(110)_p$ satellite reflections, typical for the AFE_O phase. On the other hand, it is evident that both the $(111)_p$ and $(211)_p$ peaks have small shoulders at lower Q values ($Q = 4\pi \sin\,\theta/\lambda$), indicating rhombohedral rather than orthorhombic symmetry. According to the phase diagram,[7] the composition of PNZST sample is very close to the junction of three phases (AFE_T, AFE_O, and FE_R). The appearance of weak diffraction features associated with rhombohedral symmetry is probably related to a partial structural change from the AFE_O phase (space group, *Pbam*) to the FE_R phase (space group, *R3c*) during the polishing process. The XRPD pattern of the sample 2 indeed suggests the coexistence of the AFE_O and FE_R phases. The refined unit-cell parameters assuming a two-phase mixture are a = 5.8447(5) Å, b = 11.7041(5) Å, c = 8.2008(5) Å for the AFE_O phase and a = 4.1330(5) Å, α = 89.78° for the FE_R phase.

The XRPD pattern of the sample 3 differs from the patterns observed in both sample 1 and 2. It shows a single $(200)_p$ peak but clearly split $(111)_p$ peaks, showing rhombohedral symmetry. In addition, the previously observed G ± $1/4(110)_p$ satellite reflections disappear, further suggesting that the 600 °C heat-treatment has induced the phase transition from the AFE_O to FE_R. The unit-cell parameters of the FE_R phase in the sample 3 are a = 4.1330(5) Å, α = 89.81°. The XRPD pattern of the sample 4 is very similar to that of the sample 2, i.e., it contains a two phase mixture of both AFE_O and FE_R phases.

Neutron powder diffraction (NPD) patterns using a wavelength of 2.41 Å were then collected on WOMBAT, the high-intensity powder diffractometer installed on the Opal reactor of the Bragg Institute at the Australian Nuclear Science and Technology Organisation. The details of the setup are same as that described in the previous studies.[17,21] Figure 1d, e shows the resultant NPD patterns for the samples 1−4 along with the associated detail of selected peaks in the 2.46 $Å^{-1} < Q < 3.09\ Å^{-1}$ range. This time, there is no obvious difference from one sample to the other. The clearly split $(111)_p$ peaks and unsplit $(200)_p$ peaks are characteristics of the rhombohedral symmetry. In addition to these parent Bragg reflections, G ± $1/2(111)_p$ satellite reflections such as $1/2(311)_p$, $1/2(331)_p$ and $1/2(531)_p$ are clearly observed, consistent with the presence of $a^-a^-a^-$ octahedral tilting in Glazer notation.[22,23] Thus, the bulk structure of the samples can be assigned to the FE_R phase with *R3c* space group symmetry in a sharp distinction to what is observed for the sample 1, 2, and 4 via XRPD.

As suggested by a previous study,[16] the penetration length of low energy X-rays (∼8 keV) for lead-containing perovskite materials is ∼10 μm. Because the diffraction geometry of the lab XRPD is reflection, the penetration length is even less at the low incident angles. The differences observed via XPRD and NPD must then result from structural differences between the near-surface and bulk regions of the sample. The fresh near-surface of the sample 1 shows an orthorhombic structure while the bulk structure is clearly rhombohedral. After mechanical

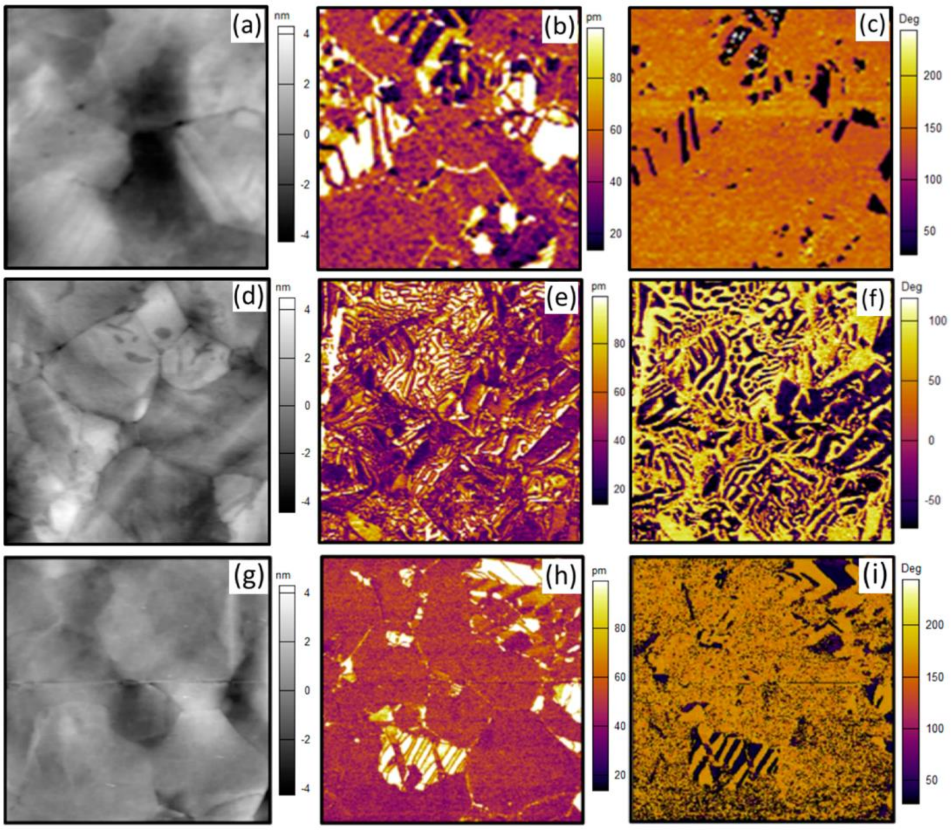

Figure 2. (a, d, g) Morphology, (b, e, h) amplitude, and (c, f, i) phase images of the samples 2, 3, and 4, respectively. All scanned areas are 6 μm × 6 μm. The sample 2 and 4 share the similar characters in terms of the (b, h) amplitude and (c, i) phase images, indicating the coexistence of the polar and nonpolar regions. Different from samples 2 and 4, the most area of sample 3 exhibits polar domains with a smaller size.

polishing, the near-surface of the sample 2 and 4 show a mixture of orthorhombic and rhombohedral phases, indicating that the material surface is very sensitive to the applied mechanical force. For the sample 3, the near-surface, two-phase mixture of orthorhombic and rhombohedral phases induced by polishing is able to revert to a single rhombohedral FE_R phase after heat treatment at 600 °C. Although the average structure of the near-surface region can clearly be tuned by external processing, the average structure of the bulk seems to remain unaffected no matter how the surface is mechanically polished or heat-treated.

The PFM (Cypher, Asylum Research) was then used to characterize the domain structures of the samples' surfaces. Because of the high roughness of the fresh sample (the sample 1)'s surface, only the sample 2, 3, and 4 were characterized. The polished samples are quite flat (Figure 2a, d, and g), excluding the effect of topography on the characterization of the amplitude and phase images. It is found that in both sample 2 and 4, the PFM amplitude and phase images are mostly homogeneous without any obvious contrast. In some areas, however, clear features and contrast were observed.

Unlike the sample 2 and 4, the sample 3 shows sharp features and clear contrast in both amplitude and phase images (Figure 2e, f). Note that the amplitude drops abruptly across domain boundaries while the phase contrast denotes the out-of-plane component of polarization (black and yellow areas correspond to opposite directions of the polarization). Instead of the typical rhombohedral domain structure, the sample 3 shows labyrinthine domains with a size distributed over the range of ∼100−200 nm. As suggested by previous studies,[24,25] the heat-treatment process releases surface residual strain and minimizes ferroelectric domain sizes. Similarly, in our case, the observed ferroelectric domains become noticeably smaller and their shapes more irregular in the sample 3. Such behavior appears closer to relaxor ferroelectric domain features,[26] although structurally the domains still retain the rhombohedral ferroelectric phase.

The PFM results are thus quite consistent with a structural change induced by heat-treatment, whereby a two-phase mixture of AFE and FE near-surface phases are converted to a single FE phase. Interestingly, it is found that the heat-treated and repolished FE phase is thereby partially transferred back to AFE again, leading to a combination image showing both FE domains and nonpolar regions as observed in the sample 4. That is, mechanical force polishing in the surface region again leads to a partial phase transition from a FE to an AFE phase.

This work shows clearly that the phase structure at the near-surface region of PNZST ceramic samples differs from that of the interior region, and is also easily influenced by external stimuli. The near-surface unit-cell volume of each phase varies accordingly, which is probably due to the different lattice strain induced. Therefore, the origin of the phenomenon is most likely related to a stress/strain induced AFE/FE phase transition.[10,11] As shown in Figure 3, heat-treated powders exhibit a single $(200)_p$ peak in their NPD pattern at ambient pressure (zero hydrostatic pressure), suggesting the FE_R phase. When the powders are under mechanical load (hydrostatic pressure in this case), however, the initially single $(200)_p$ peak

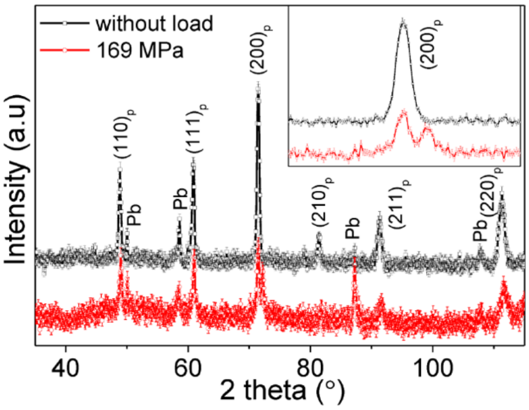

Figure 3. Neutron diffraction patterns of the heat-treated powder sample collected under a hydrostatic pressure of 169 MPa and without pressure.

splits into two peaks with an unambiguous intensity ratio of 2:1, suggesting the AFE_O phase. This in situ neutron powder diffraction characterization proves that, at this composition, compressive stress stabilizes the AFE phase. The coexistence of the AFE and FE phases at the near-surface region of the sample 2 and 4 is thus directly correlated with the mechanical polishing process which changes strain/stress near the surface. By contrast, the sample 3 reverts to the FE_R phase as a result of the relief of surface stress/strain after heat-treatment. As strain induced by polishing only exists near the surface region of ceramics, the bulk material remains in the FE_R phase in regardless of processing conditions.

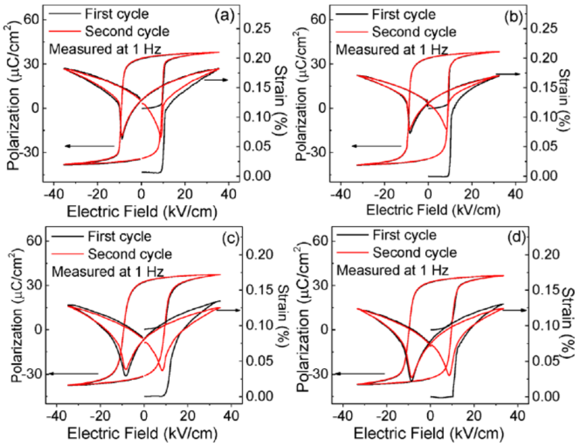

Figure 4. Polarization-electric field ($P-E$) and strain-electric field ($S-E$) hysteresis loops of the (a) sample 1, (b) sample 2, (c) sample 3, and (d) sample 4 measured during the first and second electric cycle at 1 Hz.

Figure 4 shows polarization-field ($P-E$) and strain-field ($S-E$) hysteresis loops of the samples 1−4 measured at 1 Hz. Both *P-E* and *S-E* loops of all samples show typical ferroelectric behavior. Note that, even for the first quarter of the electrical cycle, the observed polarization shows no trace of AFE behavior. Although the XRPD patterns of the sample 1, 2, and 4 show either a pure AFE phase or a coexistence of AFE and FE phases, the macroscopic FE properties are mainly determined by the bulk structure, which is the FE_R phase. Furthermore, the dielectric properties of these samples were also characterized. All samples present almost identical temperature-dependent dielectric spectra with a sharp dielectric peak at T = 169.9 °C (the transition point of the ferroelectric and paraelectric phases) and small variation at T = 80 °C (the transition point of the low-temperature ferroelectric phase $R3c$ and high temperature ferroelectric phase $R3m$). No additional change in dielectric property is observed from the near-surface structure.

In summary, the surface of the PNZST ceramics with chemical composition very close to the AFE/FE phase boundary is quite sensitive to the external stimuli such as mechanical force and temperature. The surface processing therefore results in the difference in both structure and property at the near-surface and in the bulk region. This work thus provides a new insight into AFE polycrystalline materials and AFE/FE phase transitions, suggesting that the considerable complexity of near-surface structures and properties needs to be taken into account to comprehensively understand and control this class of AFE materials.

■ AUTHOR INFORMATION

Corresponding Author

*E-mail: yun.liu@anu.edu.au.

Author Contributions

T.L., A.J.S., and D.Y. collected the neutron data; Y.F. and Z.X. prepared the ceramic samples; Y.L. applied the beam-time, planned the experiment, and supervised the students. T.L. did all property measurements and analyses. T.L., D.C., R.L.W., and Y.L. drafted and revised the M.P. K.L. helped measure the PFM. All authors contributed to discussion, data analysis. and the manuscript writing.

Notes

The authors declare no competing financial interest.

■ ACKNOWLEDGMENTS

T.L., D.C., Y.L., and R.L.W. thank the Australian Research Council (ARC) for financial support from in the form of a joint ARC Discovery Project. YL also acknowledges the ARC's support in the form of an ARC Future Fellowship. The authors also thank the Australian Nuclear Science and Technology Organization for support in the form of beam time and postdoctoral fellowship.

■ REFERENCES

(1) Sharifzadeh Mirshekarloo, M.; Yao, K.; Sritharan, T. Large Strain and High Energy Storage Density in Orthorhombic Perovskite $(Pb_{0.97}La_{0.02})(Zr_{1-x-y}Sn_xTi_y)O_3$ Antiferroelectric Thin Films. *Appl. Phys. Lett.* **2010**, *97* (14), 142902.

(2) Hao, X.; Yue, Z.; Xu, J.; An, S.; Nan, C.-W. Energy-Storage Performance and Electrocaloric Effect in (100)-Oriented $Pb_{0.97}La_{0.02}(Zr_{0.95}Ti_{0.05})O_3$ Antiferroelectric Thick Films. *J. Appl. Phys.* **2011**, *110* (6), 064109.

(3) Ge, J.; Remiens, D.; Dong, X.; Chen, Y.; Costecalde, J.; Gao, F.; Cao, F.; Wang, G. Enhancement of Energy Storage in Epitaxial $PbZrO_3$ Antiferroelectric Films Using Strain Engineering. *Appl. Phys. Lett.* **2014**, *105* (11), 112908.

(4) Zhao, Y.; Hao, X.; Zhang, Q. A Giant Electrocaloric Effect of a $Pb_{0.97}La_{0.02}(Zr_{0.75}Sn_{0.18}Ti_{0.07})O_3$ Antiferroelectric Thick Film at Room Temperature. *J. Mater. Chem. C* **2015**, 3 (8), 1694−1699.

(5) Peng, B.; Fan, H.; Zhang, Q. A Giant Electrocaloric Effect in Nanoscale Antiferroelectric and Ferroelectric Phases Coexisting in a Relaxor $Pb_{0.8}Ba_{0.2}ZrO_3$ Thin Film at Room Temperature. *Adv. Funct. Mater.* **2013**, 23 (23), 2987−2992.

(6) Mischenko, A.; Zhang, Q.; Scott, J.; Whatmore, R.; Mathur, N. Giant Electrocaloric Effect in Thin-Film $PbZr_{0.95}Ti_{0.05}O_3$. *Science* **2006**, *311* (5765), 1270−1271.

(7) Berlincourt, D. A. Transducers Using Forced Transitions between Ferroelectric and Antiferroelectric States. *IEEE Trans. Sonics Ultrason.* **1966**, *13*, 116.

(8) Berlincourt, D.; Krueger, H. H. A.; Jaffe, B. Stability of Phases in Modified Lead Zirconate with Variation in Pressure, Electric Field, Temperature and Composition. *J. Phys. Chem. Solids* **1964**, *25* (7), 659−674.

(9) Pan, W.; Zhang, Q.; Bhalla, A.; Cross, L. E. Field-Forced Antiferroelectric-to-Ferroelectric Switching in Modified Lead Zirconate Titanate Stannate Ceramics. *J. Am. Ceram. Soc.* **1989**, *72* (4), 571−578.

(10) Avdeev, M.; Jorgensen, J. D.; Short, S.; Samara, G. A.; Venturini, E. L.; Yang, P.; Morosin, B. Pressure-Induced Ferroelectric to Antiferroelectric Phase Transition in $Pb_{0.99}(Zr_{0.95}Ti_{0.05})_{0.98}Nb_{0.02}O_3$. *Phys. Rev. B: Condens. Matter Mater. Phys.* **2006**, *73* (6), 064105.

(11) Zeuch, D. H.; Montgomery, S. T.; Holcomb, D. J. Uniaxial Compression Experiments on Lead Zirconate Titanate 95/5−2Nb Ceramic: Evidence for an Orientation-Dependent, "Maximum Compressive Stress" Criterion for Onset of the Ferroelectric to Antiferroelectric Polymorphic Transformation. *J. Mater. Res.* **2000**, *15* (03), 689−703.

(12) Liu, X.; Tan, X. Suppression of the Antiferroelectric Phase during Polarization Cycling of an Induced Ferroelectric Phase. *Appl. Phys. Lett.* **2015**, *107* (7), 072908.

(13) Tan, X.; Frederick, J.; Ma, C.; Aulbach, E.; Marsilius, M.; Hong, W.; Granzow, T.; Jo, W.; Rödel, J. Electric-Field-Induced Antiferroelectric to Ferroelectric Phase Transition in Mechanically Confined $Pb_{0.99}Nb_{0.02}((Zn_{0.56}Sn_{0.43})_{0.94}Ti_{0.06})_{0.98}O_3$. *Phys. Rev. B: Condens. Matter Mater. Phys.* **2010**, *81* (1), 014103.

(14) Dai, Z.; Xu, Z.; Yao, X. Effect of DC Bias on Pressure-Induced Depolarization of $Pb(Nb,Zr,Sn,Ti)O_3$ Ceramics. *Appl. Phys. Lett.* **2008**, *92* (7), 072904.

(15) Frederick, J.; Tan, X.; Jo, W. Strains and Polarization During Antiferroelectric−Ferroelectric Phase Switching in $Pb_{0.99}Nb_{0.02}[(Zr_{0.57}Sn_{0.43})_{1-y}Ti_y]_{0.98}O_3$ Ceramics. *J. Am. Ceram. Soc.* **2011**, *94* (4), 1149−1155.

(16) Xu, G.; Zhong, Z.; Bing, Y.; Ye, Z. G.; Stock, C.; Shirane, G. Ground State of the Relaxor Ferroelectric $Pb(Zn_{1/3}Nb_{2/3})O_3$. *Phys. Rev. B: Condens. Matter Mater. Phys.* **2003**, *67* (10), 104102.

(17) Studer, A. J.; Hagen, M. E.; Noakes, T. J. Wombat: the High-Intensity Powder Diffractometer at the OPAL Reactor. *Phys. B (Amsterdam, Neth.)* **2006**, *385−386*, 1013−1015.

(18) Le Bail, A. Whole Powder Pattern Decomposition Methods and Applications: A Retrospection. *Powder Diffr.* **2005**, *20* (04), 316−326.

(19) Petříček, V.; Dušek, M.; Palatinus, L. Crystallographic Computing System JANA2006: General Features. *Z. Kristallogr. - Cryst. Mater.* **2014**, *229* (5), 345−352.

(20) Íñiguez, J.; Stengel, M.; Prosandeev, S.; Bellaiche, L. First-Principles Study of the Multimode Antiferroelectric Transition in $PbZrO_3$. *Phys. Rev. B: Condens. Matter Mater. Phys.* **2014**, *90* (22), 220103.

(21) Lu, T.; Studer, A. J.; Noren, L.; Hu, W.; Yu, D.; McBride, B.; Feng, Y.; Withers, R. L.; Chen, H.; Xu, Z.; Liu, Y. Electric-Field-Induced AFE-FE Transitions and Associated Strain/Preferred Orientation in Antiferroelectric PLZST. *Sci. Rep.* **2016**, *6*, 23659.

(22) Glazer, A. Simple Ways of Determining Perovskite Structures. *Acta Crystallogr., Sect. A: Cryst. Phys., Diffr., Theor. Gen. Crystallogr.* **1975**, *31* (6), 756−762.

(23) Woodward, P. Octahedral Tilting in Perovskites. I. Geometrical Considerations. *Acta Crystallogr., Sect. B: Struct. Sci.* **1997**, *53* (1), 32−43.

(24) Schmitt, L. A.; Kungl, H.; Hinterstein, M.; Riekehr, L.; Kleebe, H.-J.; Hoffmann, M. J.; Eichel, R.-A.; Fuess, H. The Impact of Heat Treatment on the Domain Configuration and Strain Behavior in $Pb[Zr,Ti]O_3$ Ferroelectrics. *J. Am. Ceram. Soc.* **2015**, *98* (1), 269−277.

(25) Kholkin, A.; Morozovska, A.; Kiselev, D.; Bdikin, I.; Rodriguez, B.; Wu, P.; Bokov, A.; Ye, Z.-G.; Dkhil, B.; Chen, L.-Q.; Kosec, M.; Kalinin, S. V. Surface Domain Structures and Mesoscopic Phase Transition in Relaxor Ferroelectrics. *Adv. Funct. Mater.* **2011**, *21* (11), 1977−1987.

(26) Li, Q.; Liu, Y.; Schiemer, J.; Smith, P.; Li, Z.; Withers, R. L.; Xu, Z. Fully-Inverted Piezoresponse Hysteresis Loops Mediated by Charge Injection in $0.29Pb(In_{1/2}Nb_{1/2})O_3-0.44Pb(Mg_{1/3}Nb_{2/3})O_3-0.27PbTiO_3$ Single Crystals. *Appl. Phys. Lett.* **2011**, *98* (9), 092908.

Supporting information

The penetrating profile of X-ray for $Pb_{0.99}(Nb_{0.02}Zr_{0.73}Sn_{0.21}Ti_{0.04})O_3$ ceramics.

For a beam of photons with an incident intensity I_0, penetrating a layer of material with traveling distance x, the intensity I follows the exponential attenuation law:

$$I=I_0 e^{-\mu x} \tag{1.1}$$

where x is the travelling distance, and μ is the linear attenuation coefficient which is decided by the atomic number. For each element, the mass attenuation coefficient μ/ρ can be found in the *International Tables for Crystallography*.[1] Moreover, values of the mass attenuation coefficient for the mixtures and compounds can be obtained according to simple additivity:

$$\frac{\mu}{\rho}=\sum_i w_i \left(\frac{\mu}{\rho}\right)_i \tag{1.2}$$

where w_i is the fraction by weight of the ith atomic constituent. Therefore, the μ of the target compound in this research - $Pb_{0.99}(Nb_{0.02}Zr_{0.73}Sn_{0.21}Ti_{0.04})O_3$ (ρ = 8.32 g/cm^3) as a function of photon energies is shown in Figure S1.

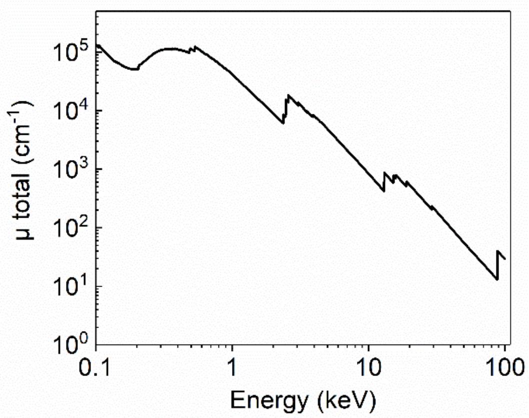

Figure S1 The estimated linear attenuation coefficient of the $Pb_{0.99}(Nb_{0.02}Zr_{0.73}Sn_{0.21}Ti_{0.04})O_3$ as a function of the X-ray photon energy.

Normally the attenuation length is defined as the distance where the intensity of the beam has dropped to 1/*e*, *i.e.*, $x = 1/\mu$.[2] For this research, the photon energy of the Cu Kα source is 8.04 keV. Additionally, the diffraction geometry is bragg-brento, and the penetration depth (d) is calculated as:

$$d = \frac{x}{2}\sin\theta \tag{1.3}$$

where the θ is the angle between the incident beam and sample surface. Therefore, d value for $Pb_{0.99}(Nb_{0.02}Zr_{0.73}Sn_{0.21}Ti_{0.04})O_3$ is in the range of 0.3 to 2.69 μm.

References:

1. Creagh D.C. and Hubbell J.H. (1992), X-Ray Absorption (or Attenuation) Coefficients, Sec. 4.2.4. in *International Tables for Crystallography,* Vol. **C,** A.J.C. Wilson, ed. (Kluwer Academic Publishers, Dordrecht), 189-206.

2. Heenan T M M; Brett D J L; Shearing P R. X-ray Attenuation Properties of Commonly Employed Solid Oxide Fuel Cell Materials. *J. Phys.: Conf. Ser.* **2017**, *849*, 12017.

3.3 Critical Role of the Coupling between the Octahedral Rotation and A-site Ionic Displacements in $PbZrO_3$-based Antiferroelectric Materials Investigated by *In-situ* Neutron Diffraction

The research presented in this manuscript was solely completed by the author of this thesis. The author planned the relative experiments and applied the neutron beam time grant at ANSTO. The author was the principle investigator in charge of this *in-situ* neutron experiment. The author has done all the properties, structural analyses and written manuscript.

PHYSICAL REVIEW B **96**, 214108 (2017)

Critical role of the coupling between the octahedral rotation and *A*-site ionic displacements in PbZrO$_3$-based antiferroelectric materials investigated by *in situ* neutron diffraction

Teng Lu,[1] Andrew J. Studer,[2] Dehong Yu,[2] Ray L. Withers,[1] Yujun Feng,[3] Hua Chen,[4] S. S. Islam,[5] Zhuo Xu,[3] and Yun Liu[1,*]
[1] *Research School of Chemistry, The Australian National University, ACT 2601, Australia*
[2] *Australian Centre for Neutron Scattering, Australian Nuclear Science and Technology Organisation, Lucas Height, NSW 2234, Australia*
[3] *Electronic Materials Research Laboratory, Xi'an Jiaotong University, Xi'an 710049, Shaanxi, China*
[4] *Centre for Advanced Microscopy, The Australian National University, ACT 2601, Australia*
[5] *Nano Sensor Research Laboratory, Jamia Millia Islamia, New Delhi 110025, India*

(Received 29 July 2017; published 21 December 2017)

This *in situ* neutron-diffraction study on antiferroelectric (AFE) $\mathrm{Pb_{0.99}(Nb_{0.02}Zr_{0.65}Sn_{0.28}Ti_{0.05})O_3}$ polycrystalline materials describes systematic structural and associated preferred orientation changes as a function of applied electric field and temperature. It is found that the pristine AFE phase can be poled into the metastable ferroelectric (FE) phase at room temperature. At this stage, both AFE and FE phases consist of modes associated with octahedral rotation and *A*-site ionic displacements. The temperature-induced phase transition indicates that the octahedral rotation and ionic displacements are weakly coupled in the room-temperature FE phase and decoupled in the high-temperature FE phase. However, both temperature and *E*-field-induced phase transitions between the AFE and high-temperature FE phase demonstrate the critical role of coupling between octahedral rotation and *A*-site ionic displacements in stabilizing the AFE structure, which provides not only experimental evidence to support previous theoretical calculations, but also an insight into the design and development of AFE materials. Moreover, the associated preferred orientation evolution in both AFE and FE phases is studied during the phase transitions. It is found that the formation of the preferred orientation can be controlled to tune the samples' FE and AFE properties.

DOI: 10.1103/PhysRevB.96.214108

I. INTRODUCTION

Antiferroelectric (AFE) materials such as PbZrO$_3$ (PZO) and PZO-based materials exhibit many distinctive and useful properties, such as large electric-field (*E*-field) -induced strains, double-polarization–electric-field (*P-E*) hysteresis loops, and thermal/mechanical depolarization. These distinctive properties have many possible applications and have already led to the development of various devices, including potential generators, energy storage devices, and sensors [1–7]. The origin of these useful properties is associated with the distinctive structural transition between the AFE and FE phases induced by external stimuli such as *E*-field, mechanical force, and temperature [5,8–11]. From the Kittel two-sublattice model, the AFE-FE phase transition could be attributed to the switching of the sign of one of the two sets of antiparallel, off-center atomic displacements, i.e., the resultant antiparallel dipoles of the AFE phase [shown in Fig. 1(a)] [12]. In reality, the AFE-FE transition is considerably more complicated. Recently, the origin of antiferroelectricity in PZO and PZO-related materials has been under intensive discussion, particularly from the soft mode and overall energy points of view [13–18].

Relative to an undistorted, parent perovskite (subscript p), PZO has a $\sqrt{2}\times2\sqrt{2}\times2$ unit cell and space-group symmetry of *Pbam* under ambient conditions. A symmetry mode decomposition [19,20] of, for example, Corker *et al.*'s structure refinement [21] shows that the ground state of PZO is dominated by two large-amplitude primary modes. The first mode is associated with the modulation wave vector $\mathbf{q}_1 = [1/4,1/4,0]_\mathrm{p}{}^*$ (of Σ_2 symmetry) and results in antiparallel displacements of *A*-site Pb^{2+} and the neighboring apical O^{2-} ions along the resultant $\boldsymbol{a}$, or $[1\text{-}10]_\mathrm{p}$, directions [of magnitudes 0.277 and 0.215 Å, respectively; see Fig. 1(a)]. These large-amplitude displacements give rise to $(010) \equiv (110)_\mathrm{p}$ slabs (two octahedra wide) polarized along the $\pm\boldsymbol{a}$ direction. It is evident that the $\mathbf{q}_1$ mode is responsible for the antiferroelectricity in PZO, hereafter referred to as the AFE mode. The second soft mode is a conventional octahedral rotation, or antiferrodistortive (AFD) mode around the resultant $\boldsymbol{a}$, or $\boldsymbol{a}_p - \boldsymbol{b}_p$, direction, associated with the modulation wave vector $\mathbf{q}_2 = 1/2[111]_\mathrm{p}{}^*$ (of R_4 symmetry), as shown in Fig. 1(b). Obviously, the distorted structure induced by this octahedral rotation mode presents higher symmetry than the ground state of PZO. The resultant lattice vectors have the following relationship with those of the parent perovskite: $\boldsymbol{a} \equiv \boldsymbol{a}_p - \boldsymbol{b}_p, \boldsymbol{b} \equiv \boldsymbol{a}_p + \boldsymbol{b}_p$, and $\boldsymbol{c} \equiv 2\boldsymbol{c}_p$. It is noted that an additional, much smaller amplitude, the secondary mode (of S_4 symmetry) associated with the modulation wave vector $\mathbf{q}_3 = \mathbf{q}_2 - \mathbf{q}_1 = 1/4[112]_\mathrm{p}{}^*$, and induced "via a cooperative trilinear coupling" with the $\mathbf{q}_1$ and $\mathbf{q}_2$ modes, has recently been reported as being essential to the stabilization of the overall PZO structure [16].

Ideally, when switching the AFE phase into the FE phase by applying the *E*-field, the AFE mode will totally disappear and all the *A*-site Pb^{2+} are forced to align in the same direction of the *E*-field. That is, rather than the antiparallel displacements associated with the $\mathbf{q}_1$ mode, *A*-site ions displace in the same direction, correlated with the zone center, $\mathbf{q} = [000]_\mathrm{p}{}^*$, mode (FE mode) [18]. In PZO, especially for the polycrystalline materials, the large critical *E*-field for an AFE-to-FE phase transition rules out potential applications, thus the perovskite *B*-site modified Pb(Zr,Sn,Ti)O$_3$ (PZST) ternary systems have been developed to overcome this limitation

---

[*] Corresponding author: yun.liu@anu.edu.au

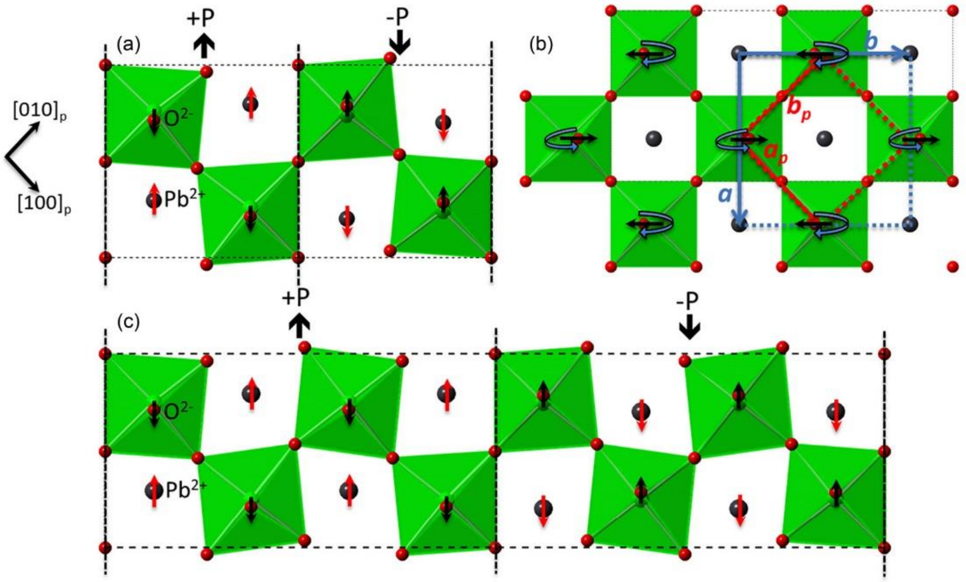

FIG. 1. (a) The distorted structure induced by $\mathbf{q}_1 = {}^1/_4\,[110]_p{}^*$ of the PZO structure in projection along $\boldsymbol{c}$. The resultant $\boldsymbol{a} \equiv [1\text{-}10]_p$ and $\boldsymbol{b} \equiv [220]_p$ are shown by the lighter dashed lines, while the heavier dashed vertical lines separate the two octahedral layer wide regions, which are alternately polarized up and down. (b) The distorted structure induced by $\mathbf{q}_2 = {}^1/_2\,[111]_p{}^*$, the octahedral tilting mode, and the resultant lattice vectors $\boldsymbol{a}$ and $\boldsymbol{b}$ (blue line) are described by the lattice vectors of parent perovskite structure (red line) as follows: $\boldsymbol{a} = \boldsymbol{a}_p - \boldsymbol{b}_p; \boldsymbol{b} = \boldsymbol{a}_p + \boldsymbol{b}_p$. (c) A suggested schematic structure for a proposed $\mathbf{q} = 1/8[110]_p{}^*$ AFE-type mode. Here the heavier dashed vertical lines separate four octahedral layer wide regions, which are again alternately polarized up and down, respectively. Note that the oxygens on these lines do not move in both (a) and (c).

[22–24]. Intriguingly, *B*-site modified PZO has been shown via electron diffraction [25–29] to change the modulation wave vector of the AFE mode from $\mathbf{q}_1 = 1/4[110]_p{}^*$ to $\mathbf{q}_1 = \gamma[110]_p{}^*$, where γ is significantly reduced from the parent PZO value of 1/4 to $1/6 \leqslant \gamma \leqslant 1/8$ (see Table 1 in Ref. [29]). Tan *et al.* [28,29], following Sawaguchi *et al.* [30], have proposed a simplified Pb shift-only model to explain the antiferroelectricity observed in these doped PZST material systems. Figure 1(c) shows a somewhat more sophisticated model for these La/Nb modified PZST materials, based on the AFE mode discussed above, for $\gamma = 1/8$.

Clearly, following Sawaguchi *et al.* [30] and Tan *et al.* [28,29], it is not difficult to generalize this model for other commensurate values ($1/\gamma$ is an integer) or, in general, an incommensurate value. Lowering γ from its $1/4$ value for PZO, for example, to $1/8$ simply increases the average distance between the boundaries along $\boldsymbol{b} \equiv [110]_p$ [the heavier vertical dashed lines in Figs. 1(a) and 1(c)]. In parent PZO, where $\gamma = 1/4$, only two *A*-site Pb^{2+} ions are involved in one FE slab region, while for $\gamma = 1/8$, the number of Pb^{2+} involved in one FE slab [cf. Figs. 1(a) with 1(c)] is four. It is not hard to see that although the modulation wave vector of the $\mathbf{q}_1$ mode can move along the Σ line in the first Brillouin zone of the parent perovskite structure, it is still responsible for the resultant antiferroelectricity.

Theoretical calculations [14,17] suggest the collaborative coupling between the *A*-site ionic displacements, $\mathbf{q}_1$, and the octahedral rotation, $\mathbf{q}_2$, mode(s) that can lead to "*hybrid* normal modes," which can explain the experimental fact that both modes condense simultaneously at a certain temperature in the case of PZO as well as the existence of a soft phonon branch along the $\gamma[110]_p{}^*$ reciprocal space direction. The calculations [14,31] also point out that the coupling between the AFD mode and the FE mode is present in a competitive rather than a collaborative nature. The AFE-FE phase transition provides an experimental case to compare the different nature of the coupling between the *A*-site ionic displacements (AFE/FE) and the octahedral rotation (AFD) mode(s). In this paper, *in situ* neutron-powder diffraction has been employed to investigate the structural evolution of $\mathrm{Pb_{0.99}(Nb_{0.02}Zr_{0.65}Sn_{0.28}Ti_{0.05})O_3}$ (PNZST hereafter) ceramics under different *E*-fields and temperatures. By measuring the diffraction peaks associated with the AFE/FE and AFD modes as a function of different external stimuli, the roles of the *A*-site ionic displacements and octahedral rotation are investigated across the AFE-FE phase transition. Additionally, in real PZO-related materials, in particular polycrystalline materials, the preferred orientation as well as the crystal structure play a very important role in determining the material properties [8,32,33]. Therefore, the associated preferred orientation evolution and its impacts on the relative properties during the phase-transition process have also been investigated, and this may lead to a new method to tune the electrical properties.

II. EXPERIMENTAL METHOD

A. Sample preparation

The PNZST ceramic samples were prepared by the conventional solid-state reaction. The reagent oxides $\mathrm{Pb_3O_4}$(99.9%), $\mathrm{ZrO_2}$(99.9%), $\mathrm{SnO_2}$(99.9%), $\mathrm{TiO_2}$(99.6%), and $\mathrm{Nb_2O_5}$ (99.9%) were mixed thoroughly in a planetary ball mill for 4 h using ethanol as a medium. The resultant milled powders

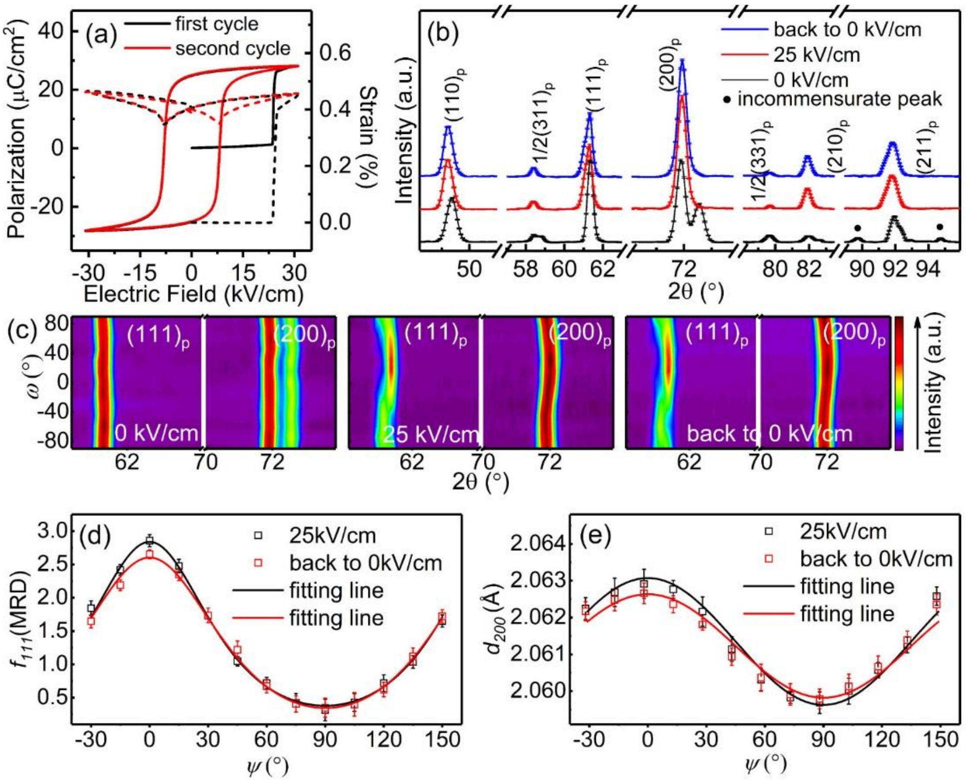

FIG. 2. (a) *P-E* (solid lines) and *S-E* (dashed lines) hysteresis loops of the PNZST ceramic sample at room temperature. (b) *In situ* neutron-diffraction patterns observed at different electric-field points (initial state, 25 kV/cm, and back to 0 field). (c) The ω dependence of the $(111)_p$ and $(200)_p$ peaks. (d) f_{111}(MRD) and (e) d_{200} as a function of the azimuthal angle ψ.

were then granulated, pressed into pellets, and sintered at 1300 °C for 1.5 h in a lead-rich environment to minimize lead volatilization, followed by annealing at 860 °C for 6 h to release residual stress resulting from the manufacturing process. Silver paint was then coated onto the pellets' surface and then heat-treated at 550 °C to achieve good electrical contact.

B. *In situ* neutron diffraction

In situ neutron-diffraction patterns (NDPs) were collected on WOMBAT, the high-intensity powder diffractometer at the Australian Nuclear Science and Technology Organisation, with a neutron wavelength of 2.41 Å. The setup was the same as previously reported [8,34]. At room temperature, an external *E*-field was applied normal to the ceramic pellet surface in a sequence of 0 → 25 → 0 kV/cm. Then the sample was heated to 398 and 438 K successively. At 438 K, the *E*-field sequence (0 → 20 → 0 kV/cm) was applied to the sample. After the *in situ* high-temperature measurements, the pellet was cooled down to room temperature and its neutron-diffraction patterns were remeasured. At each *E*-field point, the sample was initially set so that the applied field was orthogonal to the incident beam (i.e., at $\omega = -90^\circ$, where ω is the angle between the incident beam and the applied *E*-field). The sample was then rotated anticlockwise from $\omega = -90^\circ$ to $+90^\circ$ in-plane at an increment of 15°. In total, 13 patterns were collected for each point.

C. Electrical properties

The pristine ceramic pellet was initially exposed to an *E*-field of 30 kV/cm for 15 min at room temperature in silicone oil. Then the temperature-dependent dielectric spectra of the poled sample were measured as a function of frequencies, f, ranging from $1 \leqslant f \leqslant 200$ kHz using a precision LCR meter (Agilent, 4980A). The *P-E* and strain-electric field (*S-E*) hysteresis loops at different temperatures were collected by a TFAnalyzer 2000 with an aixACCT FE test unit, a laser interferometer, and a temperature controller.

III. RESULTS AND DISCUSSION

A. Electric-field-induced phase transition at room temperature

The measured, room-temperature, *P-E* (solid lines), and *S-E* (dashed lines) hysteresis loops for the first and second electric cycles are shown in Fig. 2(a). The *P-E* loop shows a linear relationship during the first quarter cycle, corresponding to the typical AFE behavior, until the applied *E*-field reaches ~24 kV/cm. After this critical field, the polarization increases abruptly from near zero to 35 μC/cm^2. The following *P-E* hysteresis loop behaves as a typical FE hysteresis loop with a coercive field (E_C) ~ 8.3 kV/cm and a remnant polarization (P_r) ~ 30 μC/cm^2. Similar to the *P-E* behavior, no evident change is observed for the longitudinal strain before reaching the critical *E*-field ~24 kV/cm. Then a sudden jump to ~0.45% occurs. However, residual strain was measured even with

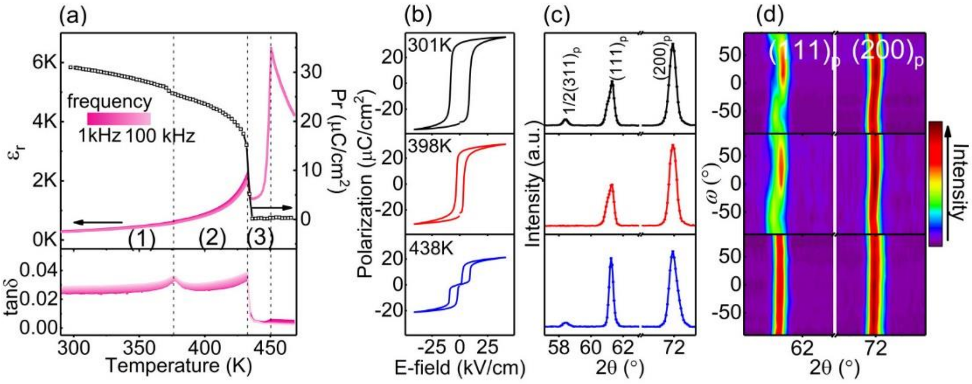

FIG. 3. (a) Temperature-dependent dielectric spectra and the spontaneous polarization of the poled PNZST sample from 290 to 470 K. (b) The *P-E* hysteresis loops, (c) average NDPs and (d) ω-dependent NDPs of the poled PNZST sample at selected temperature points.

the formation of the preferred orientation, large lattice strains are also obtained during this process [Fig. 2(e)]. The measured d_{200}-ψ relation follows very well the elliptical function used before [8]:

$$d_{200} = d_{200}^{\max}\cos^2\psi + d_{200}^{\min}\sin^2\psi. \tag{2}$$

It is also apparent that d_{200} shows a strong expansion in the direction parallel to the *E*-field, contributing to the macroscopic 0.45% expansion along the longitudinal direction. Finally, upon returning to zero field, the relaxation of the lattice strain is also weak, suggesting a large residual strain is stored in the metastable $\mathrm{FE_R}$ phase.

During the *E*-field-induced AFE-FE phase transition at room temperature, obviously both AFE and FE phases contain AFD modes but in different forms. The $a^-a^-c^0$-type tilting remains in the AFE phase. Referring to the calculation results [14,39], this type of tilting is coupled with the AFE mode associated with the $\mathbf{q} = [\mathrm{uu0}]_\mathrm{p}{}^*$ modulation wave vector, which in our case is the $\mathbf{q_1} = \gamma[110]_\mathrm{p}{}^*$ incommensurate structure mode. The induced $\mathrm{FE_R}$ phase presents $a^-a^-a^-$-type octahedral tilting, while none of the AFE mode can be deduced from the calculation for this kind of tilting, and only the zone-center FE mode can be coupled with this rotation mode [14].

B. Temperature-induced phase transition

As shown by the room-temperature *P-E* hysteresis loop and *in situ* neutron-diffraction results, the sample will remain in the $\mathrm{FE_R}$ state at room temperature after exposure to an *E*-field at or above 25 kV/cm. When this metastable $\mathrm{FE_R}$ state is heated, it experiences a sequence of phase transitions. Figure 3(a) shows the temperature-dependent dielectric spectra and remnant polarization (P_r) of the poled sample. Two obvious peaks in the dielectric constant appear around 432 and 450 K, respectively. The dielectric loss spectrum shows an obvious change around 376 K, at which temperature no abrupt variation in the dielectric constant occurs. The P_r versus temperature curve has a small discontinuous drop around 376 K before an abrupt decrease to zero around 432 K. The variation in temperature-dependent dielectric properties and P_r shows that the poled PNZST sample experiences at least two phase transitions before entering the paraelectric phase. Figure 3(b) shows *P-E* hysteresis loops at three different temperatures corresponding to the three typical regions in Fig. 3(a). In both regions (1) and (2), the sample exhibits a single *P-E* hysteresis loop, suggesting that the dielectric anomaly around 376 K is possibly related to a phase transition between two FE phases (note that the three *P-E* hysteresis loop measurements are single-loop measurements without a prepoling pulse). The small change in spontaneous polarization and a peak in dielectric loss are consistent with the disappearance of the $a^-a^-a^-$ $\mathrm{ZrO_6}$ octahedral rotation, as reported previously in several studies [40–42].

Upon increasing the temperature to 432 K, the observed P_r declines sharply to zero. In temperature region (3), the sample shows a typical double *P-E* hysteresis loop [see the bottom panel of Fig. 3(b)]. This behavior indicates that the depolarization process occurring around 432 K is associated with a FE-AFE phase transition. Figure 3(c) shows the corresponding neutron-diffraction patterns. At 301 K, the poled sample is still in the metastable $\mathrm{FE_R}$ phase. When heated to 398 K, the split $\langle 111\rangle_\mathrm{p}{}^*$ peaks are still obvious, but no trace of the $1/2\langle 331\rangle_\mathrm{p}{}^*$ peak(s) or other $\mathbf{G}_\mathrm{p} \pm 1/2\,[111]_\mathrm{p}{}^*$-type reflections can be obtained. In other words, the amplitude of the AFD mode effectively goes to zero at this temperature, denoting that the initially ordered octahedral rotation becomes significantly disordered, and hence unobservable due to the higher thermal energy. The NDPs further support the interpretation that the dielectric loss and P_r responses occurring at 376 K are thus attributed to a low-temperature FE ($R3c$) to high-temperature FE ($R3m$) phase transition. In the high-temperature FE phase, the *A*-site ionic shifts and octahedral tilting become decoupled, in the sense that the FE, $\mathbf{q} = [000]_\mathrm{p}{}^*$ mode still remains nonzero in the complete absence of the $\mathbf{q}_2 = 1/2\,[111]_\mathrm{p}{}^*$ octahedral rotation mode. Even if these two modes become formally independent above 376 K, the small drop of P_r around 376 K indicates a weak coupling between the $\mathbf{q} = [000]_\mathrm{p}{}^*$ and $\mathbf{q}_2 = 1/2\,[111]_\mathrm{p}{}^*$ modes for the low-temperature FE phase, consistent with the previous research on lead zirconate titanate [40].

Upon further increasing temperature to 438 K, the initially split $\langle 111\rangle_\mathrm{p}{}^*$ peaks merge together to form a single and symmetric peak. At the same time, the $\langle 200\rangle_\mathrm{p}{}^*$ peak becomes broader and asymmetric with a shoulder at higher angle, in accordance with the pseudotetragonal AFE structure. Additionally, the $1/2\langle 331\rangle_\mathrm{p}{}^*$ peaks reappear and the

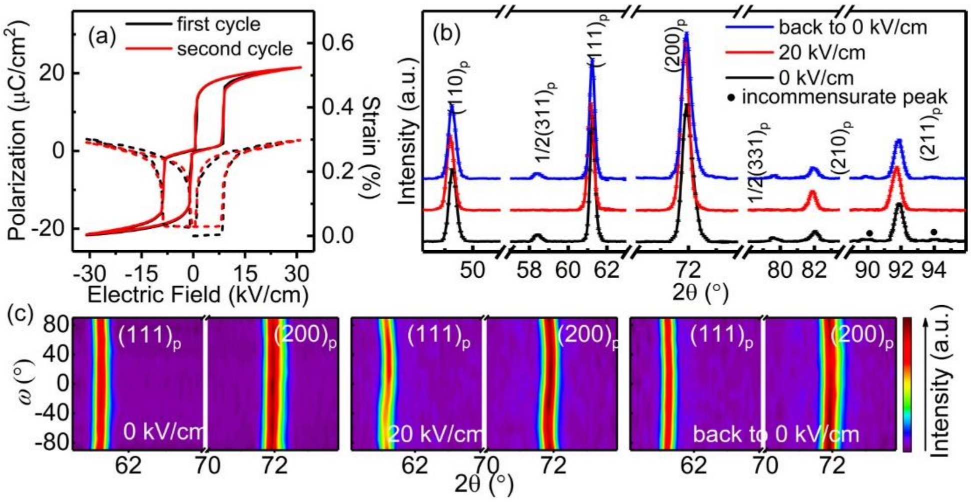

FIG. 4. (a) *P-E* (solid lines) and *S-E* (dashed lines) hysteresis loops of the PNZST ceramic sample at 438 K. (b) *In situ* neutron-diffraction patterns observed at different electric-field points (initial state, 20 kV/cm, and back to 0 field). (c) The ω dependence of the $(111)_p$ and $(200)_p$ peaks.

diffraction pattern becomes quite similar to that observed for the original AFE phase, consistent with the proposition that a FE-to-AFE phase transition occurs around 432 K. During this process, the amplitude of the $\mathbf{q} = [000]_p{}^*$ FE mode goes to zero, leading to the abrupt increase in the temperature-dependent dielectric spectra and the zero P_r. It is interesting to note the condensation of the $\mathbf{q}_2 = {}^1/_2[111]_p{}^*$ mode at high temperature. The simultaneous reappearance of the octahedral rotation and the antiparallel ionic displacements further supports the fact that the strong coupling between the AFE and AFD modes contributes to the AFE structure and the antiferroelectricity described by the first-principles calculation [17].

The ω-dependent NDPs [see Fig. 3(d)] show the variation in preferred orientation during the temperature-induced phase transitions in a poled PNZST sample. The preferred orientation at 301 K is the same as that analyzed in the previous section. When the low-temperature FE phase transfers into the high-temperature FE phase, no obvious change can be observed in the ω-dependent NDPs, i.e., the FE $[111]_p$ direction still prefers to align parallel to the *E*-field. This is also the reason that the origin of the polarization starts from $-25\ \mu\text{C/cm}^2$ rather than zero when measuring the *P-E* hysteresis loop at 398 K. This phenomenon suggests that the destabilization of the octahedral rotation in the FE phase does not strongly influence the redistribution of the non-180 domains. Upon further increasing the temperature to trigger the FE-to-AFE phase transition, the structure changes from rhombohedral to pseudotetragonal. Both the positions and intensities of the $\langle 111\rangle_p{}^*$ and $\langle 200\rangle_p{}^*$ peaks revert to unchanged as the pellet sample is rotated. That is, during the temperature-induced FE-to-AFE phase transition, the grain orientation returns to an isotropic distribution, essentially identical to the original AFE state.

C. Electric-field-induced phase transition at high temperature

As mentioned earlier, when the temperature is in the range of 430–450 K, the poled sample reverts to the AFE phase. Figure 4(a) shows *P-E* (solid lines) and *S-E* (dashed lines) hysteresis loops at $T = 438\,\text{K}$. The observed double *P-E* hysteresis loop suggests that the PNZST sample shows a reversible AFE-FE phase transition at this temperature, i.e., the macroscopic polarization exhibits a sudden increase when the applied *E*-field is larger than 10 kV/cm and returns to zero after withdrawal of the field. Although the observed *P-E* behavior is almost the same during the first and second cycles, the *S-E* loops show a slight difference.

Figure 4(b) shows *in situ* NDPs taken at 438 K. Before applying the external field, note that the $\langle 200\rangle_p{}^*$ peak is quite broad and asymmetric due to a small shoulder at a higher 2θ angle, while the $\langle 111\rangle_p{}^*$ peak is much narrower and more symmetric. In addition to these parent reflections, the same $\mathbf{G}_p \pm 1/2\,[111]_p{}^*$ satellite reflections as that at room temperature in the absence of an *E*-field are again evident. The incommensurate peaks associated with the AFE mode can still be observed even though they have now broadened noticeably. The diffraction data at this elevated temperature are thus quite consistent with that of the AFE structure at room temperature.

Upon applying an *E*-field of 20 kV/cm, the broadness and asymmetry of the $\langle 200\rangle_p{}^*$ peak disappear while the $\langle 111\rangle_p{}^*$ peak appears to remain unsplit, indicating the formation of a new phase with metric cubic symmetry. However, the fact that the measured polarization rises steeply up to $15\ \mu\text{C/cm}^2$ after an applied *E*-field exceeding the critical value $\sim$10 kV/cm requires the structure of the phase obtained under an *E*-field of 20 kV/cm to be a FE structure, presumably with lower than cubic symmetry. The disappearance of the $\mathbf{G}_p \pm 1/2\,[111]_p{}^*$ satellite reflections under the applied *E*-field suggests the disappearance of octahedral tilting during the *E*-field-induced AFE-FE phase transition. This indicates that the high-temperature, field-induced FE phase belongs to the $R3m$ structure described in the PNZST phase diagram [23]. When the applied field returns to zero, the NDP reverts to the same state as that observed initially, consistent with a reversible AFE-FE phase transition characterized by the double *P-E* hysteresis loop.

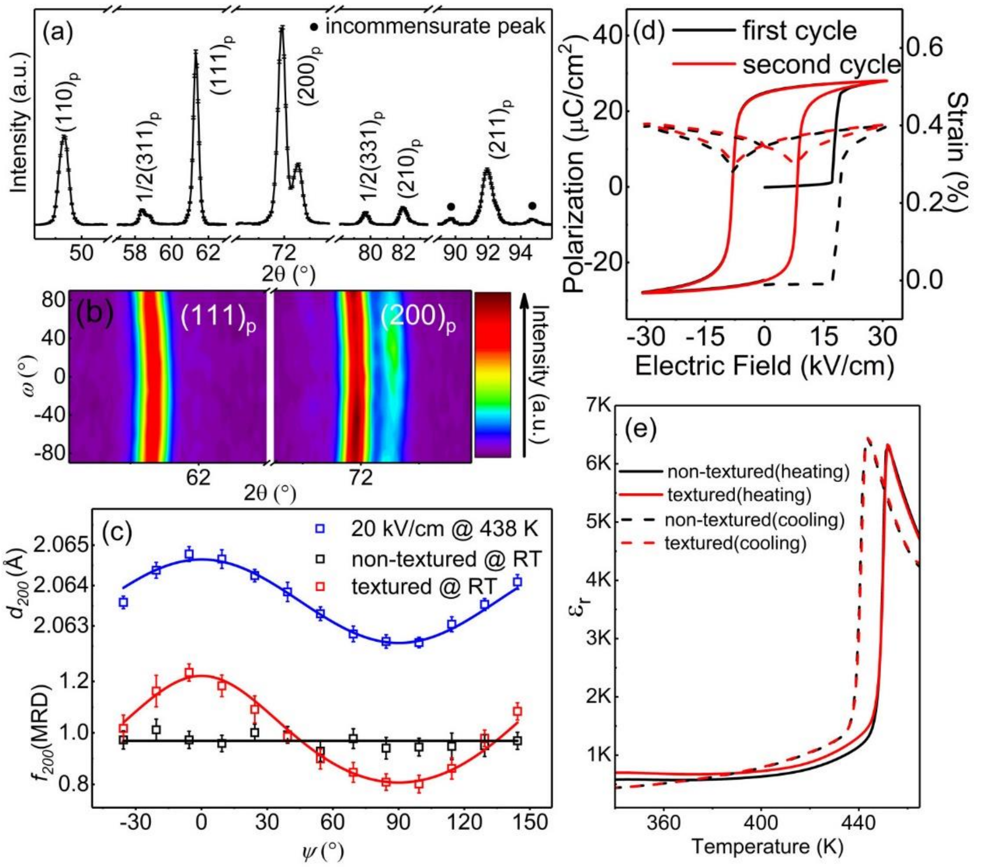

FIG. 5. Room-temperature (a) average and (b) ω-dependent NDPs of the sample, which has been exposed to an external field at 438 K. (c) d_{200} as a function of the azimuthal angle, ψ, for the induced FE state at 438 K (with applying 20 kV/cm) and the f_{200}(MRD)-ψ curves for the virgin PNZST sample (black) and textured sample (red) at room temperature. Note that the solid line is the fitting line. (d) *P-E* (solid lines) and *S-E* (dashed lines) hysteresis loops of the textured PNZST ceramic sample at room temperature. (e) The temperature-dependent dielectric spectra for nontextured (black) and textured (red) AFE PNZST samples during the heating (solid lines) and cooling (dot-lines) process, measured at 10 kHz.

The primitive unit-cell lattice parameters were calculated to be $a_p = 4.1255(5)$ Å and $c_p = 4.1123(5)$ Å for the AFE phase, and $a_r = 4.1274(5)$ Å and $\alpha_r = 89.89(6)^\circ$ for the induced FE phase. Comparison with the room-temperature values shows that the AFE phase exhibits thermal expansion with the c_p parameter expanding significantly more quickly ($\sim$0.51%) while the a_p parameter barely expands at all ($\sim$0.03%), in accordance with previous temperature-dependent diffraction studies [43]. Note that the refined a_p and c_p parameters at high temperature are closer to the refined a_r parameter of the induced FE phase. This most likely facilitates the reversible AFE-FE phase transition at high temperature but not at room temperature. Figure 4(c) shows the ω dependence of the $\langle 111\rangle_p{}^*$ and $\langle 200\rangle_p{}^*$ peaks at three different electric-field points. For the initial AFE state, both the peak positions and peak widths of the $\langle 111\rangle_p{}^*$ and $\langle 200\rangle_p{}^*$ peaks are independent of the rotation angle ω. In the FE state, the peak positions of both the $\langle 111\rangle_p{}^*$ and $\langle 200\rangle_p{}^*$ peaks exhibit typical S-shaped trajectories as a function of ω, characteristic of preferred orientation as described above for the field-induced FE phase at room temperature. Note also that this time, the $\langle 111\rangle_p{}^*$ peak does not split into two peaks as a function of ω.

Finally, for the AFE phase recovered from the induced FE phase, the shape of the $\langle 200\rangle_p{}^*$ peak behaves differently from that observed in the initial AFE state. Over the ω value range from -20° to 40°, the peak width is broadened relative to that obtained at other ω values. In addition, the intensity of the $\langle 200\rangle_p{}^*$ peak seems to have a minimum value around $\omega = 40^\circ$ and a maximum value around $\omega = -60^\circ$, suggesting the formation of preferred orientation after the reversible AFE-FE phase transition. This phenomenon is consistent with our previous report on a closely related system [8]. Because the $\langle 200\rangle_p{}^*$ peaks at high temperature do not present evident splitting, it is difficult to reliably calculate f_{200}(MRD), necessary as an index for the domain fractions along the $\boldsymbol{a}_p$ and $\boldsymbol{c}_p$ directions. Upon cooling the sample to room temperature, there is no obvious difference between the average structure observed after experiencing the above experimental sequence and that of the virgin sample [see Fig. 5(a)], but the preferred orientation induced at high temperature has been stored [see Fig. 5(b)].

By contrast with the broad and asymmetric $\langle 200\rangle_p{}^*$ peak at high temperature, after cooling to room temperature the $\langle 200\rangle_p{}^*$ peak splits into two peaks with the relative intensities of this doublet showing a clear dependence on ω. Starting

TABLE I. Summary of the *in situ* neutron-diffraction results carried on the PNZST samples. The experimental sequence suggests that the sample state is decided by previous experiments.

Experimental sequence	Temperature (K)	Electric field (kV/cm)	Sample phase	Dominated modes	Preferred orientation
1	301	0	AFE	AFE + AFD	No
2	301	25	FE	FE+ AFD	Yes
3	301	0	FE	FE+ AFD	Yes
4	398	0	FE	FE	Yes
5	438	0	AFE	AFE + AFD	No
6	438	20	FE	FE	Yes
7	438	0	AFE	AFE + AFD	Yes
8	301	0	AFE	AFE + AFD	Yes

from the $+\omega$ side (in the vicinity of 90°), the intensity of the ($[200]_p^*$,$[020]_p^*$) peak (on the low 2θ side) is strong while that of the $[002]_p^*$ peak is weak. Upon decreasing $+\omega$ to 30°, however, the $[002]_p^*$ peak on the high-angle side becomes much stronger while the intensity of the ($[200]_p^*$,$[020]_p^*$) peak decreases. Upon further decreasing ω to the $-\omega$ side, the intensity of the $[002]_p^*$ peak gradually drops down until $\omega = -60°$ while the intensity of the ($[200]_p^*$, $[020]_p^*$) peak follows the opposite trend, i.e., the maximum of I_{200} appears when ω is around $-60°$. Figure 5(c) shows the details about the formation of preferred orientation at room temperature. The d_{200} value of the induced FE phase at 438 K shows a strong dependence on ψ, and the data could be fitted well using Eq. (2). Note that the maximum value of d_{200} appears parallel to the E-field. The f_{200}(MRD) was calculated as follows:

$$f_{200}(\mathrm{MRD}) = 3\left(\frac{I_{200}}{I'_{200}}\right)\Big/\left[\frac{I_{200}}{I'_{200}} + 2\left(\frac{I_{002}}{I'_{002}}\right)\right]. \quad (3)$$

Again, the maximum value of f_{200} appears parallel to the E-field. These results further support the proposition reported above that the elastic strain observed in the induced FE phase drives the preferred orientation distribution during the reversible AFE-FE phase transition [8]. As the *a/c* domains have already nucleated in the AFE phase at high temperature, they will grow along their preferred orientation during the cooling process.

Figure 5(d) shows *P-E* (solid lines) and *S-E* (dashed lines) hysteresis loops of the textured sample, suggesting that the AFE phase experiences a steplike transition into the FE phase at $E \sim 18$ kV/cm while afterward the system displays a "classical" ferroelectric hysteresis loop. Although the general behavior of the textured AFE phase is similar to that of the nontextured one [Fig. 1(a)], there are a few features that show a slight divergence, e.g., (i) the critical field to trigger the irreversible AFE-FE phase transition is ~25 kV/cm in the nontextured sample and 18 kV/cm in the textured sample, and (ii) the maximum strain measured at 30 kV/cm is ~0.45% in the nontextured sample and ~0.40% in the textured sample.

Finally, Fig. 5(e) displays the temperature-dependent dielectric spectra of the textured and nontextured samples during the heating and cooling process. It is evident that for the nonpoled sample, only one dielectric anomaly, corresponding to the AFE-to-PE phase transition, can be observed in this temperature range. The textured sample shows a larger dielectric constant. After transferring into the paraelectric phase, the crystallographic texture disappears so that during the cooling process the dielectric constants of the textured and nontextured samples overlap. The variation in properties between the textured and nontextured samples further suggests that, in addition to the average structure, the preferred orientation of polycrystalline materials has a strong impact on their properties.

IV. CONCLUSION

The study of *in situ* neutron diffraction of polycrystalline PNZST samples, together with the associated electrical property characterization, presents a clear picture of the evolution of the AFE, FE, and AFD modes and preferred orientation with respect to E-field and/or temperature. The details are summarized in the Table I.

The room-temperature E-field-induced irreversible AFE-FE phase transition is in accordance with the calculation results that the different kinds of octahedral rotation will comply with different kinds of A-site ionic shifts, i.e., the $a^-a^-c^0$ tilting system prefers to be coupled with the AFE mode associated with the $[uu0]_p^*$ modulation wave vector while the $a^-a^-a^-$ tilting is only happy to be coupled with the zone-center FE mode. During the temperature-induced FE ($R3c$) to FE ($R3m$) to AFE phase transitions, the AFD mode is first decoupled with the FE mode, i.e., the amplitude of the $a^-a^-a^-$ tilting mode drops to zero with increasing thermal energy. Additionally, the small change in P_r indicates that the coupling between the FE and AFD modes in FE ($R3c$) is quite weak. Upon further increasing the temperature to trigger the FE ($R3m$) to AFE phase transition, interestingly, the simultaneous condensation of AFD and AFE modes further proves the importance of the coupling between AFD and AFE modes in stabilizing the AFE structure, which is indicated by previous calculation results. The high-temperature E-field-induced reversible AFE-FE phase transition also supplies evidence that with aligning Pb^{2+} displacements along the same direction by the E-field, the $a^-a^-c^0$ octahedral tilting will disappear, but it will reappear together with the AFE mode after withdrawal of the E-field. In addition to the average structure, the preferred orientation is also formed and modified during the AFE-FE phase-transition process, and its correlation to the properties has also been developed.

We believe this work firstly addresses the critical role of the coupling between the AFD mode and the AFE mode in stabilizing the AFE structure, and thus establishing a solid interaction between the structure, crystal texture, and properties of AFE materials under different external stimuli and their combination, facilitating the design and development of new AFE materials.

ACKNOWLEDGMENTS

T.L., Y.L., and R.L.W. thank the Australian Research Council (ARC DP160104780) for financial support in the form of a joint ARC Discovery Project. Y.L. also acknowledges the ARC's support in the form of an ARC Future Fellowship. The authors also thank the Australian Nuclear Science and Technology Organisation for support in the form of beam time.

[1] W. Y. Pan, C. Q. Dam, Q. M. Zhang, and L. E. Cross, J. Appl. Phys. **66**, 6014 (1989).

[2] Z. Liu, X. Chen, W. Peng, C. Xu, X. Dong, F. Cao, and G. Wang, Appl. Phys. Lett. **106**, 262901 (2015).

[3] M. S. Mirshekarloo, K. Yao, and T. Sritharan, Adv. Funct. Mater. **22**, 4159 (2012).

[4] J. Ge, D. Remiens, X. Dong, Y. Chen, J. Costecalde, F. Gao, F. Cao, and G. Wang, Appl. Phys. Lett. **105**, 112908 (2014).

[5] F. Zhuo, Q. Li, J. Gao, Y. Wang, Q. Yan, Z. Xia, Y. Zhang, and X. Chu, J. Mater. Chem. C **4**, 7110 (2016).

[6] M. Pešić, M. Hoffmann, C. Richter, T. Mikolajick, and U. Schroeder, Adv. Funct. Mater. **26**, 7486 (2016).

[7] Y. Tian, L. Jin, H. Zhang, Z. Xu, X. Wei, E. Politova, S. Y. Stefanovich, N. V. Tarakina, I. Abrahams, and H. Yan, J. Mater. Chem. A **4**, 17279 (2016).

[8] T. Lu, A. J. Studer, L. Noren, W. Hu, D. Yu, B. McBride, Y. Feng, R. L. Withers, H. Chen, Z. Xu, and Y. Liu, Sci. Rep. **6**, 23659 (2016).

[9] M. Avdeev, J. D. Jorgensen, S. Short, G. A. Samara, E. L. Venturini, P. Yang, and B. Morosin, Phys. Rev. B **73**, 064105 (2006).

[10] Z. Dai, Z. Xu, and X. Yao, Appl. Phys. Lett. **92**, 072904 (2008).

[11] T. Lu, A. J. Studer, D. Cortie, K. Lau, D. Yu, Y. Feng, H. Chen, Z. Xu, R. L. Withers, G. J. McIntyre, and Y. Liu, ACS Appl. Mater. Interf. **8**, 14313 (2016).

[12] L. E. Cross, J. Phys. Soc. Jpn. **23**, 77 (1967).

[13] A. K. Tagantsev, K. Vaideeswaran, S. B. Vakhrushev, A. V. Filimonov, R. G. Burkovsky, A. Shaganov, D. Andronikova, A. I. Rudskoy, A. Q. R. Baron, H. Uchiyama, D. Chernyshov, A. Bosak, Z. Ujma, K. Roleder, A. Majchrowski, J. H. Ko, and N. Setter, Nat. Commun. **4**, 2229 (2013).

[14] L. Bellaiche and J. Íñiguez, Phys. Rev. B **88**, 014104 (2013).

[15] J. Hlinka, T. Ostapchuk, E. Buixaderas, C. Kadlec, P. Kuzel, I. Gregora, J. Kroupa, M. Savinov, A. Klic, J. Drahokoupil, I. Etxebarria, and J. Dec, Phys. Rev. Lett. **112**, 197601 (2014).

[16] J. Íñiguez, M. Stengel, S. Prosandeev, and L. Bellaiche, Phys. Rev. B **90**, 220103 (2014).

[17] K. Patel, S. Prosandeev, Y. Yang, B. Xu, J. Íñiguez, and L. Bellaiche, Phys. Rev. B **94**, 054107 (2016).

[18] P. Tolédano and M. Guennou, Phys. Rev. B **94**, 014107 (2016).

[19] D. Orobengoa, C. Capillas, M. I. Aroyo, and J. M. Perez-Mato, J. Appl. Crystallogr. **42**, 820 (2009).

[20] B. J. Campbell, H. T. Stokes, D. E. Tanner, and D. M. Hatch, J. Appl. Crystallogr. **39**, 607 (2006).

[21] D. L. Corker, A. M. Glazer, J. Dec, K. Roleder, and R. W. Whatmore, Acta Cryst. Sect. B **53**, 135 (1997).

[22] D. Berlincourt, H. H. A. Krueger, and B. Jaffe, J. Phys. Chem. Solids **25**, 659 (1964).

[23] D. A. Berlincourt, IEEE Trans. Son. Ultrason. **13**, 116 (1966).

[24] X. Tan, C. Ma, J. Frederick, S. Beckman, and K. G. Webber, J. Am. Ceram. Soc. **94**, 4091 (2011).

[25] Z. Xu, D. Viehland, P. Yang, and D. A. Payne, J. Appl. Phys. **74**, 3406 (1993).

[26] D. Viehland, D. Forst, Z. Xu, and J.-F. Li, J. Am. Ceram. Soc. **78**, 2101 (1995).

[27] D. Forst, J. F. Li, and Z. K. Xu, J. Am. Ceram. Soc. **81**, 2225 (1998).

[28] H. He and X. Tan, Appl. Phys. Lett. **85**, 3187 (2004).

[29] H. He and X. Tan, Phys. Rev. B **72**, 024102 (2005).

[30] E. Sawaguchi, H. Maniwa, and S. Hoshino, Phys. Rev. **83**, 1078 (1951).

[31] I. A. Kornev, L. Bellaiche, P. E. Janolin, B. Dkhil, and E. Suard, Phys. Rev. Lett. **97**, 157601 (2006).

[32] J. L. Jones, M. Hoffman, and K. J. Bowman, J. Appl. Phys. **98**, 024115 (2005).

[33] A. Pramanick, D. Damjanovic, J. E. Daniels, J. C. Nino, and J. L. Jones, J. Am. Ceram. Soc. **94**, 293 (2011).

[34] J. Wang, Y. Liu, R. L. Withers, A. Studer, Q. Li, L. Norén, and Y. Guo, J. Appl. Phys. **110**, 084114 (2011).

[35] X. Tan, S. E. Young, Y. H. Seo, J. Y. Zhang, W. Hong, and K. G. Webber, Acta Mater. **62**, 114 (2014).

[36] J. S. Speck, M. De Graef, A. P. Wilkinson, A. K. Cheetham, and D. R. Clarke, J. Appl. Phys. **73**, 7261 (1993).

[37] V. Petříček, M. Dušek, and L. Palatinus, Z. Kristallogr. **229**, 345 (2014).

[38] J. L. Jones, E. B. Slamovich, and K. J. Bowman, J. Appl. Phys. **97**, 034113 (2005).

[39] B. Dupé, S. Prosandeev, G. Geneste, B. Dkhil, and L. Bellaiche, Phys. Rev. Lett. **106**, 237601 (2011).

[40] N. Cereceda, B. Noheda, T. Iglesias, J. R. Fernández-del-Castillo, J. A. Gonzalo, N. Duan, Y. L. Wang, D. E. Cox, and G. Shirane, Phys. Rev. B **55**, 6174 (1997).

[41] J. Frantti, S. Ivanov, S. Eriksson, H. Rundlöf, V. Lantto, J. Lappalainen, and M. Kakihana, Phys. Rev. B **66**, 064108 (2002).

[42] C. A. Randall, M. G. Matsko, W. Cao, and A. S. Bhalla, Solid State Commun. **85**, 193 (1993).

[43] Y. Li, Q. Li, Q. Yan, Y. Zhang, X. Xi, X. Chu, and W. Cao, Appl. Phys. Lett. **101**, 132904 (2012).

3.4 Symmetry-Mode Analysis for Intuitive Observation of Structure-Properties Evolution in Lead-Free Antiferroelectric (1-*x*)$AgNbO_3$-*x*$LiTaO_3$

The research presented in this manuscript was mainly completed by the author of this thesis. The ceramic samples were prepared by collaborators from Xi’an Jiaotong University. Dr. Ye Tian helped characterize the electrical properties and the author has also re-measured the properties for consistency. The author planned the study and independently applied for the neutron beam time grant at ANSTO. The author was the principal investigator in charge of this neutron experiment. The author has done the structural analyses, interpreted the experimental results and written this manuscript.

1. Introduction

Polar functional materials such as ferroelectric (FE) and antiferroelectric (AFE) materials offer innumerable applications for sensors, actuators, memory and energy storage devices.[1-4] The lead-containing materials such as $Pb(Zr,Ti)O_3$, $Pb(Zr,Sn,Ti)O_3$ and $Pb(In_{1/2}Nb_{1/2})O_3$-$PbTiO_3$ have already been manufactured into the commercial devices due to their prominent properties,[5-9] but nowadays, the environmental concerns prompt plenty of the investigations on the lead-free alternatives.[10-11] Recently, $AgNbO_3$ (AN) has attracted researchers' attention as a novel lead-free AFE material. It is reported the recoverable energy density of the pure AN ceramics can reach 2.1 J/cm^3 and after substituting 20% Nb^{5+} with Ta^{5+}, the recoverable energy density is doubled (~ 4.2 J/cm^3), which is the highest value in the lead-free AFE ceramics.[12-13] One of the important reason for such a high energy density observed in AN is its large field-induced polarisation (~ 52 μC/cm^2), which indicates AN has the potential to form the lead-free piezoelectric materials.[14-17] Referring to the investigation carried out by Fu *et al.*[15], Li^+ doping can stabilize the ferroelectricity of AN and $(Ag_{0.914}Li_{0.086})NbO_3$ single crystal performs a relative large piezoelectric coefficient with higher curie temperature (T_C). Although currently a large amount of effort is being made to improve their properties for the potential applications, the underlying structure and structural evolution still remain ambiguous and controversial.

When compared to their typically higher symmetry, paraelectric phases, lots of room temperature FE and/or AFE structures exhibit at least one, large amplitude (primary), distortive mode in addition to the fundamental FE (polar $\mathbf{q} = \mathbf{0}$ modes) and/or AFE modes which are directly responsible for their FE and/or AFE properties.[18-19] The traditional single soft mode approach is unable to describe the complete structural distortion in such circumstances. In seeking to understand the competing structural instabilities underlying the behaviour of such FE and AFE phases, it is thus very useful to utilise a mode crystallography approach whereby the primary and induced secondary modes of distortion are clearly identified via symmetry mode decomposition.[20] In such an approach, the room temperature structure is described in terms of an undistorted, parent structure and the various distortive modes. Each mode is then associated with a specific allowed modulation wave-vector and irreducible representations (irreps) as well as mode amplitude. For AN, which belongs to the perovskite family, mode crystallography provides an ideal method to investigate its distorted structure at room temperature. The present work, which is based on neutron powder diffraction on pellets, is divided into three parts: In the first part, the symmetry mode decomposition approach was successfully applied to the pure AN within the non-polar *Pbcm* and polar $Pmc2_1$ space groups, respectively. It provides new sight into these two controversial symmetries, the origin of which will be addressed in following chapters, in terms of the distortive modes. In the second part we extend the application of the symmetry mode analysis to the newly synthesized $(1\text{-}x)AgNbO_3\text{-}xLiNbO_3$ (ANLT100*x* hereafter) material system, in order to build a more precise correlation between the structure and electrical properties of the ANLT system, which is presented in the third part. The symmetry mode decomposition approach shows the variation in the relative amplitudes of the different modes as a function of $LiTaO_3$ dopant level, thereby enabling a better understanding of the structure of AN itself and its phase transition behaviour under the chemical modification, in comparison with the conventional Rietveld coordinate refinement. We believe this work not only presents a systematic investigation on one new AN-based solid solution system, but also illustrates the distorted modes' influence on the relative properties, which can guide the future work in enhancing the AFE or FE properties of AN-based materials.

2. Symmetry-mode decomposition of $AgNbO_3$(AN)

Nowadays, the average structure of AN at room temperature still remains controversial because either *Pbcm* or $Pmc2_1$ space group can be used reasonably well for structural refinement based on its X-ray and neutron powder diffraction patterns.[21-23] In current work, the symmetry-mode decomposition approach[20] is thus adopted to describe obvious differences between these two distorted structures proposed by Levin *et al.*[22] and Yashima *et al.*[23], respectively, to reveal the "hidden structural correlation". Note that *Pbcm* and $Pmc2_1$ space group use different axes settings, in order to make them comparable and decomposed from the same parent structure, the *Pbcm* symmetry is transferred into *Pmca*, based on the settings used by Yashima *et al.*[23] The parent structure was chosen as the undistorted *Ammm* space group (Figure 1), which accommodates the octahedral rotation and avoids the lattice strain. The unit-cell axes relationship between the *Ammm* structure (subscript A) and pseudo-cubic perovskite structure with *Pm*-3*m* symmetry (subscript p) is: $\mathbf{c_p} \equiv \mathbf{a_A}$, $\mathbf{a_p} + \mathbf{b_p} \equiv \mathbf{b_A}$, $-\mathbf{a_p} + \mathbf{b_p} \equiv \mathbf{c_A}$.

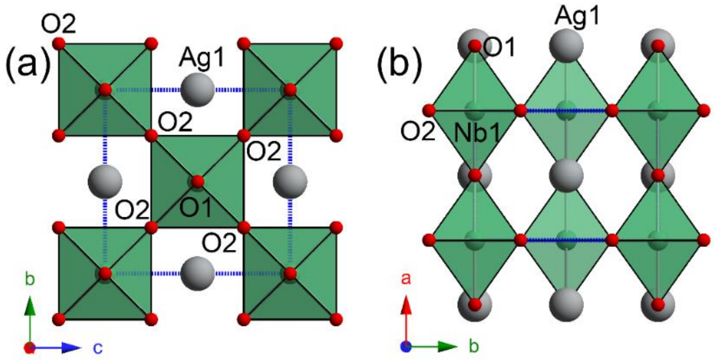

Figure 1. The parent *Ammm* structure viewed along the a) *a*-axis and c) *c*-axis.

Atomic displacements from the mode decomposition on the distorted *Pmca* and $Pmc2_1$ structures are listed in the supplement information (Table S1 and S2). The *Pmca* structure is the result of the irrep distortions of *Ammm* parent structure with 5 different irrep modes: Λ3, Y3-, Z2-, T4+ and H2. However, the associated atomic displacements for different modes display strong discrepancies. Taking O3 as an example, the shift associated with T4+ mode along the *a*-axis is around 0.217 Å while the shift resulted from the Z2- is only 0.004 Å which is smaller than the standard deviation for the refinement. For the $Pmc2_1$ symmetry, it contains the polar axis, the origin of the structure is hence allowed to shift along the *c*-axis. In this case, five more modes are involved in comparison with *Pmca* symmetry (Table S2), which are Γ4-, Λ1, Y2+, Z3+ and H4. Similarly, the atomic displacements associated with the modes like Λ1 and Z2- are much smaller than the standard deviation. For each individual mode, the dimensions indicate the number of the independent components, or basis modes involved and it is larger for $Pmc2_1$ (32) than for *Pmca* (15). The global amplitude, A_τ, is calculated by $(\Sigma_m A_{\tau,m}^2)^{1/2}$, where $A_{\tau,m}$ denotes the amplitude for the specific component, *m*. The common modes T4+, H2 and Λ3 have relatively larger global amplitudes in both cases. The dimensions and global amplitudes for each mode are listed together with the corresponding wave-vectors **q** in Table 1 for both distorted structures. In the following we identify the irrep modes whose condensation directly leads to the observed distortions. Referring to the *Isotropy* subgroups[24], these are the primary modes, which usually contain a larger amplitude. For the *Pmca* symmetry, any two of the Λ3, T4+ and H2 modes could result in the observed distortions. Taking the amplitude into consideration, we identify T4+ and H2 as the primary modes. Referring to the wave-vectors listed in the Table 1, the Λ3 mode is therefore possibly assigned to the secondary mode induced by T4+ and H2 modes, *i.e.*, $\mathbf{q}_2=\mathbf{q}_7-\mathbf{q}_8$. However, for the lowering of the symmetry to *Pmc*2$_1$, the condensation of T4+ and H2 modes are not sufficient. To obtain this structure, another primary mode, the Γ4- at the zone centre with relative large amplitude is thus required and the *Pmc*2$_1$ structure can be referred as the subgroup of *Pmca.* Therefore, we will focus on the four main modes T4+, H2, Λ3, Γ4- step by step to understand the structural origin of the properties observed in this material system.

Table 1. The dimensions and global amplitude of distortive modes observed in *Pmca* and *Pmc*2$_1$ structures. The **q** vector basis refers to the *Ammm* and pseudo-cubic perovskite structure setting.

Ammm	Pseudo-cubic			Dimensions		A_τ (Å)	
Wave-vector **q**		$\mathbf{q}_i$	Irreps	*Pmca*	*Pmc*2$_1$	*Pmca*	*Pmc*2$_1$
[0 0 0]*	[0 0 0]$_p$*	$\mathbf{q}_0$	Γ4-	-	5	-	0.21
[1/4 0 0]*	[0 0 1/4]$_p$*	$\mathbf{q}_1$	Λ1	-	4	-	0.09
[1/4 0 0]*	[0 0 1/4]$_p$*	$\mathbf{q}_2$	Λ3	5	5	0.48	0.47
[0 1 0]*	[1/2 1/2 0]$_p$*	$\mathbf{q}_3$	Y2+	-	2	-	0.17
[0 1 0]*	[1/2 1/2 0]$_p$*	$\mathbf{q}_4$	Y3-	3	3	0.16	0.16
[1/2 0 0]*	[0 0 1/2]$_p$*	$\mathbf{q}_5$	Z3+	-	2	-	0.03
[1/2 0 0]*	[0 0 1/2]$_p$*	$\mathbf{q}_6$	Z2-	2	2	0.04	0.02
[1/2 1 0]*	[1/2 1/2 1/2]$_p$*	$\mathbf{q}_7$	T4+	3	3	1.23	1.22
[1/4 1 0]*	[1/2 1/2 1/4]$_p$*	$\mathbf{q}_8$	H2	2	2	1	0.97
[1/4 1 0]*	[1/2 1/2 1/4]$_p$*	$\mathbf{q}_9$	H4	-	4	-	0.11

Figure 2a and b presents the distorted AN structure induced only by the T4+ mode. The softening of the $\mathbf{q}_7$=[1/2 1 0]*, T point occurs in the first Brillouin zone boundary from its parent *Ammm* structure. This mode is a pure R(<110>$_p$) type octahedral rotation around the $\mathbf{c}_2=\mathbf{c}_A\equiv-\mathbf{a}_p+\mathbf{b}_p$, *i.e.*, the $a^-a^-c^0$ octahedral tilting described by Glazer notation.[25] Figure 2c and d show the distorted structure induced by $\mathbf{q}_8$=[1/4 1 0] (equivalent to [1/2 1/2 1/4]$_p$*), H2 mode, which also occurs at the first Brillouin zone boundary and is associated with the octahedral rotation but different from the T4+ mode. The H2 mode exhibits a R(<001>$_p$) type octahedral rotation, *i.e.*, the rotation around the $\mathbf{a}_2=4\mathbf{a}_A=4\mathbf{c}_p$

axis. If the structure is viewed along **a** (Figure 2c), it seems that the NbO_6 octahedra are antiphase tilted. In fact, it is due to the adjacent NbO_6 octahedra rotate alternatively in a single column along the *a*-axis as (Figure 2d). If the '+' sign denotes that the octahedron rotates clockwise while the '-' sign suggests the anticlockwise rotation viewed along **a**, the NbO_6 octahedra rotates in the form of '--++--' around *a*-axis, or $a^0a^0c^+/a^0a^0c^-$. In other words, if the adjacent octahedra with in-phase tilt together are regarded as one unit, the red dash-line could be considered as an antiphase boundary between these units. Combined with the T4+ mode, the distorted structure contains the $a^-a^-c^+/ a^-a^-c^-$ tilting system, which is close to the reported $a^-b^-c^+/ a^-b^-c^-$. In fact, Yashima *et al.*[23] suggest equal tilting angles along $[100]_p$ and $[010]_p$, *i.e.*, $a^-b^-c^+/ a^-b^-c^- = a^-a^-c^+/ a^-a^-c^-$.

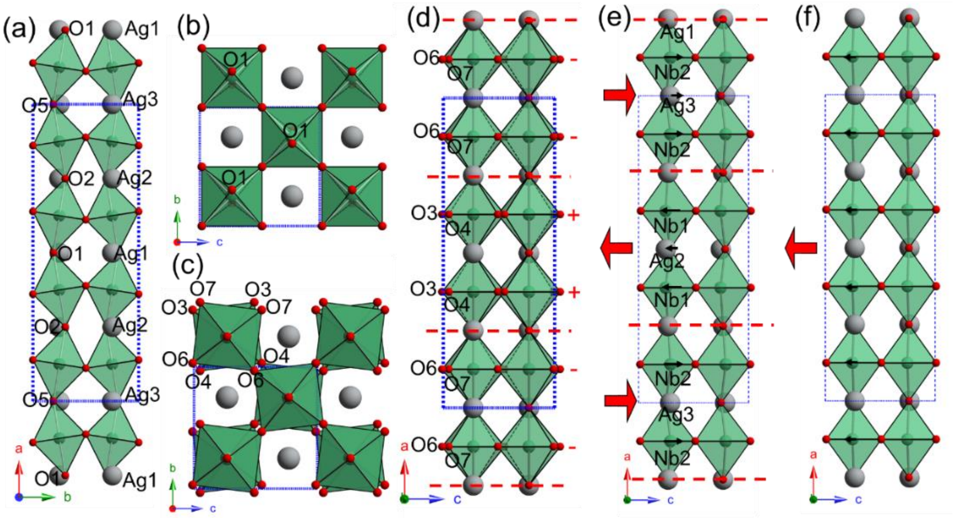

Figure 2. The distorted AN structure induced by a single T4+ mode viewed along (a) *c*-axis and (b) *a*-axis. The distorted AN structure induced by the H2 mode viewed along (c) *a*-axis and (d) *b*-axis. The +/- signs suggest the clockwise/anticlockwise rotation about the *a*-axis, viewed along **a**. The distorted structure induced by the (e) Λ3 mode and (f) Γ4- mode. The black arrows suggest the cations displacements and red arrow directs the spontaneous polarisation. The red-dash line is the antiphase boundary for both octahedral tilting and cation displacements along the *c*-axis.

The T4+ and H2 modes together construct the octahedral tilting system in AN. It is worthy to note that the octahedral tilting originates from the oxygen displacements and the mode amplitude is given in Angstroms. The larger amplitude corresponds to a larger distortion. Furthermore, we will also include the tilting angles apart from the amplitude to describe the octahedral tilting. As abovementioned, the primary T4+ and H2 modes can directly produce the *Pmca* structure.

The distortive structure induced by the secondary Λ3 mode is shown in figure 2e. It is mainly related to the atomic displacements. Within one unit (two octahedra layers between two red dash-lines), cations, *e.g.*, Nb2, Ag3, displace along **c** shown by the black arrow while anions such as O6, O7 and O5 displace along the opposite direction. In this unit, the displacive ions would generate the spontaneous polarisation along **c** as shown by the red arrow. Furthermore, in the adjacent unit, the cations such as Nb1 and Ag2 displace along **-c** while O2, O3 and O4 displace oppositely, forming the dipole moment along **-c**. Note that the Ag1 and O1 ions are located at the boundary, which are not allowed to move along *c*-axis as a consequence of the required symmetry operation. The dipole moment formed within each unit has the same magnitude but the direction alternatively switches 180 degrees, resulting in the antiparallel dipole alignment. In other words, the Λ3 mode contributes to the observed antiferroelectricity in AN. Interestingly, the units drawn in Figure 2d and e are the same, *i.e.*, after crossing the antiphase boundary, both octahedral rotation around *a*-axis and dipole moment change their sign. Considering the Λ3 mode as the induced mode, it is evident that the antiferroelectric alignment in AN, is closely related to the $a^0a^0c^+/a^0a^0c^-$ octahedral rotation.

Finally, the distortive structure associated with the zone-centre Γ4- mode which as a primary mode differentiates $Pmc2_1$ from the *Pmca* structure by an additional 'softening', is shown in Figure 3f. For this distorted structure, all ions move along **-c** direction but the magnitudes are quite different. For cations, the displacements of Ag1, Ag2 and Ag3 (0.002 Å) are quite smaller than those of Nb1 and Nb2 (0.059 Å). For anions, the apical oxygens, *i.e.*, O1 O2 and O5, displace 0.025 Å while it is 0.027 Å for the equatorial oxygens, O3, O4, O6 and O7. As a result, the spontaneous polarisation is formed and directs along **-c**. The Γ4- mode is therefore the origin of the weak ferroelectricity observed in silver niobate under the low electric field (E-field).[14] Undoubtedly, both AFE, Λ3-mode and the FE, Γ4- mode respond to the externally applied E-field but the global amplitude of FE, Γ4-mode is only half of value of the AFE, Λ3-mode. Therefore, the competition of these two modes results in the observed 'ferrielectricity',[23] and explains the appearance of a non-zero remnant polarisation (P_r) observed in the double *P*-*E* hysteresis loop of the AN.

3. The symmetry mode refinement

In the previous section, we gave a detailed description of the condensation of the symmetry modes, resulting in the two space groups reported for AN. In this section, we apply the above relationships to the ANLT100*x* samples, for a systematic study of the variation of the modes by a mode refinement procedure, which was conducted by FullProf suite and ISODISTORT[24, 26]. The advantage of the refinement of the distortive modes in comparison with the conventional Rietveld refinement is that it can supply a reasonable sequence for refining the distorted structure, *e.g.* the primary modes should be firstly involved and the modes with large amplitudes have higher priority. The reference structure was chosen to be distorted perovskite-type structure with $Pmc2_1$ space group. This is due to the fact that both the convergent beam electron diffraction (CBED) and selected area electron diffraction (SAED) prove the existence of the polar structure in the local scale.[23, 27] Furthermore, as described in the previous section, $Pmc2_1$ space group exhibits an additional primary mode, the Γ4- mode which explains the observed weak ferroelectric at the low E-field. It is thus more reasonable to investigate its variation as a function of the $LiTaO_3$ content. A systematic correlation of this mode with the related ferroic properties may solve the puzzle regarding the room temperature AN structure.

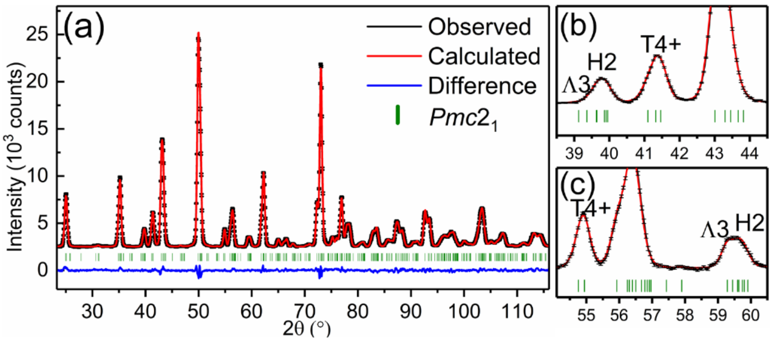

Figure 3. (a) Rietveld symmetry mode refinement based on a $Pmc2_1$ space group with the neutron powder diffraction data of AN at room temperature. (b) and (c) show the selected reflections associated with the T4+, H2, Λ3 modes.

Figure 3a shows the neutron powder diffraction (NPD) data of pure AN collected in the 2θ range of 22°-116°, where Figure 3b and c show the selected reflections associated with the T4+, H2, Λ3 modes. It is clear that the symmetry mode refinement provides the detailed information about the reflection intensities associated with different modes. For example, the reflections around $2\theta = 41.5°$ and 55° are induced by the T4+ mode, related to the antiphase NbO_6 octahedral rotation around the $[110]_p$. Additionally, the reflections around 39.8° and 59.5° are attributed to the combination of Λ3 and H2 modes and these two reflections' intensities are mainly determined by the H2 mode as a result of its larger global amplitude.

The $Pmc2_1$ single phase model was also attempted on other NPD patterns of ANLT100x samples. Considering the small doping level which is less than 10%, Li^+ and Ta^{5+} ions are fixed at the same position of Ag^+ and Nb^{5+}, respectively. For the sample with relative smaller x value, *e.g.*, $x = 0.03$ and 0.045, a single $Pmc2_1$ phase model can lead to a reasonable refinement results (Figure 4a and b). However, for higher x value ~ 0.053, the single $Pmc2_1$ phase model fails to fit the experimental data (Figure 4c), and a large divergence is observed especially in the 2θ range of 70° to 80°. The insert plot indicates that the selected peaks are poorly fitted. Referring to the pseudo-cubic perovskite structure (subscript p), it is found that the largest difference appears when the parent reflections such as $<220>_p*$ and $<221>_p*$are fitted. For example, the intensity ratio of the split $[220]_p*/[202]_p*$ reflections is incorrectly estimated. Furthermore, the intensity of the $1/2<531>_p*$ (labelled by T4+), which is determined by the amplitude of the T4+ mode, is underestimated. Interestingly, the calculated intensities of the Λ3 and H2 modes associated with the reflections are in a good agreement with the experimental data. The bond valence sum calculation[28] suggests the substitution of Ta^{5+} for Nb^{5+} does not make a big difference but the replacement of Li^+ ion for Ag^+ would strongly destabilize the parent structure of the AN. Previous studies on the Li-doped $AgNbO_3$ systems[17, 29-30] also reported that with higher Li^+ content, the average structure is transformed into the rhombohedral phase and the properties is changed accordingly. As shown in Figure 4c, the main divergences arise from the additional reflection intensities of the low angle $[220]_p*$ reflections and $\mathbf{G_p} \pm [1/2\ 1/2\ 1/2]_p*$. Note that the features of the underestimated reflection are consistent with the $R3c$ space group. Therefore, two-phase models within $Pmc2_1$ and $R3c$ space groups are applied to the patterns of ANLT5.3, which evidently improved the refinement quality (Figure 4d).

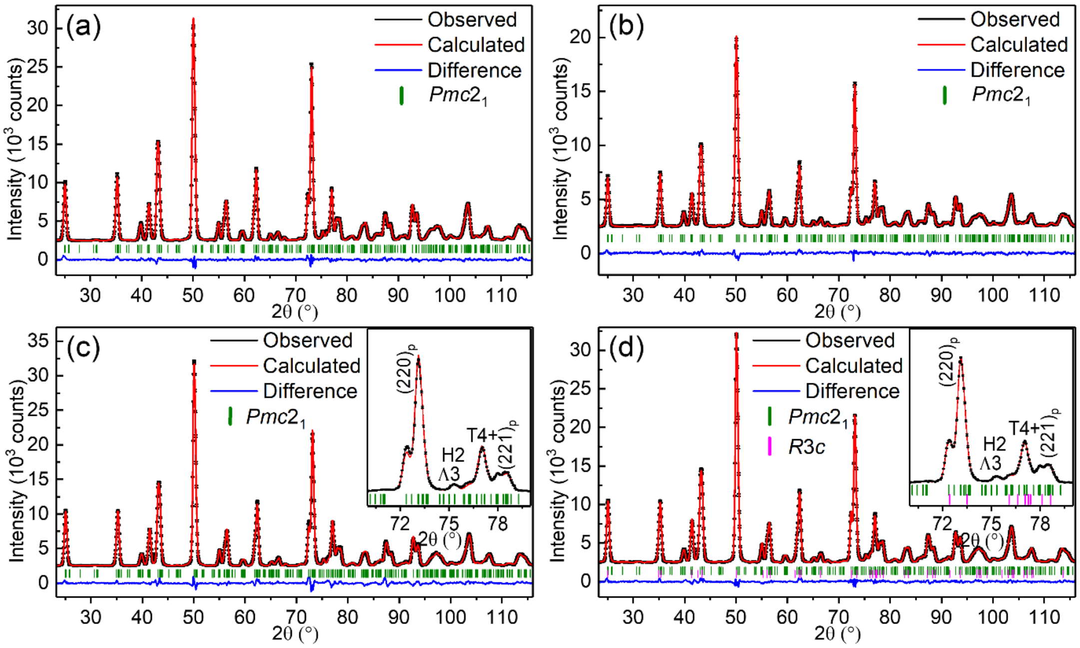

Figure 4. Rietveld symmetry mode refinement of the neutron powder diffraction (NPD) data of ANLT100*x* (a) *x* = 0.03, (b) *x* = 0.045 and (c) *x* = 0.053 with a space group of *Pmc*2_1, collected at room temperature. (d) Rietveld symmetry mode refinement of the NPD pattern of ANLT5.3 in terms of two-phase model (*R*3*c*+*Pmc*2_1). The insert plots in (c) and (d) are the enlargement of the selected reflections, indexed by the associated irrep mode notation.

For the *R*3*c* phase, the symmetry-mode decomposition has been done with referring to the high temperature cubic structure of AN (*Pm*-3*m* symmetry, ICSD 55649).[21] The basis of this distorted structures is set as: $\mathbf{a}_r \equiv \mathbf{a}_p + \mathbf{c}_p$, $\mathbf{b}_r \equiv \mathbf{b}_p - \mathbf{c}_p$, $\mathbf{c}_r \equiv -2\mathbf{a}_p + 2\mathbf{b}_p + 2\mathbf{c}_p$. For the *R*3*c* structure, condensation of two primary modes with a large amplitude, namely Γ4-, $\mathbf{q}_{r0}$=[0 0 0]$_p$* and R4+, $\mathbf{q}_{r1}$=[1/2 1/2 1/2]$_p$* will lead to the observed distortions. The Γ4-, $\mathbf{q}_{r0}$=[0 0 0]$_p$* mode, which denotes the ionic shifts along the *c*-axis ([111]$_p$ direction), leads to the FE spontaneous polarisation. The R4+, $\mathbf{q}_{r1}$=[1/2 1/2 1/2]$_p$*, mode on the other hand, is associated with the antiphase octahedral rotation around the [111]$_p$ direction, *i.e.*, $a^-a^-a^-$ octahedral tilting in Glazer notation.[25] With further doping of $LiTaO_3$, *i.e.*, *x* = 0.06 and 0.09, the features associated with the *R*3*c* phase becomes more obvious. As shown in Figure 5a, the <111>$_p$* reflections contain a small shoulder at the lower 2θ angles which does not belong to the *Pmc*2_1 phase. The two-phase model is also applied to the refinement of both ANLT6 and ANLT9 compositions (Figure 5), which has significantly improved the agreement between the observed and refined pattern. It should be noted that both T4+ mode in $Pmc2_1$ phase and R4+ mode in $R3c$ phase contribute to the $\mathbf{G_p} \pm [1/2\ 1/2\ 1/2]_p^*$ reflections' intensity, therefore both irrep notations are labelled. For x=0.09, An additional peak observed at 26° (Figure 5b) is probably from the impure $LiNbO_3$ phase as previously reported (labelled by red rectangular symbol in Figure 5b).[30] Even after the inclusion of the $LiNbO_3$ phase (ICSD 28295),[31] the reliability factors are not satisfactory, with R_{Bragg}=10.85% and R_F=6.57% for this phase. This is probably due to the overlapping of most of the $LiNbO_3$ reflections with other phases and their intensities are easily influenced by the crosstalk. Additionally, it was not possible to distinguish between a pure $LiNbO_3$ or its solid solution like $LiNb_{1-x}Ta_xO_3$. The existence of such an impure phase makes the Rietveld refinement difficult due to the unclear precise chemical composition. Furthermore, the bond valance sum calculation excludes the same location for both Li^+ and Ag^+, since Li^+ prefers entering the interstitial site.[32-33] Therefore, the reliability factors of the refinement on ANLT9 are not as good as those for lower level $LiTaO_3$ doped samples (Table S3). Due to the extraction of the secondary phase, the deviations from 9% for $LiTaO_3$ are experimentally known. Refinement results revealed that the molar fraction of this secondary phase is around 2.5%, suggesting the dopant of $LiTaO_3$ is around 6.5%. Application of the modified composition indeed improved the reliable factors of the refinement (R_p changes from 2.68% to 2.60%). Therefore, in the following parts, we focus our discussion on 6.5% $LiTaO_3$ for ANLT9 in order to guide readers' eye for the structural evolution as a function of $LiTaO_3$ contents. The details on the refined atomic positions of ANLT100*x* systems are shown in the supporting information (Table S4-S9).

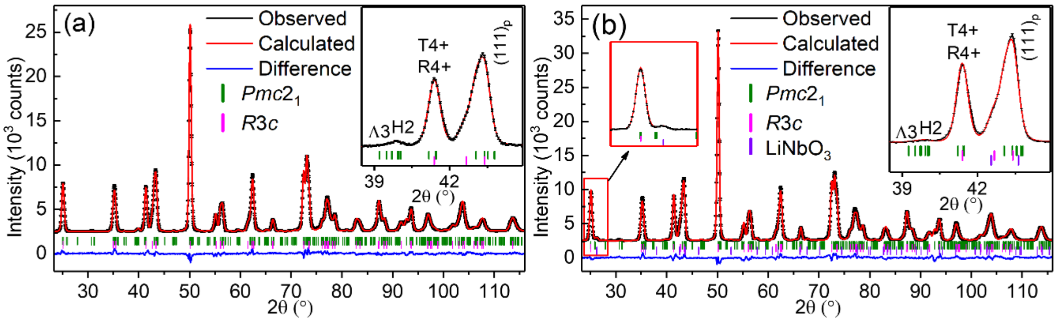

Figure 5. Rietveld refinement of the NPD data of (a) ANLT6 and (b) ANLT9. The ANLT6 is fitted with the $R3c$+$Pmc2_1$ phases while the ANLT9 are fitted with the 3 phases model ($R3c$+$Pmc2_1$ for the main phases, $LiNbO_3$ for the secondary phase). The insert plots at the top right is the enlargement of the selected region and the insert plot with a red frame is the enlargement to show the impure phase.

Figure 6 shows the structural evolution of ANLT materials as a function of $LiTaO_3$ content. In the single $Pmc2_1$ phase region, *i.e.*, x < 0.053, the unit-cell parameters (*a, b* and *c*) decrease gradually with respect to the x value (Figure 6a). The shrinkage of the unit cells is possibly due to the introduction of the Li^+, whose ionic radius is 92 pm compared with 128 pm of Ag^+.[34] When the second phase appears (x = 0.053), the *a, b* and *c* values in orthorhombic phase exhibit a slight increase. In the two-phase region, *i.e.*, x ≥ 0.053, with further doping, the lattice parameter *a* increases, whereas *b* and c decrease. On the other hand, the fraction of the $R3c$ phase increases from 12.1% to 58.1% for 0.53≤ x ≤0.06 and reaches a saturated value with further increase of the doping. For $R3c$, both *a* and *c* are reduced with increasing x (Figure 6b). The variation of the unit-cell parameters in both $Pmc2_1$ and $R3c$ structures cannot be simply explained by the ionic radii, which is probably linked to the octahedral rotation and the two-phase interaction.

Figure 6c shows the global amplitude of the main modes A_τ changing as a function of $LiTaO_3$ content, in both $Pmc2_1$ and $R3c$ phases. The larger A_τ values imply the larger atomic displacements and highly distorted structure. In the $Pmc2_1$ phase, referring to the mode decomposition in pure AN, all four modes can be divided into ionic displacements (FE Γ4- and AFE Λ3) and octahedral rotations (H2 and T4+). The amplitudes of the H2 and Λ3 modes decrease upon Li+ doping. However, the slope has an inflexion point at x=0.053 and descends rapidly upon further Li+ doping. The amplitude of the FE Γ4- mode on the other hand displays the opposite trend to that of the AFE Λ3 mode. Furthermore, the amplitude of T4+ mode increases initially and drops upon reaching the inflexion point at x=0.053. In the $R3c$ phase, it is evident that the amplitude of the rotation mode, *i.e.* R4+, increases while that of the zone centre FE mode (Γ4-) descends with increasing Li^+ doping.

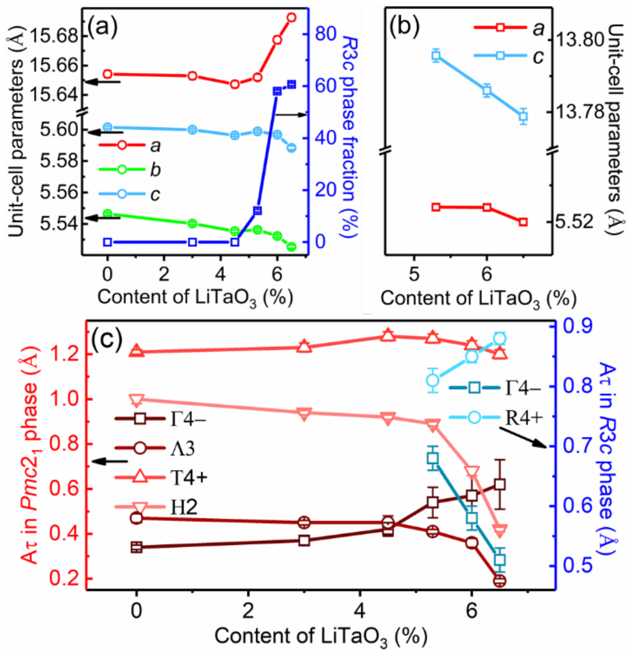

Figure 6. (a) Lattice parameters of the $Pmc2_1$ phase and the phase fraction of the $R3c$ phase, (b) lattice parameters of the $R3c$ phase and (c) the global amplitudes of the main modes in both $Pmc2_1$ and $R3c$ phases changing as a function of the $LiTaO_3$ composition.

In section 2, we have plotted out the distorted structure induced by the single mode and also found that the associated octahedral tilting is induced by the combination of T4+ and H2 modes. Instead of the related oxygen displacements, the tilting angles can also be used to reflect the distortion degrees for these octahedral rotation modes. As shown in Figure 7a, the structure induced by the T4+ mode can be visually expressed by the tilting angles between the two adjacent NbO_6 octahedra viewed along either $[100]_p$ or $[010]_p$. Here, Ψ_{O1} and Ψ_{O2} (subscript O denotes the orthorhombic phase) are used to illustrate the tilting angles. If there is no octahedral distortion, $\Psi_{O1} = \Psi_{O2}$. The H2 mode is associated with the in/out of phase rotation around the $[001]_p$ and Ψ_{O3} is used to characterize the tilting angle for this mode (Figure 7b). The R4+ mode denotes the $a^-a^-a^-$ octahedral tilting and therefore, the tilting angle along any $\langle 100\rangle_p$ directions, Ψ_{R1} (subscript R denotes the rhombohedral phase) is used to describe this distorted structure (Figure 7c). Figure 7d shows the quantitative analysis of these rotation angles. For Ψ_{O1} and Ψ_{O2}, they are almost equivalent when $x \leq 0.053$, and both increase slightly when the doping level of $LiTaO_3$ increases. When $x \geq 0.053$, Ψ_{O1} and Ψ_{O2} behave differently: Ψ_{O1} increases, whereas Ψ_{O2}

decreases. This suggests that the octahedral distortion is accompanied by the appearance of the $R3c$ phase. Furthermore, the decrease in Ψ_{O2} also explains the increase of the unit-cell parameter a for $x \geq 0.053$. The Ψ_{R1} increases in $R3c$ phase with the increment of the heavily underbonded Li^+ dopants. For the H2 mode, Ψ_{O3} decreases slightly before the appearance of the $R3c$ phase and then sharply when the $R3c$ phase dominates the phase fraction. This behaviour is very similar to that of primary modes that vary as a function of temperature in other materials.[35-37] Therefore, the destabilisation of the H2 mode is very important to this compositional-driven phase transition in ANLT100*x* system. Note that the sudden drop of Ψ_{O3} is deduced by the ordered degree for $a^0a^0c^+/a^0a^0c^-$ octahedral tilting in the average length scale. This is probably due to the fact that the rotation around the $[001]_p$ creates differing periodicities or total disorder, [29-30, 38-40] *i.e.*, the modulation wave-vector moves along the H line in the first Brillouin zone of the parent *Ammm* structure. In the Li-doped $AgNbO_3$ material system,[29-30] the electron diffraction patterns present the $\mathbf{G_p} \pm [1/2\ 1/2\ 1/3]_p^*$ satellite reflection, which in turn indicates the movement to the zone boundary (T point) of the H2 mode. Finally, the combination of the T2+ ($a^0a^0c^-$) and T4+ modes induces the $a^-a^-a^-$ octahedral tilting observed in the $R3c$ phase, therefore the variation of the H2 mode locally builds the intermediate structure to bridge the $Pmc2_1$ and $R3c$ phases.

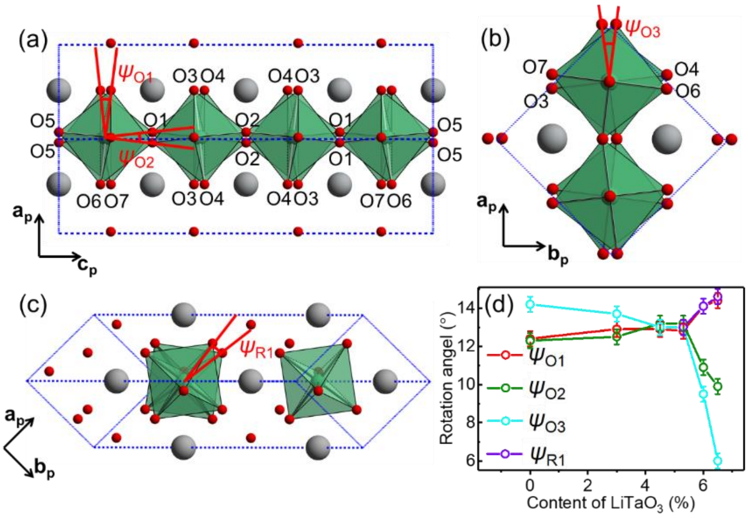

Figure 7. The distorted structure induced by (a) the T4+ mode for $Pmc2_1$ phase viewed along the b_p-axis (b) the H2 mode for $Pmc2_1$ phase viewed along the c_p-axis and

(c) the R4+ mode for *R*3*c* phase viewed along the c_p-axis. (d) The $LiTaO_3$ doping-dependent rotation angles.

As aforementioned, the Γ4- mode is responsible for the ferroelectricity in both *Pmc*2_1 and *R*3*c* phases while Λ3 mode is associated with the antiferroelectricity for the *Pmc*2_1 phase. Note that the Λ3 mode is regarded as the induced secondary mode by primary H2 and T4+ modes, and its composition-dependent amplitude follows the same trend as the H2 mode, indicating the improper AFE nature of the AN.[41] In order to further analyse the anti/ferroelectricity, the ionic displacements associated with different modes are extracted and plotted in Figure 8. As discussed in Section 2, although some atomic displacements along the *b*-axis are involved in the Γ4- and Λ3 modes in the *Pmc*2_1 phase (Table S2), the values are quite small. Furthermore, because the anti-/parallel aligned dipole moments are along the *c*-axis, only the displacements from *z* coordinates are considered. For the Γ4- mode in *Pmc*2_1 phase (Figure 8a), $dO2_{O1}$ (displacement of the apical oxygen), $dO3_{O1}$ (displacement of the equatorial oxygens), dAg_{O1} (Ag/Li) and dNb_{O1} (Nb/Ta) denote the relative ionic displacements along the **-c** from the undistorted position (subscripts O and 1 indicate the orthorhombic phase and the Γ4- mode respectively). Figure 8b schematically describes the ion displacements associated with the Λ3 mode. As the dipole moments in this structure exhibit antiparallel alignment with the same amplitude, therefore only atoms involved in one unit are used for analysis (subscript 2 denotes the Λ3 mode). In this case, only the displacements of Ag/Li2 (dAg_{O2}), Nb/Ta1(dNb_{O2}), apical oxygen ($dO2_{O2}$) and equatorial oxygens ($dO3_{O2}$) are extracted. Similarly, dAg_{R1} (Ag/Li) and dNb_{R2} (Nb/Ta) are used to describe the ferroelectricity in the *R*3*c* phase (Figure 8c). Note that in the *R*3*c* phase, the *z* coordinate of the oxygen is fixed to zero, therefore cationic shifts are enough to describe the spontaneous polarisation. It is interesting that even though the amplitude of Γ4- mode in the *Pmc*2_1 phase exhibit systematic increase as a function of x, the increment of both $dO2_{O1}$ and dNb_{O1} indicates the spontaneous polarisation does not follow the same trend (Figure 8d). This zone centre mode is very hard to be calculated accurately by the powder diffraction because of the average effects, which probably explains why structure models based on both *Pmc*2_1 and *Pbcm* reproduce the experimental pattern reasonably well. The ionic displacements associated with Γ4- mode are non-systematic. In contrast, the $dO2_{O2}$, $dO3_{O2}$, dAg_{O2} and dNb_{O2} involved in the Λ3 mode follow the systematic change as a function of the $LiTaO_3$ contents (Figure 8e). Before introducing the $LiTaO_3$, the cations and anions displace in the opposite direction, where the oxygens are negative, and cations are positive. This induces a strong spontaneous polarisation within one unit drawn by the red dash-lines. With increasing x values, the displacements of the anions and cations begin to converge, and a sudden change occurs at x ~ 0.053. This behaviour suggests that the spontaneous polarisation in one sub-lattice becomes weak, *i.e.*, barrier between the AFE and FE phases decreases with the introduction of more $LiTaO_3$. For $x \geq 0.053$, the *R*3*c* phase emerges and its fraction increases upon further increment of x, whereas the diminishing *Pmc*2_1 phase is simultaneously accompanied by a weakening antiferroelectricity. As a consequence, the ferroic properties are expected to be dominated by the *R*3*c* phase. As shown in Figure 8f, for the sample with large *R*3*c* phase fraction ($x \geq 0.06$), dAg_{R1} remains unchanged while dNb_{R1} shows a slight decrease.

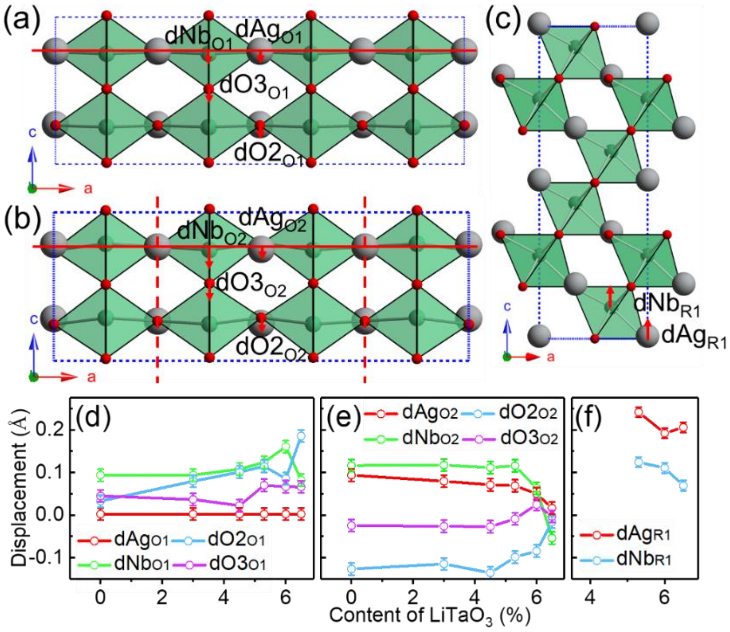

Figure 8. The distorted structure induced by the (a) Γ4- mode and (b) Λ3 mode for *Pmc*2_1 phase viewed along the *b*-axis, the red solid-line indicates the *z* coordinates for the undistorted structure, the red dash-line indicates the boundary of the units where dipole moments share the same direction and the red arrow denotes the displacements of the relative ions. (c) The distorted structure induced by the Γ4- mode for *R*3*c* phase

viewed along the *b*-axis in hexagonal setting, and the red arrow denotes the displacements of the relative ions. The displacements of the ions involved in the (d) Γ4- mode, (e) Λ3 mode in the $Pmc2_1$ phase and (f) Γ4- mode in the *R*3*c* phase vary as a function of $LiTaO_3$ content.

4. Electric properties of the ANLT100*x* material system

Figure 9 presents the temperature-dependent dielectric spectra of ANLT100*x* bulk ceramics. The pure AN contains three evident dielectric constant peaks, T_{I} (~ 70 °C), T_{II} (~ 270°C) and T_{III} (~ 350°C), in the measured temperature range from -150 °C to 480 °C, which is in a good agreement with the experimental results reported previously.[14] In this temperature range, AN contains six phases: M_1, M_2, M_3, O_1, O_2, T. The M_1, M_2 and M_3 phases belong to the orthorhombic structure (M denotes the monoclinic distortions for the primitive unit-cell) and all of them exhibit antiferroelectricity.[42-43] The peaks at around T_{I} and T_{II} points are assigned to the M_1-M_2 and M_2-M_3 phase transition. The sharp peak at T_{III} point is attributed to the phase transition between the AFE M_3 phase and paraelectric O1 phase with a space group symmetry of *Cmcm*. Previously the average structures of M_1, M_2 and M_3 phases are all assigned to the *Pbcm* space group and the phase transition among the three phases is interpreted as the cation displacements.[22, 44-45] The broad T_{II} peak is proved to be the result of the dynamics of Nb^{5+} displacement while the origin of the frequency dependent T_{I} peak is still under debate.[22] Recently, the T_{I} related peak is explicated as the disappearance of weak ferroelectricity, within the recently proposed polar $Pmc2_1$ phase. *i.e.*, the softening of the above mentioned Γ4- mode. [23, 46]

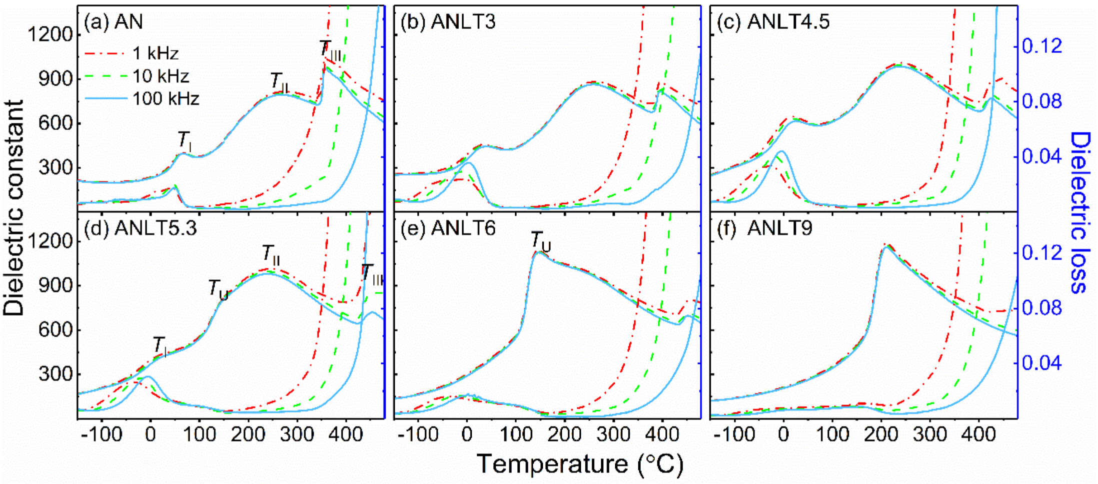

Figure 9. Temperature-dependent dielectric spectra of (a) AN, (b) ANLT3, (c) ANLT4.5, (d) ANLT5.3, (e) ANLT6 and (f) ANLT9 bulk ceramics.

The temperature-dependent dielectric spectra of ANLT3 and ANLT4.5 (Figure 9b and c) are quite similar to the pure AN, again accompanied by three dielectric peaks at T_I, T_{II} and T_{III} respectively. In this composition region, single *Pmc*2$_1$ phase is obtained, and the increment of the $LiTaO_3$ contents will shift both T_I and T_{II} peaks to lower temperature with larger dielectric constant. Referring to Levin *et al.*' results,[22] M3-M2 phase transition is associated with different degrees of ordering for Nb ions and the ordered octahedral tilting will promote the long-range ordering of the Nb displacements. In our experiment, the amplitude of octahedral tilting related mode, H2 mode drops slightly with increasing x value ($x \leq 0.045$), *i.e.*, ordering degrees of the octahedral tilting decrease. Therefore, this order-disorder transition can be activated by a lower thermal energy, and thereby the transition point is moved to the lower temperature range. For T_I peak, as the powder diffraction cannot provide a clear picture about the evolution of the Γ4- mode, it is hard to uncover the origin of the T_1 peak. With further increasing x, an additional dielectric peak T_U is firstly observed around 140 °C in ANLT5.3 and becomes dominated in ANLT6 and ANLT9. After the appearance of the peak T_U, the trace of T_I, T_{II} and T_{III} related dielectric peaks become more blurred with the increasing x and almost unobservable in ANLT9 while there still are traces in the dielectric loss spectra. The appearance of T_U peak is quite consistent with the results in the Li-doped $AgNbO_3$ material systems, which is related to the phase transition between the *R*3*c* FE and AFE phase.[17] Therefore, the variation of T_U peak as a function of x can be well explained by the growth of the *R*3*c* phase in the ANLT100*x* material systems.

Figure 10 shows the polarization-electric field (*P-E*) hysteresis loops of ANLT100*x* bulk ceramics. The pure AN presents a double *P-E* hysteresis loop with an induced polarization of 41 μC/cm^2 under an externally applied, triangular E-field of 175 kV/cm. The critical E-field (E_F) to induce the FE state at 1 Hz is about 125 kV/cm and the non-zero remnant polarization (P_r) is around 6 μC/cm^2 after a withdrawal of the E-field which are almost identical to the results reported by Fu *et al.*[14] The observed *P-E* hysteresis loop confirms the AFE nature of AN, accompanying with a weak ferroelectricity. Similar to pure AN, a double *P-E* hysteresis loop is also observed in ANLT3 (Figure 10a) but the E_F decreases to 100 kV/cm and non-zero P_r is ~ 14 μC/cm^2. The decrease of the critical field, with increasing x value indicates the decreasing energy barrier between the AFE and induced FE state. This is consistent with the trend that the amplitude of Λ3 mode, AFE mode, decreases with increasing x values. The AFE feature, *i.e.* double *P-E* hysteresis loop disappears at the composition of ANLT4.5. Instead, a highly saturated single hysteresis loop is observed with the maximum polarization (P_m) ~ 42 μC/cm^2 and P_r ~ 36 μC/cm^2 when a cycled field of 100 kV/cm is applied. With a further increment of *x*, ANLT100*x* samples exhibit the typical FE features and both P_m and P_r values slightly decrease. For the samples showing two phases coexistence ($x \geq 0.053$), the FE properties seem to be determined by the Γ4- mode in the *R*3*c* phase. As discussed in Section 3, with further increasing the *x* value, the amplitude of the Γ4- mode, *i.e.*, spontaneous polarisation decreases. Therefore, both P_m and P_r of ANLT100*x* ($x \geq 0.053$) exhibit a similar trend.

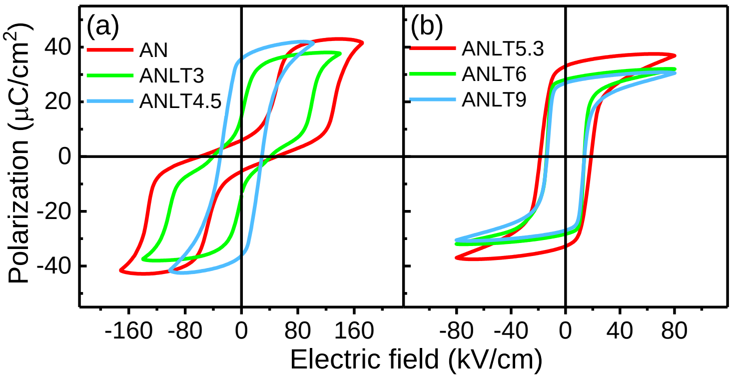

Figure 10. *P-E* hysteresis loops of (a) AN, ANLT3 and ANLT4.5 and (b) ANLT5.3, ANLT6 and ANLT9 bulk ceramics measured at 1 Hz at room temperature.

The NPD pattern and temperature-dependent dielectric spectrum of ANLT4.5 suggest the pristine sample contains a single AFE phase but its *P-E* hysteresis loop shows FE nature (Figure 10a). In order to understand AFE/FE behavior observed in ANLT100*x* systems, the *P-E* hysteresis loops measured in the 1st and 2nd cycles are displayed in Figure 11. It is evident that the polarization of ANLT4.5 increases abruptly after the 1st quarter electric cycle, and after that the *P-E* loop behaves like what observed in a classical FE material. This is very similar to the irreversible E-field induced AFE-FE phase transition observed in the $PbZrO_3$-based AFE materials.[47-48] Furthermore, the E_F for ANLT4.5 is around 90 kV/cm, presenting a further decrease compared with that observed in ANLT3.

For $x \geq 0.053$, the steep increase of the polarization is hardly observed, and instead, the polarization raises gradually in the 1st quarter electric cycle. After the first quarter E-field cycle (with the same amplitude), the P_r values of ANLT53, ANLT60 and ANLT90 are around 13 μC/cm^2, 17 μC/cm^2 and 20 μC/cm^2, respectively. Furthermore, after the 2nd electric cycle, the P_r values of ANLT53 and ANLT60 present slightly increase while that of ANLT90 keeps almost constant. From the structural point of view, the virgin state of the ANLT100x ($x \geq 0.053$) samples contains both $Pmc2_1$ and $R3c$ phases. The different P-E behavior measured in the 1st and 2nd cycles indicates the E-field induced phase transition from $Pmc2_1$ to $R3c$ phase. Additionally, for the $Pmc2_1$ phase in the virgin state, the mode dominating the antiferroelectricity becomes weak with increasing x. For the $R3c$ phase, the phase fraction increases with increasing $LiTaO_3$ content. These structural analyses suggest that the energy barrier between the $Pmc2_1$ and $R3c$ phases is further lower with doping more $LiTaO_3$. Therefore, after triggered by the same E-field, the ANLT90 exhibits the strongest ferroelectricity.

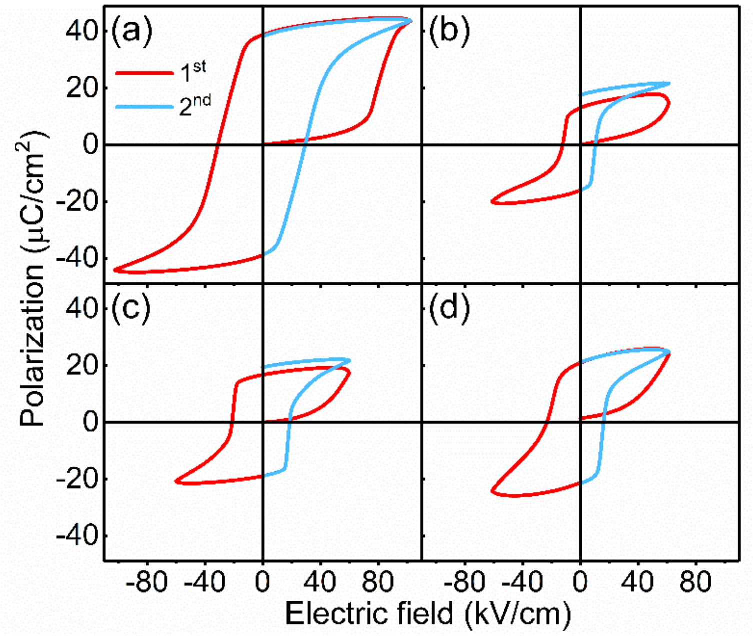

Figure 11. P-E loops of (a) ANLT4.5, (b) ANLT5.3, (c) ANLT6 and (d) ANLT9 measured at 1Hz in 1st cycle and 2nd semi-cycle.

Conclusion

The symmetry mode decomposition of $AgNbO_3$ identifies the difference between the *Pbcm* and *Pmc*2_1 space group. Both distorted structures share 3 main modes (T4+, H2, Λ3) with large amplitudes. The only difference between the *Pbcm* and *Pmc*2_1 structures is the 'softening' of the zone-centre Γ4- mode. This mode lowers the *Pbcm* symmetry into *Pmc*2_1 and is regarded as the origin of the weak ferroelectricity in $AgNbO_3$.

The Rietveld refinement of the symmetry mode on the NPD data of the ANLT100*x* system provides a comprehensive understanding of the structural evolution and thus enables building an intuitive relationship between the structure and electric properties. With increasing the $LiTaO_3$ level to 5.3%, the rhombohedral *R*3*c* phase appears, *i.e.*, the sample presents two-phase coexistence and with further increasing x, the *R*3*c* phase becomes dominated. The appearance of such an *R*3*c* phase is closely related to the dielectric peak T_U in the temperature-dependent dielectric spectra. And a further increase in the *R*3*c* phase fraction results in the disappearance of the T_I, T_{II} and T_{III} dielectric peaks, the characters of the *Pmc*2_1 phase. Among the primary order parameters in the *Pmc*2_1 distorted structure, only H2 mode becomes destabilized when x is around 0.053, which coincides with the appearance of the *R*3*c* phase. The T4+ mode, $a^-a^-c^0$ octahedral rotation, does not show significant variation during this composition-driven phase transition. The secondary Λ3 mode, which is induced by these 2 octahedral rotation modes and controls the antiferroelectricity observed in the samples, is damped as a result of the H2 mode destabilisation. Therefore, the antiferroelectricity becomes weak with the increasing $LiTaO_3$, which is directly reflected by the E_F. Finally, we can conclude that with doping the $LiTaO_3$ into the AN, the heavily underbonded Li^+ will induce the structure distortion. The disappearance of the H2 mode is proposed to be the driving force for the phase transition occurred in ANLT100*x* material system.

This work not only presents a successful synthesis of new lead-free piezoelectric materials that possess promising properties, but also for the first time the analysis of the structural evolution was performed using the symmetry mode decomposition approach, which depict a detailed physical picture for the phase transition in ANLT100*x* and build a close connection between the structure and electrical properties. It is believed that this work provides an insight to tune the electrical properties by controlling relative amplitude of the modes in antiferroelectric and ferroelectric materials. It also introduces a novel approach for structural refinement that provide information on the hidden structural correlations for a better understanding of the physical properties.

Acknowledgement

TL and YL acknowledge the Australian Research Council (ARC) for financial support in the form of Discovery Project (DP160104780). This work is supported by the International Science & Technology Cooperation Program of China under Grant No. 2015DFA51100. The authors also thank the Australian Nuclear Science and Technology Organization for support in the form of beam time.

References:

1. Damjanovic, D., Ferroelectric, Dielectric and Piezoelectric Properties of Ferroelectric Thin Films and Ceramics. *Rep. Prog. Phys.* **1998,** *61* (9), 1267.
2. Haertling, G. H., Ferroelectric Ceramics: History and Technology. *J. Am. Ceram. Soc.* **1999,** *82* (4), 797-818.
3. Setter, N.; Damjanovic, D.; Eng, L.; Fox, G.; Gevorgian, S.; Hong, S.; Kingon, A.; Kohlstedt, H.; Park, N.; Stephenson, G., Ferroelectric Thin Films: Review of Materials, Properties, and Applications. *J. Appl. Phys.* **2006,** *100* (5), 051606.
4. Hao, X.; Zhai, J.; Yao, X., Improved Energy Storage Performance and Fatigue Endurance of Sr-Doped $PbZrO_3$ Antiferroelectric Thin Films. *J. Am. Ceram. Soc.* **2009,** *92* (5), 1133-1135.
5. Park, S.-E.; Shrout, T. R., Ultrahigh Strain and Piezoelectric Behavior in Relaxor Based Ferroelectric Single Crystals. *J. Appl. Phys.* **1997,** *82* (4), 1804-1811.
6. Bellaiche, L.; Vanderbilt, D., Intrinsic Piezoelectric Response in Perovskite Alloys: PMN-PT versus PZT. *Phys. Rev. Lett.* **1999,** *83* (7), 1347.
7. Guo, R.; Cross, L.; Park, S.; Noheda, B.; Cox, D.; Shirane, G., Origin of the High Piezoelectric Response in $PbZr_{1-x}Ti_xO_3$. *Phys. Rev. Lett.* **2000,** *84* (23), 5423.
8. Mirshekarloo, M. S.; Yao, K.; Sritharan, T., Large Strain and High Energy Storage Density in Orthorhombic Perovskite, $(Pb_{0.97}La_{0.02})(Zr_{1-x-y}Sn_xTi_y)O_3$ Antiferroelectric Thin Films. *Appl. Phys. Lett.* **2010,** *97* (14), 3.
9. Liu, Z.; Chen, X.; Peng, W.; Xu, C.; Dong, X.; Cao, F.; Wang, G., Temperature-dependent Stability of Energy Storage Properties of $Pb_{0.97}La_{0.02}(Zr_{0.58}Sn_{0.335}Ti_{0.085})O_3$ Antiferroelectric Ceramics for Pulse Power Capacitors. *Appl. Phys. Lett.* **2015,** *106* (26), 262901.
10. Saito, Y.; Takao, H.; Tani, T.; Nonoyama, T.; Takatori, K.; Homma, T.; Nagaya, T.; Nakamura, M., Lead-free Piezoceramics. *Nature* **2004,** *432* (7013), 84-87.
11. Shrout, T. R.; Zhang, S. J., Lead-free Piezoelectric Ceramics: Alternatives for PZT? *J. Electroceram.* **2007,** *19* (1), 113-126.
12. Tian, Y.; Jin, L.; Zhang, H.; Xu, Z.; Wei, X.; Politova, E.; Stefanovich, S. Y.; Tarakina, N. V.; Abrahams, I.; Yan, H., High Energy Density in Silver Niobate Ceramics. *J. Mater. Chem. A* **2016,** *4* (44), 17279-17287.

13. Zhao, L.; Liu, Q.; Gao, J.; Zhang, S.; Li, J. F., Lead-Free Antiferroelectric Silver Niobate Tantalate with High Energy Storage Performance. *Adv. Mater.* **2017,** *29* (31), 1701824.

14. Fu, D. S.; Endo, M.; Taniguchi, H.; Taniyama, T.; Itoh, M., $AgNbO_3$: A Lead-free Material with Large Polarization and Electromechanical Response. *Appl. Phys. Lett.* **2007,** *90* (25), 3.

15. Fu, D.; Endo, M.; Taniguchi, H.; Taniyama, T.; Koshihara, S.-y.; Itoh, M., Piezoelectric Properties of Lithium Modified Silver Niobate Perovskite Single Crystals. *Appl. Phys. Lett.* **2008,** *92* (17), 172905.

16. Fu, D.; Itoh, M.; Koshihara, S.-y., Dielectric, Ferroelectric, and Piezoelectric Behaviors of $AgNbO_3$–$KNbO_3$ Solid Solution. *J. Appl. Phys.* **2009,** *106* (10), 104104.

17. Fu, D.; Endo, M.; Taniguchi, H.; Taniyama, T.; Itoh, M.; Koshihara, S.-y., Ferroelectricity of Li-doped Silver Niobate (Ag, Li)NbO_3. *J. Phys.: Condens. Matter* **2011,** *23* (7), 075901.

18. Dove, M. T., Review: Theory of Displacive Phase Transitions in Minerals. *Am. Mineral.* **1997,** *82* (3-4), 213-244.

19. Stokes, H. T.; Hatch, D. M.; Wells, J. D., Group-theoretical methods for obtaining distortions in crystals: Applications to vibrational modes and phase transitions. *Phys. Rev. B* **1991,** *43* (13), 11010.

20. Perez-Mato, J. M.; Orobengoa, D.; Aroyo, M. I., Mode Crystallography of Distorted Structures. *Acta Crystallogr. Sect. A: Found. Crystallogr.* **2010,** *66* (5), 558-590.

21. Sciau, P.; Kania, A.; Dkhil, B.; Suard, E.; Ratuszna, A., Structural Investigation of $AgNbO_3$ Phases Using X-ray and Neutron Diffraction. *J. Phys.: Condens. Matter* **2004,** *16* (16), 2795.

22. Levin, I.; Krayzman, V.; Woicik, J. C.; Karapetrova, J.; Proffen, T.; Tucker, M. G.; Reaney, I. M., Structural Changes Underlying the Diffuse Dielectric Response in $AgNbO_3$. *Phys. Rev. B* **2009,** *79* (10), 104113.

23. Yashima, M.; Matsuyama, S.; Sano, R.; Itoh, M.; Tsuda, K.; Fu, D. S., Structure of Ferroelectric Silver Niobate AgNbO3. *Chem. Mater.* **2011,** *23* (7), 1643-1645.

24. Campbell, B. J.; Stokes, H. T.; Tanner, D. E.; Hatch, D. M., ISODISPLACE: a Web-based Tool for Exploring Structural Distortions. *J. Appl. Crystallogr.* **2006,** *39* (4), 607-614.

25. Glazer, A., Simple Ways of Determining Perovskite Structures. *Acta Crystallogr., Sect. A: Cryst. Phys., Diffr., Theor. Gen. Crystallogr.* **1975,** *31* (6), 756-762.

26. Rodríguez-Carvajal, J., Recent Advances in Magnetic Structure Determination by Neutron Powder Diffraction. *Physica B* **1993,** *192* (1), 55-69.

27. Tian, Y.; Jin, L.; Zhang, H.; Xu, Z.; Wei, X.; Viola, G.; Abrahams, I.; Yan, H., Phase Transitions in Bismuth-Modified Silver Niobate Ceramics for High Power Energy Storage. *J. Mater. Chem. A* **2017,** *5*, 17525.

28. Brown, I., The Bond-valence Method: An Empirical Approach to Chemical Structure and Bonding. *Structure and bonding in crystals* **1981,** *2*, 1-30.

29. Khan, H. U.; Sterianou, I.; Han, Y.; Pokorny, J.; Reaney, I. M., Phase Transitions in $Li_xAg_{1-x}(Nb_{0.5}Ta_{0.5})O_3$ Solid Solutions. *J. Appl. Phys.* **2010,** *108* (6), 064117.

30. Khan, H. U.; Sterianou, I.; Miao, S.; Pokorny, J.; Reaney, I. M., The Effect of Li-substitution on the M-phases of $AgNbO_3$. *J. Appl. Phys.* **2012,** *111* (2), 024107.

31. Abrahams, S.; Reddy, J. M.; Bernstein, J., Ferroelectric Lithium Niobate. 3. Single crystal X-ray diffraction study at 24 °C. *J. Phys. Chem. Solids* **1966,** *27* (6-7), 997-1012.

32. Alonso, J. A.; Sanz, J.; Santamaría, J.; León, C.; Várez, A.; Fernández-Díaz, M. T., On the Location of Li+ Cations in the Fast Li-Cation Conductor $La_{0.5}Li_{0.5}TiO_3$ Perovskite. *Angew. Chem. Int. Ed.* **2000,** *39* (3), 619-621.

33. Brant, W. R.; Schmid, S.; Kuhn, A.; Hester, J.; Avdeev, M.; Sale, M.; Gu, Q., Rapid Lithium

Insertion and Location of Mobile Lithium in the Defect Perovskite Li0.18Sr0.66Ti0.5Nb0.5O3. *ChemPhysChem* **2012,** *13* (9), 2293-2296.

34. Shannon, R. D., Revised Effective Ionic Radii and Systematic Studies of Interatomic Distances in Halides and Chalcogenides. *Acta Crystallogr., Sect. A: Cryst. Phys., Diffr., Theor. Gen. Crystallogr.* **1976,** *32* (5), 751-767.

35. Gómez-Pérez, A.; Hoelzel, M.; Muñoz-Noval, A. l.; García-Alvarado, F.; Amador, U., Effect of Internal Pressure and Temperature on Phase Transitions in Perovskite Oxides: The Case of the Solid Oxide Fuel Cell Cathode Materials of the $La_{2-x}Sr_xCoTiO_6$ Series. *Inorg. Chem.* **2016,** *55* (24), 12766-12774.

36. Khalyavin, D. D.; Salak, A. N.; Olekhnovich, N. M.; Pushkarev, A. V.; Radyush, Y. V.; Manuel, P.; Raevski, I. P.; Zheludkevich, M. L.; Ferreira, M. G. S., Polar and Antipolar Polymorphs of Metastable Perovskite $BiFe_{0.5}Sc_{0.5}O_3$. *Phys. Rev. B* **2014,** *89* (17), 174414.

37. Faik, A.; Orobengoa, D.; Iturbe-Zabalo, E.; Igartua, J. M., A Study of the Crystal Structures and the Phase Transitions of the Ordered Double Perovskites Sr_2ScSbO_6 and Ca_2ScSbO_6. *J. Solid State Chem.* **2012,** *192*, 273-283.

38. Peel, M. D.; Thompson, S. P.; Daoud-Aladine, A.; Ashbrook, S. E.; Lightfoot, P., New Twists on the Perovskite Theme: Crystal Structures of the Elusive Phases R and S of $NaNbO_3$. *Inorg. Chem.* **2012,** *51* (12), 6876-6889.

39. Prosandeev, S.; Wang, D.; Ren, W.; Iniguez, J.; Bellaiche, L., Novel Nanoscale Twinned Phases in Perovskite Oxides. *Adv. Funct. Mater.* **2013,** *23* (2), 234-240.

40. Wang, J.; Liu, Y.; Withers, R. L.; Studer, A.; Li, Q.; Norén, L.; Guo, Y., A Correlated Electron Diffraction, In Situ Neutron Diffraction and Dielectric Properties Investigation of Poled $(1-x)Bi_{0.5}Na_{0.5}TiO_3-xBaTiO_3$ Ceramics. *J. Appl. Phys.* **2011,** *110* (8), 084114.

41. Bellaiche, L.; Íñiguez, J., Universal Collaborative Couplings between Oxygen-Octahedral Rotations and Antiferroelectric Distortions in Perovskites. *Phys. Rev. B* **2013,** *88* (1), 014104.

42. Kania, A., Dielectric Properties of $Ag_{1-x}A_xNbO_3$ (A: K, Na and Li) and $AgNb_{1-x}Ta_xO_3$ Solid Solutions in the Vicinity of Diffuse Phase Transitions. *J. Phys. D: Appl. Phys.* **2001,** *34* (10), 1447.

43. Ratuszna, A.; Pawluk, J.; Kania, A., Temperature Evolution of the Crystal Structure of $AgNbO_3$. *Phase Transitions* **2003,** *76* (6), 611-620.

44. Krayzman, V.; Levin, I., Reverse Monte Carlo Refinements of Local Displacive Order in Perovskites: $AgNbO_3$ Case Study. *J. Phys.: Condens. Matter* **2010,** *22* (40), 404201.

45. Levin, I.; Woicik, J. C.; Llobet, A.; Tucker, M. G.; Krayzman, V.; Pokorny, J.; Reaney, I. M., Displacive Ordering Transitions in Perovskite-Like $AgNb_{1/2}Ta_{1/2}O_3$. *Chem. Mater.* **2010,** *22* (17), 4987-4995.

46. Manish, K. N.; Prasad, K. G.; Saket, A.; Rayaprol, S.; Siruguri, V., Investigation of Structural, Vibrational and Ferroic Properties of AgNbO 3 at Room Temperature Using Neutron Diffraction, Raman Scattering and Density-Functional Theory. *J. Phys. D: Appl. Phys.* **2015,** *48* (21), 215303.

47. Guo, H.; Tan, X., Direct Observation of the Recovery of an Antiferroelectric Phase During Polarization Reversal of an Induced Ferroelectric Phase. *Phys. Rev. B* **2015,** *91* (14), 144104.

48. Tan, X.; Frederick, J.; Ma, C.; Jo, W.; Rödel, J., Can an Electric Field Induce an Antiferroelectric Phase Out of a Ferroelectric Phase? *Phys. Rev. Lett.* **2010,** *105* (25), 255702.

Supporting information 1. The symmetry-mode decomposition of *Pmca* and *Pmc*2_1 space groups.

Table S1. The symmetry-mode decomposition results of the *Pmca* structure referring to the *Ammm* parent structure. The coordinates after the atomic label are those for the undistorted structure. The unit-cell parameters for *Pmca* are: *a*=15.6503 Å, *b*=5.5517 Å, *c*=5.6080 Å, *α*=*β*=*γ*=90°.

Wave-vector	Irreps	Atomic Label			
		O1	0.75	0.75	0.75
			δx	δy	δz
[1/4 0 0]*	Λ3		0	0	0.01361
[0 1 0]*	Y3-		0	0.00605	0
[1/2 1 0]*	T4+		0	-0.05526	0
		O2	0.5	0.75	0.75
			δx	δy	δz
[0 1 0]*	Y3-		0	0.00605	0
[1/2 1 0]*	T4+		0	0.05526	0
		O3	0.625	0.5	0.5
			δx	δy	δz
[1/4 0 0]*	Λ3		0	0.00085	0.00325
[1/2 0 0]*	Z2-		-0.00025	0	0
[1/2 1 0]*	T4+		-0.01387	0	0
[1/4 1 0]*	H2		0	-0.03193	0.03186
		O4	0.625	0	0.5
			δx	δy	δz
[1/4 0 0]*	Λ3		0	-0.00085	0.00325
[1/2 0 0]*	Z2-		-0.00025	0	0
[1/2 1 0]*	T4+		0.01387	0	0
[1/4 1 0]*	H2		0	-0.03193	-0.03186
		Ag1	0.75	0.75	0.25
			δx	δy	δz
[1/4 0 0]*	Λ3		0	0	-0.01681
[0 1 0]*	Y3-		0	0.00705	0
[1/2 1 0]*	T4+		0	0.00035	0
		Ag2	0.5	0.75	0.25
			δx	δy	δz
[0 1 0]*	Y3-		0	0.00705	0
[1/2 1 0]*	T4+		0	-0.00035	0
		Nb1	0.625	0.75	0.75
			δx	δy	δz
[1/4 0 0]*	Λ3		0	0	-0.02558
[0 1 0]*	Y3-		0	-0.0044	0

Table S2. The symmetry-mode decomposition results of the *Pmc*2_1 structure referring to the *Ammm* parent structure. The coordinates after the atomic label are those for the undistorted structure. Note that as the *Pmc*2_1 contains polar axis along the c-axis, the atomic coordinates exhibit origin shifts. The unit-cell parameters for *Pmc*2_1 are: *a*=15.6459 Å, *b*=5.5525 Å, *c*=5.6091 Å, *α*=*β*=*γ*=90°.

Wave-vector	Irreps	Atomic Label							
		O1	0.75	0.75	0.768	Ag1	0.75	0.75	0.268
			δx	*δy*	*δz*		*δx*	*δy*	*δz*
[0 0 0]*	Γ4-		0	0	-0.00441		0	0	-0.00042
[1/4 0 0]*	Λ1		0.0004	0	0		0.0004	0	0
[0 1 0]*	Y3-		0	0.00455	0		0	-0.0042	0
[1/2 0 0]*	Z3+		0	0	-0.00125		0	0	-0.00125
[1/2 1 0]*	T4+		0	-0.05497	0		0	0.0013	0
		O2	0.5	0.75	0.768	Ag2	0.5	0.75	0.268
			δx	*δy*	*δz*		*δx*	*δy*	*δz*
[0 0 0]*	Γ4-		0	0	-0.00441		0	0	-0.00042
[1/4 0 0]*	Λ3		0	0	0.01849		0	0	-0.01949
[0 1 0]*	Y3-		0	0.00455	0		0	-0.0042	0
[1/2 0 0]*	Z3+		0	0	0.00125		0	0	0.00125
[1/2 1 0]*	T4+		0	0.05497	0		0	-0.0013	0
[1/4 1 0]	H4		0	0.0095	0		0	0.0015	0
		O3	0.625	0.5	0.518	O4	0.625	0	0.518
			δx	*δy*	*δz*		*δx*	*δy*	*δz*
[0 0 0]*	Γ4-		0	0.00175	-0.00492		0	-0.00175	-0.00492
[1/4 0 0]*	Λ1		-0.00135	0	0		-0.00135	0	0
[1/4 0 0]*	Λ3		0	0.00025	0.00275		0	-0.00025	0.00275
[0 1 0]*	Y2+		0	0.00575	-0.00525		0	0.00575	0.00525
[1/2 0 0]*	Z2-		0.0002	0	0		0.0002	0	0
[1/2 1 0]*	T4+		-0.01392	0	0		0.01392	0	0
[1/4 1 0]*	H2		0	0.03123	-0.03027		0	0.03123	0.03027
[1/4 1 0]*	H4		-0.00055	0	0		0.00055	0	0
		O5	0	0.25	0.268	Ag3	0	0.75	0.268
			δx	*δy*	*δz*		*δx*	*δy*	*δz*
[0 0 0]*	Γ4-		0	0	-0.00441		0	0	-0.00042
[1/4 0 0]*	Λ3		0	0	-0.01849		0	0	0.01949
[0 1 0]*	Y3-		0	-0.00455	0		0	-0.0042	0
[1/2 0 0]*	Z3+		0	0	0.00125		0	0	0.00125
[1/2 1 0]*	T4+		0	-0.05497	0		0	-0.0013	0
[1/4 1 0]	H4		0	0.0095	0		0	-0.0015	0
		O6	0.125	0	0.018	O7	0.125	0.5	0.518
			δx	*δy*	*δz*		*δx*	*δy*	*δz*
[0 0 0]*	Γ4-		0	0.00175	-0.00492		0	0.00175	-0.00492

[1/4 0 0]*	Λ1		0.00135	0	0		0.00135	0	0
[1/4 0 0]*	Λ3		0	-0.00025	-0.00275		0	-0.00025	-0.00275
[0 1 0]*	Y2+		0	-0.00575	0.00525		0	0.00575	-0.00525
[1/2 0 0]*	Z2-		0.0002	0	0		0.0002	0	0
[1/2 1 0]*	T4+		0.01392	0	0		-0.01392	0	0
[1/4 1 0]*	H2		0	0.03123	-0.03027		0	-0.03123	0.03027
[1/4 1 0]*	H4		-0.00055	0	0		-0.00055	0	0
		Nb1	0.625	0.75	0.768	Nb2	0.125	0.25	0.268
			δx	*δy*	*δz*		*δx*	*δy*	*δz*
[0 0 0]*	Γ4-		0	0	-0.01046		0	0	-0.01046
[1/4 0 0]*	Λ1		0.0001	0	0		-0.0001	0	0
[1/4 0 0]*	Λ3		0	0	-0.02259		0	0	0.02259
[0 1 0]*	Y3-		0	0.00776	0		0	-0.00776	0
[1/2 0 0]*	Z2-		0.0005	0	0		0.0005	0	0
[1/4 1 0]	H4		0	-0.00066	0		0	-0.00066	0

Supporting information 2. Bond valance sum calculation on AgNbO3 and LiTaO3

Bond valence calculations using conventional BV parameters: AgNbO$_3$ $Pmc2_1$ space group; *a* = 15.6542 Å; *b* = 5.5464 Å, *c* = 5.6015 Å.

Ag3-O5: 2.8867Å s=0.0594v.u. ; 2.6833Å s=0.1029v.u. ; 2.5666Å s=0.1411v.u. ; 3.0739Å s=0.0358v.u.
Ag3-O6: 2.7756Å s=0.0802v.u. ; 2.7756Å s=0.0802v.u. ; 3.2319Å s=0.0234v.u. ; 3.2319Å s=0.0234v.u.
Ag3-O7: 2.6635Å s=0.1086v.u. ; 2.5475Å s=0.1486v.u. ; 2.6635Å s=0.1086v.u. ; 2.5475Å s=0.1486v.u.

BV-sum of Ag3: 1.0608v.u. ; BV sum deviation: 0.0608v.u.

Ag1-O1: 2.8492Å s=0.0657v.u. ; 2.7866Å s=0.0779v.u. ; 2.4125Å s=0.2140v.u. 3.1343Å s=0.0304v.u.
Ag1-O6: 2.4489Å s=0.1939v.u. ; 2.8339Å s=0.0685v.u.
Ag1-O7: 2.7741Å s=0.0805v.u. ; 3.0003Å s=0.0437v.u.
Ag1-O4: 2.8590Å s=0.0640v.u. ; 2.4426Å s=0.1973v.u.
Ag1-O3: 2.7697Å s=0.0815v.u. ; 3.1595Å s=0.0284v.u.

BV-sum of Ag1: 1.1458v.u. ; BV sum deviation: 0.1458v.u.

Ag2-O2: 2.6267Å s=0.1199v.u. ; 3.0089Å s=0.0427v.u. ; 2.4885Å s=0.1742v.u. ; 3.0713Å s=0.0361v.u.
Ag2-O4: 2.7250Å s=0.0920v.u. ; 2.7250Å s=0.0920v.u. ; 3.1798Å s=0.0269v.u. ; 3.1798Å s=0.0269v.u.
Ag2-O3: 2.4273Å s=0.2056v.u. ; 2.7798Å s=0.0793v.u. ; 2.4273Å s=0.2056v.u. ;

2.7798Å s=0.0793v.u.

BV-sum of Ag2: 1.1804v.u. ; BV sum deviation: 0.1804v.u.

Nb2-O5: 1.9777Å s=0.8351v.u.
Nb2-O1: 1.9829Å s=0.8234v.u.
Nb2-O6: 2.0102Å s=0.7648v.u. ; 1.9263Å s=0.9594v.u.
Nb2-O7: 1.9437Å s=0.9155v.u. ; 2.0928Å s=0.6117v.u.

BV-sum of Nb2: 4.9100v.u. ; BV sum deviation: -0.0900v.u.

Nb1-O1: 1.9895Å s=0.8088v.u.
Nb1-O2: 2.0120Å s=0.7611v.u.
Nb1-O4: 1.8653Å s=1.1316v.u. ; 2.1852Å s=0.4766v.u.
Nb1-O3: 1.8645Å s=1.1340v.u. ; 2.1263Å s=0.5589v.u.

BV-sum of Nb1: 4.8709v.u. ; BV sum deviation: -0.1291v.u.

Ag3-O5: 2.5666Å s=0.1411v.u. ; 2.6833Å s=0.1029v.u. ; 2.8867Å s=0.0594v.u. ; 3.0739Å s=0.0358v.u.
Nb2-O5: 1.9776Å s=0.8352v.u. ; 1.9776Å s=0.8352v.u.

BV-sum of O5: 2.0096v.u. ; BV sum deviation: 0.0096v.u.

Ag1-O1: 2.4125Å s=0.2140v.u. 2.8492Å s=0.0657v.u. ; 2.7866Å s=0.0779v.u. ; 3.1343Å s=0.0304v.u.
Nb2-O1: 1.9829Å s=0.8234v.u.
Nb1-O1: 1.9895Å s=0.8089v.u.

BV-sum of O1: 2.0202v.u. ; BV sum deviation: 0.0202v.u.

Ag2-O2: 2.4886Å s=0.1742v.u. ; 2.6266Å s=0.1200v.u. ; 3.0089Å s=0.0427v.u. ; 3.0713Å s=0.0361v.u.
Nb1-O2: 2.0120Å s=0.7610v.u. ; 2.0120Å s=0.7610v.u.

BV-sum of O2: 2.015v.u. ; BV sum deviation: 0.015v.u.

Ag3-O6: 2.7757Å s=0.0802v.u. ; 3.2319Å s=0.0234v.u.
Ag1-O6: 2.4490Å s=0.1939v.u. ; 2.8339Å s=0.0685v.u.
Nb2-O6: 2.0103Å s=0.7646v.u. ; 1.9263Å s=0.9595v.u.

BV-sum of O6: 2.09v.u. ; BV sum deviation: 0.09v.u.

Ag3-O7: 2.6635Å s=0.1086v.u. ; 2.5476Å s=0.1485v.u.
Ag1-O7: 2.7741Å s=0.0805v.u. ; 3.0003Å s=0.0437v.u.
Nb2-O7: 1.9437Å s=0.9155v.u. ; 2.0929Å s=0.6116v.u.

BV-sum of O7: 1.9134v.u. ; BV sum deviation: -0.0866v.u.

Ag1-O4: 2.4426Å s=0.1973v.u. ; 2.8590Å s=0.0640v.u.
Ag2-O4: 2.7249Å s=0.0920v.u. ; 3.1798Å s=0.0269v.u.
Nb1-O4: 1.8653Å s=1.1315v.u. ; 2.1852Å s=0.4766v.u.

BV-sum of O4: 1.8974v.u. ; BV sum deviation: -0.0117v.u.

Ag1-O3: 2.7697Å s=0.0815v.u. ; 3.1595Å s=0.0284v.u.
Ag2-O3: 2.4274Å s=0.2055v.u. ; 2.7798Å s=0.0793v.u.
Nb1-O3: 1.8645Å s=1.1340v.u. ; 2.1262Å s=0.5591v.u.

BV-sum of O3: 2.0878v.u. ; BV sum deviation: 0.0878v.u.

Global instability index GII = 0.0945v.u.

Bond valence calculations using conventional BV parameters: $LiTaO_3$ *Pmc*2_1 space group; *a* = 15.6542 Å; *b* = 5.5464 Å, *c* = 5.6015 Å.

Li3-O5: 2.8867Å s=0.0215v.u. ; 2.6833Å s=0.0373v.u. ; 2.5666Å s=0.0511v.u. ; 3.0739Å s=0.0130v.u.
Li3-O6: 2.7756Å s=0.0290v.u. ; 2.7756Å s=0.0290v.u. ; 3.2319Å s=0.0085v.u. ; 3.2319Å s=0.0085v.u.
Li3-O7: 2.6635Å s=0.0393v.u. ; 2.5475Å s=0.0538v.u. ; 2.6635Å s=0.0393v.u. ; 2.5475Å s=0.0538v.u.

BV-sum of Li3: 0.3841v.u. ; BV sum deviation: -0.6159v.u.

Li1-O1: 2.8492Å s=0.0238v.u. ; 2.7866Å s=0.0282v.u. ; 2.4125Å s=0.0774v.u. 3.1343Å s=0.0110v.u.
Li1-O6: 2.4489Å s=0.0702v.u. ; 2.8339Å s=0.0248v.u.
Li1-O7: 2.7741Å s=0.0292v.u. ; 3.0003Å s=0.0158v.u.
Li1-O4: 2.8590Å s=0.0232v.u. ; 2.4426Å s=0.0714v.u.
Li1-O3: 2.7697Å s=0.0295v.u. ; 3.1595Å s=0.0103v.u.

BV-sum of Li1: 0.4148v.u. ; BV sum deviation: -0.5852v.u.

Li2-O2: 2.6267Å s=0.0434v.u. ; 3.0089Å s=0.0155v.u. ; 2.4885Å s=0.0631v.u. ; 3.0713Å s=0.0131v.u.
Li2-O4: 2.7250Å s=0.0333v.u. ; 2.7250Å s=0.0333v.u. ; 3.1798Å s=0.0097v.u. ; 3.1798Å s=0.0097v.u.
Li2-O3: 2.4273Å s=0.0744v.u. ; 2.7798Å s=0.0287v.u. ; 2.4273Å s=0.0744v.u. ; 2.7798Å s=0.0287v.u.

BV-sum of Li2: 0.4273v.u. ; BV sum deviation: -0.5727v.u.

```
Ta2-O5: 1.9777Å s=0.8557v.u.
Ta2-O1: 1.9829Å s=0.8437v.u.
Ta2-O6: 2.0102Å s=0.7836v.u. ; 1.9263Å s=0.9831v.u.
Ta2-O7: 1.9437Å s=0.9380v.u. ; 2.0928Å s=0.6268v.u.
----------------------------------------------------------------
BV-sum of Ta2: 5.0309v.u. ; BV sum deviation: 0.0309v.u.

Ta1-O1: 1.9895Å s=0.8287v.u.
Ta1-O2: 2.0120Å s=0.7798v.u.
Ta1-O4: 1.8653Å s=1.1594v.u. ; 2.1852Å s=0.4884v.u.
Ta1-O3: 1.8645Å s=1.1619v.u. ; 2.1263Å s=0.5726v.u.
----------------------------------------------------------------
BV-sum of Ta1: 4.9909v.u. ; BV sum deviation: -0.0091v.u.

Ta2-O5: 1.9776Å s=0.8558v.u. ; 1.9776Å s=0.8558v.u.
Li3-O5: 2.8867Å s=0.0215v.u. ; 2.6833Å s=0.0373v.u. ; 2.5666Å s=0.0511v.u. ; 3.0739Å
s=0.0130v.u.
----------------------------------------------------------------
BV-sum of O5: 1.7115v.u. ; BV sum deviation: -0.2885v.u.

Ta2-O1: 1.9829Å s=0.8436v.u.
Ta1-O1: 1.9895Å s=0.8288v.u.
Li1-O1: 2.8492Å s=0.0238v.u. ; 2.7866Å s=0.0282v.u. ; 2.4125Å s=0.0774v.u. 3.1343Å
s=0.0110v.u.
----------------------------------------------------------------
BV-sum of O1: 1.8128v.u. ; BV sum deviation: -0.1872v.u.

Ta1-O2: 2.0120Å s=0.7798v.u. ; 2.0120Å s=0.7798v.u.
Li2-O2: 2.6267Å s=0.0434v.u. ; 3.0089Å s=0.0155v.u. ; 2.4885Å s=0.0631v.u. ; 3.0713Å
s=0.0131v.u.
----------------------------------------------------------------
BV-sum of O2: 1.6947v.u. ; BV sum deviation: -0.3035v.u.

Ta2-O6: 2.0103Å s=0.7834v.u. ; 1.9263Å s=0.9831v.u.
Li3-O6: 2.7756Å s=0.0290v.u. ; 3.2319Å s=0.0085v.u.
Li1-O6: 2.4489Å s=0.0702v.u. ; 2.8339Å s=0.0248v.u.
----------------------------------------------------------------
BV-sum of O6: 1.8989v.u. ; BV sum deviation: -0.1011v.u.

Ta2-O7: 1.9437Å s=0.9380v.u. ; 2.0929Å s=0.6267v.u.
Li3-O7: 2.6635Å s=0.0393v.u. ; 2.5475Å s=0.0538v.u.
Li1-O7: 2.7741Å s=0.0292v.u. ; 3.0003Å s=0.0158v.u.
----------------------------------------------------------------
BV-sum of O7: 1.7028v.u. ; BV sum deviation: -0.2972v.u.
```

Ta1-O4: 1.8653Å s=1.1594v.u. ; 2.1852Å s=0.4883v.u.
Li1-O4: 2.8590Å s=0.0232v.u. ; 2.4426Å s=0.0714v.u.
Li2-O4: 2.7250Å s=0.0333v.u. ; 3.1798Å s=0.0097v.u.

BV-sum of O4: 1.7853v.u. ; BV sum deviation: -0.2147v.u.

Ta1-O3: 1.8645Å s=1.1619v.u. ; 2.1262Å s=0.5728v.u.
Li1-O3: 2.7697Å s=0.0295v.u. ; 3.1595Å s=0.0103v.u.
Li2-O3: 2.4273Å s=0.0744v.u. ; 2.7798Å s=0.0287v.u.

BV-sum of O3: 1.8776v.u. ; BV sum deviation: -0.1224v.u.

Global instability index GII = 0.3794v.u.

Supporting information 3: The atomic position of Rietveld refinements on ANLT100*x* (*x*=0, 0.03, 0.045, 0.053, 0.06 and 0.09)

Table S3. The refined crystal lattice parameters and reliability factors of the ANLT100*x* materials resulting from the Rietveld analysis based on the neutron powder diffraction data.

Chemical composition		AN	ANLT3	ANLT4.5	ANLT5.3		ANLT6		ANLT9	
Space group		*Pmc*2_1	*Pmc*2_1	*Pmc*2_1	*Pmc*2_1	*R*3*c*	*Pmc*2_1	*R*3*c*	*Pmc*2_1	*R*3*c*
Unit-cell parameters (Å)	*a*	15.6542(25)	15.6530(25)	15.6473(24)	15.6520(22)	5.5241(8)	15.6775(26)	5.5240(8)	15.6927(25)	5.520(1)
	b	5.5464(8)	5.5402(8)	5.5354(8)	5.5362(8)	5.5241(8)	5.5323(8)	5.5240(8)	5.5254(11)	5.520(1)
	c	5.6015(7)	5.6000(7)	5.5964(7)	5.5989(7)	13.7957(18)	5.5968(7)	13.7860(18)	5.5884(12)	13.7788(22)
R_p		1.88%	1.99%	1.80%	1.87%	1.87%	2.00%	2.00%	2.60%	2.60%
R_{wp}		2.33%	2.50%	2.22%	2.30%	2.30%	2.51%	2.51%	3.35%	3.35%
R_{ex}		1.44%	1.44%	1.45%	1.43%	1.43%	1.45%	1.45%	1.45%	1.45%
R_{Bragg}		2.60%	2.64%	3.55%	2.25%	2.50%	4.54%	3.93%	5.71%	4.15%
R_F		1.89%	1.93%	2.68%	1.89%	1.25%	3.67%	1.77%	5.40%	2.14%

Table S4. Refined crystal parameters of neutron powder diffraction data for $AgNbO_3$ at room temperature.

Space group	*Pmc*2_1	Fractional coordinate			Biso(Å^2)
Atomic Label	Wickoff site	x	y	z	
Ag3	2a	0	0.7295(10)	0.2855(13)	1.108(7)
Ag1	4c	0.7504(9)	0.7454(10)	0.2663(13)	1.108(7)
Ag2	2b	0.5	0.7485(10)	0.2521(13)	1.108(7)
Nb2	4c	0.1254(5)	0.2412(10)	0.2717(11)	0.61(3)

Nb1	4c	0.6256(5)	0.7502(10)	0.7302(11)	0.61(3)
O5	2a	0	0.2110(14)	0.240(2)	0.93(2)
O1	4c	0.7504(13)	0.6895(14)	0.761(2)	0.93(2)
O2	2b	0.5	0.8021(14)	0.783(2)	0.93(2)
O6	4c	0.1391(3)	0.0309(5)	-0.0192(18)	0.93(2)
O7	4c	0.1144(3)	0.4721(5)	0.5297(18)	0.93(2)
O4	4c	0.6391(3)	0.0327(5)	0.5521(18)	0.93(2)
O3	4c	0.6086(3)	0.5367(5)	0.4760(18)	0.93(2)

Table S5. Refined crystal parameters of neutron powder diffraction data for 97%AgNbO$_3$-3%LiTaO$_3$ at room temperature.

Space group	$Pmc2_1$	Fractional coordinate			Biso(Å^2)
Atomic label	Wickoff site	x	y	z	
Ag3/Li3	2a	0	0.733(2)	0.284(2)	1.09(5)
Ag1/Li1	4c	0.7533(9)	0.750(2)	0.2651(18)	1.09(5)
Ag2/Li2	2b	0.5	0.751(2)	0.256(2)	1.09(5)
Nb2/Ta2	4c	0.1244(8)	0.2394(10)	0.2722(15)	0.56(3)
Nb1/Ta1	4c	0.6277(8)	0.7537(10)	0.7303(15)	0.56(3)
O5	2a	0	0.1909(17)	0.235(3)	1.05(2)
O1	4c	0.7505(10)	0.6992(17)	0.752(3)	1.05(2)
O2	2b	0.5	0.8055(17)	0.776(2)	1.05(2)
O6	4c	0.1401(7)	0.02725	-0.014(2)	1.05(2)
O7	4c	0.1140(7)	0.47881	0.528(2)	1.05(2)
O4	4c	0.6391(7)	0.03597	0.554(2)	1.05(2)
O3	4c	0.6080(7)	0.53691	0.478(2)	1.05(2)

Table S6. Refined crystal parameters of neutron powder diffraction data for 95.5%AgNbO$_3$-4.5%LiTaO$_3$ at room temperature.

Space group	$Pmc2_1$	Fractional coordinate			Biso(Å^2)
Atomic label	Wickoff site	x	y	z	
Ag3/Li3	2a	0	0.732(2)	0.283(1)	0.92(3)
Ag1/Li1	4c	0.752(1)	0.752(2)	0.2644(16)	0.92(3)
Ag2/Li2	2b	0.5	0.758(2)	0.258(2)	0.92(3)
Nb2/Ta2	4c	0.1260(8)	0.2382(11)	0.2686(17)	0.45(2)
Nb1/Ta1	4c	0.6282(9)	0.7529(11)	0.7288(17)	0.45(2)
O5	2a	0	0.1902(19)	0.226(3)	0.974(18)
O1	4c	0.7509(11)	0.6949(19)	0.74979	0.974(18)
O2	2b	0.5	0.8118(19)	0.774(3)	0.974(18)
O6	4c	0.1405(9)	0.0225(18)	-0.010(2)	0.974(18)
O7	4c	0.1152(9)	0.4773(18)	0.529(2)	0.974(18)
O4	4c	0.6410(9)	0.0390(18)	0.556(2)	0.974(18)

O3	4c	0.6087(9)	0.5341(18)	0.480(2)	0.974(18)

Table S7. Refined crystal parameters of neutron powder diffraction data for 94.7%$AgNbO_3$-5.3%$LiTaO_3$ at room temperature.

Space group	$Pmc2_1$	Fractional coordinate			Biso(Å^2)
Atomic label	Wickoff site	x	y	z	
Ag3/Li3	2a	0	0.739(2)	0.2836(12)	1.00(4)
Ag1/Li1	4c	0.7545(18)	0.762(2)	0.264(1)	1.00(4)
Ag2/Li2	2b	0.5	0.7614(9)	0.2590(12)	1.00(4)
Nb2/Ta2	4c	0.1256(3)	0.2458(12)	0.2666(12)	0.81(2)
Nb1/Ta1	4c	0.6283(3)	0.7461(11)	0.7253(12)	0.81(2)
O5	2a	0	0.1883(6)	0.230(3)	1.254(18)
O1	4c	0.7482(10)	0.7033(6)	0.748(3)	1.254(18)
O2	2b	0.5	0.8272(6)	0.765(3)	1.254(18)
O6	4c	0.1380(3)	0.0202(6)	-0.017(3)	1.254(18)
O7	4c	0.1113(3)	0.4801(6)	0.525(3)	1.254(18)
O4	4c	0.6385(3)	0.0394(6)	0.543(3)	1.254(18)
O3	4c	0.6086(3)	0.5341(6)	0.472(3)	1.254(18)
Space group	$R3c$	Fractional coordinate			Biso(Å^2)
Atomic label	Wickoff site	x	y	z	
Ag1/Li1	6a	0	0	0.3253	1.00(4)
Nb1/Ta1	6a	0	0	0.0838(10)	0.81(2)
O1	18b	0.5726(17)	1.0265(19)	0.3163(8)	1.254(18)

Table S8. Refined crystal parameters of neutron powder diffraction data for 94%$AgNbO_3$-6%$LiTaO_3$ at room temperature.

Space group	$Pmc2_1$	Fractional coordinate			Biso(Å^2)
Atomic label	Wickoff site	x	y	z	
Ag3/Li3	2a	0	0.741(3)	0.2899(18)	1.02(3)
Ag1/Li1	4c	0.750(2)	0.746(3)	0.2542(18)	1.02(3)
Ag2/Li2	2b	0.5	0.756(3)	0.2721(18)	1.02(3)
Nb2/Ta2	4c	0.1233(18)	0.245(2)	0.251(3)	0.62(2)
Nb1/Ta1	4c	0.6235(18)	0.747(2)	0.728(3)	0.62(2)
O5	2a	0	0.225(2)	0.243(3)	1.1490(6)
O1	4c	0.7504(10)	0.688(2)	0.748(2)	1.1490(6)
O2	2b	0.5	0.790(2)	0.772(2)	1.1490(6)
O6	4c	0.1387(7)	0.0088(15)	-0.002(3)	1.1490(6)
O7	4c	0.1096(7)	0.4833(15)	0.523(3)	1.1490(6)
O4	4c	0.6387(7)	0.0226(15)	0.534(3)	1.1490(6)
O3	4c	0.6042(7)	0.5258(15)	0.473(3)	1.1490(6)
Space group	$R3c$	Fractional coordinate			Biso(Å^2)

Atomic label	Wickoff site	x	y	z	
Ag1/Li1	6a	0	0	0.3253	1.02(3)
Nb1/Ta1	6a	0	0	0.0811(6)	0.62(2)
O1	18b	0.5659(10)	1.0086(9)	0.3175(5)	1.1490(6)

Table S9. Refined crystal parameters of neutron powder diffraction data for 91%$AgNbO_3$-9%$LiTaO_3$ at room temperature.

Space group	$Pmc2_1$	Fractional coordinate			Biso(Å^2)
Atomic label	Wickoff site	x	y	z	
Ag3/Li3	2a	0	0.754(3)	0.251(3)	0.77(6)
Ag1/Li1	4c	0.749(2)	0.749(3)	0.287(2)	0.77(6)
Ag2/Li2	2b	0.5	0.769(3)	0.245(2)	0.77(6)
Nb2/Ta2	4c	0.1248(12)	0.243(1)	0.243(3)	0.79(4)
Nb1/Ta1	4c	0.6284(12)	0.749(1)	0.762(3)	0.79(4)
O5	2a	0	0.183(2)	0.230(3)	1.26(3)
O1	4c	0.7505(10)	0.723(2)	0.732(3)	1.26(3)
O2	2b	0.5	0.800(2)	0.736(3)	1.26(3)
O6	4c	0.141(1)	0.023(2)	-0.022(3)	1.26(3)
O7	4c	0.110(1)	0.485(2)	0.528(3)	1.26(3)
O4	4c	0.643(1)	0.0088(17)	0.510(3)	1.26(3)
O3	4c	0.610(1)	0.4963(17)	0.499(3)	1.26(3)
Space group	$R3c$	Fractional coordinate			Biso(Å^2)
Atomic label	Wickoff site	x	y	z	
Ag1/Li1	6a	0	0	0.3253	0.77(6)
Nb1/Ta1	6a	0	0	0.0848(8)	0.79(4)
O1	18b	0.5687(6)	1.010(1)	0.3200(7)	1.26(3)

Supporting information 4: Experimental

Polycrystalline ceramic samples were synthesized by a conventional solid-state reaction. Raw metal oxides, Ag_2O (99.7%), Nb_2O_5 (99.99%), Li_2CO_3 (99.5%), Ta_2O_5 (99.99%) were weighed according to the nominal formula of $(1-x)AgNbO_3$-$xLiTaO_3$ (ANLT*x,* where *x*=0, 3, 4.5, 5.3, 6 and 9 mole%) and ball-milled in ethanol for 12 hours. After drying, the mixtures were put into alumina porcelain boats and calcined at 850~950 °C for 4 hours in oxygen atmosphere with a hearting rate of 5 ºC/min. The resultant powders were ball-milled again for 4 hours in ethanol medium. After drying, the powders were mixed with 5 wt% polyvinyl alcohol (PVA) solution and pressed into pellets with a diameter of 15 mm and thickness of 1~2 mm under 400 MPa uniaxial pressure. These pellets were heat-treated at 600 °C for 2 hours to burn out PVA, and then finally sintered at 1060~1120°C for 6 hours in oxygen atmosphere, followed a cooling process with a speed of 5 ºC/min down to 500 ºC and natural cooling to room temperature in oxygen atmosphere. The resultant ceramic pellets are bright yellow. All the samples possess a higher relative density than 97%.

The neutron diffraction patterns were collected at a wavelength of 1.635 Å using WOMBAT, the high-intensity powder diffractometer at the Australian Nuclear Science and Technology Organisation (ANSTO). The neutron diffraction set-up is same as the previous description. The ANLT100x samples were fixed at the centre stage and rotated around the vertical axis by a step size of 15°. In order to minimize the effect of the texture, the total 13 patterns were added together to produce the diffraction patterns presented hereafter.

For electrical property measurement, the silver electrode was made on both the surfaces of the ceramic pellets. The temperature-dependent dielectric spectra were collected during the heating process by an LCR meter (Agilent E4980A, Agilent Technologies, Penang, Malaysia) that is connected to a computer-controlled temperature chamber. For polarization-electric field (*P-E*) hysteresis loop, gold electrodes were sputtered on the two main surfaces of annealed specimens for 3 minutes. The measurement was carried out using a ferroelectric measurement system (TF Analyzer 2000, Aachen, Germany).

3.5 Ferroelectric Wake-up Effect and Underlying Mechanism Observed in $AgNbO_3$-based Antiferroelectric Materials

The research presented in this manuscript was mainly completed by the author of this thesis. The author planned the study and applied the neutron beam time grant at ANSTO. The electron diffractions patterns were collected by Prof. Ray Withers. The author independently conducted the structural, properties analyses and wrote the manuscript. The draft will be submitted to a peer-reviewed journal *Chemistry of Materials*.

Introduction

Polar functional materials, especially ferroelectric/antiferroelectric (FE/AFE) materials, have been developed for a wide range of applications, *e.g.*, as the capacitors, sensors and energy storage devices.[1-6] Lead-containing AFE/FE materials have historically attracted tremendous attention and been predominant in commercial applications.[7-8] However, the toxicity of lead oxide becomes a big concern and hence leads to an urgent search for alternative lead-free, AFE/FE materials.[9-12] Among many potential candidates, silver niobate ($AgNbO_3$) is regarded as the promising one due to its special properties.

$AgNbO_3$ (AN) exhibits a double polarisation-electric field (*P-E*) hysteresis loop at room temperature, characteristic of the AFE materials. In order to comply with the antiferroelectricity, a perovskite-related, *Pbcm* structure has been assigned to AN, although there is some controversies on the exact space group.[13-16] The presence of antiferroelectricity combined with a large induced polarization (52 $\mu C/cm^2$)[17] endows AN with promising energy storage density (2.1 J/cm^3 for AN, 2.5 J/cm^3 for 0.1 wt % Mn-doped AN, 2.6 J/cm^3 for Bi-doped AN ceramics and 4.2 J/cm^3 for $Ag(Ta, Nb)O_3$ solid solutions) capabilities.[18-21] In addition to enhance the antiferroelectricity, the properties of AN can be tuned from AFE to FE by chemical modifications with Li^+.[22-23] The Li-doped AN single crystal was reported to exhibit a relatively high piezoelectric coefficient d_{33} = 210 pC/N with a high Curie temperature, T_C = 548 K, favouring various applications operating at high temperature.[24]

As the material component parts in real electrical/electronic devices, FE/AFE materials are subject to electrical loading and cycling. High-field stress cycling will inevitably impact their properties, especially the remnant polarization (P_r) of FE materials.[2] In addition to the well-known fatigue effect, *i.e.* E-field cycling decreasing P_r, a wake-up effect, corresponding to an increase in P_r with increased electrical cycling, has recently attracted much attention. The possible mechanisms for wake-up effects are attributed to the activation/diffusion of defects in the material, as observed in novel HfO2-related thin film FE materials and the traditional FE materials such as lead zirconate titanate (PZT).[25-30] In this paper, we report a FE wake-up effect in polycrystalline $LiTaO_3$-

doped $AgNbO_3$, apparent in polarization-electric field (*P-E*) hysteresis measurements. Temperature-dependent dielectric spectra and neutron powder diffraction (NPD) illustrate that the observed wake-up effect is a direct consequence of the AFE-to-FE phase transition. With the assistance of electron diffraction and piezoresponse force microscopy (PFM) techniques, the corresponding local structure/s and domain switching behaviour were further investigated. This sheds further insights on the origin of the wake-up effects from a local perspective. Finally, a physical picture is depicted for this field cycling induced phase transition. The studies strongly suggest this wake-up effect is universal for AFE perovskite-based materials with complex octahedral rotation patterns.

2. Experimental

2.1 Sample preparation. The $(1-x)AgNbO_3$-$xLiTaO_3$ ($x = 0.045$ and 0.060, denoted as AN45LT and AN60LT hereafter) ceramic samples were synthesized by traditional solid state reaction method. The raw oxide materials, Ag_2O (99.7%), Nb_2O_5 (99.99%), Li_2CO_3 (99.5%) and Ta_2O_5 (99.99%), were first mixed and then ball milled in ethanol for 12 hours. After removal of the ethanol (via gentle baking in an oven), the mixtures were then calcined at 850 ~ 950 °C for 4 hours in an oxygen atmosphere at a heating rate of 5 ºC/min. The resultant powders were then ball-milled again for 4 hours in an ethanol medium. After mixing with a 5 wt % polyvinyl alcohol (PVA) solution, the resultant powders were pressed into pellets (diameter of 15 mm, thickness 1~2 mm) under 400 MPa uniaxial pressure. After removing the PVA via heating at 600 °C for 2 hours, the pellets were sintered at 1060 ~ 1120°C for 6 hours in an oxygen atmosphere, followed by cooling down to 500 ºC at a speed of 5 ºC/min and then natural cooling to room temperature in an oxygen atmosphere. Finally, the resultant ceramic pellets were cut into small pieces and prepared for neutron diffraction experiments and electrical properties measurements.

2.2 Structural Characterizations. NPD patterns were collected at a wavelength of 1.635 Å using WOMBAT, the high-intensity powder diffractometer at the Australian Nuclear Science and Technology Organisation (ANSTO). The neutron diffraction set-up used is the same as given earlier.[31-32] Both pristine samples as well as the samples after electric-field cycling were attached to a sample stage and rotated around the vertical axis using in a step size of 15°. In order to minimize the effect of texture, orientation-dependent NPD patters were integrated to produce the NPD patterns as presented below. Powder samples were dispersed in n-butanol and then deposited onto lacy carbon coated grids which are suitable for the transmission electron microscopy (TEM) studies. Electron diffraction patterns (EDPs) were collected using a JEOL 2100 TEM operating at 300 kV.

2.3 Properties measurements. For dielectric and ferroelectric characterization, silver paste was firstly coated onto the pellets and then heated up to 550°C for 30 min to ensure good electrical contact. The temperature-dependent dielectric constants were then measured from 10 K to 470 K in the frequency range of 100 - 200 kHz with a precision LCR meter (Agilent, 4980A). The *P-E* hysteresis loop measurements and electric-field cycling were performed with an aixACCT TF 2000 FE analyser. PFM investigations were performed under ambient conditions on a commercial AFM system (Cypher, Asylum Research) with Pt/Ir coated conductive tips (Asylum01, spring constant ~ 2 N/m). For local poling studies, an internal high voltage amplifier was used to provide a bias of 20 V on the tip.

3. Results and discussion:

3.1 Electrical properties of the AN45LT and AN60LT samples

The *P-E* hysteresis loops of AN45LT and AN60LT measured at different cycles and E-field amplitudes are shown in Figure S1, which provides sufficient evidence that the pristine state of either AN45LT or AN60LT contains AFE nature. Figure 1 presents the evolution of the P_r and *P-E* hysteresis loops of a pristine AN45LT and AN60LT samples under a bipolar cycling. As the E-field is progressively cycled up and down, the P_r increases gradually, which signifies the FE wake-up effects phenomenally. Previously, the wake-up effect is commonly observed in doped $Pb(Zr,Ti)O_3$ and HfO_2 thin films, whose pristine constricted *P-E* hysteresis loops open as the E-field is progressively cycled.[30, 33-35] Interestingly, the pristine *P-E* hysteresis loops of ANLT samples behave like lossy dielectrics with tiny induced and remnant polarizations. Cyclic switching unambiguously changes the profile of the *P-E* hysteresis loops from the initial lossy dielectrics to the typical ferroelectrics. The different behaviour during the wake-up process suggests the wake-up mechanisms in doped $Pb(Zr,Ti)O_3$ and HfO_2 thin films are unlikely applicable to the ANLT samples.

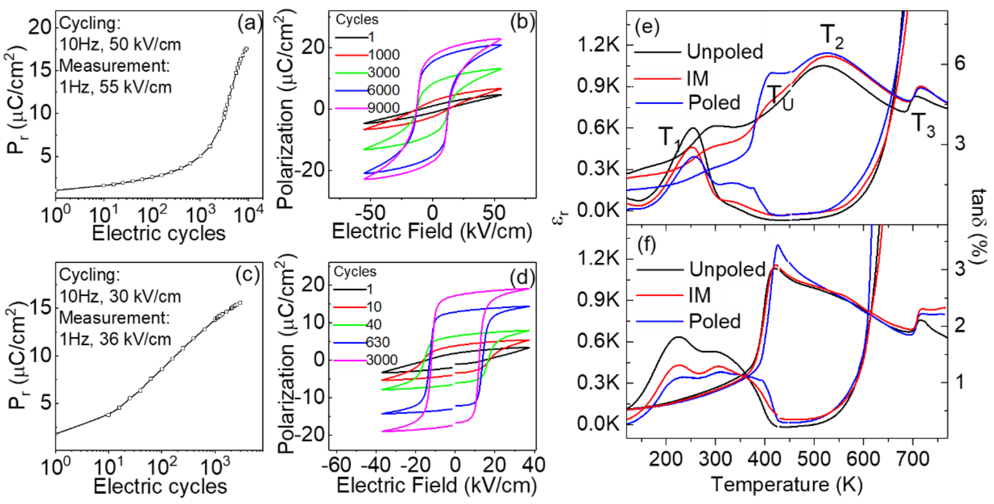

Figure 1. The evolution of P_r and *P-E* hysteresis loops of AN45LT ((a) and (b)) and AN60LT ((c) and (d)) with increasing the E-field cycles. Temperature-dependent dielectric constant and loss of (e)AN45LT and (f)AN60LT samples

To better understand the underlying mechanisms contributing to the FE wake-up effects, three states (Unpoled, Intermediate (IM) and Poled) of both samples were selected for further investigations. The Poled state corresponds to that with 9000 and 3000 electric cycles treatment for AN45LT sample and AN60LT sample, respectively. The IM state represents that with 3000 cycles treatment having $P_r \sim 6$ μC/cm^2 for the AN45LT sample and with 40 cycles treatment having $P_r \sim 8$ μC/cm^2) for the AN60LT sample. Figure 1e and f shows the dielectric properties of AN45LT and AN60LT over the temperature range from 120 to 780 K. The dielectric behaviour of Unpoled AN45LT is almost identical to that of pure $AgNbO_3$,[36] containing three detectable anomalies (T_1, T_2 and T_3) in the dielectric constant and/or the dielectric loss during heating.[36] After AN45LT is triggered into the IM state, an additional dielectric peak appears around 400 K (T_U) while the dielectric constant of T_1 peak decreases. In the Poled state, the dielectric constant anomaly related to T_U becomes sharper and the T_1 dielectric peak further diminishes to be barely observable. Similar trends are also apparent in the dielectric loss behaviour, *e.g.*, the dielectric loss peak around T_1 declines from Unpoled to Poled states. By contrast, the temperature-dependent dielectric spectra of Unpoled AN60LT is quite different from that observed in pure $AgNbO_3$ and shares similarities with the 6% Li^+-doped $AgNbO_3$ ceramic previously reported.[22] Although the T_1-related dielectric anomaly is hardly observed, the dielectric loss still contains a strong response around 260 K. In the high temperature range, the T_U-related dielectric constant peak is sharp while the broad dielectric peak (T_2) barely exists. Accompanied with the enhanced ferroelectricity, the dielectric response related to the pure $AgNbO_3$ (T_1 peak) becomes weaker, as is seen in the decrease in dielectric loss. In contrast, the dielectric anomaly around T_U grows from Unpoled to Poled states. Fu *et al.*[22, 24] suggested that the sharp dielectric anomaly occurring around T_U can be ascribed to the appearance of a rhombohedral FE phase in the Li-doped $AgNbO_3$. If this assumption is also applicable to the ANLT materials system, we can deduce that applied field cycling can induce the rhombohedral FE phase in both AN45LT and AN60LT.

3.2 Neutron diffraction

The room temperature crystal structures of Unpoled, IM and Poled AN45LT and AN60LT samples were determined by neutron powder diffraction (NPD) (see Figures 2 and 3). Instead of a conventional coordinates Rietveld refinement, symmetry-mode refinement was applied by using software Fullprof and ISODISTORT.[37-38] The details of the symmetry-mode decomposition are shown in the supporting information, and all the nomination follows Ref 39.[39] As corroborated by its dielectric properties that closely resemble pure $AgNbO_3$, the NPD pattern of Unpoled AN45LT was refined with respect to the $Pmc2_1$ space group (Figure 2a). Using this starting structure, a good refinement can be obtained for AN45LT. The selected reflections are indexed by the pseudo-cubic $Pm\text{-}3m$, perovskite structure (subscript p). For IM AN45LT sample, the single $Pmc2_1$ phase cannot model the experimental data, instead, as a small shoulder at the low angle region of the $\langle 1\ 1\ 1\rangle_p^*$ peaks cannot be predicted. Compared with the pattern of Unpoled AN45LT, the intensity ratio of the $1/4\langle 6\ 2\ 1\rangle_p^*/1/2\langle 3\ 1\ 1\rangle_p^*$ in IM AN45LT undergoes a reduction. For Poled AN45LT, the NPD pattern exhibits a distinct change. The $\mathbf{G}_p \pm [{}^1\!/_2\ {}^1\!/_2\ {}^1\!/_4]_p^*$ and the $\mathbf{G}_p \pm [0\ 0\ {}^1\!/_4]_p^*$ satellite reflections are barely observed. Besides satellite reflections, it is noticeable that the small shoulder perceived at the lower 2θ angle of $\langle 1\ 1\ 1\rangle_p^*$ reflections in IM AN45LT develops as one strong peak.

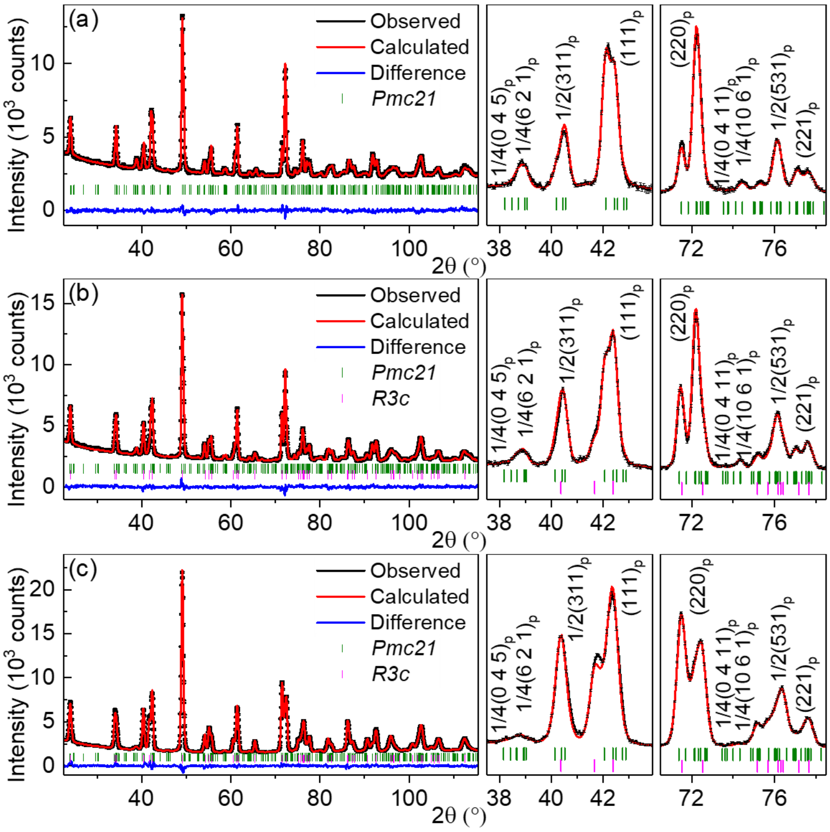

Figure 2. Rietveld refinement of NPD data of the (a) Unpoled, (b) IM and (c) Poled AN45LT at room temperature. The right parts of figures are the enlargement of the selected angles.

Comparing the NPD patterns of the three states, the systematic decreasing intensities of the peaks associated with the H2 and Λ3 modes, *i.e.*, $\mathbf{G}_p \pm [{}^1/_2\,{}^1/_2\,{}^1/_4]_p^*$ and the $\mathbf{G}_p \pm [0\ 0\ {}^1/_4]_p^*$ reflections and increasing intensities of the small shoulder for $<1\ 1\ 1>_p^*$ peaks suggest the continuous structural variation during the wake-up, in accordance with the dielectric properties. As assumed in the previous section, the appearance of the T_U-related dielectric peak is ascribed to the $R3c$ phase. Therefore, for IM AN45LT and Poled AN45LT NPD patterns, a ($Pmc2_1$ + $R3c$) two phase model were found to achieve good refinement of the observed data (Figure 2b and c). The conventional atomic positions of the refinement are shown in the supporting information 3. Note that there is a small divergence between the observed and calculated $<1\ 1\ 1>_p^*$ reflections in the data of Poled AN45LT, which possibly arises from the preferred orientation in Poled sample.

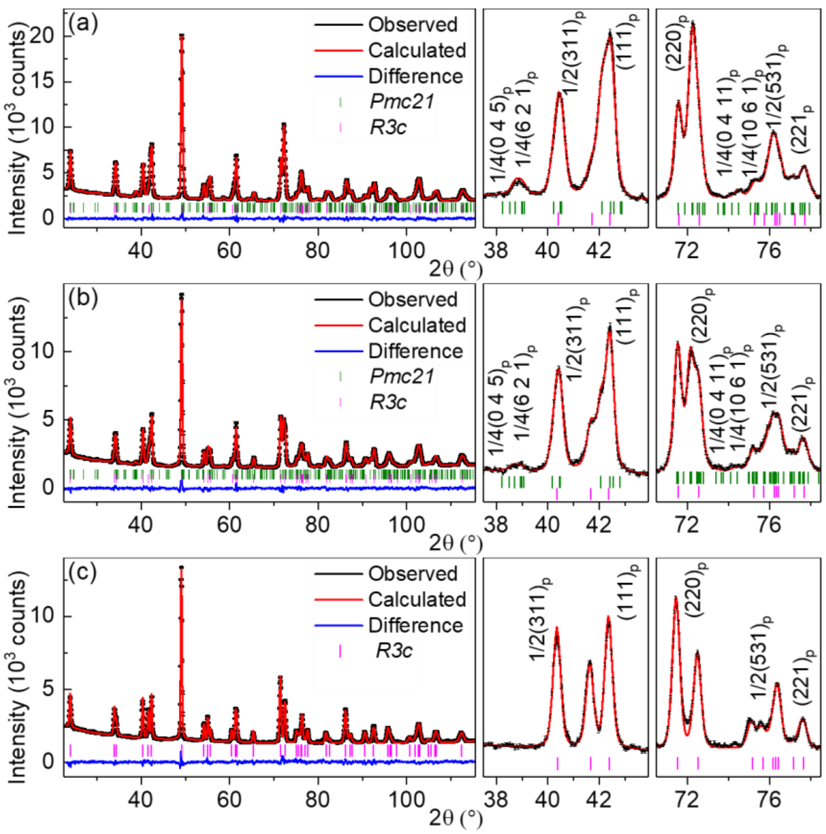

Figure 3. Rietveld refinement of NPD data of (a) Unpoled, (b) IM and (c) Poled AN60LT at room temperature. The right parts of the figures are the enlargement of the selected angles.

Figure 3a shows the NPD pattern of Unpoled AN60LT. The unambiguous H4 and Λ3 modes related satellite reflections conform with the orthorhombic structure while the small shoulder observed at the low angle side of $<1\ 1\ 1>_p^*$ peak is in agreement with the rhombohedral distortion. The $Pmc2_1$ + $R3c$ two-phase model are acceptably applied to Unpoled AN60LT sample. For IM AN60LT, two-phase model is also applied for the refinement (Figure 3b). Apparently, the intensities of the $R3c$ phase associated peaks raise while those related to the $Pmc2_1$ phase, especially for the H2 and Λ3 modes related satellite reflections, drop, suggesting that the field-cycling can adjust the phase fraction between $Pmc2_1$ and $R3c$ phases. After tuning the sample into the poled state (Figure 3c), the $\mathbf{G}_p \pm [^1/_2\ ^1/_2\ ^1/_4]_p^*$ and the $\mathbf{G}_p \pm [0\ 0\ ^1/_4]_p^*$ satellite reflections become barely visible and $<1\ 1\ 1>_p^*$ and $<2\ 2\ 0>_p^*$ peaks change to two clearly split peaks. Note that, the centre parts of the $<2\ 2\ 0>_p^*$ peaks for Poled AN60LT are not well fitted, one possible reason is that Poled AN60LT may contain some trace of orthorhombic phase (*cf.* the $<2\ 2\ 0>_p^*$ peak intensities in Unpoled AN45LT). Even though, the single $R3c$ phase model yields reasonably good results (Table S3).

Figure 4 shows the essential information obtained from the refinement analyses. AN45LT does not present evident change in terms of the unit-cell parameters for both *Pmc*2_1 and *R*3*c* phases; however, the increase of the *R*3*c* phase fraction are unambiguous during the wake-up process. For AN60LT sample, the unit-cell parameters for *Pmc*2_1 phase increase, especially for the *a*-axis from Unpoled to IM state. The rise of the *R*3*c* phase fraction is also evident during the wake-up process. Therefore, the FE wake-up effects observed in AN45LT and AN60LT have close relationship with the increment of *R*3*c* phase fraction, which consequently influences the ferroelectricity and T_U-related dielectric peak. Figure 4c presents the global amplitude ($A\tau$) of the main modes for both *Pmc*2_1 and *R*3*c* phases in the three states of AN45LT and AN60LT. The symmetry decomposition of *R*3*c* phase has been conducted through ISODISTORT suite[37] with respect to the 5-atoms pseudo-cubic perovskite structure with *Pm*-3*m* space group. The distorted *R*3*c* structure is mainly dominated by two modes:1) Γ4- mode denoting the atomic displacements along the $[1\ 1\ 1]_p$ direction, leading to the FE spontaneous polarisation; and 2) R4+ mode which is related to the antiphase octahedral rotation along the $[1\ 1\ 1]_p$ direction, *i.e.*, $a^-a^-a^-$ octahedral titling. The details of the symmetry mode decomposition in *Pmc*2_1 are listed in supporting information. The distorted modes can be basically divided into two types, the octahedral rotation (T4+ and H2 modes in *Pmc*2_1 phase, R4+ in *R*3*c* phase) and ionic displacements (Γ4-, Λ3 modes). As shown in figure 4c, for the octahedral rotation modes, the amplitude for nearly all rotation modes for AN45LT samples remain almost unchanged from Unpoled to Poled state in both *Pmc*2_1 and *R*3*c* phases, except for the H2 mode showing a systematic decrease in amplitude. For AN60LT, the amplitudes of both T4+ mode in *Pmc*2_1 phase and R4+ mode in *R*3*c* phase exhibit systematic reduction during the wake-up process. From average structural point of view, the decreasing amplitudes of the octahedral rotation modes suggest the decrease of the tilting angles between the adjacent NbO_6 octahedra, which in turns induces the expansion of the related axes.

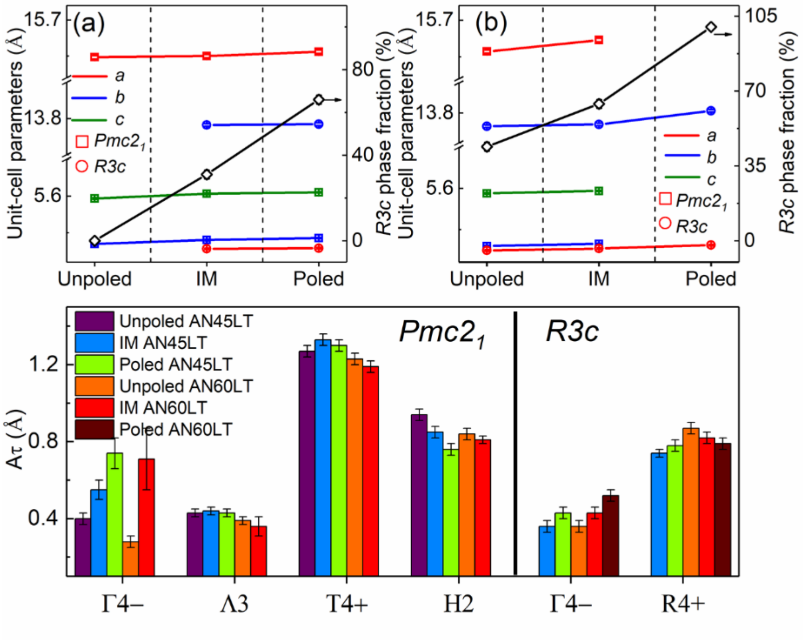

Figure 4. Unit-cell parameters and *R*3*c* phase fractions of three states sample for both (a) AN45LT and (b) AN60LT.

As aforementioned, the Γ4- mode determines samples' ferroelectricity. It is worthy to note that although the *Pmc*2_1 space group was adopted for Rietveld refinement as being in conformity with the weak ferroelectricity in $AgNbO_3$, the powder diffraction is not an effective way to quantitatively analyse its Γ4- mode, especially under the dominance of the additional phase. Moreover, under the cyclic switching, the FE *R*3*c* phase dominates the sample. Therefore, the atomic displacements associated with Γ4- mode of the *R*3*c* (hexagonal setting) phase were plot in Figure 5 (the *z*-coordinates of the oxygen is fixed). The increasing displacements of dAg_R and dNb_R directly lead to the enlargement of the spontaneous polarisation, thereby enhancing the ferroelectricity.

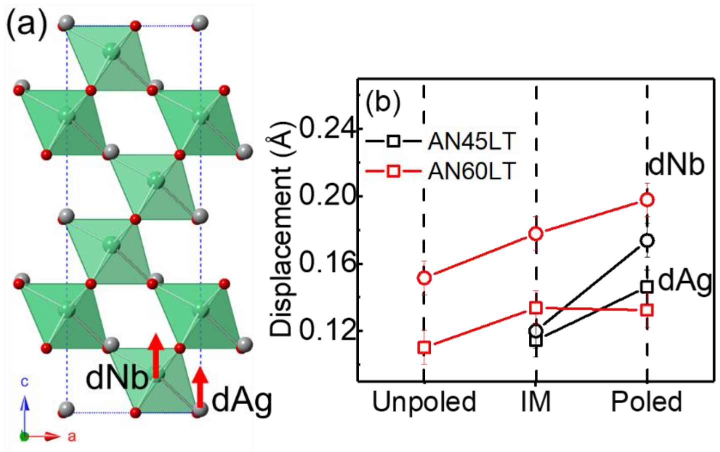

Figure 5. (a) The distorted structure induced by Γ4- mode for *R*3*c* phases viewed along *b*-axis. (b) The displacements associated with the Γ4- mode in *R*3*c* phases.

3.3 Electron diffraction

Figure 6a shows a typical <001>$_p$ zone axis EDP of the AN45LT sample. All indexes are based on the pseudo-cubic perovskite structure. In addition to a well-defined set of parent perovskite Bragg reflections $\mathbf{G_p}$, the unambiguous appearance of the $\mathbf{G}_p$ ± [1/2 1/2 0]$_p$* satellite reflections are well in accordance with the Y2+ mode in distorted $AgNbO_3$ structure with *Pmc*2$_1$ symmetry. Other weak reflections are obtained at the first order Laue zone (FOLZ). The reflections (as shown by the arrow) are indexed as [1, 8, 1/4]$_p$*, *i.e.*, the $\mathbf{G}_p$ ± [0 0 1/4]$_p$* satellite reflections, associated with the Λ3 mode. Another typical satellite reflections, $\mathbf{G_p}$ ± [1/2 1/2 1/4]$_p$*, involved in the large amplitude mode, H2, are also observable (Figure 6b). Figure 6c displays the <1 -2 1>$_p$, zone axis EDPs, respectively. The $\mathbf{G_p}$ ± [1/2 1/2 1/2]$_p$* type satellite reflections present strong intensities, which are in accordance with NPD patterns. It is evident that the broaden diffuse streaking runs along <2 1 0>$_p$* (the dash-line in Figure 6c) and <3 1 0>$_p$* through all parent perovskite Bragg reflections, forming the {0 0 1}$_p$* diffuse sheets. The appearance of the {0 0 1}$_p$* diffuse sheet is in consistency with the previous investigations on doped $BaTiO_3$, $AgNbO_3$ and Ag(Nb,Ta)O_3,[13, 40-42] suggesting the one dimensional polar chain along the <0 0 1>$_p$ direction in real space. The satellite reflections marked by the white arrow appear only around the higher order $\mathbf{G_p}$, which indicates they are located at the FOLZ. These tiny peaks possibly belong to $\mathbf{G_p}$ ± **a*** (where **a*** ≡ ¼ [001]$_p$* for the pure $AgNbO_3$ structure). All of the abovementioned diffractions are in accordance with the pure $AgNbO_3$, *i.e.*, the structure of *Pmc*2$_1$ phase. With further tilting the crystal close to <1 -3 1>$_p$ zone axis (Figure 6d), 1/6<3 2 3>$_p$* which can be indexed as 1/6[3 3 2]$_p$* reflections as considering the twinning structure, are observed. Similarly to the $\mathbf{G}_p$ ± [1/2 1/2 1/4]$_p$* reflections, the appearance of the $\mathbf{G}_p$ ± [1/2 1/2 1/3]$_p$* can be regarded as the soften phonon mode associated with the modulation wave vector, [1/2 1/2 1/3]$_p$*, located at the H line in the first Brillouin zone of the parent *Ammm* structure, resulting in the new octahedral twist form, which has also been reported in $NaNbO_3$ and Li-doped $AgNbO_3$ material systems.[23, 43] Besides the new octahedral twist system, tiny peaks associated with $\mathbf{G_p}$ ± **a*** are still visible at FOLZ. According to previous results,[43-45] the variation of the octahedral tilting around c_p-axis (H2 mode) induces the change of the mode ($\Lambda 3$ mode) associated with the antiferroelectricity. In Unpoled AN45LT, the octahedral tilting around the c_p-axis has changed its periodicity in local scale, and it is thus not hard to deduce that the $\Lambda 3$ mode also changed correspondingly.

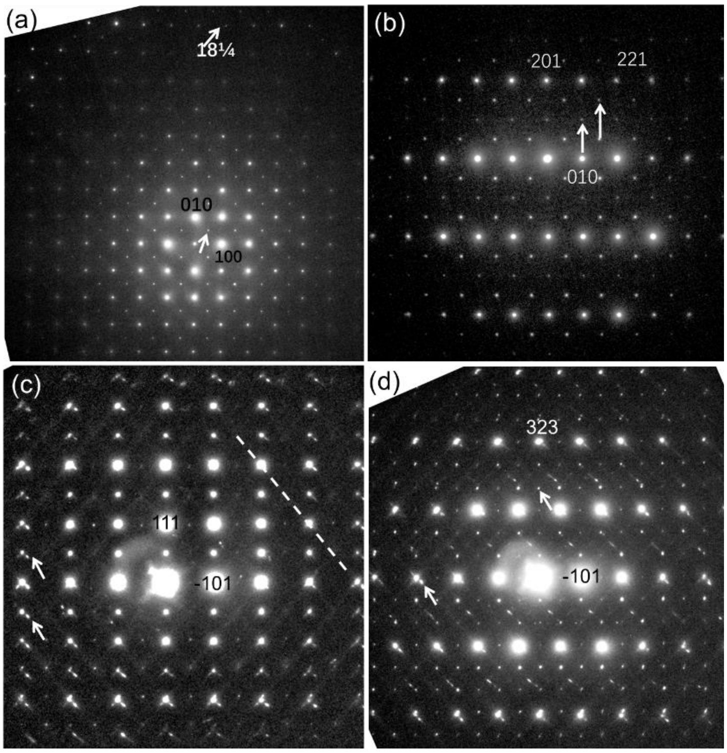

Figure 6. The (a) $\langle 0\ 0\ 1\rangle_p$ (b) $\langle 0\ -1\ 2\rangle_p$ (c) $\langle 1\ -2\ 1\rangle_p$ (d) $\langle 1\ -3\ 1\rangle_p$ zone axis electron diffraction patterns of AN45LT at room temperature

Figure 7 shows the selected area EDPs of AN60LT at room temperature, showing systematic tiling along the $[0\ 1\ -1]_p^*$ direction. Similarly to AN45LT, the transverse polarised diffuse streaking along the $\mathbf{G_p} \pm \langle h\ k\ 0\rangle_p^*$, forms the $\{0\ 0\ 1\}_p^*$ diffuse sheets which arise from correlated longitudinal motions of ions along the $\langle 001\rangle_p$ real space direction. In addition to the $\mathbf{G_p} \pm [1/2\ \ 1/2\ \ 1/2]_p^*$ reflections which is related to the octahedral rotation, a series of satellite reflections, $\mathbf{G_p} \pm [1/n\ 1/2\ 1/2]_p^*$ (here, n = 3, 4 and 5) are obtained in Figure 7b, c and d. Note that the intensities of these reflections are quite weak in the centre, *e.g.*, $[1/3\ \ 1/2\ \ 1/2]_p^*$, $[1/4\ \ 1/2\ \ 1/2]_p^*$ and $[1/5\ \ 1/2\ \ 1/2]_p^*$, and grow stronger as close to the edge (as shown by the white arrows), *i.e.*, alter into stronger $\mathbf{G_p} \pm [1/2\ \ 1/2\ \ 1/2]_p^*$ reflections. These apparent reflections arise from the diffuse streaking at $\mathbf{G}_p \pm [1/2\ 1/2\ 1/2]_p^*$ reflections (Figure 7e) and they can be expressed as $\mathbf{G}_p \pm [1/2\ 1/2\ \xi]_p^*$ (ξ is continuous). When tilting away from the <2 -1 -1> zone axis, the cut-off of this diffuse streaking results in the $\mathbf{G}_p \pm [1/n\ 1/2\ 1/2]$ 'satellite reflections'. This phenomenon is quite similar to previous investigations on the $0.93(Bi_{0.5}Na_{0.5})TiO_3$-$0.07BaTiO_3$ material, which is around the phase boundary between the FE and AFE phases.[32, 46] The unambiguous $\mathbf{G}_p \pm [1/2\ 1/2\ \xi]_p^*$ diffuse streaking suggests the disordered octahedral tilting along the $< 0\ 0\ 1>_p$ direction.

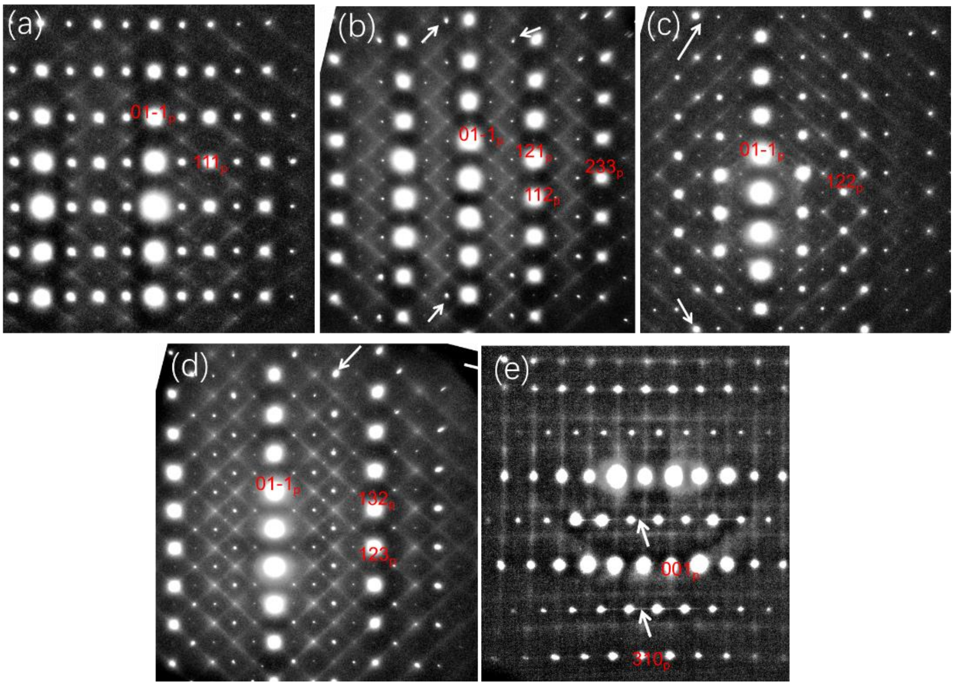

Figure 7. The (a) $<2\ -1\ -1>_p$ (b) $<3\ -1\ -1>_p$ (c) $<4\ -1\ -1>_p$ (d) $<5\ -1\ -1>_p$ (e) $<-1\ 3\ 0>_p$ zone axis electron diffraction patterns of AN60LT at room temperature

Figure 8a shows the distorted structure induced by the H2 and T4+ modes. If considering the two octahedra between the blue dash-lines as one unit. Each unit locally rotates around one of two possible $<1\ 1\ 1>_p$ directions and changes alternatively across the blue dash lines. Within each of these regions, the structure is locally in *R*3*c* symmetry. It is evident that the rotation direction (black arrows) is decided by the H2 mode. EDPs indicates doping $LiTaO_3$ will disrupt the original octahedral rotation around c_p-axis, *i.e.*, $a^0a^0c^-/a^0a^0c^+$ tilting system. Figure 8b draws the first Brillouin zone of the parent *Ammm* structure. It is found in AN45LT, the modulation wave-vector of H2 mode can change from [1/4 1 0]* ($[1/2\ 1/2\ 1/4]_p^*$) to [1/3 1 0] ($[1/2\ 1/2\ 1/3]_p^*$), *i.e.*, the condensation point on the H line is moving towards T point, finally leading to $a^0a^0c^-$ tilting system. The combination between this tilting system and that induced by the T4+ mode results in the *R*3*c* symmetry. According to the relationship between the modulation wave-vectors of H2 and Λ3 modes (details in supporting information) and previous EDP results [23], the wave-vector of the Λ3 mode moves simultaneously towards the zone centre. Intriguingly, Prosandeev *et.al.* [44] have predicted that moving the wave-vector of H2 mode will decrease the energy barrier between the AFE and FE phases by theoretical calculation, and our observation in this work provides experimental evidence to support this hypothesis. Due to the local inhomogeneous, the lower E-field is capable to induce the FE *R*3*c* phase.

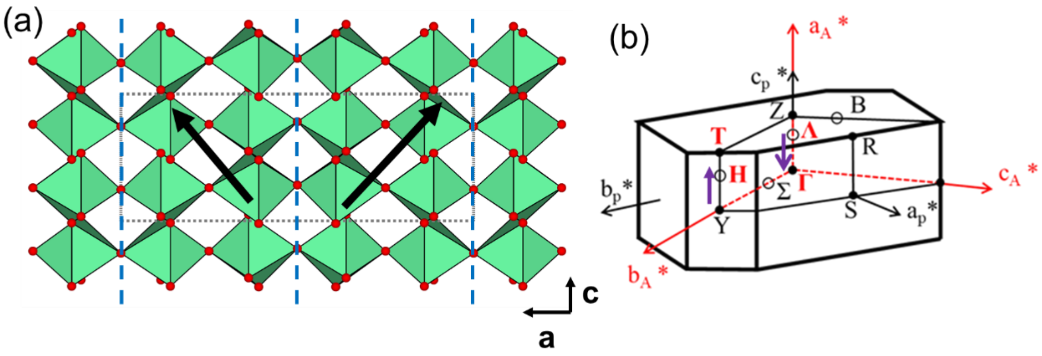

Figure 8. (a) The schematic drawing of the distorted $AgNbO_3$ structure associated with H2 and T4+ modes. (b) The first Brillouin zone of the parent *Ammm* structure.

3.4 Piezoresponse force microscopy

The PFM technique was applied to further investigate the response of the local domain structure to the external field. Here Unpoled AN60LT is studied as it consists of both polar and non-polar regions for characterisation. Figure 9 presents the PFM images acquired in Unpoled AN60LT. As the polishing may induce residual stress which possibly has strong influence on the domain structure,[47] the as-polished sample was heat-treated before PFM measurements. The polished sample is quite flat (Figure S4), excluding the effect of topography on the PFM signals. As shown in Figure 9a, the pristine sample surface contains areas displaying both piezoelectrically active (red and blue regions) and inactive (green regions), in consistency with the NPD analysis showing two phases (non-polar or weak polar *Pmc*2₁ and polar *R*3*c*) coexistence. Additionally, the domain patterns of the area with the strong piezoelectric signal are consistent with those observed in other rhombohedral FEs.[48-50] The 2 × 2 μm^2 non-polar area (area 1) was selected for local poling measurement (Figure 9a and e). After application of -10 V via the tip, part of the region presents positive piezoresponse (Figure 9b and f), indicating the polarisation has been induced and aligned by the tip voltage. The appearance of polarisation in the enlargement area does not have significant impacts on the domain patterns of the large scale (10 × 10 μm^2) region. The same process, *i.e.*, poling the area 1 with -10 V, was repeated for 4 times, and after that the PFM images (Figure 9c and g) display that the regions containing piezoresponse enlarge, indicating the growth of the FE phase during the cycling process, which is in accordance with the macroscopic wake-up effect.

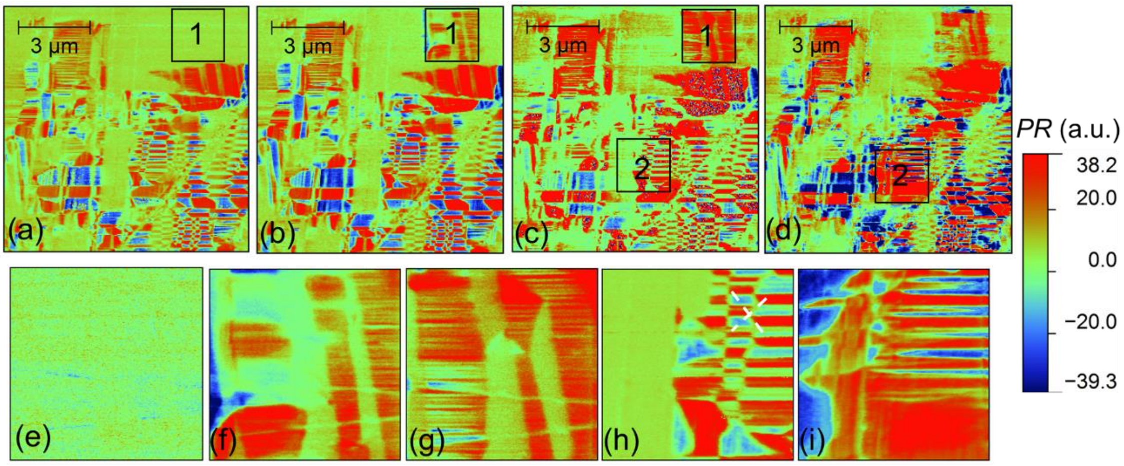

Figure 9. PFM images (*Acosφ* signal) of domain structure in AN60LT. (a) pristine state; (b) after poling selected area 1 with -10V once. (c) After poling selected area 1 with -10V four times. (d) After poling selected area 2 with -10V once. (e), (f) and (g) are the enlargement of the selected area 1 in (a), (b) and (c). (h) and (i) are the enlargement of the selected area 2 in (c) and (d).

The area 2 is the region combing both polar and non-polar characters (Figure 9c and h). It is hard to distinguish the exact boundaries between the polar and non-polar regions from the morphology (Figure S4), suggesting an intergrowth of the $Pmc2_1$ and $R3c$ phases, which is similar to that observed in rare earth-doped $BiFeO_3$ ceramics.[51-52] The parallel and diagonal (indicated by the white dash-lines) domain boundaries are typical characters for the rhombohedral ferroelastic domains (twins), which denotes the 109° and 71° domain walls in $R3c$ phase. With applying -10 V via the tip, the domain patterns exhibit pronounced variation. Most of the polarisation prefers aligning upwards, parallel to the applied field. Additionally, all the pristine non-polar regions show piezoelectric response, indicating the phase transition from AFE to FE phase. After domain switching, some areas show negative piezo-response (blue colour), possibly related to the domain back switching to reduce the electrostatic energy. Clearly, switching the AFE to FE phase is easier in two phases mixture area, which may result from the strain induced by non-180° domain switching in *R*3*c* phase. The phase transition from *Pmc*2_1 to *R*3*c* phase will generate volume expansion, inducing a strong compressive strain around, increasing the energy barrier between the AFE and FE phases and finally stabilizing surrounding AFE phase.[53-56] However, re-orientation of the 109° and 71° domain towards the vertical direction can release the surrounding areas' strain, finally favouring the AFE-FE phase transition under applied field.

3.5 Phase evolution during the field cycling

The underlying mechanism and possible impact factors for the wake-up effects have been developed in the ANLT material systems. It is concluded the variation of the complex in/antiphase octahedral around $<001>_p*$ direction and the local strain are decisive factors for the stabilization of *Pmc*2_1 and *R*3*c* phases. As shown in Figure 10, taking AN45LT as an example, the pristine state contains *Pmc*2_1 phase (light yellow) from average aspects but it is inhomogeneous locally, *i.e.*, the octahedral tilting along the $<001>_p$ direction is not exact ++-- form. As this rotation mode has close relationship with the AFE mode, the disorder of this mode lowers the energy barrier between *Pmc*2_1 and *R*3*c* phases, that is, lower E-field is capable to induce ferroelectric *R*3*c* phase (dark brown). The new local scale FE phases become seeds and under the E-field cycling, the response of the FE seeds to the E-field influences the surrounded AFE regions and the seeds grow up gradually.

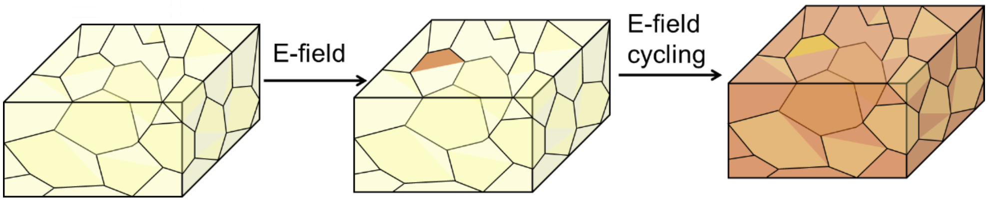

Figure 10. schematic drawing of the phase transition during the ferroelectric wake-up process.

The wake-up effects we discovered in the doped AN material are supposed to be universal when the perovskite, or layered perovskite structure contains complex in/antiphase octahedral rotation, which behaves disordered or inhomogeneous locally. Therefore, it can be predicted that the similar behaviour is possible to be observed for the high temperature $NaNbO_3$, improper ferroelectrics and rare-earth doped $BiFeO_3$.[43, 45, 57-58]

Conclusion

This work firstly discovered the ferroelectric wake-up effects in the $AgNbO_3$-$LaTiO_3$ AFE ceramics. Based on the neutron diffraction and temperature-dependent dielectric spectra analyses, the field-cycling-induced phase transition from $Pmc2_1$ to $R3c$ has been identified as the main driving force for the wake-up effects. The mechanism is quite different from the defect mechanism underlying similar observations in doped PZT and HfO_2 thin films. The local-probes such as EDPs and PFM suggest that the inhomogeneity of the local structures, especially the complex in/antiphase octahedral rotation around $<001>_p*$ direction and local strain states, impacts on the nucleation and growth process of the $R3c$ phase. Our work extends the wake-up effects to AFE materials with the compelling mechanisms and proposes a universal model for the materials with similar structures.

Acknowledgement

TL and YL acknowledge the Australian Research Council (ARC) for financial support in the form of Discovery Project (DP160104780). The authors also thank the Australian Nuclear Science and Technology Organization for support in the form of beam time.

References:

1. Jaffe, B., Antiferroelectric Ceramics with Field-Enforced Transitions: A New Nonlinear Circuit Element. *Proc. IRE* **1961,** *49* (8), 1264-1267.
2. Damjanovic, D., Ferroelectric, Dielectric and Piezoelectric Properties of Ferroelectric Thin Films and Ceramics. *Rep. Prog. Phys.* **1998,** *61* (9), 1267.
3. Haertling, G. H., Ferroelectric Ceramics: History and Technology. *J. Am. Ceram. Soc.* **1999,**

82 (4), 797-818.

4. Tan, X.; Ma, C.; Frederick, J.; Beckman, S.; Webber, K. G., The Antiferroelectric ↔ Ferroelectric Phase Transition in Lead-Containing and Lead-Free Perovskite Ceramics. *J. Am. Ceram. Soc.* **2011,** *94* (12), 4091-4107.

5. Chauhan, A.; Patel, S.; Vaish, R.; Bowen, C. R., Anti-ferroelectric Ceramics for High Energy Density Capacitors. *Materials* **2015,** *8* (12), 8009-8031.

6. Liu, Z.; Chen, X.; Peng, W.; Xu, C.; Dong, X.; Cao, F.; Wang, G., Temperature-Dependent Stability of Energy Storage Properties of $Pb_{0.97}La_{0.02}(Zr_{0.58}Sn_{0.335}Ti_{0.085})O_3$ Antiferroelectric Ceramics for Pulse Power Capacitors. *Appl. Phys. Lett.* **2015,** *106* (26), 262901.

7. Shrout, T. R.; Zhang, S. J., Lead-free Piezoelectric Ceramics: Alternatives for PZT? *J. Electroceram.* **2007,** *19* (1), 113-126.

8. Sharifzadeh Mirshekarloo, M.; Yao, K.; Sritharan, T., Large Strain and High Energy Storage Density in Orthorhombic Perovskite $(Pb_{0.97}La_{0.02})(Zr_{1-x-y}Sn_xTi_y)O_3$ Antiferroelectric Thin Films. *Appl. Phys. Lett.* **2010,** *97* (14), 142902.

9. Takenaka, T., Piezoelectric Properties of Some Lead-free Ferroelectric Ceramics. *Ferroelectrics* **1999,** *230* (1), 87-98.

10. Wu, Y.; Zhang, H.; Zhang, Y.; Ma, J.; Xie, D., Lead-free Piezoelectric Ceramics with Composition of $(0.97\text{-}x)Na_{1/2}Bi_{1/2}TiO_3\text{-}0.03NaNbO_3\text{-}xBaTiO_3$. *J. Mater. Sci.* **2003,** *38* (5), 987-994.

11. Saito, Y.; Takao, H.; Tani, T.; Nonoyama, T.; Takatori, K.; Homma, T.; Nagaya, T.; Nakamura, M., Lead-free Piezoceramics. *Nature* **2004,** *432* (7013), 84-87.

12. Shimizu, H.; Guo, H.; Reyes-Lillo, S. E.; Mizuno, Y.; Rabe, K. M.; Randall, C. A., Lead-free Antiferroelectric: $xCaZrO_3\text{-}(1-x)\ NaNbO_3$ System ($0\leq x \leq 0.10$). *Dalton Trans.* **2015**.

13. Levin, I.; Krayzman, V.; Woicik, J. C.; Karapetrova, J.; Proffen, T.; Tucker, M. G.; Reaney, I. M., Structural Changes Underlying the Diffuse Dielectric Response in $AgNbO_3$. *Phys. Rev. B* **2009,** *79* (10), 104113.

14. Yashima, M.; Matsuyama, S.; Sano, R.; Itoh, M.; Tsuda, K.; Fu, D. S., Structure of Ferroelectric Silver Niobate AgNbO3. *Chem. Mater.* **2011,** *23* (7), 1643-1645.

15. Sciau, P.; Kania, A.; Dkhil, B.; Suard, E.; Ratuszna, A., Structural Investigation of $AgNbO_3$ Phases Using X-ray and Neutron Diffraction. *J. Phys.: Condens. Matter* **2004,** *16* (16), 2795.

16. Manish, K. N.; Prasad, K. G.; Saket, A.; Rayaprol, S.; Siruguri, V., Investigation of Structural, Vibrational and Ferroic Properties of $AgNbO_3$ at Room Temperature Using Neutron Diffraction, Raman Scattering and Density-Functional Theory. *J. Phys. D: Appl. Phys.* **2015,** *48* (21), 215303.

17. Fu, D. S.; Endo, M.; Taniguchi, H.; Taniyama, T.; Itoh, M., $AgNbO_3$: A Lead-free Material with Large Polarization and Electromechanical Response. *Appl. Phys. Lett.* **2007,** *90* (25), 3.

18. Tian, Y.; Jin, L.; Zhang, H.; Xu, Z.; Wei, X.; Politova, E.; Stefanovich, S. Y.; Tarakina, N. V.; Abrahams, I.; Yan, H., High Energy Density in Silver Niobate Ceramics. *J. Mater. Chem. A* **2016,** *4* (44), 17279-17287.

19. Zhao, L.; Liu, Q.; Zhang, S.; Li, J.-F., Lead-Free $AgNbO_3$ Anti-ferroelectric Ceramics with Enhanced Energy Storage Performance by MnO_2 Modification. *J. Mater. Chem. C* **2016,** *4* (36), 8380.

20. Zhao, L.; Liu, Q.; Gao, J.; Zhang, S.; Li, J. F., Lead-Free Antiferroelectric Silver Niobate Tantalate with High Energy Storage Performance. *Adv. Mater.* **2017,** *29* (31), 1701824.

21. Tian, Y.; Jin, L.; Zhang, H.; Xu, Z.; Wei, X.; Viola, G.; Abrahams, I.; Yan, H., Phase Transitions in Bismuth-Modified Silver Niobate Ceramics for High Power Energy Storage. *J. Mater. Chem. A* **2017,** *5*, 17525.

22. Fu, D.; Endo, M.; Taniguchi, H.; Taniyama, T.; Itoh, M.; Koshihara, S.-y., Ferroelectricity of Li-doped Silver Niobate (Ag, Li)NbO_3. *J. Phys.: Condens. Matter* **2011,** *23* (7), 075901.

23. Khan, H. U.; Sterianou, I.; Miao, S.; Pokorny, J.; Reaney, I. M., The Effect of Li-substitution on the M-phases of $AgNbO_3$. *J. Appl. Phys.* **2012,** *111* (2), 024107.

24. Fu, D.; Endo, M.; Taniguchi, H.; Taniyama, T.; Koshihara, S.-y.; Itoh, M., Piezoelectric Properties of Lithium Modified Silver Niobate Perovskite Single Crystals. *Appl. Phys. Lett.* **2008,** *92* (17), 172905.

25. Schenk, T.; Schroeder, U.; Pešić, M.; Popovici, M.; Pershin, Y. V.; Mikolajick, T., Electric Field Cycling Behavior of Ferroelectric Hafnium Oxide. *ACS Appl. Mater. Interfaces* **2014,** *6* (22), 19744-19751.

26. Pešić, M.; Fengler, F. P. G.; Larcher, L.; Padovani, A.; Schenk, T.; Grimley, E. D.; Sang, X.; LeBeau, J. M.; Slesazeck, S.; Schroeder, U., Physical Mechanisms behind the Field-Cycling Behavior of HfO2-Based Ferroelectric Capacitors. *Adv. Funct. Mater.* **2016,** *26* (25), 4601-4612.

27. Starschich, S.; Menzel, S.; Böttger, U., Evidence for Oxygen Vacancies Movement During Wake-up in Ferroelectric Hafnium Oxide. *Appl. Phys. Lett.* **2016,** *108* (3), 032903.

28. Schenk, T.; Hoffmann, M.; Ocker, J.; Pešić, M.; Mikolajick, T.; Schroeder, U., Complex Internal Bias Fields in Ferroelectric Hafnium Oxide. *ACS Appl. Mater. Interfaces* **2015,** *7* (36), 20224-20233.

29. Zhou, D.; Xu, J.; Li, Q.; Guan, Y.; Cao, F.; Dong, X.; Müller, J.; Schenk, T.; Schröder, U., Wake-up Effects in Si-doped Hafnium Oxide Ferroelectric Thin Films. *Appl. Phys. Lett.* **2013,** *103* (19), 192904.

30. Fengler, F. P.; Pešić, M.; Starschich, S.; Schneller, T.; Künneth, C.; Böttger, U.; Mulaosmanovic, H.; Schenk, T.; Park, M. H.; Nigon, R., Domain Pinning: Comparison of Hafnia and PZT based Ferroelectrics. *Adv. Electron. Mater.* **2017**.

31. Lu, T.; Studer, A. J.; Noren, L.; Hu, W.; Yu, D.; McBride, B.; Feng, Y.; Withers, R. L.; Chen, H.; Xu, Z.; Liu, Y., Electric-Field-Induced AFE-FE Transitions and Associated Strain/Preferred Orientation in Antiferroelectric PLZST. *Sci. Rep.* **2016,** *6*, 23659.

32. Wang, J.; Liu, Y.; Withers, R. L.; Studer, A.; Li, Q.; Norén, L.; Guo, Y., A Correlated Electron Diffraction, In Situ Neutron Diffraction and Dielectric Properties Investigation of Poled $(1-x)Bi_{0.5}Na_{0.5}TiO_3-xBaTiO_3$ Ceramics. *J. Appl. Phys.* **2011,** *110* (8), 084114.

33. Menou, N.; Muller, C.; Baturin, I. S.; Shur, V. Y.; Hodeau, J.-L., Polarization Fatigue in $PbZr_{0.45}Ti_{0.55}O_3$-based Capacitors Studied from High Resolution Synchrotron X-ray Diffraction. *J. Appl. Phys.* **2005,** *97* (6), 064108.

34. Lupascu, D.; Rödel, J., Fatigue In Bulk Lead Zirconate Titanate Actuator Materials. *Adv. Eng. Mater.* **2005,** *7* (10), 882-898.

35. Hall, D. A.; Mori, T.; Comyn, T. P.; Ringgaard, E.; Wright, J. P., Residual Stress Relief due to Fatigue in Tetragonal Lead Zirconate Titanate Ceramics. *J. Appl. Phys.* **2013,** *114* (2), 024103.

36. Kania, A., Dielectric Properties of $Ag_{1-x}A_xNbO_3$ (A: K, Na and Li) and $AgNb_{1-x}Ta_xO_3$ Solid Solutions in the Vicinity of Diffuse Phase Transitions. *J. Phys. D: Appl. Phys.* **2001,** *34* (10), 1447.

37. Campbell, B. J.; Stokes, H. T.; Tanner, D. E.; Hatch, D. M., ISODISPLACE: a Web-based Tool for Exploring Structural Distortions. *J. Appl. Crystallogr.* **2006,** *39* (4), 607-614.

38. Rodriguez-Carvajal, J. In *FULLPROF: A program for Rietveld Refinement and Pattern Matching Analysis*, satellite meeting on powder diffraction of the XV congress of the IUCr, Toulouse, France:[sn]: 1990.

39. Perez-Mato, J. M.; Orobengoa, D.; Aroyo, M. I., Mode Crystallography of Distorted Structures. *Acta Crystallogr. Sect. A: Found. Crystallogr.* **2010,** *66* (5), 558-590.

40. Liu, Y.; Withers, R. L.; Wei, X.; Fitz Gerald, J. D., Structured Diffuse Scattering and Polar Nano-Regions in the Ba($Ti_{1-x}Sn_x$)O_3 Relaxor Ferroelectric System. *J. Solid State Chem.* **2007,** *180* (3), 858-865.

41. Liu, Y.; Withers, R. L.; Nguyen, B.; Elliott, K., Structurally Frustrated Polar Nanoregions in $BaTiO_3$-based Relaxor Ferroelectric Systems. *Appl. Phys. Lett.* **2007,** *91* (15), -.

42. Levin, I.; Woicik, J. C.; Llobet, A.; Tucker, M. G.; Krayzman, V.; Pokorny, J.; Reaney, I. M., Displacive Ordering Transitions in Perovskite-Like $AgNb_{1/2}Ta_{1/2}O_3$. *Chem. Mater.* **2010,** *22* (17), 4987-4995.

43. Peel, M. D.; Thompson, S. P.; Daoud-Aladine, A.; Ashbrook, S. E.; Lightfoot, P., New Twists on the Perovskite Theme: Crystal Structures of the Elusive Phases R and S of $NaNbO_3$. *Inorg. Chem.* **2012,** *51* (12), 6876-6889.

44. Prosandeev, S.; Wang, D.; Ren, W.; Iniguez, J.; Bellaiche, L., Novel Nanoscale Twinned Phases in Perovskite Oxides. *Adv. Funct. Mater.* **2013,** *23* (2), 234-240.

45. Xu, B.; Paillard, C.; Dkhil, B.; Bellaiche, L., Pinched Hysteresis Loop in Defect-free Ferroelectric Materials. *Phys. Rev. B* **2016,** *94* (14), 140101.

46. Liu, Y.; Norén, L.; Studer, A. J.; Withers, R. L.; Guo, Y.; Li, Y.; Yang, H.; Wang, J., Response of Intergrown Microstructure to an Electric Field and its Consequences in the Lead-free Piezoelectric Bismuth Sodium Titanate. *J. Solid State Chem.* **2012,** *187*, 309-315.

47. Lu, T.; Studer, A. J.; Cortie, D.; Lau, K.; Yu, D.; Feng, Y.; Chen, H.; Xu, Z.; Withers, R. L.; McIntyre, G. J.; Liu, Y., Susceptible Ferroelectric/Antiferroelectric Phase Transition near the Surface of Nb-Doped Lead Zirconate Stannate Titanate from Surface Processing. *ACS Appl. Mater. Interfaces* **2016,** *8* (23), 14313-14317.

48. Shvartsman, V.; Kleemann, W.; Haumont, R.; Kreisel, J., Large Bulk Polarization and Regular Domain Structure in Ceramic $BiFeO_3$. *Appl. Phys. Lett.* **2007,** *90* (17), 172115.

49. Andreeva, N. V.; Pertsev, N. A.; Andronikova, D. A.; Filimonov, A. V.; Leontiev, N. G.; Leontyev, I. N.; Vakhrushev, S. B., Domain Structures and Correlated out-of-Plane and in-Plane Polarization Reorientations in Pb($Zr_{0.96}Ti_{0.04}$)O_3 Single Crystal via Piezoresponse Force Microscopy. *AIP Adv.* **2016,** *6* (9), 095211.

50. Schmitt, L. A.; Kungl, H.; Hinterstein, M.; Riekehr, L.; Kleebe, H.-J.; Hoffmann, M. J.; Eichel, R.-A.; Fuess, H., The Impact of Heat Treatment on the Domain Configuration and Strain Behavior in Pb[Zr,Ti]O_3 Ferroelectrics. *J. Am. Ceram. Soc.* **2015,** *98* (1), 269-277.

51. Alikin, D. O.; Turygin, A. P.; Walker, J.; Bencan, A.; Malic, B.; Rojac, T.; Shur, V. Y.; Kholkin, A. L., The Effect of Phase Assemblages, Grain Boundaries and Domain Structure on the Local Switching Behavior of Rare-Earth Modified Bismuth Ferrite Ceramics. *Acta Mater.* **2017,** *125*, 265-273.

52. Alikin, D. O.; Turygin, A. P.; Walker, J.; Rojac, T.; Shvartsman, V. V.; Shur, V. Y.; Kholkin, A. L., Quantitative Phase Separation in Multiferroic $Bi_{0.88}Sm_{0.12}FeO_3$ Ceramics via Piezoresponse Force Microscopy. *J. Appl. Phys.* **2015,** *118* (7), 072004.

53. Avdeev, M.; Jorgensen, J. D.; Short, S.; Samara, G. A.; Venturini, E. L.; Yang, P.; Morosin, B., Pressure-Induced Ferroelectric to Antiferroelectric Phase Transition in $Pb_{0.99}(Zr_{0.95}Ti_{0.05})_{0.98}Nb_{0.02}O_3$. *Phys. Rev. B* **2006,** *73* (6), 064105.

54. Nomura, K.; Shingai, T.; Yasuda, N.; Ohwa, H.; Terauchi, H., Pressure-Induced Structural Phase Transition from Relaxor Phase to Antiferroelectric Phase in Disordered Pb($In_{1/2}Nb_{1/2}$)O_3. *J. Phys. Soc. Jpn.* **1999,** *68* (3), 866-870.

55. Dong, W. D.; Carlos Valadez, J.; Gallagher, J. A.; Jo, H. R.; Sahul, R.; Hackenberger, W.; Lynch, C. S., Pressure, Temperature, and Electric Field Dependence of Phase Transformations in

Niobium Modified 95/5 Lead Zirconate Titanate. *J. Appl. Phys.* **2015,** *117* (24), 244104.
56. Hall, D. A.; Evans, J. D. S.; Covey-Crump, S. J.; Holloway, R. F.; Oliver, E. C.; Mori, T.; Withers, P. J., Effects of Superimposed Electric Field and Porosity on the Hydrostatic Pressure-induced Rhombohedral to Orthorhombic Martensitic Phase Transformation in PZT 95/5 Ceramics. *Acta Mater.* **2010,** *58* (20), 6584-6591.
57. Mishra, S. K.; Mittal, R.; Pomjakushin, V. Y.; Chaplot, S. L., Phase Stability and Structural Temperature Dependence in Sodium Niobate: A High-resolution Powder Neutron Diffraction Study. *Phys. Rev. B* **2011,** *83* (13), 134105.
58. Lu, X.-Z.; Rondinelli, J. M., Epitaxial-Strain-Induced Polar-to-Nonpolar Transitions in Layered Oxides. *Nat. Mater.* **2016,** *15* (9), 951-955.

Supporting information 1: *P-E* hysteresis loops of AN45LT and AN60LT measured at 1 Hz

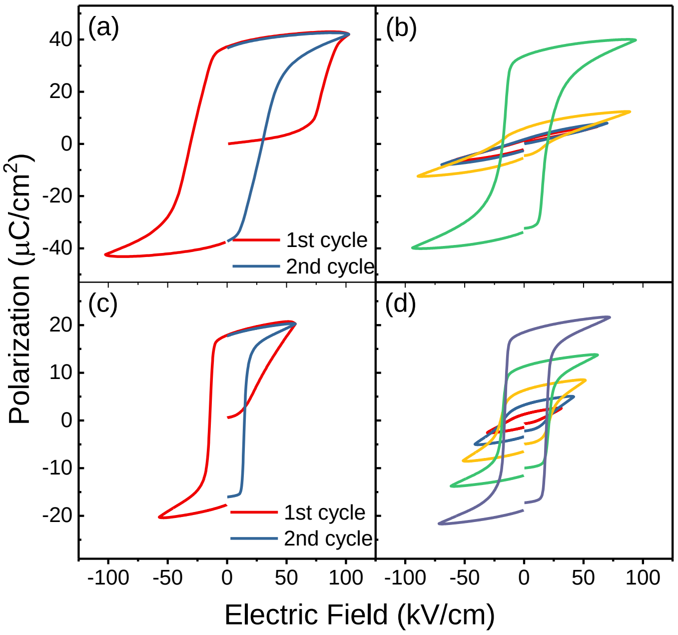

Figure S1 *P-E* hysteresis loops of AN45LT measured at (a) 1st and 2nd cycles, (b) different applied field amplitude. *P-E* hysteresis loops of AN60LT measured at (a) 1st and 2nd cycles, (b) different applied field amplitude.

The *P-E* hysteresis loops of AN45LT and AN60LT measured at different cycles and E-field amplitudes are shown in Figure S1. For AN45LT, the sudden increase of the polarisation around 90 kV/cm during the 1st cycle is commonly associated with the E-field induced AFE to FE phase transition.[1] Furthermore, the square shape single *P-E* hysteresis loop with P_r ~ 38 μC/cm^2 measured at the 2nd cycle suggest that the induced FE phase is metastable after withdrawal of the applied field. The *P-E* hysteresis loops of AN60LT sample measured at different cycles show the similar behaviour while instead of the sudden jump observed in AN45LT, the polarisation increases gradually during the 1st quarter electric cycle. The evolution of *P-E* hysteresis loops with increasing external field amplitude is quite different from that in the normal FE materials (Figure S1c and d)[2-3]. When the E-field is sufficient high, which is around 100 kV/cm for AN45LT and 70 kV/cm for AN60LT, *P-E* hysteresis loops of both samples follow the typical FE features (coercive field, E_C ~ 25 kV/cm for AN45LT and AN60LT, remnant polarisation, P_r ~ 38 μC/cm^2 for AN45LT and 18 μC/cm^2 for AN60LT). It is worthy to note that *P-E* hysteresis loops of both samples measured at the low field, *e.g.*, 70 kV/cm for AN45LT and 40 kV/cm for AN60LT (which surpass the E_C), behave like the lossy dielectric materials, whose profiles are quite similar to that of the pure $AgNbO_3$ measured at the low field [4]. The abovementioned *P-E* hysteresis loops suggest that the pristine AN45LT and AN60LT samples contain similar features of their prototype $AgNbO_3$.

Supporting information 2: The symmetry-mode decomposition of silver niobate

Relative to an undistorted, *Pm*-3*m*, pseudo-cubic perovskite sub-structure (subscript p below), silver niobate ($AgNbO_3$) has a weakly strain distorted, 4x√2x√2 unit-cell and a space group symmetry of $Pmc2_1$ under ambient conditions.[5] The symmetry-mode decomposition of Yashima *et al.*'s $Pmc2_1$ neutron refinement result was carried out using the ISODISTORT software package.[6] Note that in this paper, the parent structure was chosen as the undistorted *Ammm* space group (Figure S2), which accommodates the octahedral rotation. The unit-cell relationships between the resultant $Pmc2_1$, the *Ammm* parent structure (subscript A below) and the pseudo-cubic perovskite sub-structure (subscript p) are as follows:

$\mathbf{a} = 4\mathbf{a}_A \equiv 4\mathbf{c}_p$, $\mathbf{b} = \mathbf{b}_A \equiv \mathbf{a}_p + \mathbf{b}_p$, $\mathbf{c} = \mathbf{c}_A \equiv -\mathbf{a}_p + \mathbf{b}_p$ in real space and $\mathbf{a}^* = {}^1/_4\,[100]_A^* \equiv {}^1/_4\,[001]_p^*$, $\mathbf{b}^* = [010]_A^* \equiv {}^1/_2\,[110]_p^*$, $\mathbf{c}^* = [001]_A^* \equiv {}^1/_2\,[-1,1,0]_p^*$ in reciprocal space. Tables S1 and S2 below show the results of the mode decomposition of the reported $Pmc2_1$ structure with respect to the undistorted *Ammm* structure. There are 6 modulation wave-vectors and 10 associated mode distortions. From the global amplitudes for each mode (Table S2), it is evident that the largest amplitude modes are the $\mathbf{q}_7 = {}^1/_2\,\mathbf{a}_A^*+\mathbf{b}_A^*$ ($[1/2\ 1/2\ 1/2]_p^*$), T_4^+ and $\mathbf{q}_8 = {}^1/_4\,\mathbf{a}_A^*+\mathbf{b}_A^*$, ($[1/2\ 1/2\ 1/4]_p^*$) H_2 modes. Referring to the relationship between the wave-vectors, the third largest amplitude, Λ3 with $\mathbf{q}_3 = {}^1/_4\,\mathbf{a}_A^*$ ($\mathbf{q}_3 = [0\ 0\ {}^1/_4]_p^*$) can be induced by the T4+ and H2, *i.e.*, $\mathbf{q_3=q_7-q_8}$. Therefore, taking the modes amplitude into the consideration, the Λ3 mode belongs to the secondary or induced mode. However, the T4+ and H2 modes are not able to lower the symmetry to $Pmc2_1$. The fourth largest amplitude mode, Γ4-, must be involved as the primary mode.

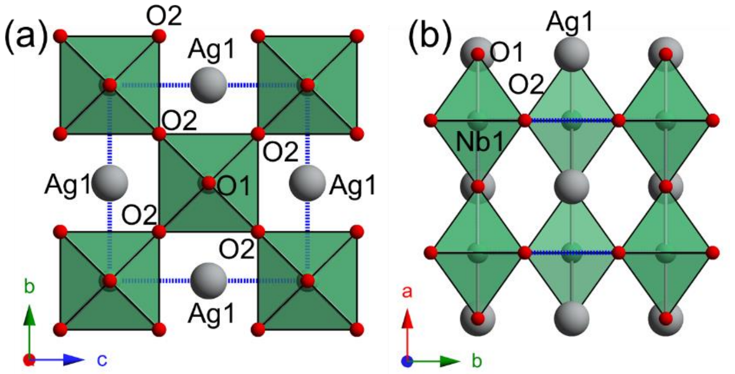

Figure S2. The parent *Ammm* structure viewed along the a) *a*-axis and c) *c*-axis

Table S1. Decomposition of the *Pmc2₁* distorted structure with the origin at ($\mathbf{a_A}$/2, $\mathbf{b_A}$/4, 0.2333$\mathbf{c_A}$) in respect of the displacive modes of the parent *Ammm* structure. The coordinates after the atomic label are for the undistorted structure. Note that as the *Pmc2₁* contains polar axis along the *c*-axis, the atomic coordinates exhibit origin shifts along *c*-axis. The unit-cell parameters for *Pmc*2₁ are: *a*=15.6459 Å, *b*=5.5525 Å, *c*=5.6091 Å, *α*=*β*=*γ*=90°.

Wave-vector	Irreps	Atomic Label							
		O1	0.75	0.75	0.768	Ag1	0.75	0.75	0.268
			δx	*δy*	*δz*		*δx*	*δy*	*δz*
[0 0 0]*	Γ_4^-		0	0	-0.00441		0	0	-0.00042
[$^1/_4$ 0 0]*	Λ_1		0.0004	0	0		0.0004	0	0
[0 1 0]*	Y3-		0	0.00455	0		0	-0.0042	0
[$^1/_2$ 0 0]*	Z3+		0	0	-0.00125		0	0	-0.00125
[$^1/_2$ 1 0]*	T4+		0	-0.05497	0		0	0.0013	0
		O2	0.5	0.75	0.768	Ag2	0.5	0.75	0.268
			δx	*δy*	*δz*		*δx*	*δy*	*δz*
[0 0 0]*	Γ4-		0	0	-0.00441		0	0	-0.00042
[1/4 0 0]*	Λ3		0	0	0.01849		0	0	-0.01949
[0 1 0]*	Y3-		0	0.00455	0		0	-0.0042	0
[1/2 0 0]*	Z3+		0	0	0.00125		0	0	0.00125
[1/2 1 0]*	T4+		0	0.05497	0		0	-0.0013	0
[1/4 1 0]	H4		0	0.0095	0		0	0.0015	0
		O3	0.625	0.5	0.518	O4	0.625	0	0.518
			δx	*δy*	*δz*		*δx*	*δy*	*δz*
[0 0 0]*	Γ4-		0	0.00175	-0.00492		0	-0.00175	-0.00492
[1/4 0 0]*	Λ1		-0.00135	0	0		-0.00135	0	0
[1/4 0 0]*	Λ3		0	0.00025	0.00275		0	-0.00025	0.00275
[0 1 0]*	Y2+		0	0.00575	-0.00525		0	0.00575	0.00525
[1/2 0 0]*	Z2-		0.0002	0	0		0.0002	0	0

[1/2 1 0]*	T4+		-0.01392	0	0		0.01392	0	0
[1/4 1 0]*	H2		0	0.03123	-0.03027		0	0.03123	0.03027
[1/4 1 0]*	H4		-0.00055	0	0		0.00055	0	0
		O5	0	0.25	0.268	Ag3	0	0.75	0.268
			δx	δy	δz		δx	δy	δz
[0 0 0]*	Γ4-		0	0	-0.00441		0	0	-0.00042
[1/4 0 0]*	Λ3		0	0	-0.01849		0	0	0.01949
[0 1 0]*	Y3-		0	-0.00455	0		0	-0.0042	0
[1/2 0 0]*	Z3+		0	0	0.00125		0	0	0.00125
[1/2 1 0]*	T4+		0	-0.05497	0		0	-0.0013	0
[1/4 1 0]	H4		0	0.0095	0		0	-0.0015	0
		O6	0.125	0	0.018	O7	0.125	0.5	0.518
			δx	δy	δz		δx	δy	δz
[0 0 0]*	Γ4-		0	0.00175	-0.00492		0	0.00175	-0.00492
[1/4 0 0]*	Λ1		0.00135	0	0		0.00135	0	0
[1/4 0 0]*	Λ3		0	-0.00025	-0.00275		0	-0.00025	-0.00275
[0 1 0]*	Y2+		0	-0.00575	0.00525		0	0.00575	-0.00525
[1/2 0 0]*	Z2-		0.0002	0	0		0.0002	0	0
[1/2 1 0]*	T4+		0.01392	0	0		-0.01392	0	0
[1/4 1 0]*	H2		0	0.03123	-0.03027		0	-0.03123	0.03027
[1/4 1 0]*	H4		-0.00055	0	0		-0.00055	0	0
		Nb1	0.625	0.75	0.768	Nb2	0.125	0.25	0.268
			δx	δy	δz		δx	δy	δz
[0 0 0]*	Γ4-		0	0	-0.01046		0	0	-0.01046
[1/4 0 0]*	Λ1		0.0001	0	0		-0.0001	0	0
[1/4 0 0]*	Λ3		0	0	-0.02259		0	0	0.02259
[0 1 0]*	Y3-		0	0.00776	0		0	-0.00776	0
[1/2 0 0]*	Z2-		0.0005	0	0		0.0005	0	0
[1/4 1 0]	H4		0	-0.00066	0		0	-0.00066	0

Table S2. The dimensions and global amplitude for the modes observed *Pmc2₁* structures. The wave-vectors are expressed in the settings of parent *Ammm* structure and pseudo-cubic perovskite structure.

Wave-vectors		Irreps	Dimensions	Global Amplitude
Ammm	Pseudo-cubic			
[0 0 0]*	$[0\ 0\ 0]_p$*	Γ4-	5	0.2149
[1/4 0 0]*	$[0\ 0\ 1/4]_p$*	Λ1	4	0.0864
[1/4 0 0]*	$[0\ 0\ 1/4]_p$*	Λ3	5	0.4726
[0 1 0]*	$[1/2\ 1/2\ 0]_p$*	Y2+	2	0.1737
[0 1 0]*	$[1/2\ 1/2\ 0]_p$*	Y3-	3	0.1559
[1/2 0 0]*	$[0\ 0\ 1/2]_p$*	Z3+	2	0.0280
[1/2 0 0]*	$[0\ 0\ 1/2]_p$*	Z2-	2	0.0254

[1/2 1 0]*	[1/2 1/2 1/2]$_p$*	T4+	3	1.2255
[1/4 1 0]*	[1/2 1/2 1/4]$_p$*	H2	2	0.9708
[1/4 1 0]*	[1/2 1/2 1/4]$_p$*	H4	4	0.1127

The following parts present the distorted structure with the 4 main modes (T_4^+, H_2, Λ_3, Γ_4^-). Figure S3a and b present the distorted structure induced by the T4+ mode. T4+ mode occurs in the zone boundary of the first Brillouin zone for the parent structure. As shown in the Figure 2a and b, this mode is a pure R(<110>$_P$) type octahedral rotation around the **c_2=c_A=-a_p+b_p**, which is same as the $a^-a^-c^0$ tilting system in Glazer notation.[7] The distorted structure induced by H2 mode is shown in Figure S3c and d. This zone boundary mode is also associated with the octahedral rotation while different from the T4+ mode, the H2 mode shows a pure R(<001>$_P$) octahedral rotation, *i.e.*, the rotation along the **a** = 4$\mathbf{a}_A$ ≡ 4$\mathbf{c}_P$ axis. Viewed along the *a*-axis (Figure S3c), the NbO_6 octahedral seems to show antiphase tilting. However, as shown in Figure S3d, in single column along the *a*-axis, the adjacent NbO_6 octahedral rotated alternatively. If the anti/clockwise rotations viewed along **a** are denoted by '-/+' respectively. The rotation shown in Figure S3d can be expressed in the form of '--++--'. This type of octahedral rotation is described as $a^0a^0c^+/a^0a^0c^-$ in Glazer notation. If considering the adjacent octahedral behaving the in-phase tilting as a unit, the red-line presents antiphase boundary between these units. Figure S3e shows the distorted structure induced by single Λ_3 mode viewed along the *b*-axis. The Λ3 mode is mainly related with the atomic displacements. The +/- signs denote the cation shifts along the **c**/-**c** directions while the corresponded oxygen shifts in the opposite directions. The red arrow indicates the dipole moment induced by ionic displacements in each sub-lattice. The direction of the spontaneous polarization switches the direction alternatively, resulting in the antiparallel dipole alignment, which suggests the Λ3 mode contributes to the observed antiferroelectricity in $AgNbO_3$. Figure S3e shows the distorted structure with the Γ4- mode. The displacements of all cations (Ag1, Ag2, Ag3, Nb1 and Nb2) and anions (O1, O2, O3, O4, O5, O6, O7) are listed in Table S1. The sum of dipole moments induced by these ionic displacements within one unit-cell is denoted by the red arrow, *i.e.*, spontaneous polarisation along -**c**. Obviously, this zone-centre mode is the origin of the ferroelectricity in silver niobate. Although the Γ4- mode is necessary to lower the symmetry from *Pmca* to *Pmc*2_1, its amplitude is quite small, less than half of the Λ3 mode. The competition between the AFE, Λ3 mode and the FE, Γ4- mode constructs the mentioned ferrielectricity, which is adopted to explain the weak ferroelectricity of silver niobate at the low field.[5]

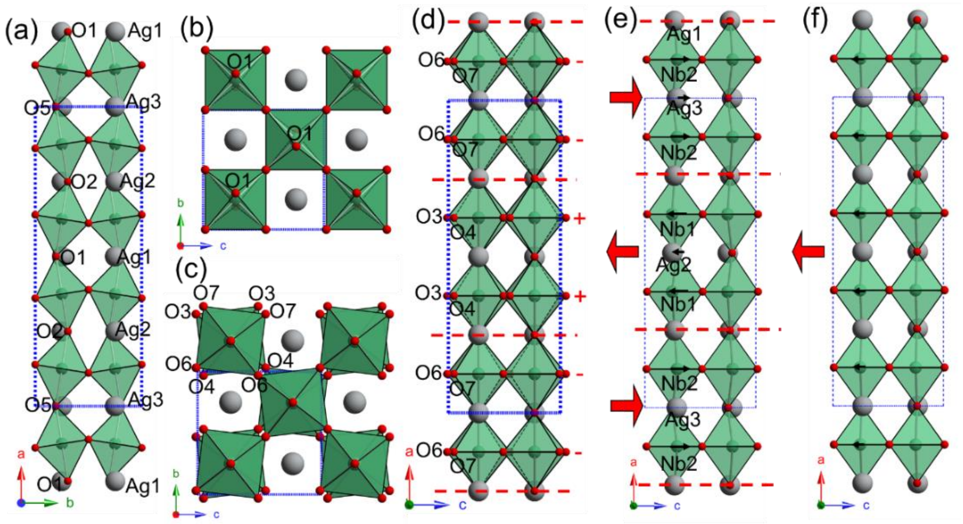

Figure S3. The distorted $AgNbO_3$ structure induced by single T4+ mode viewed along (a) *c*-axis and (b) *a*-axis and by the H2 mode viewed along (a) *a*-axis and (b) *b*-axis. The +/- signs suggest the clockwise/anticlockwise rotation about the *a*-axis, viewed along **a**. The red dash-line reflects the antiphase octahedral tilting boundary. The distorted structure induced by the (e) Λ3 mode and (f) Γ4- mode. The black arrows suggest the cations displacements and red arrow directs the spontaneous polarisation. The red dash-line shows the boundary between antiparallel dipole moment.

Supporting information 3: The results of Rietveld refinement on three states of AN45LT and AN60LT samples.

Table S4. The refined crystal lattice parameters and reliability factors in Rietveld analysis of the NPD data for Unpoled, IM and Poled AN45LT and AN60LT.

Sample name	Space group	Unit-cell parameters (Å)			R-factors				
		a	*b*	*c*	R_p	Rw_p	R_{ex}	R_{Bragg}	R_F
Unpoled AN45LT	*Pmc*2₁	15.6485(25)	5.5347(12)	5.5965(12)	1.89%	2.37%	1.76%	6.22%	5.57%
IM AN45LT	*Pmc*2₁	15.6500(25)	5.5403(12)	5.6032(10)	2.04%	2.57%	1.78%	7.25%	5.29%
	*R*3*c*	5.5281(8)	5.5281(8)	13.7910(18)	2.04%	2.57%	1.78%	5.48%	2.62%
Poled AN45LT	*Pmc*2₁	15.6561(24)	5.5427(8)	5.6050(7)	2.38%	3.10%	1.89%	4.71%	3.28%
	*R*3*c*	5.5291(8)	5.5291(8)	13.7922(18)	2.38%	3.10%	1.89%	2.92%	1.39%

Unpoled AN60LT	$Pmc2_1$	15.6570(22)	5.5298(8)	5.5940(7)	2.34%	2.98%	1.82%	4.08%	4.06%
	$R3c$	5.5244(8)	5.5244(8)	13.7779(18)	2.34%	2.98%	1.82%	2.78%	1.83%
IM AN60LT	$Pmc2_1$	15.6728(26)	5.5323(8)	5.5970(7)	2.27%	2.90%	2.07%	5.91%	5.36%
	$R3c$	5.5266(8)	5.5266(8)	13.7810(18)	2.27%	2.90%	2.07%	4.11%	2.40%
Poled AN60LT	$R3c$	5.5309(8)	5.5309(8)	13.8039(18)	2.72%	3.56%	2.20%	5.21%	3.43%

Table S5. Refined atomic positions of NPD data for unpoled AN45LT at room temperature.

Space group	$Pmc2_1$	Fractional coordinate			Biso(Å^2)
Atomic label	Wickoff site	x	y	z	
Ag3/Li3	2a	0	0.732(2)	0.2917(18)	0.71(3)
Ag1/Li1	4c	0.752(2)	0.752(2)	0.2644(16)	0.71(3)
Ag2/Li2	2b	0.5	0.758(2)	0.2502(18)	0.71(3)
Nb2/Ta2	4c	0.1260(8)	0.2371(11)	0.271(2)	0.30(2)
Nb1/Ta1	4c	0.6282(9)	0.7539(11)	0.738(2)	0.30(2)
O5	2a	0	0.1942(19)	0.231(3)	0.632(18)
O1	4c	0.7509(11)	0.6990(19)	0.749(3)	0.632(18)
O2	2b	0.5	0.8077(19)	0.768(3)	0.632(18)
O6	4c	0.1413(9)	0.0174(16)	-0.010(2)	0.632(18)
O7	4c	0.1144(9)	0.4824(16)	0.530(2)	0.632(18)
O4	4c	0.6418(9)	0.0446(16)	0.562(2)	0.632(18)
O3	4c	0.6079(9)	0.5397(16)	0.483(2)	0.632(18)

Table S6. Refined atomic positions of NPD data for IM AN45LT at room temperature.

Space group	$Pmc2_1$	Fractional coordinate			Biso(Å^2)
Atomic label	Wickoff site	x	y	z	
Ag3/Li3	2a	0	0.729(2)	0.293(2)	0.75(4)
Ag1/Li1	4c	0.752(2)	0.7512(2)	0.264(1)	0.75(4)
Ag2/Li2	2b	0.5	0.7618(9)	0.248(2)	0.75(4)
Nb2/Ta2	4c	0.1261(3)	0.2519(12)	0.2682(17)	0.43(2)
Nb1/Ta1	4c	0.6282(3)	0.7393(11)	0.7313(17)	0.43(2)
O5	2a	0	0.1865(11)	0.2200(19)	0.70(2)
O1	4c	0.751(2)	0.6913(11)	0.7400(19)	0.70(2)
O2	2b	0.5	0.8155(11)	0.7608(19)	0.70(2)
O6	4c	0.1414(5)	0.013(2)	-0.000(2)	0.70(2)
O7	4c	0.1202(5)	0.482(2)	0.521(2)	0.70(2)
O4	4c	0.6463(5)	0.044(2)	0.566(2)	0.70(2)
O3	4c	0.6093(5)	0.534(2)	0.479(2)	0.70(2)

Space group	*R*3*c*	Fractional coordinate			Biso(Å^2)
Atomic label	Wickoff site	x	y	z	
Ag1/Li1	6a	0	0	0.2663	0.75(4)
Nb1/Ta1	6a	0	0	0.0187(8)	0.43(2)
O1	18b	0.5495(14)	0.9887(19)	0.2581(4)	0.70(2)

Table S7. Refined atomic positions of NPD data for poled AN45LT at room temperature.

Space group	*Pmc*2$_1$	Fractional coordinate			Biso(Å^2)
Atomic label	Wickoff site	x	y	Z	
Ag3/Li3	2a	0	0.725(1)	0.280(3)	1.19(6)
Ag1/Li1	4c	0.752(2)	0.748(1)	0.271(2)	1.19(6)
Ag2/Li2	2b	0.5	0.773(2)	0.248(3)	1.19(6)
Nb2/Ta2	4c	0.1261(3)	0.2310(18)	0.249(3)	0.52(3)
Nb1/Ta1	4c	0.6282(3)	0.7601(18)	0.722(2)	0.52(3)
O5	2a	0	0.193(2)	0.218(2)	1.02(5)
O1	4c	0.751(2)	0.697(2)	0.744(2)	1.02(5)
O2	2b	0.5	0.809(2)	0.771(2)	1.02(5)
O6	4c	0.1389(9)	0.011(3)	-0.009(2)	1.02(5)
O7	4c	0.1168(9)	0.489(3)	0.503(2)	1.02(5)
O4	4c	0.6441(9)	0.040(3)	0.552(2)	1.02(5)
O3	4c	0.6057(9)	0.535(3)	0.466(2)	1.02(5)
Space group	*R*3*c*	Fractional coordinate			Biso(Å^2)
Atomic label	Wickoff site	x	y	z	
Ag1/Li1	6a	0	0	0.2663	1.19(6)
Nb1/Ta1	6a	0	0	0.0204(7)	0.52(3)
O1	18b	0.5610(6)	1.0056(9)	0.2578(8)	1.02(5)

Table S8. Refined atomic positions of NPD data for unpoled AN60LT at room temperature.

Space group	*Pmc*2$_1$	Fractional coordinate			Biso(Å^2)
Atomic label	Wickoff site	x	y	z	
Ag3/Li3	2a	0	0.747(2)	0.3037(17)	0.73(4)
Ag1/Li1	4c	0.750(2)	0.746(2)	0.253(1)	0.73(4)
Ag2/Li2	2b	0.5	0.7488(9)	0.2596(17)	0.73(4)
Nb2/Ta2	4c	0.1233(3)	0.2491(12)	0.276(1)	0.47(2)
Nb1/Ta1	4c	0.6236(3)	0.7516(19)	0.745(1)	0.47(2)
O5	2a	0	0.2205(19)	0.278(2)	0.57(2)
O1	4c	0.750(2)	0.6862(19)	0.778(2)	0.57(2)
O2	2b	0.5	0.7983(19)	0.796(2)	0.57(2)

O6	4c	0.1373(5)	0.014(2)	-0.009(2)	0.57(2)
O7	4c	0.1117(5)	0.479(2)	0.531(2)	0.57(2)
O4	4c	0.6390(5)	0.026(2)	0.562(2)	0.57(2)
O3	4c	0.6047(5)	0.530(2)	0.482(2)	0.57(2)
Space group	$R3c$	Fractional coordinate			Biso(Å^2)
Atomic label	Wickoff site	x	y	z	
Ag1/Li1	6a	0	0	0.2663	0.73(4)
Nb1/Ta1	6a	0	0	0.0193(8)	0.47(2)
O1	18b	0.5687(14)	1.009(2)	0.2583(8)	0.57(2)

Table S9. Refined atomic positions of NPD data for IM AN60LT at room temperature.

Space group	$Pmc2_1$	Fractional coordinate			Biso(Å^2)
Atomic label	Wickoff site	x	y	z	
Ag3/Li3	2a	0	0.748(2)	0.301(2)	0.62(4)
Ag1/Li1	4c	0.750(2)	0.743(2)	0.253(1)	0.62(4)
Ag2/Li2	2b	0.5	0.7535(9)	0.262(1)	0.62(4)
Nb2/Ta2	4c	0.1233(3)	0.2491(12)	0.256(2)	0.25(2)
Nb1/Ta1	4c	0.6236(3)	0.7516(19)	0.737(2)	0.25(2)
O5	2a	0	0.2396(19)	0.233(3)	0.48(2)
O1	4c	0.750(2)	0.6900(19)	0.734(3)	0.48(2)
O2	2b	0.5	0.8010(19)	0.753(3)	0.48(2)
O6	4c	0.1358(5)	0.041(16)	-0.024(9)	0.48(2)
O7	4c	0.1132(5)	0.4943(16)	0.505(2)	0.48(2)
O4	4c	0.6409(5)	0.030(2)	0.548(2)	0.48(2)
O3	4c	0.6027(5)	0.528(2)	0.474(2)	0.48(2)
Space group	$R3c$	Fractional coordinate			Biso(Å^2)
Atomic label	Wickoff site	x	y	z	
Ag1/Li1	6a	0	0	0.2663	0.62(4)
Nb1/Ta1	6a	0	0	0.0195(8)	0.25(2)
O1	18b	0.5626(14)	1.004(2)	0.2566(8)	0.48(2)

Table S6 Refined atomic positions of NPD data for poled AN60LT at room temperature.

Space group	$R3c$	Fractional coordinate			Biso(Å^2)
Atomic label	Wickoff site	x	y	z	
Ag1/Li1	6a	0	0	0.2663	1.10(4)
Nb1/Ta1	6a	0	0	0.0211(6)	0.55(2)
O1	18b	0.5618(14)	1.0071(9)	0.2567(5)	0.35(2)

Supporting information 4: PFM results of Unpoled AN60LT samples

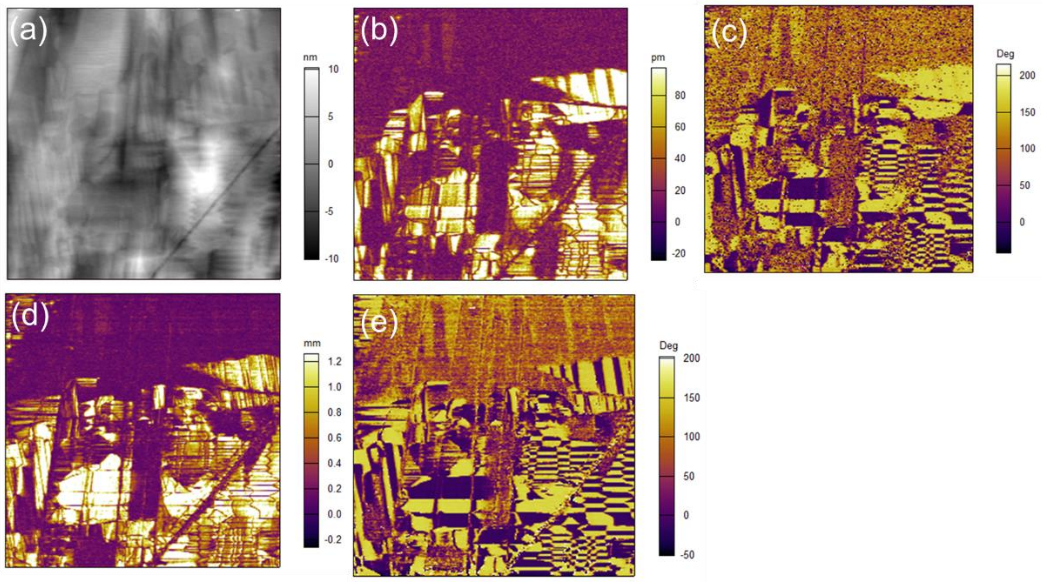

Figure S4. (a) Morphology, (b) vertical amplitude, (c) vertical phase, (d) lateral amplitude and (e) lateral phase of 10 × 10 μm area on Unpoled AN60LT.

References:

1. Tan, X.; Frederick, J.; Ma, C.; Jo, W.; Rödel, J., Can an Electric Field Induce an Antiferroelectric Phase Out of a Ferroelectric Phase? *Phys. Rev. Lett.* **2010,** *105* (25), 255702.

2. Liu, J. M.; Pan, B.; Yu, H.; Zhang, S. T., Dynamic Hysteresis Dispersion Scaling of Ferroelectric Nd-substituted $Bi_4Ti_3O_{12}$ Thin Films. *J. Phys.: Condens. Matter* **2004,** *16* (8), 1189.

3. Zhou, D.; Guan, Y.; Vopson, M. M.; Xu, J.; Liang, H.; Cao, F.; Dong, X.; Mueller, J.; Schenk, T.; Schroeder, U., Electric Field and Temperature Scaling of Polarization Reversal in Silicon Doped Hafnium Oxide Ferroelectric Thin Films. *Acta Mater.* **2015,** *99* (Supplement C), 240-246.

4. Fu, D. S.; Endo, M.; Taniguchi, H.; Taniyama, T.; Itoh, M., $AgNbO_3$: A Lead-free Material with Large Polarization and Electromechanical Response. *Appl. Phys. Lett.* **2007,** *90* (25), 3.

5. Yashima, M.; Matsuyama, S.; Sano, R.; Itoh, M.; Tsuda, K.; Fu, D. S., Structure of Ferroelectric Silver Niobate $AgNbO_3$. *Chem. Mater.* **2011,** *23* (7), 1643-1645.

6. Campbell, B. J.; Stokes, H. T.; Tanner, D. E.; Hatch, D. M., ISODISPLACE: a Web-based Tool for Exploring Structural Distortions. *J. Appl. Crystallogr.* **2006,** *39* (4), 607-614.

7. Glazer, A., Simple Ways of Determining Perovskite Structures. *Acta Crystallogr., Sect. A: Cryst. Phys., Diffr., Theor. Gen. Crystallogr.* **1975,** *31* (6), 756-762.

Chapter 4 Summary of Main Outcomes and Perspectives

Within the thesis, structure-properties relationship during the fields induced phase transitions in two typical AFE material systems – $PbZrO_3$ and $AgNbO_3$-based solid solutions has been investigated. The main analyses help to develop a strategy for designing the novel AFE materials. This chapter summarizes the experimental results reported in the main journal publications. According to the investigated materials, PLZST, PNZST and ANLT, the findings have been divided into three sections. The detailed discussions are available in the relevant papers (***bold and italics*** denote the specific links). At the end of this Chapter, the perspectives of the continuing work are briefly discussed.

4.1 Electric Field Induced Phase Transition in PLZST

The crystal structure, preferred orientation and associated lattice strain evolutions as a function of E-field in typical AFE material - $Pb_{0.97}La_{0.02}(Zr_{0.56}Sn_{0.33}Ti_{0.11})O_3$ ceramics were investigated via *in-situ* neutron diffraction. The results firstly stress the irreversible features from the structural point of view even though the property measurements support the E-field induced reversible phase transition. In addition, this work also provides an explanation for several anomalies obtained during the properties measurements.

- The average structure characterized by NPD of the PLZST sample belongs to pseudo-tetragonal with primitive unit-cell relationship: $a_p = b_p > c_p$. According to the electron diffraction patterns, the local structure of the sample presents an incommensurate modulation wave along $<110>_p$* direction. The wave-vector is $1/\gamma[110]_p^*$ with $\gamma \sim 10$ and not an integer. This structure modulation mainly reflects the off-centre Pb ions displacements, which is associated with the antiferroelectricity observed in the PLZST materials. (***3.1 Figure 1*** and ***Figure S1***)
- The *in-situ* NPD patterns at different E-field (0 kV/cm → 20 kV/cm → 33 kV/cm → 45 kV/cm → 20 kV/cm → 0 kV/cm) indicates when the field is below 33 kV/cm, the average structure is pseudo-tetragonal, showing the typical AFE_T phase. As further increasing the E-field, the structure of the induced FE phase is proposed to be pseudo-cubic while the real symmetry should be rhombohedral (FE_R) due to the large induced

polarisation and $a^-a^-a^-$ octahedral tilting. With decreasing E-field from the maximum field of 45 kV/cm, the structure of PLZST sample reverts, as expected, to the AFE$_T$ phase. ***(3.1 Figure 1***)

- Although the average structure for initial AFE$_T$ and final AFE$_T$ state are almost same, the ω-dependent NPD patterns behave quite differently, suggesting the formation of preferred orientation during this E-field induced AFE-FE phase transition. After the quantitative analysis, f_{200}(MRD), which is used to index the preferred orientation of the 200 peaks, is a flat line in the initial AFE$_T$ state but becomes a curve in the final AFE$_T$ state. (***3.1 Figure 1 and Figure 2***)

- The ω-dependent NPD patterns of the intermediate FE$_R$ state suggests that it contains a strong elliptical distributed lattice strain. *i.e.*, the strain in the sample is no longer homogeneous as a consequence of the elongation in the direction of the applied E-field and the contraction in the direction perpendicular to the E-field. This strain distribution in the FE state directly determines the preferred orientation in the final AFE$_T$ state, *i.e.* the a_P-axis of the pseudo-tetragonal cell prefers to align parallel to the E-field while the c_P-axis prefers to align perpendicular to the E-field. (***3.1 Figure 1 and Figure 2***)

- The temperature-dependent dielectric spectrum of the sample with preferred orientation has an additional and a relatively sharp dielectric peak around 131℃. Before the sample is heated into the paraelectric (PE) phase, it shows larger dielectric constant than the sample without preferred orientation. As samples experience AFE-PE phase transition, the preferred orientation disappears. Furthermore, formation of the preferred orientation reduces the longitudinal E-field induced strain associated with the AFE-FE phase transition. (***3.1 Figure 3***)

4.2 Phase Transitions in PNZST

Two PNZST samples - $Pb_{0.99}(Nb_{0.02}Zr_{0.73}Sn_{0.21}Ti_{0.04})O_3$ (PNZST1) and $Pb_{0.99}(Nb_{0.02}Zr_{0.65}Sn_{0.28}Ti_{0.05})O_3$ (PNZST2) were involved in my PhD project. They were systematically studied by XPRD and NPD for the structural characterization, and PFM for the properties characterization. The novel phenomenon, that structure at the near surface and bulk regions is different, was observed in PNZST1. Furthermore, the structure near the surface region is very sensitive to the surface processing and according to the *in-situ* NPD, the underlying reason is attributed to the mechanical force and heat-treatment induced phase transitions. In contrast, PNZST2 presents a consistent structure in surface and bulk regions. Its E-field and temperature induced crystal structure, preferred orientation and lattice strain evolutions were systematically investigated by the *in-situ* NPD. The results are interesting and important in understanding the role of the coupling between the various modes in these materials and how they affect bulk properties.

- The XPRD results of the PNZST1 sample indicate that the virgin sample shows the AFE_O phase which is quite similar to the structure of the prototype $PbZrO_3$. After the polishing, the sample contains both AFE and rhombohedral FE phases. With further heat-treatment, the sample presents single rhombohedral FE phase and after repolishing the surface, the state of AFE and FE coexistence returns. The NPD indicates that the sample only shows a single FE phase in regardless of the polishing and heat-treatment. Considering the penetration length of lab X-ray and neutron facilities, the diffraction patterns reflect the structural information for the near surface and bulk regions, respectively. This result not only reports the structural inconsistency between the surface and bulk regions, but also points out the near-surface structure is sensitive to the surface processing. (***3.2 Figure 1***)

- For the sample after polishing, the PFM results show two typical regions. Some parts present uniform amplitude and phase without obvious contrasts. Other areas present clear features of the rhombohedral FE domains. This result further proves the coexistence of AFE and FE phases after mechanical polishing. The sample after heat-treatment shows labyrinthine domains with a size distributed over the range of ~100-200 nm, similar to the domains observed in relaxor ferroelectrics. Therefore, the heat-treatment not only induces the FE phase out of AFE phase, but also reduces the domain size. (***3.2 Figure 2***)

- The *in-situ* NPD characterization at different hydrostatic pressures was carried on the powder of the sample after heat-treatment. Under ambient conditions, the powder sample presents same structure as the bulk sample – rhombohedral symmetry. When the hydrostatic pressure reaches 169 MPa, the observed NPD pattern shares the similar features with the AFE phase. Therefore, the coexistence of the AFE and FE phases in the near surface region is possibly due to the strain change induced by the mechanical polishing. The heat-treatment helps release the surface stress/strain, in turn inducing the AFE to FE phase transition. As the phase transitions only occur near the surface, the ceramic samples always present typical FE properties macroscopically. (***3.2 Figure 3 and Figure 4***)

- The NPD pattern of PNZST2 under ambient conditions suggests that the sample shows the AFE structure which is dominated by both AFE, $\mathbf{q_1} = \gamma[110]_p^*$ mode and AFD, $\mathbf{q_2} = 1/2[111]_p^*$, mode. With *in-situ* applying E-field to 25 kV/cm, the AFE phase transfers into FE phase which is dominated by FE, $\mathbf{q} = [000]_p^*$, mode and AFD, $\mathbf{q}_2 = ½[111]_p^*$ mode. After withdrawal of the E-field, the FE phase is still stable. This E-field induced structural change is in agreement with the measured *P-E* hysteresis loops. (***3.3 Figure 1 and 2***)

- The associated preferred orientation and lattice strain were investigated by the ω-dependent NPD patterns. The grains/domains in the virgin AFE phase present random distribution. After being switched into the FE phase, the $[111]_p$ polar axis prefers to align parallel to the E-field, forming a strong preferred orientation. Additionally, the lattice strain behaves elliptical distribution with elongation along the E-field. After withdrawal of the E-field, both preferred orientation and lattice strain in the metastable FE phase present little relaxation. (***3.3 Figure 2***)

- The temperature dependent dielectric spectra and *P-E* hysteresis loops indicate the metastable FE phase experiences at least 2 phase transitions before entering the paraelectric phase. The *in-situ* neutron diffraction suggests the first phase transition around 376 K, is associated with two FE phases. During this phase transition, the AFD mode disappears, *i.e.*, the high-temperature FE phase is simply dominated by the FE mode. With further increasing the temperature to 438 K, FE to AFE phase transition occurs. Interestingly, AFE and AFD modes reappear simultaneously during this phase transition. Furthermore, the obtained double *P-E* hysteresis loop also conforms to the AFE phase. According to the ω-dependent NPD patterns, the preferred orientation formed in metastable FE phase presents minor variation during the FE-to-FE phase transition but disappears during the FE-to AFE phase transition. (***3.3 Figure 3***)

- The *in-situ* NPD was carried out to investigate the E-field induced phase transitions at high temperature. With applying 20 kV/cm E-field, the induced FE phase appears, showing a pseudo-cubic symmetry without AFD mode. After withdrawal of the E-field, the AFE and AFD modes also reappear simultaneously. The temperature and E-field induced phase transitions observed in this material address that both AFE and AFD modes are required in stabilizing the AFE structure. The evolution of the preferred orientation in this E-field induced AFE-FE phase transition at high temperature are similar to that described for the PLZST sample. Once this kind of preferred orientation has been built at high temperature, it will be stored after cooling to room temperature. (***3.3 Figure 4***)
- The dielectric and FE properties between the textured and non-textured samples show differences. The resultant textured sample has a lower critical field for AFE-FE phase transition at room temperature compared with the non-textured sample, suggesting that $E_{\mathrm{AFE\text{-}FE}}$ can be tuned by the preferred orientation. (***3.3 Figure 5***)

4.3 Phase Transitions in (1-x)AgNbO$_3$-xLiTaO$_3$ Material System

Structure and properties of the (1-x)AgNbO$_3$-xLiTaO$_3$ (ANLT100x) with x = 0, 0.03, 0.045, 0.053, 0.06 and 0.09, ceramics have been characterized by the NPD and electrical properties measurements. The symmetry-mode decomposition approach and refinement of the distortive modes' amplitude were utilized in structural analysis, which assists to develop a comprehensive understanding on the composition and E-field cycling-driven phase transitions in ANLT100x.

- The symmetry-adapted mode decomposition of AgNbO$_3$ identifies the difference between the *Pbcm* and *Pmc*2$_1$ space groups, which are commonly used to solve the room-temperature AgNbO$_3$ structure. Both distorted structures share 3 main modes

(T4+, H2, Λ3) with large amplitude. The only difference between the *Pbcm* and *Pmc*2₁ structures is the zone-centre Γ4- mode in *Pmc*2₁ structure, which lowers *Pbcm* symmetry into *Pmc*2₁ and is regarded as the origin of the weak ferroelectricity in $AgNbO_3$. (***3.4 section 2***)

- The refinement of the distortive modes' amplitude on the NPD data was used to solve the structure of the ANLT100*x* ceramics. The single *Pmc*2₁ phase model is only appropriate for the samples with low $LiTaO_3$ doping level ($x < 5.3\%$). After crossing this boundary, the rhombohedral *R*3*c* phase appears. With further increasing x, the *R*3*c* phase fraction grows up while the ratio of *Pmc*2₁ phase reduces correspondingly. The appearance and growth of the *R*3*c* phase are close related to the variation of the dielectric peak, T_U in the temperature-dependent dielectric spectra. (***3.4 section 3***)

- Among the primary modes in the *Pmc*2₁ phase, H2 modes, $a^0a^0c^-/a^0a^0c^+$ octahedral tilting, becomes destabilized when x is around 0.053, which coincides with the appearance of the *R*3*c* phase. The amplitude of T4+ mode, $a^-a^-c^0$ octahedral rotation, almost remains constant during this composition-driven phase transition. The Λ3 mode, or the AFE mode, which is induced by these 2 octahedral rotation modes, varies consistently with the H2 mode as a function of the x. The destabilisation of the Λ3 mode with increasing $LiTaO_3$ content, is directly reflected by the *P-E* hysteresis loops. (***3.4 Figure 6, Figure 7, Figure 8 and Figure 10***)

- When $x > 5.3\%$, the *R*3*c* phase becomes the dominant phase. With the increment of *x*, the amplitude of FE mode in *R3c* phase drops slightly. This structural change is quite in accordance with the measured *P-E* hysteresis loops for ANLT5.3, ANLT6 and ANLT9 samples. Furthermore, the amplitude of AFD, $a^-a^-a^-$ octahedral tilting, mode in *R*3*c* phase rises with increasing x, resulting in the shrinkage of the unit-cell volume. (***3.4 Figure 6, Figure 7, Figure 8 and Figure 10***)

- In EDPs of ANLT4.5, the satellite reflections $\mathbf{G}_P \pm [1/2\ 1/2\ 1/3]_P^*$ are also observed in addition to the $\mathbf{G}_P \pm [1/2\ 1/2\ 1/4]_P^*$ which is the typical features for the H2 mode. In EDPs of ANLT6, a sharp diffuse streaking across the $\mathbf{G}_P \pm [1/2\ 1/2\ 1/2]_P^*$ was unambiguously observed. The above observations indicate that the condensation point of the H2 mode moves towards the zone boundary (T point) with more $LiTaO_3$ doping. Correspondingly, the wave-vector of Λ3 mode will shift towards the zone centre (Γ point) with increasing x. The results of the EDPs present the intermediate states between the $Pmc2_1$ and $R3c$ phases locally and highlight the importance of the H2 mode on this composition-driven $Pmc2_1$ to $R3c$ phase transition. (***3.5 Figure 6, Figure 7 and Figure 8***)

- The ferroelectric properties of ANLT4.5 and ANLT6 were carefully characterized. Their *P-E* loops measured at the low field present the profiles of lossy dielectrics with tiny remnant polarisation (P_r), which are similar to the pure $AgNbO_3$. However, when applying a strong E-field, instead of the double *P-E* hysteresis loops, both ANLT4.5 and ANLT6 display squared shape *P-E* loops with large P_r value (~ 40 μC/cm^2 for ANLT4.5 and ~ 20 μC/cm^2 for ANLT6). The *P-E* behaviours of ANLT4.5 and ANLT6 indicate their pristine states containing AFE nature. Interestingly, electrical cycling with the low field is able to increase the P_r for both ANLT4.5 and ANLT6, which is in accordance with the ferroelectric wake-up effects phenomenologically. (***3.5 Figure 1***)
- With the analyses of the NDP patterns of the sample experiencing different numbers of electrical cycles, the field cycling induced phase transition from $Pmc2_1$ to $R3c$ has been highlighted as the main driving force for the wake-up effects. From the average structure aspects, ANLT6 shows $Pmc2_1$ and $R3c$ phases coexistence while ANLT4.5 only contains single $Pmc2_1$ phase. Obviously, the energy barrier between the $Pmc2_1$ and $R3c$ is shallower in ANLT6 than that in ANLT4.5, which consists with that lower E-field is required for 'wake-up' in ANLT6. (***3.5 Figure 2, Figure 3 and Figure 4***)
- PFM results on ANLT6 demonstrate that it is easier to induce the FE phase in the two phases coexistence region rather than the non-polar region, which is in accordance with that observed during the macroscopic wake-up process. This phenomenon addresses the impacts of the local strain induced by the phase transition and non-180° domain switching in rhombohedral phase on the wake-up effects observed in the ANLT material systems. (***3.5 Figure 9***)

4.4 Future Work

In consideration of the results presented in this PhD project and the current research status reflected in the literature, several issues related to the phase transitions in AFE materials are proposed for future investigations.

- It is predicted that the AFE properties, especially the critical field, are possibly tuned by the preferred orientation (***3.3 Figure 5***). Obviously, systematic work is required for supporting this hypothesis. We therefore synthesized another PLZST ceramics which satisfy the requirement. After poling at different temperatures, the critical field is measured associated with the *P-E* hysteresis loops. The ω-dependent NPD is proposed to check the preferred orientation. This neutron beam proposal has already been approved and the relative investigations will be completed soon.
- The PFM results in both ANLT and PNZST samples (***3.2 Figure 2 and 3.5 Figure 11***) indicate that the local strain or strain gradient showing a strong impact on the polar/non-polar domains. In future, we proposed to use Nano-indenter to generate the residual strain and strain gradient on FE, AFE and relaxor ferroelectric materials. Then PFM and other local probes are used to investigate the domain structures and other properties in this region with residual strain and/or strain gradient.
- Section 3.3, 3.4 and 3.5 elucidate that symmetry mode decomposition approach and refinement of the distorted mode amplitudes are a very useful tool to analyze the crystal structure. According to our studies, it is found in $PbZrO_3$ prototype AFE material, the AFE mode is treated as the primary order parameter while in $AgNbO_3$ material, the AFE mode is suggested to be the induced mode. Comparing the driving force for the antiferroelectricity in $PbZrO_3$ and $AgNbO_3$ are meaningful in both fundamental science and practical applications. Therefore, the inelastic neutron or X-ray scattering techniques are suggested to further investigate the evolution of the phonons in PZO and ANO during phase transitions.
- Theoretical calculations such as density functional theory (DFT), molecular dynamics simulation, are useful and relative mature techniques to design the novel

materials. Recently, plenty of works have been carried out to combine these theoretical calculations with the mode decomposition approach, which helps explain the origin of the relative physical properties from the overall energy point of view. In future, we will try to utilize the theoretical calculation to understand the impacts of different modes on the structural stability of the $AgNbO_3$.

Appendix: Complete List of the Publications and Conference Presentation

1. Journal Publications

Lu, T.; Studer, A. J.; Noren, L.; Hu, W.; Yu, D.; McBride, B.; Feng, Y.; Withers, R. L.; Chen, H.; Xu, Z.; Liu, Y., Electric-field-induced AFE-FE transitions and associated strain/preferred orientation in antiferroelectric PLZST. ***Scientific reports*** 2016, *6*, 23659.

Lu, T.; Studer, A. J.; Cortie, D.; Lau, K.; Yu, D.; Feng, Y.; Chen, H.; Xu, Z.; Withers, R. L.; McIntyre, G. J.; Liu, Y., Susceptible Ferroelectric/Antiferroelectric Phase Transition near the Surface of Nb-Doped Lead Zirconate Stannate Titanate from Surface Processing. ***ACS Applied Materials & Interfaces*** 2016, *8* (23), 14313-14317.

Lu, T.; Studer, A. J.; Yu, D.; Withers, R. L.; Feng, Y.; Chen, H.; Islam, S. S.; Xu, Z.; Liu, Y., Critical role of the coupling between the octahedral rotation and A-site ionic displacements in $PbZrO_3$-based antiferroelectric materials investigated by in-situ neutron diffraction. ***Physical Review B,*** 2017*, 96* (21), 214108.

Li, Q.; **Lu, T.**; Schiemer, J.; Laanait, N.; Balke, N.; Zhang, Z.; Ren, Y.; Carpenter, M. A.; Wen, H.; Li, J.; Kalinin, S. V.; Liu, Y., Giant Thermally-Enhanced Electrostriction and Surface Polar Phase in $La_2Mo_2O_9$ Oxygen Ion Conductors. ***Physical Review Materials***, 2018, *2*, 041403.

Mai, H.; **Lu, T.**; Li, Q.; Liu, Z.; Li, Y.; Kremer, F.; Li, L.; Withers, R. L.; Wen, H.; Liu, Y., Above-bandgap Photo-Induced Stabilization of Engineered Ferroelectric Domains. ***ACS Applied Materials & Interfaces*** 2018, *10*, 12781.

Liu, Z.; **Lu, T.**; Ye, J.; Wang, G.; Dong, X.; Withers, R.; Liu, Y., Antiferroelectrics for Energy Storage Applications: A Review. ***Advanced Materials Technologies***, accepted.

Awan, M. Q.; Ahmad, J.; Norén, L.; **Lu, T.**; Liu, Y., Structure, Dielectric and Ferroelectric Properties of Lead Free (K,Na)NbO_3-x$BiErO_3$ Piezoelectric Ceramics. ***Journal of Materials Science: Materials in Electronics*** 2018, *29*, 7142.

McBride, B.; Lieschke, J.; Berlie, A.; Cortie, D. L.; Playford, H. Y.; **Lu, T.**; Narayanan, N.; Withers, R. L.; Yu, D.; McIntyre, G. J.; Liu, Y., Study of the B-site Behaviour in Bulk Ferroelectric Bismuth Iron Chromium Oxide. ***Journal of Applied Physics*** 2018, *123* (15), 154104.

Liu, Z.; Ren, W.; Peng, P.; Guo, S.; **Lu, T.**; Liu, Y.; Dong, X.; Wang, G., High

Performance $Bi_{0.5}Na_{0.5}TiO_3$-$BiAlO_3$-$K_{0.5}Na_{0.5}NbO_3$ Lead-Free Pyroelectric Ceramics for Thermal Detectors. ***Applied Physics Letters*** 2018, *112* (14), 142903.

Yu, D.; Avdeev, M.; Sun, D.; Huston, L.; Shiell, T. B.; Sun, Q.; **Lu, T.**; Gu, Q.; Liu, H.; Bradby, J., Understanding the Unusual Response to High Pressure in KBe2BO3F2. ***Scientific reports*** 2017, *7*.

Sun, Q.; Huston, L. Q.; Frankcombe, T. J.; Bradby, J. E.; **Lu, T.**; Yu, D.; Zhou, C.; Fu, Z.; Liu, Y., Trans-Regime Structural Transition of (In3++ Nb5+) Co-Doped Anatase TiO2 Nanocrystals under High Pressure. ***Crystal Growth & Design*** 2017, *17* (5), 2529-2535.

Peng, J.; Wu, Y.; Ye, W.; Jacobs, D. A.; Shen, H.; Fu, X.; Wan, Y.; Duong, T.; Wu, N.; Barugkin, C.; Nguyen, H. T.; Zhong, D.; Li, J.; **Lu, T.**; Liu, Y.; Lockrey, M. N.; Weber, K. J.; Catchpole, K. R.; White, T. P., Interface passivation using ultrathin polymer-fullerene films for high-efficiency perovskite solar cells with negligible hysteresis. ***Energy & Environmental Science*** 2017, 10, 1279.

2. Unpublished Work

Lu, T.; Tian, Y.; Studer, A. J.; Withers, R. L.; Jin, L.; Mendez-González, Y.; Peláiz-Barranco, A.; Yu, D.; Xu, Z.; Wei, X.; Yan, H.; Liu, Y., The symmetry-mode decomposition, structure refinement and ferroelectricity of $(1-x)AgNbO_3$-$xLiTaO_3$. *In preparation*.

Lu, T.; Tian, Y.; Studer, A. J.; Li, Q.; Withers, R. L.; Jin, L.; Yu, D.; Xu, Z.; Wei, X.; Yan, H.; Liu, Y., Ferroelectric wake-up effect and underlying mechanism observed in $AgNbO_3$-based antiferroelectric materials. *In preparation*.

3. Conference presentations

1. Symposium on Materials Chemistry, Kioloa Coastal Campus, The Australian National University, Oct 2014. *Oral presentation*.

2. The 2nd Australia-China Symposium on Colossal Permittivity Materials and Applications in Energy storage, The Australian National University, Jan 2016. *Oral presentation*.